The Development of a Nanoscale Coulter Counter for Rapid Genetic Sequence Recognition

by

Timothy Allman Denison

Submitted to the Department of Electrical Engineering and Computer Science
in partial fulfillment of the requirements for the degree of

Doctor of Philosophy

at the

MASSACHUSETTS INSTITUTE OF TECHNOLOGY

July 2000

Author .....
Department of Electrical Engineering and Computer Science
July 4, 2000

Certified by .....
Steven Leeb
Associate Professor of Electrical Engineering
Thesis Supervisor

Certified by .....
James Roberge
Professor of Electrical Engineering
Thesis Supervisor

Certified by ...
Daniel Branton
Professor of Biology, Harvard University
Thesis Supervisor

Accepted by .....
Arthur C. Smith
Chairman, Department Committee on Graduate Students

The Development of a Nanoscale Coulter Counter for Rapid Genetic Sequence Recognition

by

Timothy Allman Denison

Submitted to the Department of Electrical Engineering and Computer Science
on July 4, 2000, in partial fulfillment of the
requirements for the degree of
Doctor of Philosophy

Abstract

The goal of this thesis is the development of a nanoscale Coulter counter for the direct electrical detection of specific genetic sequences of deoxyribonucleic acid (DNA); the general approach used to accomplish sequence recognition is a refinement of the resistive pulse technique. Commercial Coulter counters fabricated with sub-micrometer apertures can size particles with roughly twenty nanometers of resolution. The characterization of DNA, which is more than an order of magnitude smaller than this resolution limit, requires the development of a detection system with a two nanometer limiting aperture.

To help develop the techniques and instrumentation explored in this thesis, the biological toxin, alpha hemolysin, was implemented as "prototype" limiting aperture. With the practical knowledge gained from using a toxin channel, a general model for the nanopore as a low-noise sensor was developed. With this model, two broad goals were achieved. The first achievement was the development of novel genetic recognition strategies that exploit the properties of the nanopore within the limitations imposed by DNA structure and existing channel geometries. The second achievement was the design and prototyping of novel interface picoammeter for the measurement of the current fluctuations associated with DNA translocation through a nanopore. Although the instrumentation and methods developed in this thesis are limited to genetic sequence *recognition*, the hope is that elements of this work will be integrated with the development of silicon nanopores to achieve rapid *de novo* DNA sequencing in the future.

Thesis Supervisor: Steven Leeb
Title: Associate Professor of Electrical Engineering

Thesis Supervisor: James Roberge
Title: Professor of Electrical Engineering

Thesis Supervisor: Daniel Branton
Title: Professor of Biology, Harvard University

Acknowledgments

I have had the privilege of working with many extraordinary people on this thesis project. Steve Leeb and Jim Roberge have provided outstanding feedback on the design of interface circuitry and overcoming the challenges of instrumentation design and development. Their intellectual and creative brainpower is inspiring, and coupled with their kindness and good humor, makes for excellent advising. Thank you! Dan Branton should be saluted for conceiving of this novel instrument and guiding it's development with a multidisciplinary group of scientists and engineers. I thank him for taking a chance and supporting my work. Rajeev Ram is also source of inspiration, and I thank him particularly for his input on the thesis document.

Many colleagues have helped me with this thesis, particularly the members of the Sequencing Lab at the Rowland Institute for Science and LEES Lab at MIT. In particular, Alexis Sauer, Jacky Nyamwanda, Eric Brandin, Ciaran McMullan and John Rodriguez helped to bring elements of this work to fruition. John Rodriguez also provided significant emotional support and encouragement during the more "trying" times of the nanopore project and student life at MIT.

My officemates made life enjoyable in the glorified freezer pit that is MIT LEES Lab; thanks Phinney, Hockenberry, and Nagle, life with you is always marked by conspicuous consumption.

Finally, I thank my parents for an upbringing that allowed for curious investigation, my extended family for their constant support, and especially my wife Kristen, for her unfailing faith in me. She definitely makes me a better person, and this thesis is dedicated to her.

There are more things in heaven and earth, Horatio,

Than are dreamt of in your philosophy.

William Shakespeare, *Hamlet*

Contents

List of Figures

List of Tables

Chapter 1

The Nanoscale Coulter Counter for Genetic Sequence Recognition

1.1 Thesis Overview

This thesis develops instrumentation for a nanoscale Coulter counter that could be used to detect the genetic sequence of deoxyribonucleic acid (DNA). The Coulter counter is a well-established technique for sizing objects by monitoring the modulations in ionic flux as particles pass through a limiting aperture; the conceptual diagram for this process is shown in Figure 1-1. Commercial Coulter counters fabricated with sub-micrometer apertures can size particles with roughly twenty nanometers of resolution. The characterization of DNA, which is more than an order of magnitude smaller than this resolution limit, requires the development of a detection system with a two nanometer limiting aperture. To help develop the techniques and instrumentation explored in this thesis, the biological toxin, alpha hemolysin, was implemented as a "prototype" limiting aperture. With the practical knowledge gained from using a toxin channel, a general model for the nanopore as a low-noise sensor was developed.

Even with nanometer-scale limiting apertures, the technical hurdles to achieving single base *de novo* DNA sequencing are immense. The issues of DNA translocation time, nanopore convolution, and limited physical resolution all undermine the recognition of genetic codes by direct sequencing. A novel application of the nanopore's sizing properties, however, allows for the recognition of *specific DNA sequences* within the practical limitations of existing channel

technology. Two detection methods are proposed and explored in this thesis that allow for the direct electrical detection of defined DNA sequences with single-base resolution, eliminating the need for external probing agents and chemical modifications required by other state-of-the-art techniques. A nanoscale Coulter counter, combining the work in this thesis with a robust nanopore, would prove highly useful for the rapid detection of genetic disease.

The implementation of a practical nanoscale Coulter counter incorporating these sequence detection methods must address two technical hurdles. The first challenge is the creation of a stable channel biased for low noise and physical stability. For the work in this thesis, an alpha hemolysin biotoxin pore is studied as a model channel system. The practical limitations of the toxin pore, however, motivate the development of an artificial aperture composed of silicon; this work in being pursued by the Golovchenko group at Harvard University. The second challenge is the measurement of small currents through the nanopore sensor. The physical requirements of biochemical proteins and the need for high-resolution sequence detection motivate the reduction of ionic salt concentration in the fluid baths by at least an order of magnitude below current levels. The effect of lower salt concentration is to reduce the signal current by an order-of-magnitude. The detection of DNA translocation at low salt concentrations will therefore require the resolution of 10pA current fluctuations with roughly 25kHz bandwidth. The measurement of these minute current fluctuations motivates the development of a circuit topology that uses a novel application of chopper-stabilization to implement a low-noise, wide bandwidth picoammeter. To demonstrate the feasibility of this topology, a prototype circuit was constructed to interface with a nanopore channel.

The immediate goal of this thesis is the development of instrumentation technologies and detection strategies for a novel genetic sequence detector based on enhancements of the Coulter technique. Although the instrumentation and methods currently developed are limited to *genetic sequence recognition*, the hope is that elements of this work will be integrated with the development of silicon nanopores to achieve rapid *de novo* DNA sequencing in the future.

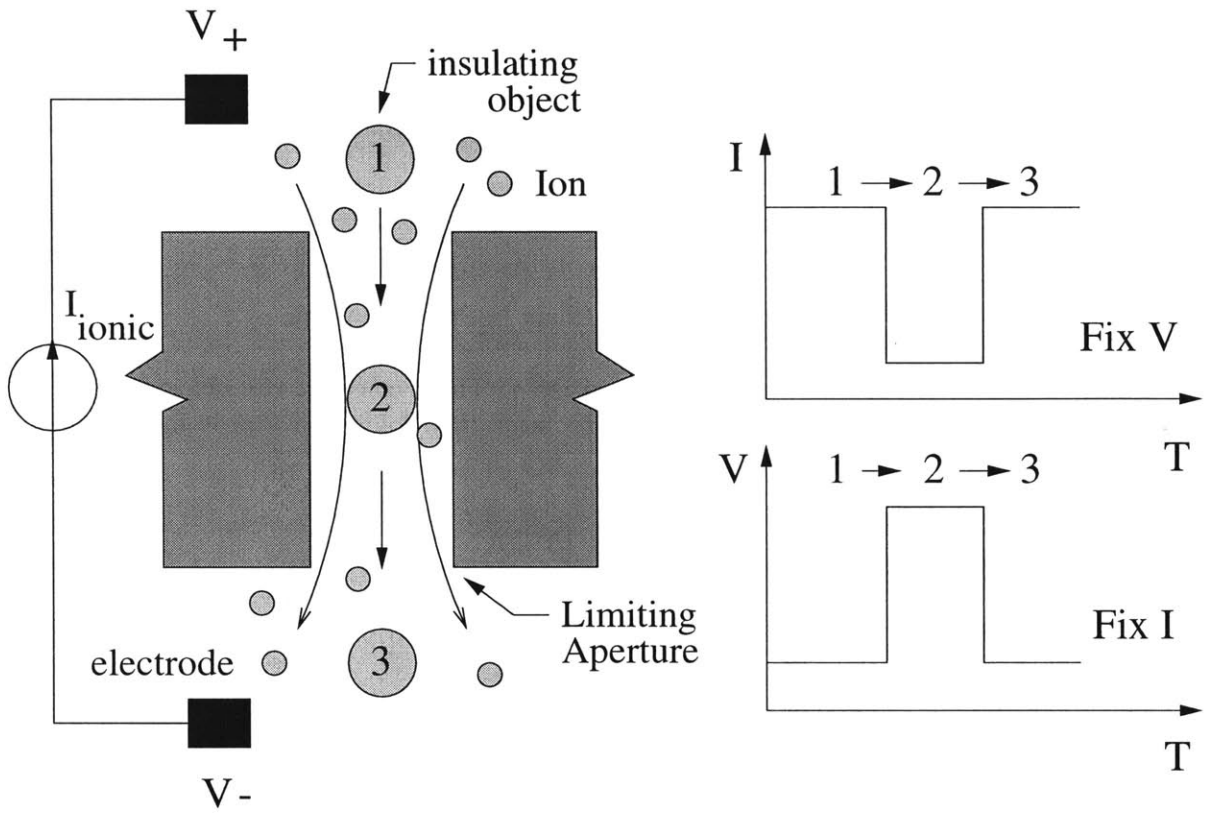

Figure 1-1: The principle of the Coulter counter. As a non-conducting object translocates through a channel (illustrated as positions 1 through 3) the modulation of the channel conductance due to the insulating obstruction can be observed. Detection is achieved by either monitoring the current through the channel with a fixed voltage bias or the dual, monitoring the voltage across a channel with a fixed current bias.

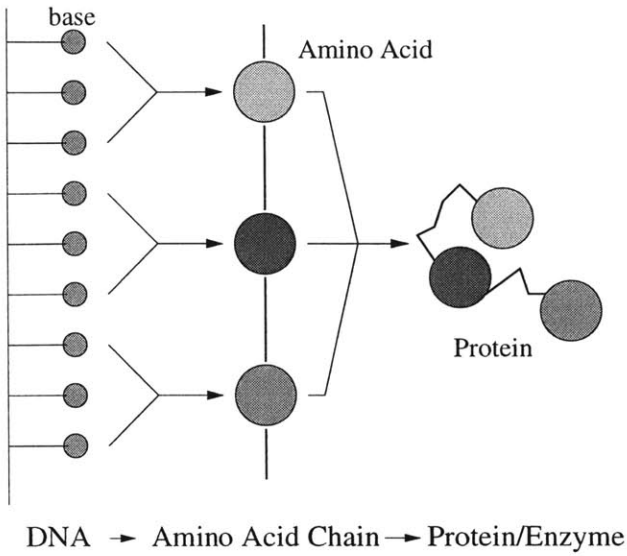

Figure 1-2: The memory storage features of DNA. Three consecutive nucleic acid bases code for an amino acid. The linear chain of amino acids then folds into a protein that performs a well-defined biological function.

1.2 Sequence Recognition in DNA

1.2.1 The Motivation for Sequence Recognition

Inside the nucleus of human cells is a memory storage device, deoxyribonucleic acid (DNA). Composed of a linear chain of 3 billion nucleic acids, DNA holds the instruction code for building the approximate 100,000 proteins required to perform discrete, but crucial, functions in the human body [84]. The actual coding scheme for DNA is strikingly simple and is illustrated in Figure 1-2. Each "memory" location in the sequence may be occupied by one of four distinct nucleic acids: adenine (A), thymine (T), guanine (G), and cytosine (C), which are commonly referred to as bases. Molecular machinery translates three adjacent bases into one of twenty amino acids or, if the three bases comprise a STOP code, the amino acid chain is terminated. The resulting chain folds into a complex three dimensional protein whose structure is determined by both the properties of the specific amino acids and their physical proximity to one another [84]. This relationship between structure and physical properties leads to the central dogma of modern genetics: the functionality of the protein is specified by the coding DNA's base sequence [84].

The sequence of nucleic acids along a strand of DNA defines a protein's structure and function, and the ability to decode a sample DNA's sequence is extremely important for many applications in biotechnology [84]. Also of major interest is the detection of *changes* in the standard base sequence, designated mutations, which allows for the diagnosis of genetic disease. As an example, one common form of cystic fibrosis is caused by the deletion of three bases in the DNA sequence coding for the transmembrane regulator protein, which is responsible for controlling the passage of chloride ions through the cell membrane [85]. The three base deletion results in the loss of a phenylalanine amino acid at the 508th slot in the protein's linear chain (Figure 1-3), causing the protein to fold differently and thereby modify its interaction with cell membranes [85, 86]. These modified interactions trigger a chain of biochemical events that eventually result in severe illness and premature death [85, 86]. The ability to rapidly and accurately detect established mutations could allow for early detection and treatment of disease, and in the future perhaps, replacement of the modified gene [86].

Another important application of sequence recognition is the detection of biological pathogens. The threat of biological warfare and terrorism with viral pathogens has motivated the U.S. Defense Department to look into novel methods that can rapidly detect the presence of specific viral sequences [87]. The ability to recognize the presence of specific viral toxins gives some hope of initiating countermeasures to contain an epidemic. The challenge of DNA sequencing or recognizing genetic mutations derives from the relative dimensions of the underlying nucleic acid code.

1.2.2 The Challenge of Sequence Recognition

The challenge of recognizing nucleic acid sequences and their mutations derives from the physical size of DNA. The nucleic acids which encode the information of interest form approximately 7 $\mathring{A}$ squares, spaced roughly 3.5 $\mathring{A}$ apart along a sugar backbone of roughly 5 $\mathring{A}$ thickness [84]. As illustrated in Figure 1-4, the physical differences between bases are roughly an $\mathring{A}$ in size between the purines (A,G) and pyrimidines (C,T), and less than roughly 0.5$\mathring{A}$ for the bases within each purine/pyrimidine group [84]. These small physical size differences are often masked by structural fluctuations caused by the sugar backbone folding and twisting as the bases interact with each other and the fluid environment [88]. The recognition of the base

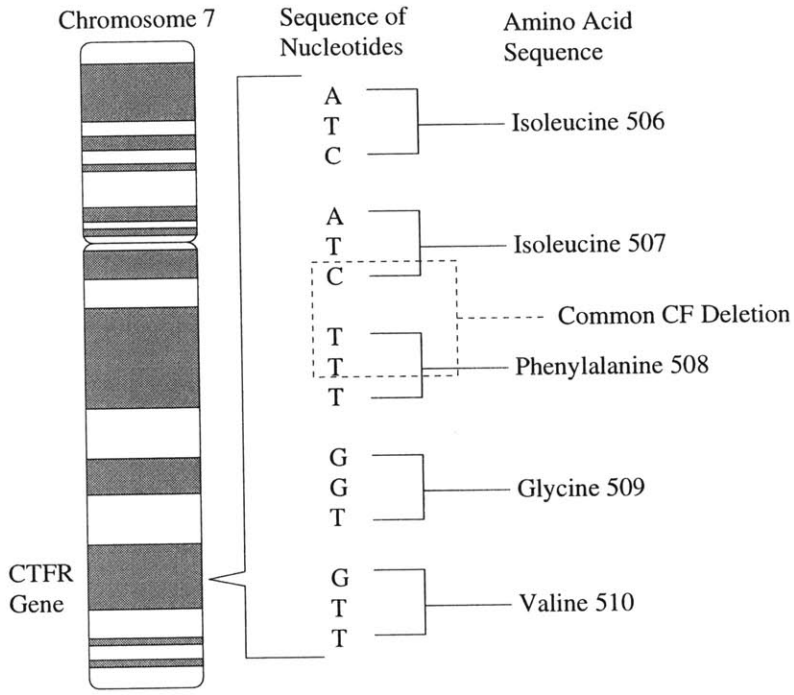

Figure 1-3: The mutation associated with Cystic Fibrosis. The 508th amino acid in the protein sequence is deleted due to the removal of three nucleic acid bases. This results in a modification of the regulator protein's activity, eventually leading to premature death. Illustration reproduced from [2].

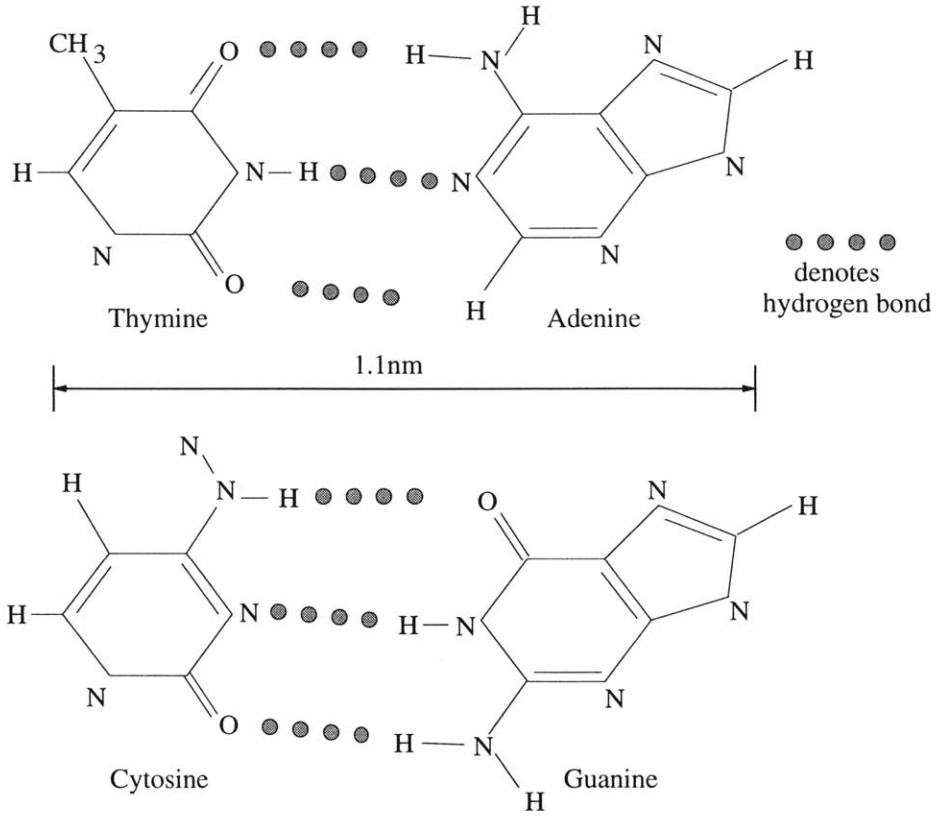

Figure 1-4: The rough physical dimensions of the nucleic acid bases; the deoxyribose backbone is not shown. Note that the physical differences between the bases are determined by the variation of a few chemical species attached to the carbon backbone. This minor variation in chemical species translate to sub-$\mathring{A}$ physical size differences between the bases. Reproduced from [42].

sequence therefore requires the resolution of features with sub-$\mathring{A}$ dimensions in a physically "noisy" environment. This challenge has been met previously in the laboratory by several approaches-overviews are presented in the next section. All of these techniques, however, suffer from limitations that limit their utility as a rapid, efficient diagnostic tool.

1.3 Existing Methods of Sequence Detection and Recognition

The challenge of genetic sequence recognition is the transduction of atomic scale variations within the DNA into detectable signatures. The existing methods that accomplish this task can be broadly grouped into two approaches: Sanger techniques and hybridization techniques.

Sanger techniques rely on the translation of nucleic acid sequence information into polymer size, while the hybridization techniques make use of the complementarity of DNA to detect when probe DNA strands attach to a matching nucleic acid template. This section provides a brief background for each approach; excellent reviews exist that give a more detailed background for these methods [89, 90, 91]. The goal for this section is to provide the context needed to discuss the new methods and instrumentation explored in this thesis.

1.3.1 The Sanger Method

The principle of Sanger sequencing is to map the base type at each "memory" location along a DNA molecule into a detectable size difference [92]. The method used to accomplish this translation is a modification of the normal DNA replication process (Figure 1-5). The standard replication process begins with a short single-stranded DNA (ssDNA) "primer" attaching to the complimentary[1] region of another ssDNA. A molecular machine denoted as DNA polymerase binds at the edge of the resulting double-stranded molecule and begins to elongate the primer, using a reservoir of single nucleic acids floating in solution to supply the required bases. The reference template for the elongating primer is provided by the strand undergoing replication. The process terminates when the polymerase reaches the far end of the original strand [84].

To map sequence information into detectable size differences, Sanger altered the standard replication process by adding modified bases to the reservoir [92]. The modified bases, called chain terminators, have the important characteristic of preventing further elongation of a nucleic acid chain. Through adjustment of the ratio of modified-to-normal nucleic acids, a distribution of replicated DNA molecules is created with discrete lengths capped by a chain terminator, as illustrated in Figure 1-6.

By running the replication process in four separate containers, with one modified base type in each, a complete mapping of DNA sequence content to polymer lengths can be achieved. The read-out of sequence is obtained by placing the product of each reaction vessel into a distinct lane within an acrylamide gel. The application of a voltage across the gel then separates the charged products into a series of distinct bands. Since each band corresponds to a distinct

[1] "Complimentary" refers to the fact that DNA forms a stable double-strand when the bases are suitably matched with one another; specifically adenine matched with thymine and guanine matched with cytosine.

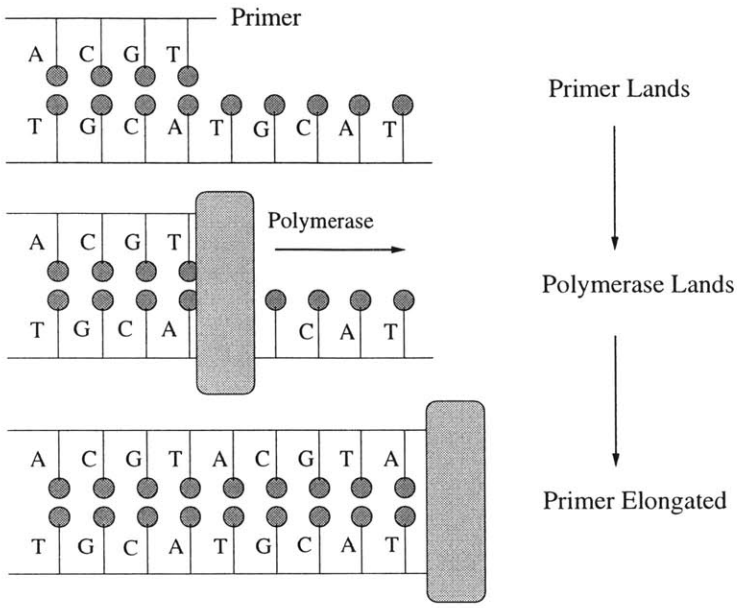

Figure 1-5: Standard Replication of DNA. A ssDNA primer lands on a longer ssDNA target. A polymerase begins to add bases to the primer, using the longer strand as a reference.

polymer length, the sequence of bands in the gel is a direct representation of the base sequence in the original DNA sample.

The Sanger method, with a few modifications, is the predominant *de novo* sequencing method in use today. The first significant modification is the use of fluorescently labeled chain terminators. By using four distinct fluorescent markers, the spectral characteristics of each band can discriminate the base instead of the lane in which the band resides. This technique improves the efficiency of gel usage and reaction vessels by a factor of four [93]. Another significant improvement is the use of small capillary tubes to hold the gel during separation. The use of capillaries scales the physical dimensions of the system down and allows for increased field strengths, and thereby faster band separation, with less severe temperature consequences from joule heating [94]. Glass capillaries also allow for increased automation in sequencing machines due to their ease of mechanical manipulation and chemical cleaning [95].

Despite the popularity of the Sanger method, it suffers from several drawbacks as an efficient diagnostic tool for genetic sequence recognition as well as *de novo* sequencing; these problems largely stem from gel electrophoresis [89]. The separation of bands in a gel by electric drift

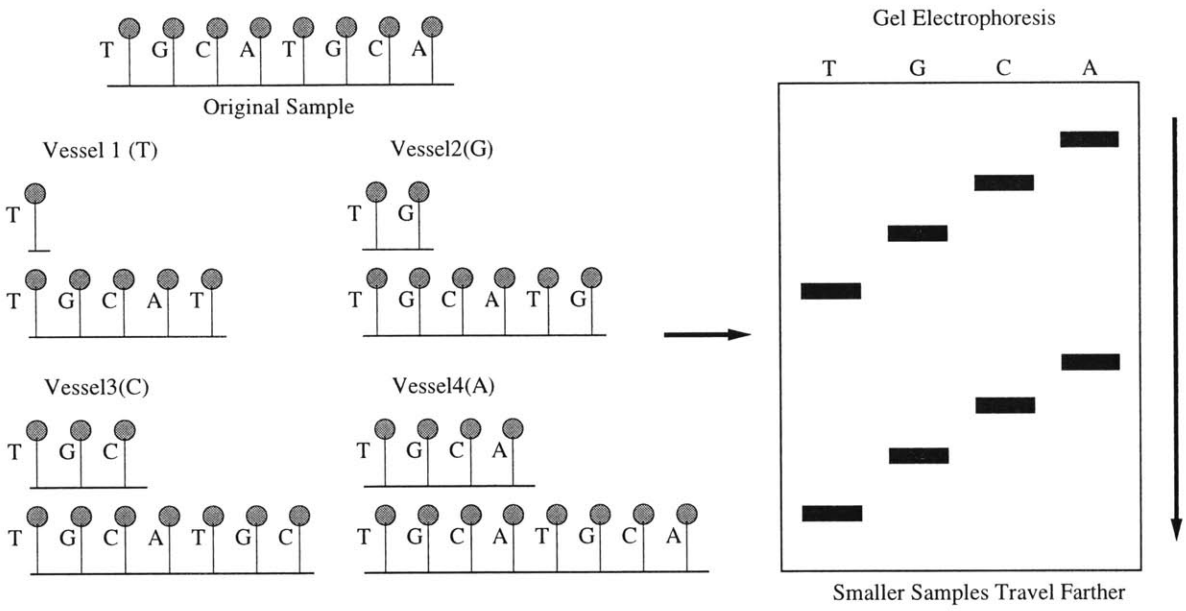

Figure 1-6: Sanger's modified replication process and its application for sequencing. The addition of chain-terminators truncates the elongation of the primer at discrete points characteristic to that base terminator. Gel electrophoresis then separates the bands and allows for direct readout of the sequence.

competes with the thermal diffusion of the polymers. After a few hours of separation by drift, the diffusing bands are no longer distinct with single-base resolution, as illustrated in Figure 1-7. This competition of drift and diffusion constrains the length of acquired sequences to a few hundred bases. Due to this size restriction, sequences of several million bases must be reconstructed from a stochastic collection of thousands of smaller samples. These samples are patched together into a proposed "master" sequence using probability theory to reconstruct the most likely template [84, 89, 90].

Attempts to substantially increase the separation rate with increased drift forces are problematic. The speed of electrophoresis is linearly related to the applied voltage, but power dissipation rises as the voltage squared [89]. Despite the use of capillaries, the constraints on temperature limit the maximum rate of of separation in state-of-the-art instruments to roughly a base/second [123]. The slow rate of sequencing, combined with the length limitation imposed by diffusion, currently limits the utility of the Sanger technique as a diagnostic instrument for rapidly sequencing novel samples or detecting genetic mutations.

1.3.2 Hybridization Techniques

An alternative approach to base terminators and gel electrophoresis is to utilize the complimentary binding properties of DNA. When DNA is placed in the proper physical environment of temperature and salt concentration, it will bind with any complimentary strands that are present [84, 96, 97]. This "key and lock" property allows for the creation of specific target probes that can sift through a diverse mixture of sample DNA and efficiently detect a template's compliment [96, 97, 84, 25].

Two practical issues must be addressed to utilize hybridization detection for sequence recognition. First, the DNA probes must be tagged with either a radioactive or fluorescent marker that serves as the transduction mechanism to report that a hybridization match has occurred [84, 96]. Second, the background signal arising from unbound probes must be removed by immobilizing either the probe or target strand, so that the non-complimentary materials can be washed away [25]. The immobilization process first introduced by Southern used nitrocellulose gel sheets, which generally limited the number of probe templates that could be simultaneously analyzed to the order of ten [84, 96].

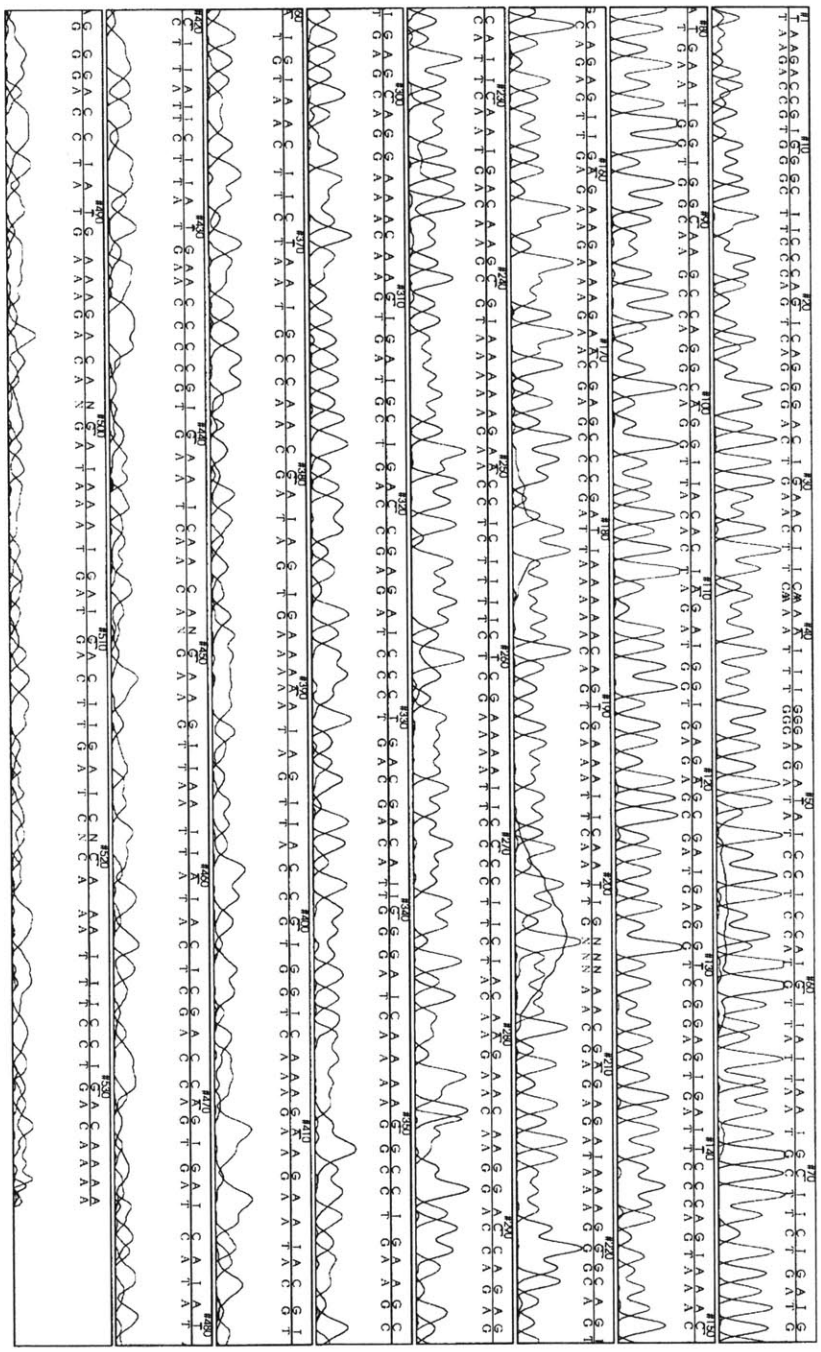

Figure 1-7: Drift vs. diffusion in gel electrophoresis. Initially the bands are clearly differentiated (top row). After the duration required to sequence a few hundred bases, however, the diffusion of the bands is too great to resolve the sequence further (bottom row). The competition between drift and diffusion limit the acquired length of Sanger sequenced DNA to a few hundred bases.

The invention of light-directed chemical synthesis in the early nineties allows for thousands of DNA probes to placed in a cm^2 region of silicon, greatly expanding the utility of the hybridization technique through massive parallelization [98]. In this method, a silicon wafer is patterned with discrete islands of DNA templates using either photolithography or ink-jet plotters [99]. After following a carefully prescribed thermo-chemical process designed to provide the optimal hybridization conditions, the fluorescently labeled sample strands will bind to the immobilized sequence strands whenever a complimentary overlap exists. The recognition of a specific sequence then reduces to matching the fluorescence signature of the silicon surface with the address of known template sequences. This technique has proven useful for the rapid detection of large numbers of target sequences in a massively parallel fashion, and with the proper choice of target probes, allows for limited *de novo* sequencing [100].

The advantage of parallel detection is offset, however, by the reduction in sensitivity resulting from a shared thermo-chemical environment [97]. The primary concern is that the probability of a template binding with its target is a function of the nucleic acid sequence [101]. This sensitivity to sequence structure makes it difficult to maintain the optimal conditions necessary for single-base sensitivity simultaneously for thousands of probe/sample reactions across the chip [97]. Another drawback of this technique is the effect of surface interactions on hybridization properties. The surface effects can often offset single-base sequence recognition due to physical obstructions and reduced strand interaction arising from the proximity of the binding substrate [134, 25]. These problems form significant technical hurdles for the development of large, highly sensitive, sequencing arrays. In many cases, however, the desired diagnostic is for the rapid and accurate recognition of a *specific* genetic sequence, e.g. the cystic fibrosis three base deletion. For these applications where sensitivity is a more important metric than sequence throughput, alternative hybridization techniques are under development.

A particularly exciting hybridization approach for genetic sequence recognition is the application of real-time fluorescence detection combined with the replication of DNA. This method uses a novel fluorescent marker and quencher attached to a DNA probe that sifts through a sample; one common scheme is illustrated in Figure 1-8 [71, 70]. When floating free in solution, the template's fluorescent emissions are suppressed by the neighboring quencher, resulting in low background fluorescent noise. If the complimentary strand exists within the sample, how-

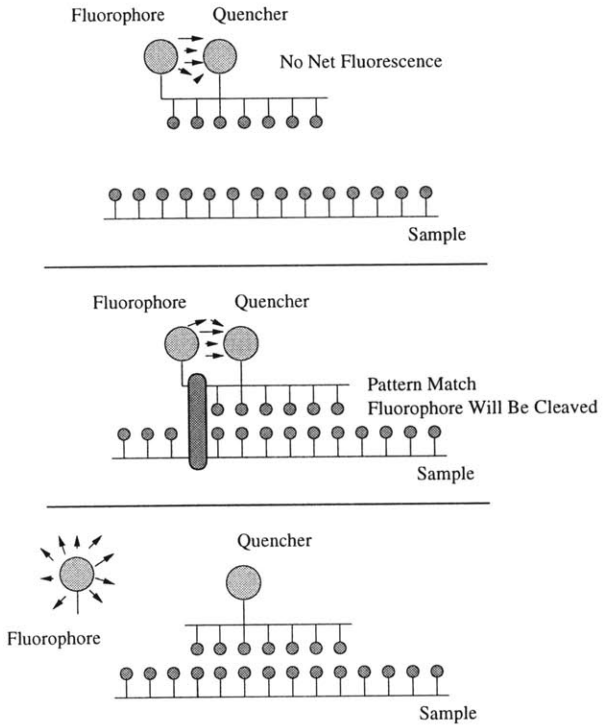

Figure 1-8: The direct monitoring of hybridization events with fluorescence. When a probe hybridizes, its quencher and beacon are separated and the fluorescence signature is detected.

ever, the template will bind to this region and the fluorescent marker will be cleaved off by the polymerase enzyme [71, 70]. Free of it's quencher, the fluorescent tag is easily observable in solution and a signal proportional to the number of hybridization events is detected. By cycling the temperature, numerous hybridization events will be created for each complimentary sample strand that results in a strong fluorescence signature in the presence of the targeted genetic sequence [71, 70].

Although this method represents the state-of-the-art for rapid genetic screening [70], it does suffer from several disadvantages, particularly the need to detect fluorescence modifications of the DNA probe. This problem, in fact, is a common drawback of all existing sequence recognition techniques: **the detection of sequence information via hybridization of a sample and a template probe relies on an external transduction process such as fluorescence or radioactivity**. The requirement of an external tagging mechanism requires the chemical modification of either the probes or the sample, which can limit instrument throughput and add significant expense to genetic typing [90, 89, 25]. A new approach to sequence recognition is explored in this thesis that maintains the single-base sequence resolution and speed of state-of-the-art techniques, but eliminates the need for an external transduction mechanism by using *direct* electrical detection and characterization of the DNA polymer's physical properties.

1.4 A New Approach to Sequence Recognition: The Nanoscale Coulter Counter

The previous section summarized the state-of-the-art in genetic sequencing and sequence recognition techniques. These approaches all suffer from significant drawbacks, but the universal weakness is the need for some external tagging feature to detect the presence and/or state of the DNA. These drawbacks motivated Branton and Church to propose a novel method of genetic sequencing that could eliminate the need for external probes by directly transducing the small physical differences in DNA nucleic acid structure into a detectable electrical signal [102]. The process through which this transduction is achieved is an extension of the Coulter counter, which has been used previously to characterize particles by monitoring the modulation of ionic current through a small channel as a particle passes through the limiting aperture [104, 106];

the popular term for this instrumentation approach is the resistive pulse technique.

The resistive pulse technique has measured particles down to the size of 100nm with 20nm resolution by using sub-micron channels track-etched in mica [107, 105]. As developed in Appendix A, the detection of single-stranded DNA, which is approximately 1.2nm wide, requires the limiting aperture to be scaled down by at least an order of magnitude. The resolution of base *differences* within a DNA strand requires a limiting aperture on the same order as the DNA. To obtain a limiting aperture of this dimension, Branton proposed the biological toxin, alpha-hemolysin, which from crystallographic measurements has been shown to have a limiting constriction of roughly 1.5nm [109].

The use of current modulation as a DNA strand passes through this nanometer limiting aperture, from here on denoted the *nanopore Coulter counter*, could conceivably allow for the direct sequencing of DNA without the need for an external tagging agent, as illustrated in Figure 1-9. In addition to the advantage of direct electrical detection, this method could presumably increase the rate of *de novo* sequencing by several orders of magnitude compared with the Sanger method, as well as eliminate the problem of limited sequence length arising from band diffusion in gel electrophoresis [1]. The following section describes the preliminary "proof-of-concept" experiments for the nanopore Coulter counter that defined the state-of-the-art at the commencement of this thesis.

1.4.1 Nanapore Sequencing: Initial Proof-of-Concept

Preliminary experiments illustrated that the alpha-hemolysin biotoxin could be used effectively as a limiting aperture for resolving ionic current fluctuations due to the presence of single nucleic acid molecules. In a series of experiments employing different lengths of poly-U RNA, a polymer with roughly the equivalent physical traits as DNA, Kazionowicz *et. al.* demonstrated that the addition of molecules to the bath surrounding the alpha toxin could be readily detected [103]. As the negatively-charged RNA is pulled through the bio-pore by an applied electric field, dimunition in the bias current from 120pA to approximately 15pA is observed (Figure 1-10). The time histograms for these events also demonstrated a definite correlation between event duration and the length of the polymer added; the mean translocation rate extrapolating to roughly 3 μs/base. The observation of a correlation between translocation time and polymer

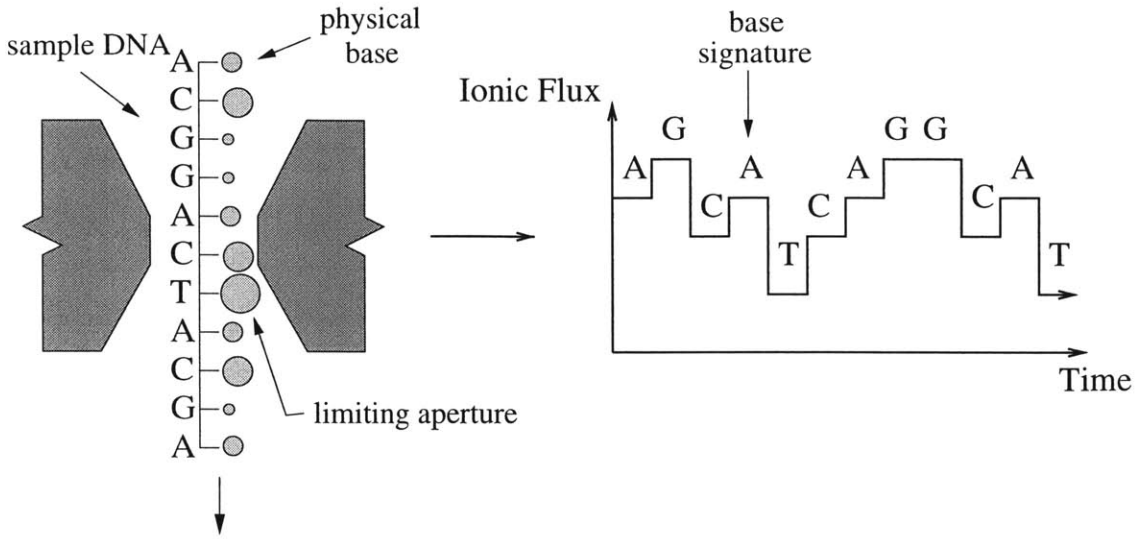

Figure 1-9: The Coulter technique applied to direct genetic sequencing. The physical size differences in the DNA are read-out as fluctuations in the ionic current through the aperture.

length established the nanopore technique as a potentially useful method for polymer sizing.

Extensions of the RNA experiments demonstrated that the nanopore technique could discriminate between different types of RNA. RNA, like DNA, is composed of four base units. Investigating two of these units, Akeson *et. al.* found that the current blockade during poly-A translocation is 15pA, while the blockade current for poly-C translocation is 7pA (standard deviation for each measurement is $\pm$ 1.5pA) [110]. In addition, the average rate of translocation for the two types of RNA differed by a factor of six, most likely due to interactions at the molecular interface between the toxin and the RNA strand [110, 111]. These observations demonstrated that the alpha-hemolysin pore has a limiting aperture small enough to resolve molecular *structure* within RNA polymers, in addition to characterizing polymer length.

As a final demonstration of the technique's feasibility for *de novo* genetic sequencing, a composite strand of the two original RNA segments was constructed and used to demonstrate, to first order, that the ionic current modulation and translocation rates appear to obey *linear superposition.* The apparent linearity of the nanopore technique further established its potential as a potential *de novo* sequencing method; the remaining issues for actual implementation were an understanding of the nature of the blockade values and durations, defining the convolution properties of the nanopore, and slowing the rate of polymer translocation.

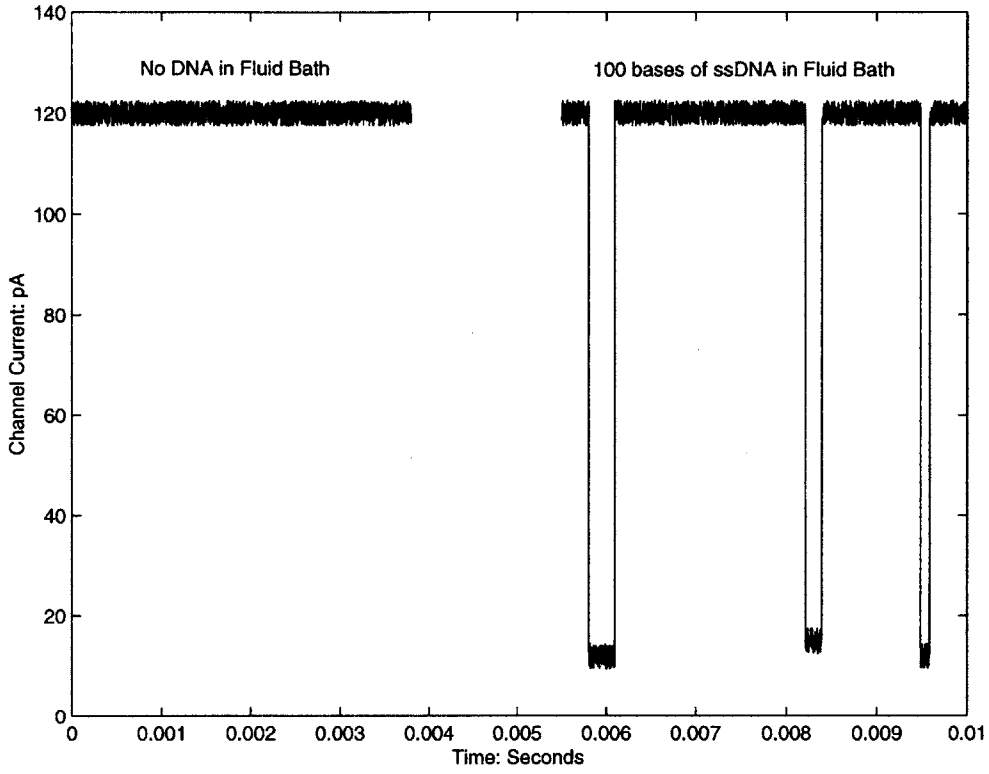

Figure 1-10: Translocation events for 100-bases of single-stranded adenine DNA passing through the alpha-hemolysin pore. The channel current prior to the addition of DNA is shown on the left, the channel current after addition of DNA is shown on the right. The dimunition of current represents the translocation of DNA through the limiting aperture.

Biological Issue	*Experimental Observation*	*Design Consequence*
Translocation Rate	1-5 μs/base	Bandwidth $\geq$ 150 kHz
Secondary Structure	Dominant Signal (R.T.)	Physical Biasing
Aperture Convolution	Averaging over 10 bases	Modify Pore Dimensions

Table 1.1: Summary of the technical hurdles to *de novo* DNA sequencing with a toxin nanopore

1.4.2 Refined Experiments and Technical Hurdles to *de novo* Sequencing

Refinements in the understanding and interpretation of these original experiments have shown that several significant technical hurdles associated with the nanopore technique need to be addressed before it becomes the useful *de novo* sequencing tool as first proposed. Extensive measurements of the blockade levels for poly-A and poly-C DNA strands have demonstrated a limited blockade difference of only 2-3pA with a standard deviation of approximately 1.5 pA [111]. In addition, the average rate of DNA translocation is still on the order of 2-5 μs/base [111]. The small difference in blockade level and the rapid rate of translocation makes it extremely difficult to discriminate between different polymer types; the peak-to-peak current noise is already greater than the signal difference at the 10-20 kHz bandwidth necessary to detect 100-base DNA strands composed of identical nucleic acids. Attempts to average the data waveforms to suppress the uncorrelated noise contribution have proven problematic, since the rate of DNA translocation appears to be highly variable. This fact results in the signal waveform also being attenuated, since the edges of the signal transitions due not align from one event to another. Perhaps the largest hurdle to *de novo* sequencing, however, is the true origin of signal differences in the observed waveforms.

The difference in both blockade differences and times between RNA and DNA has been attributed to the relative structural properties of these two polymers, and not the actual physical size of the bases. Using data from a series of temperature experiments, Meller *et. al.* has proposed that the alpha-hemolysin pore is highly sensitive to the *secondary* structure of DNA/RNA strands[2] [111]. This additional insight, when applied to the preliminary experiments, suggests that the discrimination between RNA types was due primarily to the way each

[2]Secondary structure is the way that DNA strands begin to fold in solution.

base-type folds in solution, as opposed to actually measuring differences due to the underlying physical dimensions of the individual nucleic acids [110, 111]. The drawback to detecting secondary structure is that it represents a non-linear average of tens of bases in the vicinity of the current base measurement. Eliminating secondary structure with extreme biasing conditions such as high temperature also tend to undermine the stability of the toxin channel [111]. This structural averaging, coupled with the complex spatial transfer function of the toxin channel, makes it difficult to uniquely specify the true base sequence underlying a detected waveform or even to design a reasonable blind deconvolution algorithm.

1.4.3 Moving Forward with the Nanoscale Coulter Counter

The problems of signal-to-noise and secondary structure motivate the use of a nanofabricated channel to achieve *de novo* sequencing of DNA. The use of nanofabrication should significantly decrease the capacitance of the sensor and interface electronics. By reducing the capacitance of the system, the high frequency noise performance of the current measurement would be dramatically improved, allowing for the wider bandwidth measurements to be achieved. In addition, the use of an artificial channel allows for more extreme biasing schemes to be explored that might help eliminate the effects of secondary structure in the DNA.

A major hurdle to implementing a microfabricated channel is that no existing topology for low-noise, wide bandwidth measurements of picoamp currents scales readily to an integrated circuit, given the additional constraints imposed by nanopore sequencing. In order to achieve the full benefits of this new sensor, a new interface circuit suitable for integration must be developed in parallel with a synthetic nanopore.

Even with this improved sensor system, the technical challenges to achieving *de novo* single-base sequencing are immense. For example, the convolution of the limiting aperture and the base sequence will remain an issue as long as the channel length is significantly longer that a base-to-base separation of the nucleic acids, which is on the order of 3.5 $\AA$. The resolution of the nucleic acid size differences in the presence of fundamental noise sources is also problematic. As developed in Appendix A, the required diameter of the limiting aperture, D, required to

detect an insulating cylinder of diameter, d, is shown to be

$$D \approx \frac{\sqrt{\pi} d^2 V_{bias}}{2\sqrt{4 k_b T \Delta f \rho L}},$$

where L is the estimated length of the channel, ρ is the bath resistivity, Δf is the measurement bandwidth, and V_{bias} is the quiescent voltage applied across the pore. This expression illustrates that to resolve small polymers of size d, the pore must scale as d^2 to account for both the *size* of the polymer as well as *increased noise* associated with smaller apertures. For a nanopore of diameter $2nm$, length of $4nm$, and a measurement bandwidth of $25kHz$, this metric estimates the resolution of the pore as roughly 5 $\mathring{A}$, which is on the edge of the resolution required for single-base recognition, at a bandwidth much lower than that required given the existing translocation rate of $2.5\mu s/base$. The issues of channel convolution, DNA secondary structure, and resolution limitations to nucleic acid size with reasonable bandwidth all undermine the use of the nanopore Coulter counter for *de novo* genetic sequence detection.

The preliminary experiments with the toxin channel do demonstrate two properties of a nanometer aperture that could prove very useful: the ability to detect relatively large changes in polymer width (e.g. factor of 2), and the ability to roughly measure the relative lengths of polymers by translocation duration. These features of the pore can be exploited to obtain *DNA sequence recognition* as an intermediate goal in the development of the nanoscale Coulter technique.

1.5 Thesis Contributions

The goal of this thesis is the development of instrumentation methods for the direct electrical detection of specific genetic sequences. The general approach used to accomplish sequence recognition is the resistive pulse technique, employing a biological toxin as a "prototype" limiting aperture. In addition to background work on general modeling and biasing of a nanopore as a low-noise sensor, this thesis makes two distinct contributions to the instrumentation field. The first contribution is the development of novel genetic recognition strategies that exploit the properties of the nanopore channels within the limitations imposed by DNA structure and existing channel geometries. The second contribution of the thesis is the design and proto-

typing of novel interface circuitry for the measurement of the picoampere current fluctuations associated with DNA translocation through a nanopore.

1.5.1 Novel Genetic Detection Strategies with an Nanopore

Observations of polymer translocation through a toxin channel have revealed several technical difficulties related to the originally proposed *de novo* sequencing technique that may be addressed with a micromachined nanopore. These observations, however, also motivate alternative methods that could be used to recognize *specific* genetic sequences. The first method uses the limiting aperture of the toxin to sense the presence of double-stranded versus single-stranded DNA as a target probe hybridizes with its matching template. This method is found to provide the single base sensitivity necessary for detection of many genetic mutations, but also tends to require large amounts of sample DNA. A refinement of the basic hybridization technique is proposed and demonstrated that uses the sizing capability of the pore to detect the "transformation" of short DNA primer strands to longer DNA polymers with the polymerase chain reaction. Although this method will require an artificial nanopore to succeed in practice, it maintains single-base sequence resolution with the additional benefits of single molecule sensitivity and positive controls to prevent false sequence detection. Both of these methods allow for direct electrical detection of genetic sequence information without the need for external radioactive or fluorescent markers.

1.5.2 A Novel Picoammeter Topology

The exploration of novel approaches to picoammeter design is motivated by several potential applications of the nanoscale Coulter counter. The detection of hybridization events with single-base sensitivity will require an order-of-magnitude reduction in the salt concentration of the ionic bath. As the salt is lowered by a factor of ten, the open channel currents for the nanopore sensor are reduced to approximately 10pA. The detection of DNA probes therefore requires the resolution of picoampere fluctuations through the channel with a bandwidth of 25 kHz.

The development of new picoammeter topologies is also critical to the future of *de novo* sequencing with a nanopore. The high-frequency detection of base sequences is largely limited by the capacitance of the source and interface circuit. The reduction of this capacitance,

coupled with the need to overcome the practical limitations of the toxin channel, motivates the fabrication of a silicon nanopore. To yield the full benefits of an integrated pore, the interface electronics must also scale to maintain a low shunt capacitance at the input to the current amplifier.

Current and charge measurements with these rough specifications are ubiquitous in the instrumentation field and extend over several disciplines, from nuclear physics to neurobiology. In general, these specifications require a state-of-the-art low-noise, wide bandwidth picoammeter. Commercial interface circuitry that meets these specifications is complex and expensive due to the inherent limitations of their circuit topologies. In addition, existing picoammeter topologies suitable for *de novo* sequencing do not scale effectively with integration, and alternative techniques must be developed. The exploration of more elegant solutions to this measurement problem will help with the general development of the nanoscale Coulter technique, as well as prove useful to the general instrumentation community.

The exploration of novel current measurement techniques motivates the "hourglass" integrating picoammeter. This picoammeter topology uses a novel chopper stabilization strategy to obtain low-noise, wide bandwidth current measurements suitable for nanopore measurements. A discrete version of the hourglass picoammeter was prototyped in this thesis which would be suitable for the hybridization detection strategies developed in this thesis. In the future, this topology can also scale easily with a synthetic nanopore to help achieve the ultimate goal of *de novo* sequencing of DNA.

1.6 Thesis Organization and Summary

This chapter has motivated a novel approach to genetic sequence recognition using a nanoscale Coulter device. The remaining chapters of this thesis explore the design engineering required to develop feasible instrumentation and detection methods to implement this concept.

1.6.1 Chapter Two: Genetic Sequence Detection with a Nanopore

This chapter summarizes the concepts and experiments that use the limiting aperture of a toxin channel to detect the presence of specific genetic sequences in a sample of DNA. The first

section gives a brief summary of the strategy behind using the physical aperture of a nanopore to detect the presence of single versus double-stranded DNA. The next several sections present a series of experiments that both validate the principles behind this approach and lead to a successful detection methodology for recognizing single-base mutations in a DNA sample. The drawback of direct hybridization detection is the need for excess quantities of sample material to achieve practical counting statistics.

To address the problem of excessive sample requirements, a refined hybridization protocol is proposed that uses the limiting aperture of the channel in tandem with the polymerase chain reaction to detect the presence of minute concentrations of DNA. A proof-of-principle experiment is performed to demonstrate the viability of this technique. The conditions required to achieve high resolution detection of genetic sequences are found to require the resolution of roughly 5 pA current modulations at 25kHz bandwidth.

1.6.2 Chapter Three: Interface Strategies for Nanopore Sensors

In order to detect the translocation of DNA through a nanopore, a suitable interface circuit must be designed. To develop this interface, a useful model for the future nanopore must be extrapolated from the proposed structure of the device and practical knowledge gained from working with a toxin nanopore. After establishing a reasonable electrical and noise model for the nanopore, the development of a suitable interface strategy is explored. A rough set of performance specifications suitable for both the genetic sequence recognition strategies proposed in chapter two and the *de novo* sequencing of DNA help to guide the design of a suitable interface. After briefly discussing the drawbacks of state-of-the-art techniques, a new interface strategy for the nanopore is introduced which uses the principle of chopper stabilization to achieve low-noise, wide bandwidth current measurements.

1.6.3 Chapter Four: The Hourglass Integrator

Chapter four introduces the hourglass integrator, which is the first half of the chopper-stabilized picoammeter topology. A complete low-noise design is developed and prototyped which is suitable for hybridization detection. The support circuitry required to achieve low "glitch" switching from charge injection and the maintenance of low-offset voltages across the picoammeter's

terminals are developed in detail, as well as the design considerations for stability in the cross-coupled feedback topology. The merits of this novel approach are demonstrated with sample waveforms and noise analysis.

1.6.4 Chapter Five: The Demodulating Differentiator

To complete the chopper-stabilized picoammeter, a suitable differentiation process must be designed. In particular, a circuit that both demodulates *and* takes the derivative of the signal waveform must be developed. Two possible methods are presented in this chapter. The first approach uses an analog current conveyor to yield a low-noise, wide bandwidth and inherently stable circuit for demodulation and differentiation of the signal. This topology will be well-suited for the bandwidth demands of *de novo* sequencing. For the lower frequency requirements of hybridization detection, a digital approach to differentiation is appealing.

The implementation of the demodulating differentiator with digital signal processing is also developed in this chapter. The digital implementation takes advantage of the topology's quasi-continuous operation to substantially increase the integrator's gain relative to other state-of-the-art integration topologies. The advantage of increased integrator gain is that the quantization noise from digitization will be negligible when referred back to input as an equivalent current noise source. The demodulation and differentiation can then be achieved with relatively straightforward digital signal processing. Not only does this approach eliminate the need for a low-noise, wide bandwidth analog differentiator, but it also allows for the implementation of auto-calibration procedures to further suppress the residual state transition transients due to charge injection and dielectric absorption.

1.6.5 Chapter Six: Future Developments and Summary of Contributions

This chapter reviews the key contributions of the thesis and highlights possible improvements for future work. In particular, the merging of the picoammeter, silicon nanopore, and novel detection strategies for genetic sequence recognition is reviewed, and the future viability of the nanopore for *de novo* DNA sequencing is discussed.

Chapter 2

Genetic Sequence Detection with a Nanopore

2.1 Genetic Detection Strategies with a Nanopore: Overview

The previous chapter highlighted the difficulty of sequencing DNA with a nanopore. The limitations of this technique arise from several issues including the limited resolution of the channel to single base physical differences, the convolution properties of the nanopore, the sensitivity to DNA secondary structure, and the rapid rate of DNA translocation. These issues each undermine the utility of the Coulter technique for *de novo* sequencing with state-of-the-art nanopore technology. The translocation of DNA through a nanopore does exhibit a highly useful trait, however; the length of a DNA molecule can be characterized based on the duration of the translocation event. The resolution to polymer length, illustrated in Figure 2-1, may be exploited to detect specific genetic sequences within DNA.

Several experimental methods can be designed that exploit the length characterization of the nanopore to resolve genetic sequence information. All of these methods rely on the transduction of genetic sequence information into a modification of the polymer translocation time. One method is to use the 1.5nm limiting constriction of a toxin nanopore to sense the presence of single versus double-stranded DNA. If a genetic probe strand binds with the complimentary region on the sample polymer, then the toxin should have a dramatic effect on the hybridized sample's translocation duration. This increased duration is the result of the toxin's limiting

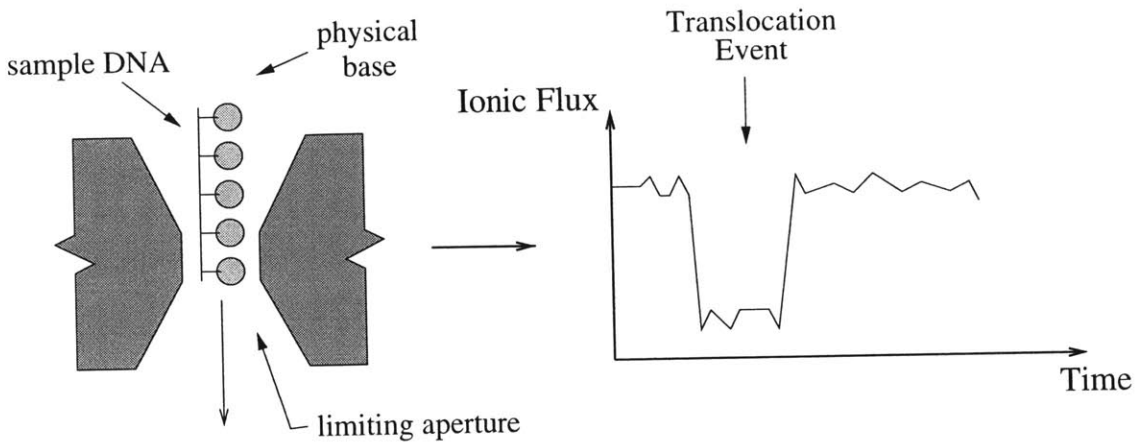

Figure 2-1: The toxin nanopore dimensions are suitable for detecting the *presence* and *length* of translocating DNA, but not the small physical differences between the single bases.

aperture preventing the double-stranded polymer's passage through the pore.

Another approach is to use a polymerase enzyme to elongate DNA probes when they bind with their complimentary region in the sample. The extension of the probe lengths should be recognizable with a nanometer limiting aperture if the reaction parameters are engineered properly. Both of these methods are developed in this chapter to illustrate the utility of a nanopore aperture for resolving genetic sequence information. Using these methods, the direct electrical detection of genetic sequences is possible without the need for radioactive or fluorescent markers.

2.2 Creating a Stable Limiting Aperture

In order to investigate the use of a nanopore aperture to recognize genetic sequences, a suitable channel must be fabricated. For the work presented in this chapter, the alpha-hemolysin toxin was used to implement an aperture with a 1.5 nm limiting constriction and a channel length of 4nm; the geometry of the toxin channel is shown in Figure 2-2. The creation of a stable, low-noise toxin channel is a challenging exercise, and the details of this procedure are included

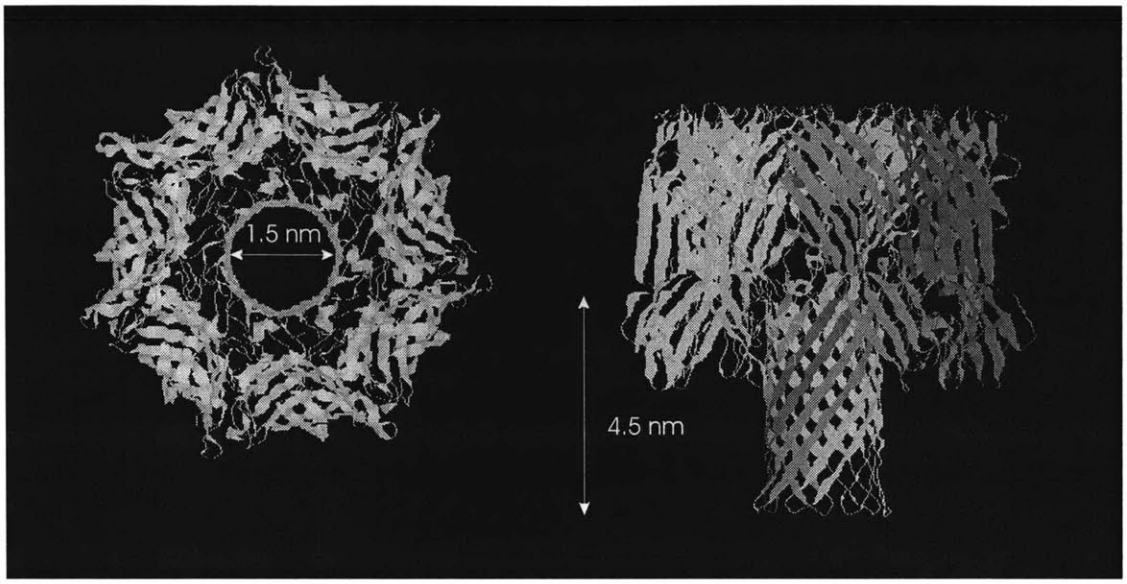

Figure 2-2: The alpha-hemolysin toxin is an almost ideal limiting aperture for distinguishing between single-stranded and double-stranded DNA.

in Appendix B; the important conclusion from the appendix is that after a suitable protocol has been followed, a highly insulating partition is formed between two ionic bathes bridged by a single toxin channel, as illustrated in Figure 2-3. The flow of ions and DNA polymers are restricted to pass through the toxin aperture, which creates effectively a nanoscale Coulter counter [107]. The use of a toxin channel limits the experimental protocols available for manipulating genetic recognition, and techniques to circumvent these limitations will be discussed in the final section of the chapter. For the purposes of illustrating the general concepts for direct electrical sequence detection, however, a toxin channel is sufficient.

The detection of DNA translocation events is a straightforward process for the toxin pore described in Appendix B. The quiescent current for the toxin channel is 120pA (1.6pA rms noise) with a 120mV applied voltage bias. The translocation of DNA through the toxin pore lowers the channel current to the order of 20pA, for a duration of 50 μs or longer, which can be detected with a commercial Axopatch 200B picoammeter. The data is analyzed and the events are characterized by level-thresholding programs implemented with either the MATLAB or IGOR software platforms. The essential code for these analysis programs is included in

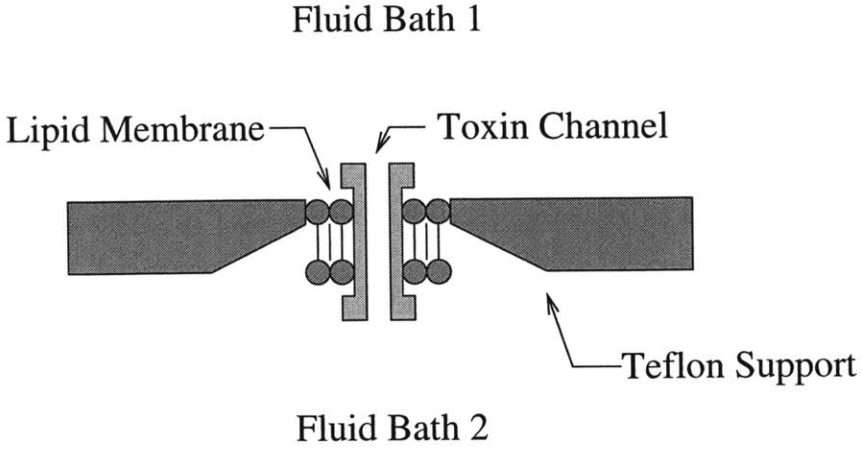

Figure 2-3: Once a toxin pore is established, a nanoscale Coulter counter is achieved. Two conducting fluid bathes are separated by an insulating Teflon/lipid partition. The only path for ions and DNA to cross this membrane is through the toxin channel.

Appendix E.

2.3 Experiment I: Establishing the Limiting Aperture

2.3.1 Experimental Purpose and Protocol

The goal of this experiment was to establish the limiting aperture of the toxin channel and the general method of detecting DNA hybridization in real-time with a nanopore. The protocol used to accomplish this goal was to add known concentration of single-stranded DNA, 100 bases in length and composed homogeneously of adenine (polyA-100), to one fluid bath of the nanoscale Coulter counter. After roughly five minutes of diffusion, the count rate of polyA-100 translocating through the toxin channel reaches equilibrium. After the equilibrium count rate of the polyA-100 is established, the complimentary single-stranded thymine DNA (polyT-100) is added to the same fluid chamber. The expectation is that after a short interval of diffusion, the complimentary strands will hybridize with each other and the duration of polymer translocation will dramatically increase as the double-stranded material is confined by the toxin's limiting aperture.

2.3.2 Results and Interpretation

The results of the hybridization experiment are shown in Figure 2-4. The translocation rate for negative time demonstrates the equilibrium count-rate observed for the 10pmol (± 1pmol) of polyA-100 DNA added to the fluid bath[1]. The mean count rate was 36 events/minute, with a standard deviation of 5.7, as expected from Poisson statistics. At time t=0, 10pmol (± 1pmol) of polyT-100 DNA was added to the fluid bath containing the polyA-100. For the initial four minutes, the translocation rate is seen to increase slightly due to the addition of polyT-100 material into the fluid bath. After five minutes, however, the translocation rate begins to fall dramatically until the translocation rate approaches 0.5 events/minute after 15 minutes. In synchrony with the decay of standard translocation events is the rise of permablocks, which are defined as events that extend beyond the characteristic blockade time for polyA-100 and polyT-100 molecules; for this experiment, a permablock was chosen as one second, which is a factor of approximately 3000 longer than the characteristic blockades of independent polyA-100/polyT-100 events.

The extension of typical blockade durations from $300\mu s$ to $> 1s$ is interpreted as the presence of double-stranded DNA confined by the limiting aperture of the toxin channel. The 1.5 restriction of the toxin channel will pass the 1.2 nm single-stranded DNA [102], but should prevent the translocation of 2.4 nm double-stranded (dsDNA) material. In order for the dsDNA sample to eventually translocate through the pore, the polyA-100 and polyT-100 must separate from each other by the *melting* of the two strands. Although the underlying dynamics of the melting process are still an active area of research, the discussion in this thesis will use the fact that a *recognizable* change in translocation duration is detectable when a probe binds to a target sample. To prevent a significant perturbation of the counting statistics by the presence of these long channel blockades, a circuit denoted the *Permabuster* was used to monitor the quiescent channel current and clear extended translocation blockades with a brief bias reversal whenever an event extends beyond some threshold duration; the Permabuster schematic is included as part of Appendix D.

The hybridization of polyA-100 and polyT-100 is clearly observed with the limiting aperture

[1]The concentration of DNA was obtained using standard UV absorption techniques [103]

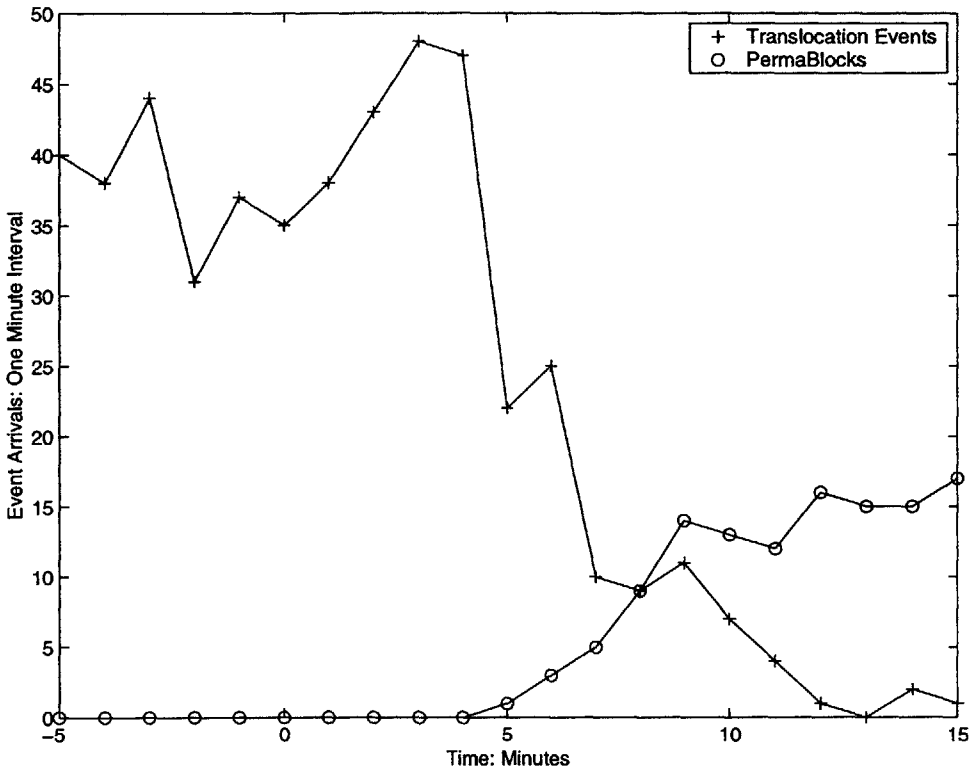

Figure 2-4: The interaction of DNA samples in real-time. Prior to t=0, the toxin pore passes the 100-base strands of adenine. At t=0, the complimentary sequence of 100-base thymine is added to the fluid volume. After some initial mixing, the hybridization of the adenine and thymine strands leads to a marked decrease in polymer translocation rate, coupled with an increase in the rate of permanent blockades.

of the toxin channel. The interaction between the polymers is relatively crude, however, since the polyA-100 and polyT-100 molecules have no defined registration with one another, and the genetic sequence is very simple. The need to establish the specific recognition of a more complicated genetic sequence motivates the next experimental series.

2.4 Experiment II: Basic Genetic Sequence Recognition

2.4.1 Experimental Purpose and Protocol

The goal of this experiment was to demonstrate the recognition of a specific genetic sequence with the nanopore Coulter counter. The sample strand is composed of a mixed sequence of 100 bases[2], which will be defined as PX. Two shorter, 22-base, ssDNA strands are used to probe the genetic sequence of the "target" strand. The first probe, P_x[3], is complimentary to the target, while the second probe, P_y[4], is composed of the same number of bases as P_x, but with a scrambled sequence that makes it *non-complimentary* to both PX and P_x.

In order to characterize polymers with the nanopore, an event plot will be used [102, 111]. The basis for the event plot is illustrated in Figure 2-5. For each translocation event, the average blockade current is plotted versus the event duration. This graphical aid will help to establish the characteristic regions associated with each polymer type.

The experimental protocol begins by characterizing the target PX and the DNA probes (P_x, P_y) with event plots. These regions are shown as the top two traces in Figure 2-6. The distinct distribution for PX is centered around $250\mu s$, designating a characteristic translocation time of $2.5\mu s/base$, as expected from previous experiments with ssDNA [111]. The distribution for the 22-base probes is skewed to significantly lower times and reduced blockades; the change in blockade level, however, is primarily an artifact of the 10 kHz filter used with the picoammeter, which has a 10-90% rise-time on the order of the translocation duration. From these control studies, it is clear that the target sample PX and the shorter probes (P_x,P_y) can be clearly distinguished from one another.

[2]5'end - CTC ACC TAT CCT TCC ACT CAT TTT CCT TAA CCA TTT CAT TCA CCC ATC TCA CTA TCA TTA TCT ACA TCC ATT ACA TCA CTA CTC CTC ACA CTA CCA TAC C - 3'

[3]3'end - GAG TGG ATA GGA AGG GTA AAA G - 5'end

[4]3'end - C CAT ACC ATC ACA CTC CTC ATC - 5'end

The hybridization interactions of the target and genetic probes can now be established with the nanopore. The experiment begins by adding 67 pmol of sample DNA PX to the fluid volume. The DNA is allowed to equilibrate in solution for fifteen minutes, after which time a shot-noise limited distribution of events was collected for a fifteen minute interval. The event plot for the polymer PX is shown in the top left corner of Figure 2-6. The non-complimentary probe P_y was then added to the same fluid volume and given an additional fifteen minutes to equilibrate, after which a second fifteen minute data interval was recorded. The amount of P_y added, 125 pmol, was selected to strongly favor the hybridization of the target strand PX. The event plot for the mixture of PX and P_y is shown in the bottom left-hand panel of Figure 2-6. From this data, it appears that the net distribution of channel events is the superposition of the PX and P_y distribution of polymers. The final procedure of the experiment was to add 125 pmol of P_x to the same fluid volume and observe the event plot, once again over a fifteen minute equilibration/data collection interval. From this event plot, it is clear that the region associated with the sample PX has been significantly modified. The binding of the complimentary probes P_x and PX has apparently shifted the distribution associated with PX to extended times, which are off the scale of the event plot.

2.4.2 Results and Interpretation

To quantify the interaction of the probes and test sample, a specific region of the event plot can be analyzed. For the experiment performed here, the region associated with the test polymer PX was designated by a box between $150 - 350\mu s$ along the x-axis and a normalized blockade level between $0.18 - 0.25$ along the y-axis; The data evaluating rates is summarized in Table 2.1. For the initial control sequence of PX, the total number of arrivals in the defined event region was 101 during a time interval of fifteen minutes. This number defines the Poisson maximum likelihood estimator for the mean number of arrivals, $N = \lambda\tau$, observed within a time interval τ.

The use of Poisson statistics is justified by analyzing the histogram of times *between* the 258 events in the event plot over a fifteen minute interval[5]. The actual histogram is plotted in

[5]This event count is associated with the illustrated event plot in Figure 2-6, which is a subset of the total 732 counts.

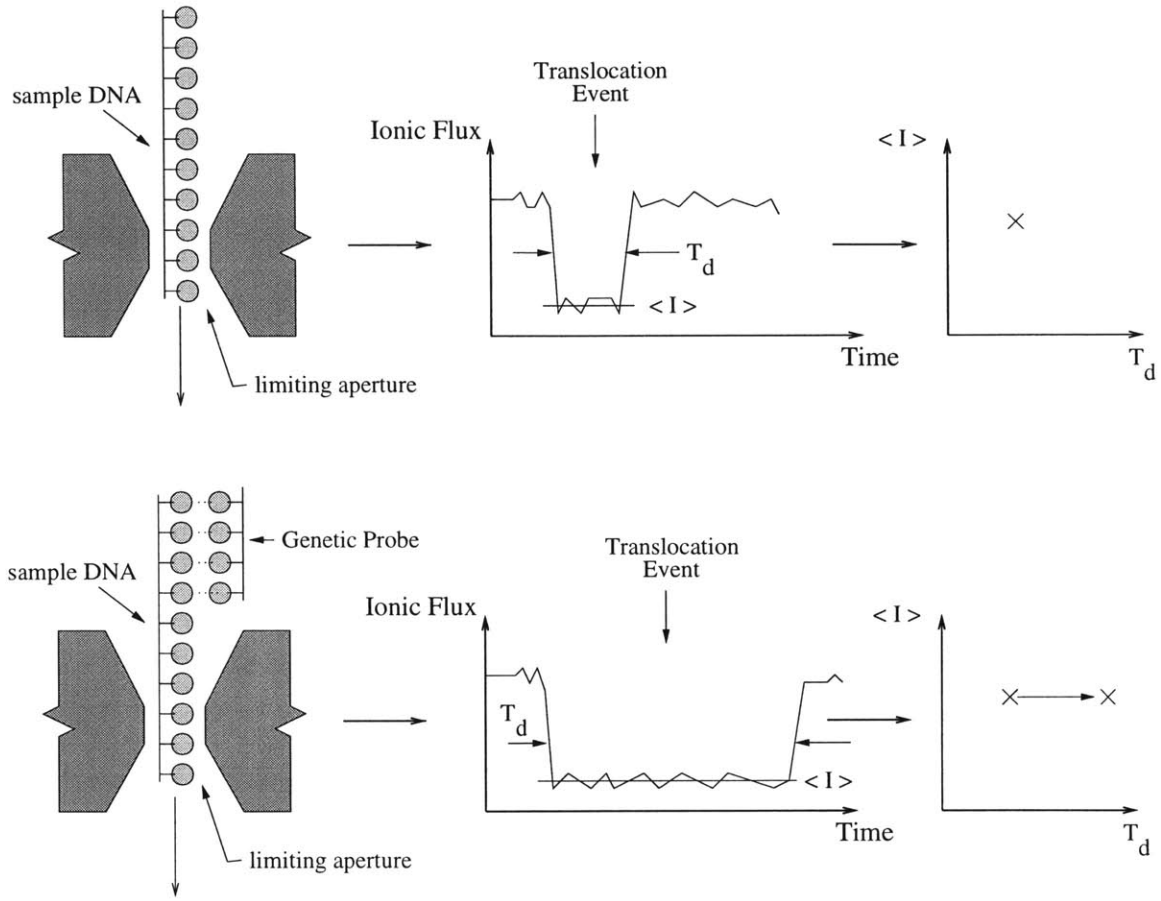

Figure 2-5: The use of a Coulter counter to recognize genetic sequences. Top: In the absence of a complimentary probe, the single-stranded sample DNA translocates through the pore with a characteristic duration and current level. Bottom: Once a target probe binds with the sample, the translocation time is greatly extended by the physical restriction of the pore, which will not pass double-stranded material.

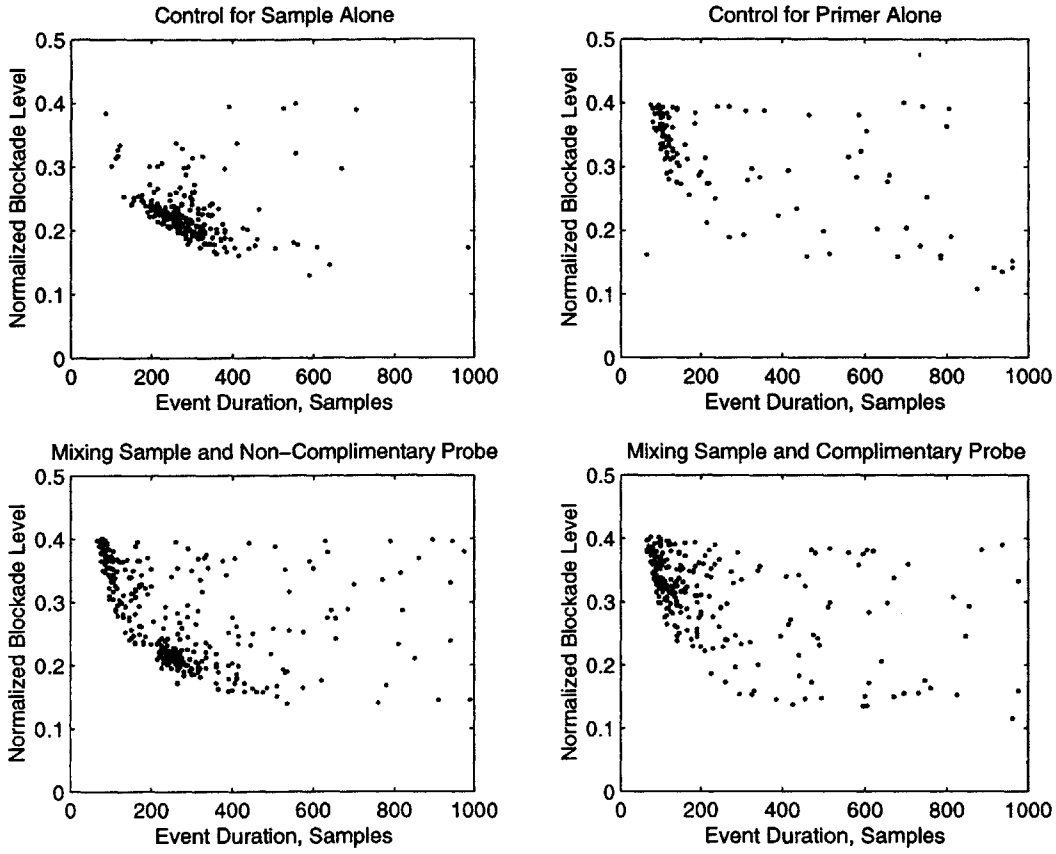

Figure 2-6: Genetic detection proof-of-principle. Top Left: The control event plot of the single-stranded 100-base sample; note the clearly defined characteristic of the polymer. Top Right: The control event plot of the 22-base probe sequence; note its relatively short duration, and the minimal overlap with the 100-base sample distribution. Bottom Left: The mixing of the 100-base sample and a "scrambled" 22-base probe, which should not bind; the event plot illustrates the linear superposition of the two controls, to first-order. Bottom Right: The addition of the complimentary probe results in the disappearance of the sample from its characteristic distribution; the binding of the probe and sample results in extended translocation times that must be cleared with external monitoring circuitry.

Experimental Stage	*Counts in Target Region*	*Counts Overall*
PX Control	101	732
PX and P_y	94 (98)	1939
PX, P_y, P_x	6 (14)	2301

Table 2.1: Summary of counts for Experiment II.

Figure 2-7. This curve represents an exponential probability distribution function (PDF), with a best fit estimate provided by $\lambda^{-1} \approx 3.5$s. This λ estimator matches the mean inter-arrival time, $258/9001/s = (3.48)^{-1}s^{-1}$, based on the fifteen minute interval of data collected.

With the estimate of the arrival rate established, the effect of the DNA probes can be clearly ascertained using probability arguments. The addition of the non-complimentary probe P_y results in a new event count of $N = 98$ over a second fifteen minute sample interval. From the control experiments for the probe P_y, approximately four of these events result from the finite overlap of P_y's event plot with the defined region of interest. Accounting for this overlap slightly lowers the estimated count rate to 94 for the target strand, after the addition of the non-complimentary probe. Based on the Poisson probability distribution function for N shown in Figure 2-8, this event count dictates that within a 95% confidence interval the underlying event rate for the target strand has not changed. The effect of the non-complimentary probe P_y on the target probe event rate is therefore minimal, suggesting little hybridization interaction.

The validation that there was actually probe DNA in solution is provided by the overall count rate. For the polymer PX, the total number of counts within the collection interval was 732, while after the addition of the probe this count number increased to 1939. This increased value is very close to the expectation of 2097 based on the estimated number of molecules added to the bath. The slight discrepancy is within the 20% confidence of the absolute concentration of the polymers based on the limitations of the UV absorption standard. The conclusion, therefore, is that the rate of PX translocation was unaffected by the addition of a non-complimentary probe.

The hybridization interaction of the complimentary probe and target strand is easily detected with the nanopore. The addition of the complimentary probe P_x results in a marked reduction of PX translocation events to 14 within the fifteen minute collection interval. Once

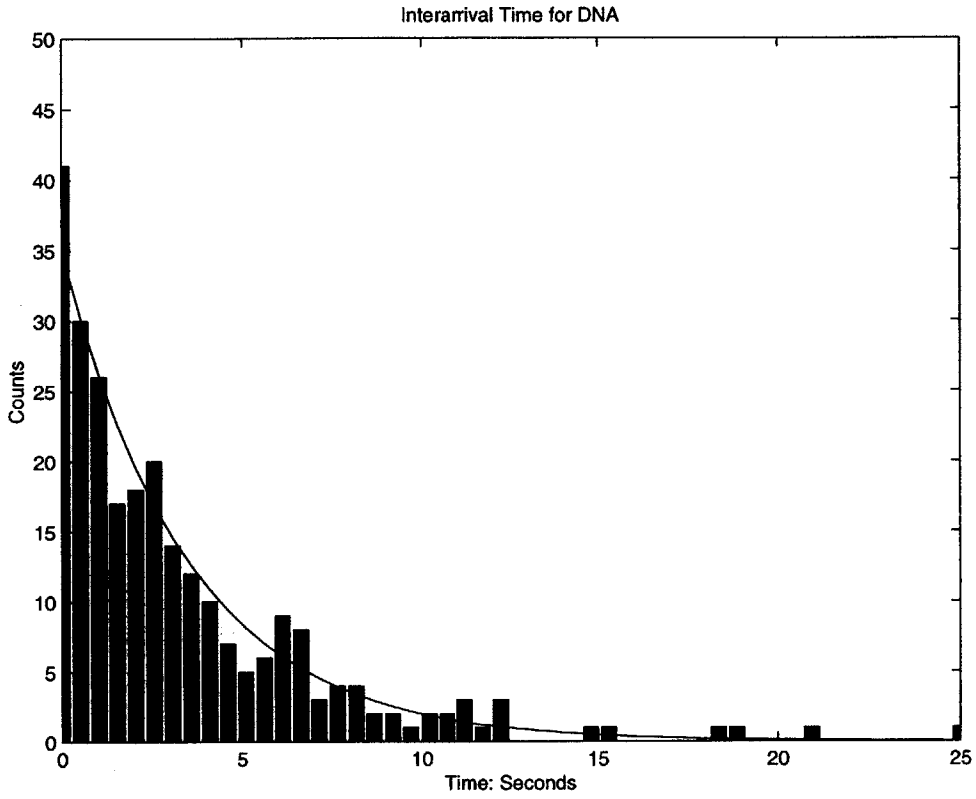

Figure 2-7: The histogram of time *between* DNA translocation events. The exponential profile suggests the use of Poisson statistics for analyzing the DNA events. The best fit curve for the exponential corresponds with the mean arrival rate, as expected.

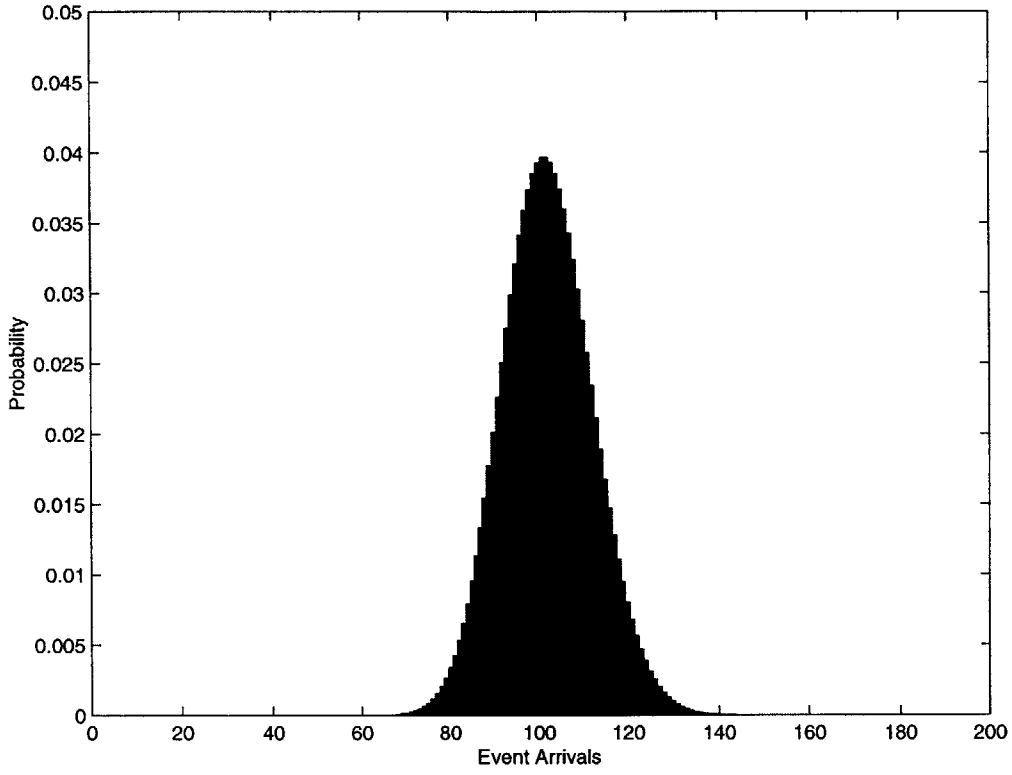

Figure 2-8: The probability distribution function for the number of events measured in a 15 minute interval, based on the estimate from PX alone.

again, roughly eight of these events are likely contributed by an overlap of the probe event plots (P_x and P_y) with the defined region of interest; this lowers the actual count number of target events to six. Based on Poisson statistics, the probability that the underlying rate of PX translocation has changed is 99.999%. The overall count rate of 2301 also supports the conclusion that the P_x probe has bound with the sample PX. The raw data count of 2301 events is justified by the approximate 1207 events associated with P_y (based on the previous time interval of counts), the contribution from the estimated number of unbound P_x probe, 475 counts, and the estimated bound PX probe, 732 counts, for a net total of 2414 events; this number is once again within the 20% confidence interval of the UV concentration estimation.

This series of experiments clearly demonstrates the recognition of genetic sequence information using the nanoscale Coulter counter. This demonstration was based on an "all-or-nothing" sequence match between the probe and target. For use as an effective diagnostic tool, however, the method must be refined to detect a single base mismatch–the equivalent of sub-$\mathring{A}$ resolution of the physical differences within the target ssDNA.

2.5 Experiment III: Enhanced Sequence Recognition with Single-Base Sensitivity

2.5.1 Experimental Purpose and Protocol

The sensitivity of the nanoscale Coulter counter can be extended to single base resolution through the use of temperature biasing. Temperature biasing allows for external control of DNA melting, where "melting" is defined as the separation of the two DNA strands from each other [19]. Because of the physical effect of temperature on probe separation, it is particularly useful for adjusting the probability that a probe and sample are hybridized with each other. The melting curve of DNA is sigmoidal, with a sharp temperature transition of roughly five degrees or less for DNA probes on the order of twenty bases long [25]. The exact melting characteristics of a probe and target is a complex function of salt, base sequence, pH, and DNA concentration, and the expressions for calculating the specific curves can be found in several references [25, 26].

For this discussion, the concept behind achieving single-base sensitivity is best illustrated

by considering the empirical melting curves illustrated in Figure 2-9. The y-axis represents the probability that a probe and target strand are separated, while the x-axis represents the temperature of the bath. At low temperatures, the complimentary pairs are joined together, while at high temperatures they melt and are physically separated. For the 10-base complimentary probe sequence, P_{x0}, used for this experiment the melting temperature is estimated to be 30^oC. This temperature estimate is based on the sequence of DNA and 1M KCL salt concentration used [19]; the melting curve for P_{x0} is represented by the sigmoid shown on the right side of Figure 2-9. The addition of a single-base mismatch between a 10-base probe P_{x1} and the target sample will shift this curve lower by approximately four to five degrees, due to the binding energy lost from a mismatched base [25]. By biasing the temperature of the nanopore's bath solution to lie at the *midpoint* of these sigmoids, the probability that a single base mismatch is melted will be relatively high, while the complimentary probe and sample should remain hybridized. The actual state of the probe-sample pair can be determined by the nanopore Coulter counter.

The procedure for this hybridization experiment is similar to that developed in experiment II. To bias the nanopore for maximum sensitivity to a single base mismatch, the fluid volume is regulated at a temperature of $28^oC \pm .5^oC$. To initiate the experiment, 56 pmol of sample PX was added to the fluid volume and allowed to equilibrate. After a fifteen minute control interval was recorded for PX, 165 pmol of the probe P_{x1} was added to the volume and allowed to interact with the sample template. P_{x1} is a 10-base ssDNA probe[6], with a single base-pair mismatch of cytosine for guanine located in the center of the sequence. The expectation is that roughly 5-10% of the P_y probe should bind with PX at this bias temperature [19, 25]. After the mixture reaches equilibrium, a fifteen minute sample interval was recorded. 165 pmol of the second probe, P_{x0}, was then added to the fluid volume. P_{x0} is also a 10-base ssDNA probe P_{x1}[7], but it is perfectly complimentary with the target PX. The expectation is that a significant number of P_{x0} probes and target samples should hybridize. The solution was once again allowed to equilibrate for fifteen minutes, and a final fifteen minute interval of events recorded.

[6]Sequence=*GAT AC*G TGA G*
[7]Sequence=*GAT AGG TGA G*

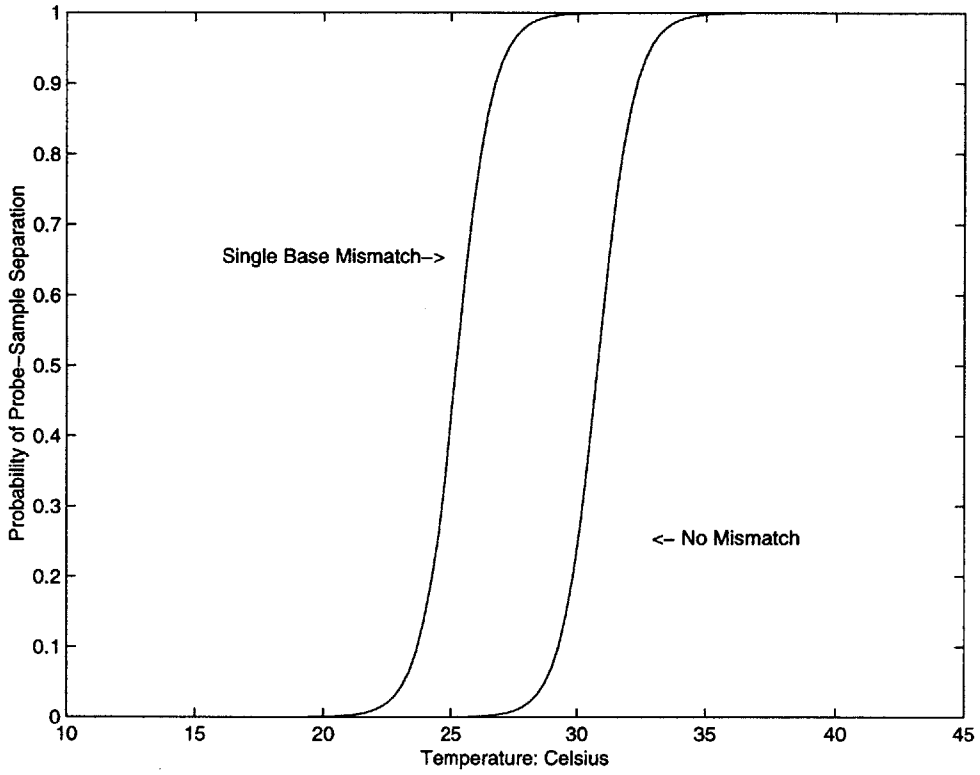

Figure 2-9: The effect of base pairing on melting temperature. The melting curves of short regions of DNA are sigmoids with a transition region of five degrees. The addition of a single-base mismatch will shift the melting point lower by roughly four degrees; biasing the nanopore temperature to lie in the middle of these curves provides single base sensitivity with the nanoscale Coulter counter.

Experimental Stage	*Counts in Target Region*
PX Control	575
PX and P_{x1}	455
PX, P_{x1}, P_{x0}	52 (87)

Table 2.2: Summary of counts for Experiment III.

2.5.2 Results and Interpretation

The event plots illustrate the relative interactions of the probe and target molecules. Figure 2-10 illustrates the control event plot for the target molecule PX; the distinct region around $250\mu s$ is once again clear. After the addition of P_{x1}, a new region appears in the event plot at short times that corresponds to the addition of the 10-base probe P_{x1}. The characteristic region associated with PX, however, is still distinct. Upon addition of the 10-base complimentary probe, P_{x0}, the region associated with PX is essentially removed from the event plot as illustrated in Figure 2-11. This is believed to result from the hybridization between the probe and target DNA strands, which shifts the PX distribution to significantly longer time durations.

To quantify the observations of probe-target hybridization, the region of the event plot associated with PX was defined as in Experiment II and the event count observed for each sequence; this data is summarized in Table 2.2. The control data registered a total of 575 events in a fifteen minute interval, which is used as the maximum likelihood estimator, $N = \lambda\tau$, for the expected target count. After addition of the non-complimentary probe P_{x1}, the detected event rate fell to 455, which is outside the 90% confidence interval for the Poisson statistics of this process. However, based on the melting curve of the DNA, we expect 5-10% of the probe/target samples to be bound, and with a relative weighting of the probe:target concentration of 3:1, the 20% reduction in translocation events is within our general expectations.

The addition of the complimentary probe yields a more dramatic change in the event counts. After the addition of the probe P_{x0}, the event count falls to 87 in a fifteen minute interval. This rate is substantially below the amount expected by a simply doubling the effects observed with P_{x1}, which would be expected to lower the event count to 335. The residual count rate can be explained by two effects; first, there is a finite overlap of the probe distribution with the defined

PX region that accounts probabilistically for roughly 35 of the counts; and second, with a bias temperature a few degrees off from the melting temperature of the DNA, the probability for some free target probe is still finite.

This experiment demonstrates that manipulation of bias conditions can allow for recognition of single base mismatches in a target sample of ssDNA. The sensitivity of this experiment to DNA concentration, however, as well as bias temperature and salt conditions is problematic, and refinements in the technique, specifically in acquiring reasonable melting curves for sample-probe interactions, are required for more quantitative results. The important conclusion to be drawn from this experiment is that through proper adjustment of nanopore's bias conditions, the physical effects of a single-base mismatch between a probe and target sequence can be detected with reasonable accuracy.

2.5.3 Concentration Requirements of Hybridization Detection

The major drawback of hybridization detection is the need for large quantities of sample material. This problem arises from the need for a substantial concentration of DNA in the fluid volume in order to obtain a sufficient rate of translocation events. To demonstrate this problem, the rate of DNA translocations as a function of polymer concentration is shown in Figure 2-12. For $0.01\mu M$ of DNA, which corresponds to 1 p-Mole of DNA material in a 100 μl fluid volume, the translocation rate is roughly one count/minute. As illustrated by the graph, the translocation rate is linearly related to the probe concentration. Assuming a standard diagnostic sample of 10,000 DNA target molecules, the translocation rate extrapolates to one event every 114 years, which is clearly unacceptable for most practical applications. The problem of sample requirements can be addressed by several strategies, but perhaps the most promising approach uses the biochemical amplification of DNA to increase the amount of detectable sample.

2.6 PCR Sequence Detection Strategies

To address the concerns of limited sample material in diagnostic applications, the polymerase chain reaction (PCR) can be used in conjunction with a nanopore. PCR is a well-established technique for amplifying a specified region of DNA within a sample sequence, and excellent

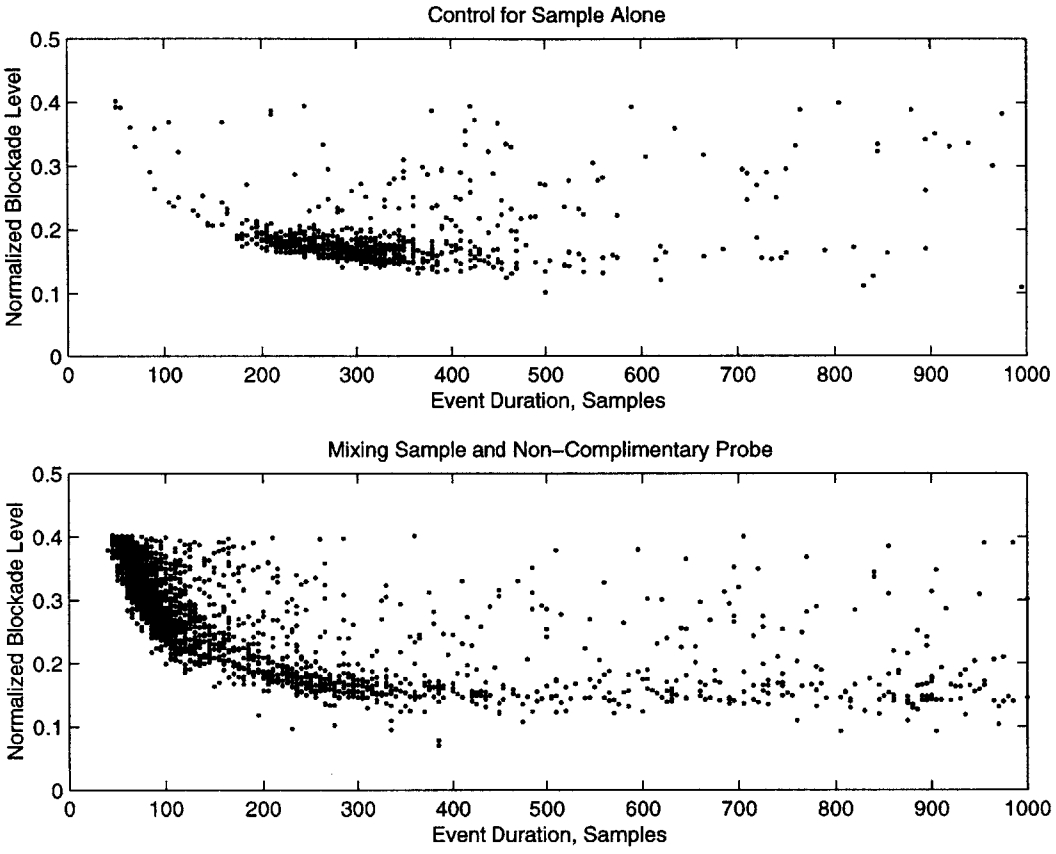

Figure 2-10: The mixing of a probe and target sample to demonstrate single-base resolution. The top event plot is the control for PX, the bottom event plot is the event plot for the mixture of PX and P_{x1}, the 10-base probe with a single base mismatch. Note the significant counts still present in the region of PX.

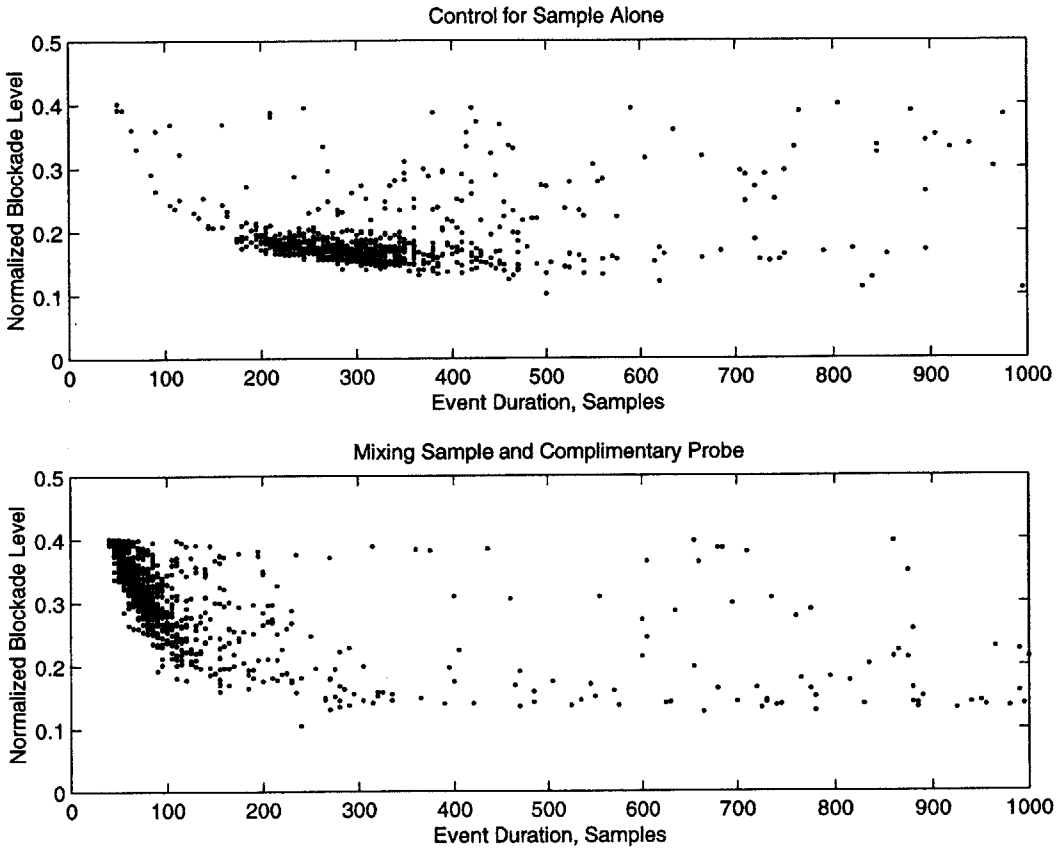

Figure 2-11: The mixing of a probe and target sample to demonstrate single-base resolution. The top event plot is the control for PX, the bottom event plot is the event plot for the mixture of PX and P_{x0}, the 10-base probe without a base mismatch. Note the disappearance of the region associated with PX.

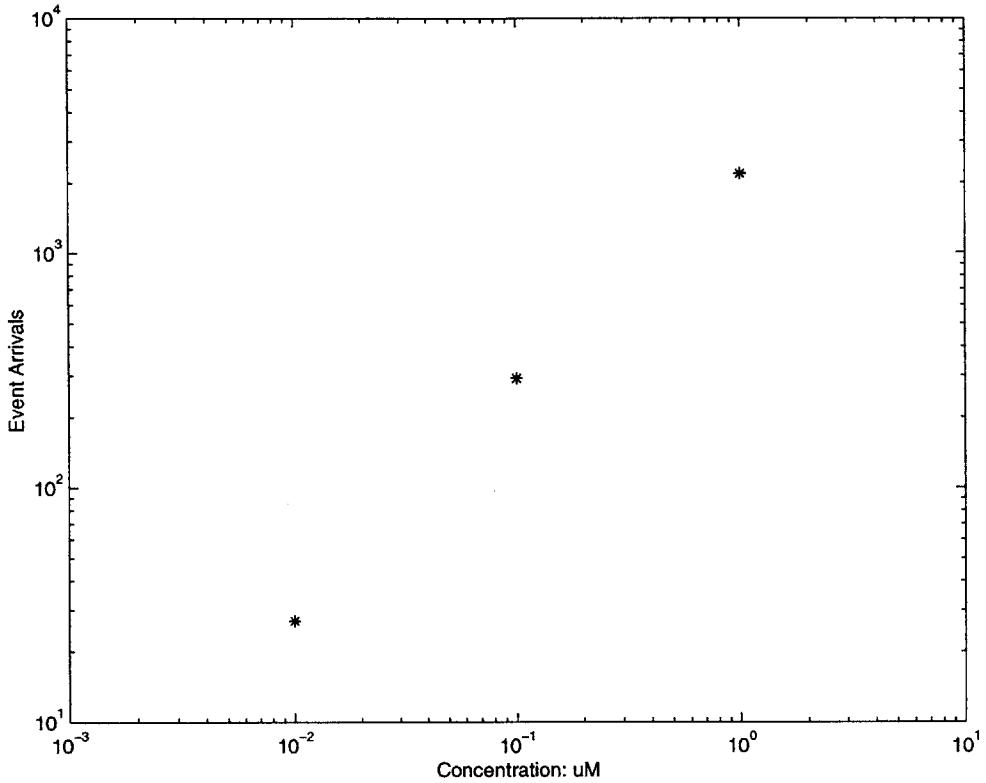

Figure 2-12: The translocation event count over a fifteen minute interval versus concentration.

reviews are provided by [17, 22]. The strategy proposed here uses the fundamental elements of this biochemical amplifier in a protocol suitable for genetic sequence detection with a nanopore Coulter counter.

The goal of this method is to translate the sequence information of the target strand into an event signature recognizable with a nanopore Coulter counter; the concept is illustrated in Figure 2-13. The target sample, X is added to the fluid volume in the presence of the DNA probes, P_x. If the probe finds its complementary sequence on the target and binds, then a polymerase molecule lands on the edge of the double-stranded region and *elongates the probe* into a new polymer, designated as Y. The fluid volume's temperature is raised past the melting point of the DNA duplex, melting X and Y, and then cooled. As long as the probe density is high enough, a new P_x probe should bind with the original sample during the annealing step. In addition, a second probe, P_y lands on the replicated DNA strand Y and is elongated as well, reconstructing a copy of X over a defined region denoted the "amplicon." This process can be cycled continuously, which results in the geometrical amplification of the original sample by roughly 2^n molecules after n temperature cycles.

The use of the polymerase chain reaction results in two important experimental outcomes. First, the original sample DNA can be amplified sufficiently to allow for detection with a nanoscale Coulter counter. Second, the relative positions of P_x and P_y can be engineered to allow for the detection of the *new* amplicon molecule distinct from the original target and probe distributions. This method provides a positive control for detecting genetic sequence that is advantageous over many fluorescent techniques, which report the presence of *any* hybridization event [70, 71].

To demonstrate the feasibility of this detection strategy, a model experiment was performed with a 22-base probe P_x and a target molecule X. The amplicon length was selected to be 150-bases long[8], which should result in a time histogram peak of roughly $375 - 450\mu s$, assuming $2.5 - 3\mu s/base$. A polymerase chain reaction was then modeled by selecting the equivalent of n = 25, 29, 33 thermo-cycles of PCR assuming an initial sample count of 10,000. Each sample was run through the nanopore for thirty minutes, and the event characteristics are summarized by

[8]CTC ACC TAT CCT TCC ACT CAT TTT CCT TAA CCA TTT CAT TCA CCC ATC TCT TCA CTC CAT CTA TCA CCT CCA TAC ATA CCC TCC ATA TTA CAC TCC CAT CAC TAT CAT TAT CTA CAT CCA TTA CAT CAC TAC TCC TCA CAC TAC CAT ACC.

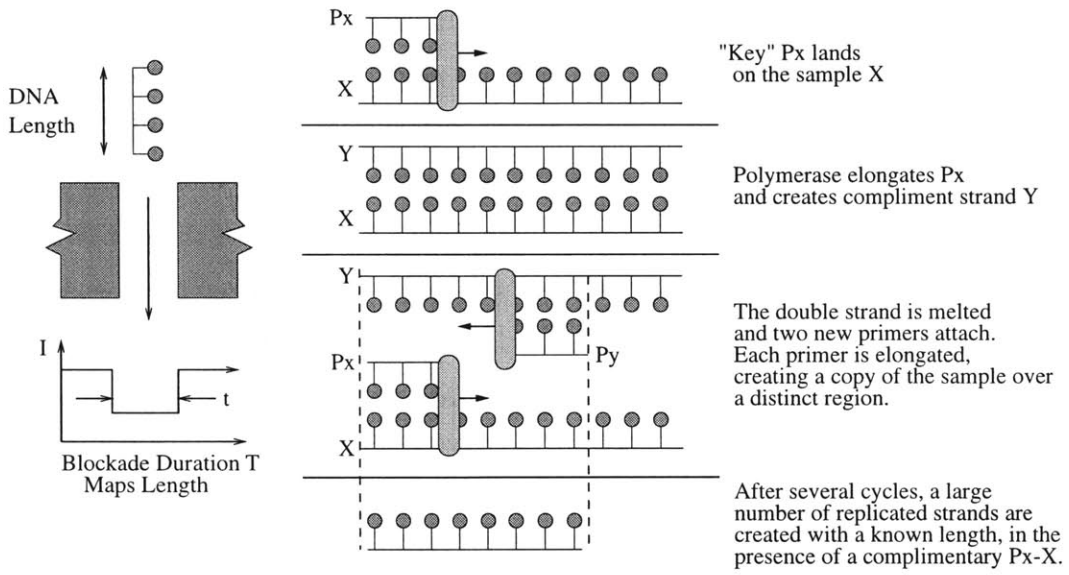

Figure 2-13: The use of the polymerase chain reaction to increase the sensitivity of the nanopore to low numbers of target molecule.

the time histogram in Figure 2-14 (Note the different scales of the y-axis). The relative height of each PCR run can be compared to the background "noise" from 125 pmol of hybridization probe, P_x. The distribution of the amplicon is clear after roughly 29 cycles of PCR, which corresponds to roughly 10 pmol of DNA in the fluid bath. The requirement of 29 PCR cycles is well within the limitations of state-of-the-art techniques [25], and overcomes the nanopore's limitations due to sample concentration requirements.

In order to detect single base mutations, the nanoscale Coulter counter can use competitive PCR. Competitive PCR is a refinement to "standard" PCR that monitors the reaction products of two distinct genetic probes, P_{x1} and P_{x2}, simultaneously present in the target sample's fluid bath [17]. The base differences within the probes represent the mutations for which the diagnostic instrument is testing. By running the PCR reaction with both probes present, the *relative* concentration of the probes' reaction products provides a strong indicator of the target's genetic sequence; this technique is similar to the relative hybridization interactions explored in the previous sections. The use of competitive PCR provides a natural set of controls that help to quantify the experiment and provides a meaningful interpretation of the reaction products [17]; the challenge of applying this technique to a nanopore Coulter counter is separating the reaction products of the two probes, which is usually achieved with fluorescence detection [17].

By using a molecular "bar-code", the reaction products of competitive PCR experiments can be discriminated with a nanopore. A molecular bar-code represents an engineered molecule with physical differences that are easily detectable to a nanopore aperture [21]. One method of constructing a bar-code is to remove large regions of nucleic acids along the ssDNA probe which allows for significantly more ionic current flow through the nanopore [21]. Another method is to attach large fluorophores to the ssDNA that result in diminished current blockades [23]. By altering the relative signature of each genetic probe's bar-code, the amplicon products can be detected by their length, and then sorted by the current/time signature of that probe's particular bar-code. This concept, illustrated in Figure 2-15, allows for the direct electrical recognition of genetic mutations with high accuracy, from a low initial concentration of target molecules.

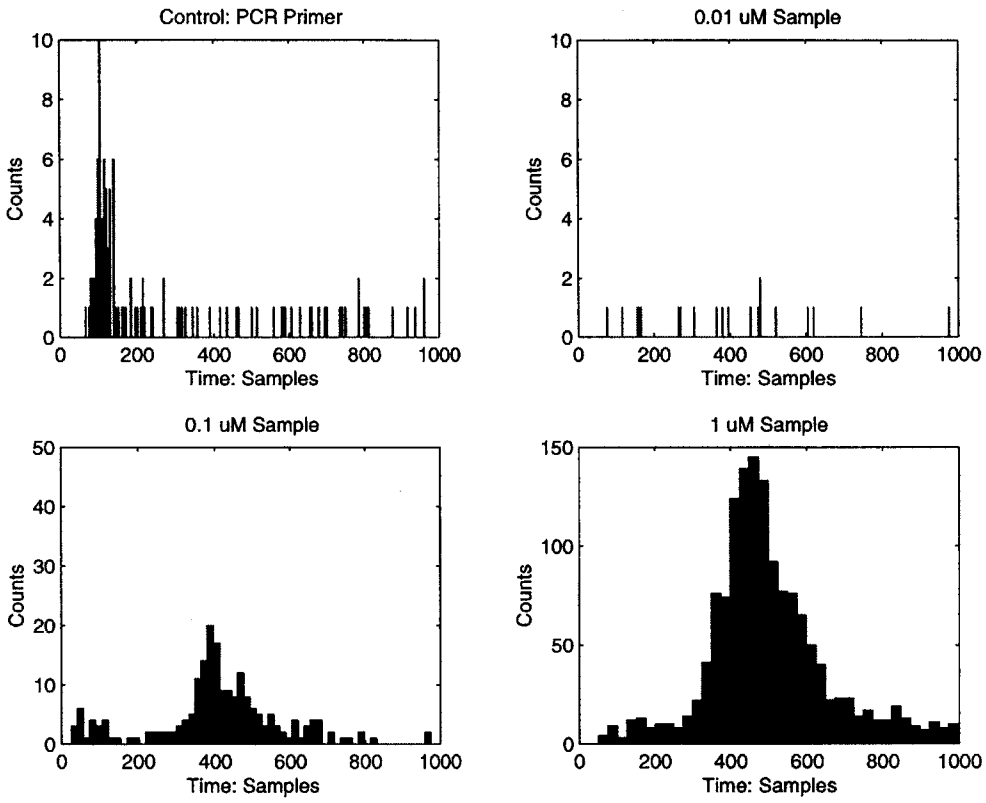

Figure 2-14: The proof-of-concept for PCR detection with a nanopore. The top left is the time histogram of event durations for the 22-base probe P_x, with 125 pmol of sample in the 100 μL fluid chamber. The other three panels are the time histograms of amplicon translocation after 25, 29, and 33 cycles of PCR. These correspond to 0.01 μM, 0.1 μM, and 1 μM of amplicon concentration, respectively. Considering the total fluid volume of 100 μL, these numbers correspond to 1 pM, 10 pM, and 100 pM of total sample in the chamber. (Note the different scales of the y-axis.)

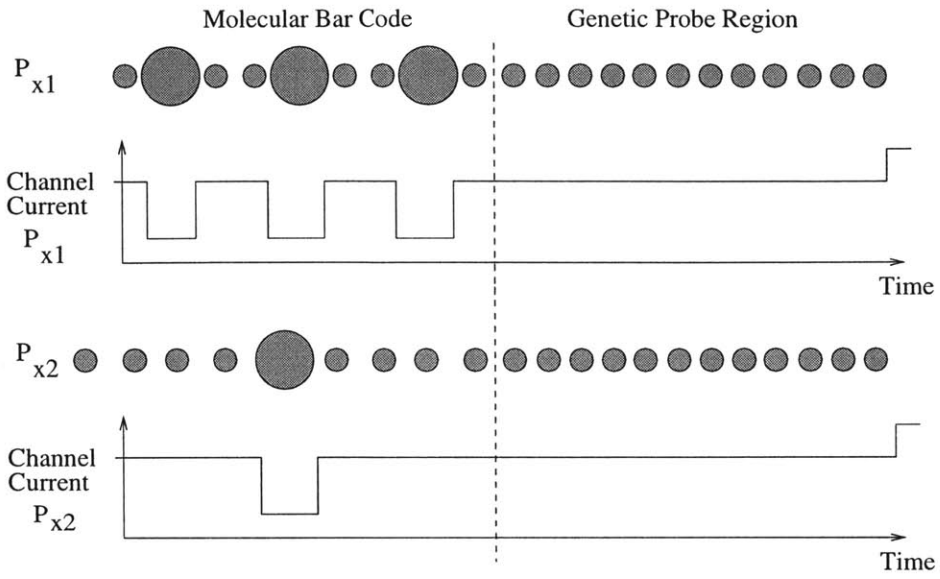

Figure 2-15: The molecular bar-code can be used to discriminate between two genetic probes. The bar-codes can be engineered to provide signatures suitable for detection with a nanopore.

2.7 Towards A Viable Instrument

The past several sections have demonstrated the novel genetic detection strategies possible with a nanoscale Coulter counter. The hurdles to implementing this technique as a practical instrument arise primarily from the toxin pore. The toxin pore was used as a prototype channel because the geometrical characteristics of the limiting aperture allow for the detection of single-stranded DNA. The problem with the toxin for use with PCR detection is that the toxin/membrane biochemical system cannot survive the thermal cycling required for PCR implementation; temperatures beyond 50^oC tend to destabilize the channel [111].

The bias restrictions imposed by a toxin pore also limit its general utility for genetic sequence detection. As described in Appendix B, the salt concentration used for these studies was 1 Molar Potassium Chloride. The high salt concentration helps to prevent gating of the toxin channel that would be difficult to distinguish from the DNA translocation events. The accurate recognition of genetic sequences with complimentary DNA probes, however, requires a salt concentration at least a factor of ten lower in concentration than those used here [26, 25]. Although the detection of single-base mismatches was detectable by the 10-base probes used

in Experiment III, a probe length of twenty bases is required for the *unique* identification of genetic sequences based on the statistics of the four-base coding sequence [25]. For these longer probe sequences, the use of lower salt is required to achieve accurate differentiation of single-base mismatches [19, 26]. In addition, the use of biological polymerases for PCR fixes the maximum allowable salt concentration at 100mM, beyond which the enzymes become inactive [20]. With salt concentrations on this order, the toxin channel begins to gate stochastically and the detection of DNA translocation events within the 10pA quiescent current then becomes problematic.

The inherent drawbacks of the toxin channel and the need for lower salt concentration demand two parallel avenues of development for the implementation of a nanoscale Coulter counter. First, the need for thermo-cycling motivates the development of a silicon, or other "artificial," nanopore. A silicon aperture could theoretically withstand more extreme temperature variations and salt bias conditions, which would allow for the full implementation of the techniques developed in this chapter. Second, the lowering of the salt concentration for better sequence resolution and PCR compatibility immediately drops the characteristic signal level by at least a factor of ten. The resolution of 10pA current fluctuations from DNA translocation and molecular bar-codes requires the development of state-of-the-art current measurement techniques. Only after these two design challenges are met will the direct electrical detection of genetic sequence information truly be viable.

2.8 Chapter Summary

This chapter demonstrated the use of a nanoscale Coulter counter for the direct electrical sensing of genetic sequence information. By refining basic hybridization techniques with temperature biasing, the recognition of single-base mismatches between a genetic probe and target molecule is possible. This achievement represents the first direct electrical detection of DNA sequence without the use of external fluorescent or radioactive markers.

The major drawback of this technique, however, is the requirement for large amounts of sample DNA. To address the issue of concentration requirements for reasonable detection rates, a PCR amplification strategy which uses the nanopore was developed. A proof-of-concept ex-

periment demonstrated that only 29 thermo-cycles of PCR are required for the clear recognition of the amplicon product. In combination with molecular bar-codes, this technique could allow for the *practical* detection of genetic sequence information without the need for external DNA probes. In order to implement this technique, however, two technical hurdles must be overcome.

In order to use the polymerase chain reaction for genetic sequence detection an artificial channel must be developed. The reason for this is two-fold. First, the thermo-cycling inherent in the PCR reaction is not sustainable by a toxin pore. Second, the physical limitations of the polymerase molecule require the lowering of the bath salt conditions by a factor of ten. At salt concentrations of this level, the toxin channel begins to stochastically gate. The development of a silicon nanopore is a major focus of the Golovchenko laboratory at Harvard University.

The second issue with this technique is the practical measurement of channel current fluctuations as the signal-to-noise ratio is lowered by at least a factor of ten. The requirement of detecting the nanopore's picoampere current fluctuations with a signal-to-noise and bandwidth capable of resolving genetic ssDNA probes and bar-codes motivates the design of a sensitive picoammeter. In addition to it's application for sequence recognition, an improved picoammeter would also be useful for the proposed *de novo* sequencing of DNA, which also requires the resolution of small current fluctuations with wide bandwidth. The design and prototyping of a picoammeter suitable for interfacing with the nanoscale Coulter counter forms the remainder of this thesis.

Chapter 3

Interface Strategies for Nanopore Sensors

3.1 Chapter Overview

This chapter introduces a new topological approach for measuring current fluctuations on the scale of those found in a nanopore sensor biased for genetic sequence recognition. In order to investigate possible interface strategies for the nanopore, a set of performance specifications is derived based on the nanopore's properties and its application for genetic sequence recognition. With these specifications established, a general strategy for measuring conductance variations with a voltage clamp topology can be pursued. Existing approaches to implementing a low-noise, wide bandwidth voltage clamp are then briefly explored that may be suitable as an interface picoammeter for the nanopore.

Of the suitable topologies for a low-noise picoammeter, the integrator/differentiator has shown the best performance characteristics in terms of bandwidth, noise, and dynamic range. The drawback of existing integrator/differentiator topologies, however, is the need to periodically reset the system's capacitors. This discontinuous reset results in lost data due to instrument dead-time, as well as the danger of voltage transients across the channel and ill-defined dynamic behavior due to dielectric absorption. These drawbacks motivate the use of an alternative topology that eliminates reset transients with a novel approach to capacitor discharging.

A new picoammeter topology suitable for a nanoscale Coulter counter is introduced that applies the principle of chopper stabilization as an alternative approach to "resetting" an integration capacitor. The concepts underlying the circuit topology, particularly the application of capacitor state-conserving switching, are described in detail. With this new topology, the benefits of an integrator's low-noise and wide bandwidth can be achieved without the compromise of reset transients.

3.2 The Silicon Nanopore: Design Overview

This section gives a brief overview of one approach to fabricating a silicon nanopore [13]; this protocol is being pursued with our collaborators at the MIT Lincoln Laboratory. A general overview of the fabrication process is illustrated in Figure 3-1. This device will be used to extrapolate a reasonable model for the nanopore sensor in the next few sections. A silicon substrate is selected so that the (100) crystal silicon plane lies at the surface of the wafer. A small hole is patterned in a silicon oxide etch mask, exposing a small region of the underlying silicon substrate. A KOH etch is then applied to the wafer, and the begins to etch the (100) crystal plane. When the etch reaches the (111) plane of the substrate, however, the etch rate essentially ceases. The result of this process is the creation of pyramids with atomic dimensions at the tip, as represented by the top illustration in Figure 3-1. The ≈ 50 angle of the pyramid wall is determined by the silicon's crystal orientation.

The silicon pyramid serves as a sacrificial mold for the creating an insulating membrane with a nanometer-scale limiting aperture. A layer of silicon nitride is deposited over the surface of the silicon wafer, forming a negative physical copy of the underlying pyramid. The thickness of the membrane is chosen to insure complete coverage of the pyramid. When the silicon mold is etched away, an insulating membrane with a pyramidal limiting aperture is left behind.

A final surface etch opens the limiting aperture. The insulating membrane is bombarded with 10 keV argon atoms to remove the excess silicon nitride over the limiting aperture. Using a novel sputtering process developed by the Golovchenko group at Harvard [13], a detector on the opposing side of the membrane measures the flux of argon atoms through the aperture. By measuring this flux, the removal of silicon nitride can be terminated when an aperture of

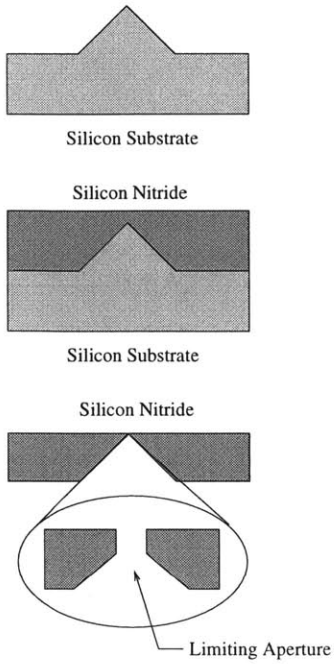

Figure 3-1: The fabrication of a limiting aperture in a silicon nitride window.

the desired size is created. Using this feedback technique, silicon nanopores of roughly 5-10 nm have been fabricated in silicon nitride windows. The refinement of this technique to create 1.5nm apertures is an active area of research [13].

This section has provided a brief overview of one method for fabricating a silicon nanopore. The details of the fabrication process are not critical to the development of this thesis, but are meant to provide a reasonable physical model for designing an electrical interface.

3.3 An Electrical Model of the Nanopore

This section develops an equivalent circuit model for the nanopore channel proposed for genetic sequence detection. The circuit model for the channel will help specify the requirements for interface circuitry to sense conductance modulations due to DNA translocation. In addition, this channel model will provide a means of analyzing sensor noise that clearly defines the channel's resolution to polymer size differences. The major shortcoming of this analysis is that

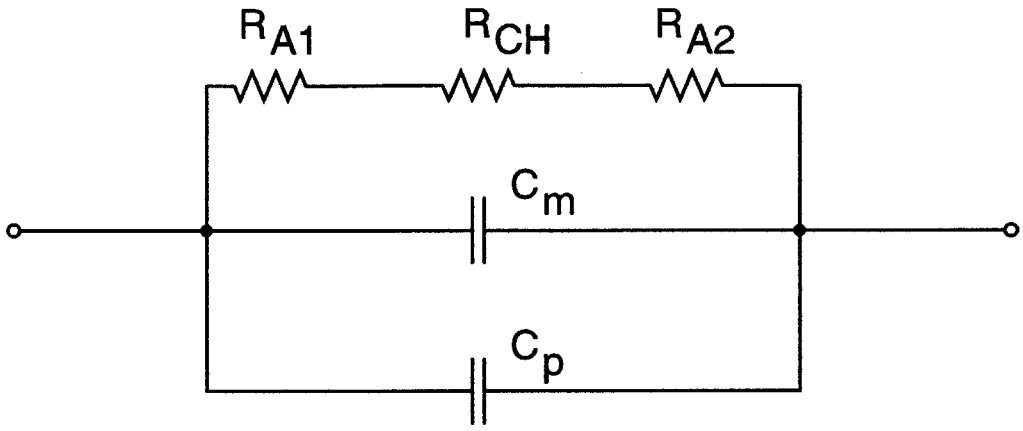

Figure 3-2: The equivalent circuit representation of the proposed nanopore channel.

a prototype silicon nanopore does not currently exist that meets the specifications for detecting single molecule translocations. We can develop, however, the critical parameters needed to characterize the sensor based on first principles applied to the silicon aperture described in the previous section, and the practical experience gained with a toxin pore (chapter Two and Appendix B)[1]. The electrical components that need to be modeled are the channel resistance, access resistance, membrane capacitance, and parasitic capacitance; the equivalent circuit model is shown in Figure 3-2.

The nanopore's resistance, R_{ch}, can be modeled to first order as a cylindrical conducting channel. The resistivity of the channel is assumed to be that of the 100mM KCL ionic bath, which was measured to be $140\Omega - cm(\pm 2\Omega - cm)$ at 300K with a Accumet AR20 conductivity meter [79]. Using the limiting aperture of the toxin channel as a general estimate for the nanopore's geometrical profile, the channel will be modeled as a tube with a diameter of 2nm

[1]This electrical circuit also models the toxin sensor system well, with characteristic numbers of $R_{ch} \approx 1$ GΩ, $R_A \approx 10$ kΩ,$C_m \approx 10$pF, and $C_p \approx 5$pF

and length of 4.5nm. This model estimates the channel resistance,

$$R_{ch} = \frac{\rho L}{A} = \frac{100 \cdot 2 \cdot 10^{-7}}{\pi(1 \cdot 10^{-7})^2}\Omega,$$

to be $2.0G\Omega$; this number is significantly smaller than the experimental value of $10G\Omega \pm 100M\Omega$ observed in the alpha toxin pore. Given the nanometer length scales of the toxin channel, however, the failure of the simple cylindrical model is not surprising. In particular, the effects of surface charges on the channel wall can have a significant effect on the nanopore's electrical properties, since the DeBye length of the ionic solution is roughly 2nm and extends across the fluid channel [79, 73, 74]. The channel's properties are incrementally resistive, however, about the 100mV bias point used for hybridization detection. The fact that the silicon nanopore's dimensions must be on the same order as those of the toxin channel to resolve single-stranded DNA motivates an equivalent empirical estimate for the fabricated device. The assumption of a 10 $G\Omega$ channel resistance may require modification, however, once actual prototype nanopores are fabricated.

The convergence of ions into the nanopore is modeled by the access resistances, R_{A1} and R_{A2}. The specific model for the access resistance depends on which side of the membrane is being analyzed. For the access resistance seen from "inside" the silicon membrane, R_{A1} is modeled as a conic resistor,

$$R_{cone} = \frac{\rho L tan\theta}{\pi a(a + L tan\theta)} \ \Omega,$$

where the physical dimensions are defined by Figure 3-3. The proposed nanopores have a large length L compared with the nanopore radius, a, and an angle θ of roughly 45 degrees. With these approximations, the resistance equation can be simplified to

$$R_{A1} \approx \frac{\rho}{\pi a}.$$

For a conducting bath of $140\Omega - cm$, this expression yields a resistance R_{A1} of $450M\Omega$ for an aperture $2nm$ in diameter.

On the other side of the insulating membrane, the nanopore is exposed to a hemisphere of

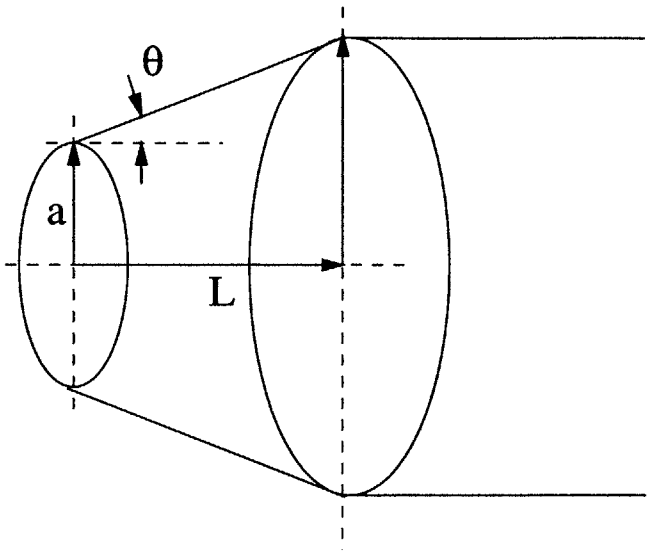

Figure 3-3: The model for the access resistance, R_{A1}.

bath solution. The resistance seen from this aperture can be modeled by

$$R_{A2} \approx \frac{\rho}{4a},$$

which is calculated by integrating the resistance from the bath at "infinity" up to a disk of radius a [28]. Assuming the same $140\Omega - cm$ bath is used on this side of the membrane, the estimated resistance for R_{A2} is $350M\Omega$, assuming a limiting aperture that is $2nm$ in diameter.

The capacitance of the silicon nitride membrane can be lumped into a discrete model for specifying the interface circuit. The equation for the lumped model is derived by integrating the effective membrane capacitance,

$$\delta C = \frac{\epsilon_r \epsilon_o 2\pi r dr}{d(r)},$$

over the estimated radius of the nanopore's insulating partition. The nanopore sensor is assumed to have a converging angle of roughly 45^o, which fixes $d(r) \approx r$. Using this approximation for $d(r)$ and integrating from the inner radius to the outer radius of the insulating membrane,

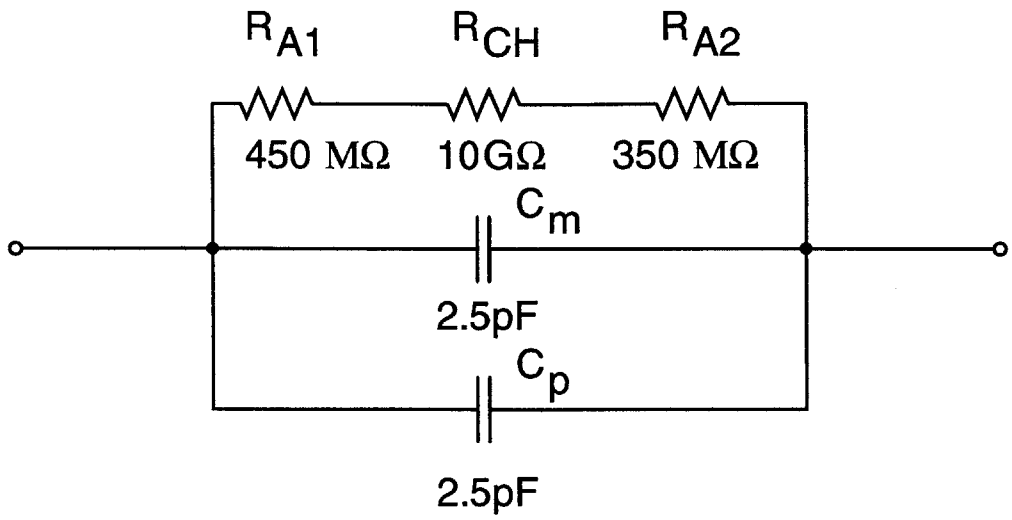

Figure 3-4: The estimated circuit model for a silicon nanopore.

a simple metric for the capacitance

$$C_m = \int_{r_i}^{r_o} 2\pi\epsilon_r\epsilon_o dr \approx 2\pi\epsilon_r\epsilon_o r_o \; Farads,$$

is derived. For a $1cm$ diameter window, the lumped capacitance of the silicon nitride membrane is estimated as 2.5 pF. The estimated capacitance scales linearly with adjustments in the window diameter, which motivates the reduction of the partition area to maintain a low sensor capacitance.

In addition to the membrane capacitance, the parasitic capacitance, C_p, of the picoammeter-nanopore interface must be considered. These parasitics are harder to accurately model, but given the dielectric constant of 8.85 pF/m for free space, it is challenging to lower these parasitics to below 2.5 pF without resorting to co-integration of the channel and interface electronics [72]. The parasitic capacitance of the interface limits the utility of scaling down the nanopore sensor without integrating the interface circuitry; the shunt parasitics would then dominate instrument performance.

The equivalent electrical model for a silicon nanopore with a channel diameter of $2nm$ and a channel length of $4nm$ is summarized in Figure 3-4; the model is derived by combining the observations of toxin pore behavior with the derivation of electrical parameters from first prin-

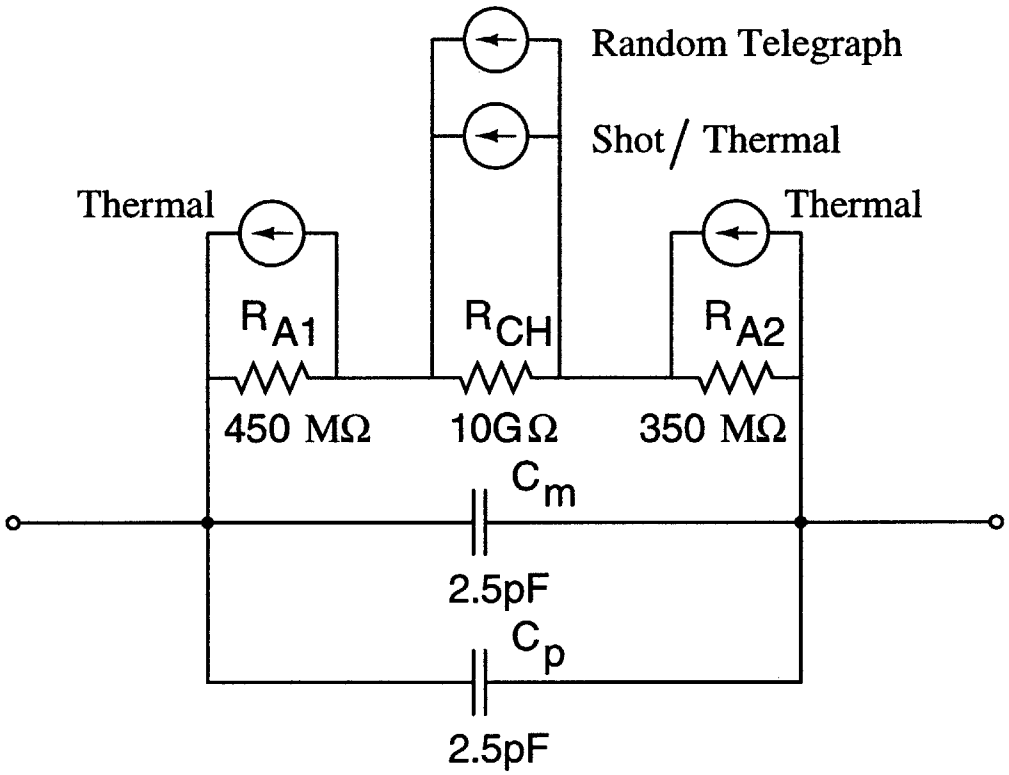

Figure 3-5: The estimated noise model for a silicon nanopore.

ciples. The channel will be estimated as a 10 $G\Omega$ resistor in parallel with 2.5 pF of membrane capacitance and 2.5 pF of parasitic shunt capacitance. The access resistances of 350 $M\Omega$ and 450 $M\Omega$ should in practice be distributed with respect to C_m to model their behavior. For the general design of the interface circuit, the lumped model is sufficient for estimating specifications; this simplification will be revisited, however, when calculating the noise performance of the nanopore channel.

3.4 A Noise Model for the Nanopore

The noise model for a nanopore will specify the minimum detectable fluctuation in the channel and help determine the noise specifications for the interface circuitry. Referring to the electrical noise model in Figure 3-5, the noise sources of interest are the access resistances R_{A1} and R_{A2}, the shot and thermal noise of the nanopore, and low-frequency conductance fluctuations of the channel [131, 73].

3.4.1 White Noise Properties of a Nanometer Channel

The white noise characteristics of the nanopore define the noise floor of the sensor. The general model for noise in a channel with nanometer dimensions was derived by Lauger [27, 29], and those results are applied here. Assuming that the ionic charges pass through the channel independently[2] and that the pore can be modeled as a single potential barrier[3], then the spectral noise density for the current is given by

$$S(f)_i = 2qIcoth(\nu/2)\ \frac{A^2}{Hz},$$

where I is the quiescent channel current, and

$$\nu = \frac{qV_{bias}}{k_bT},$$

is the ratio of the channel bias voltage to the thermal voltage. For large bias voltages, where $\nu >> 1$, the equivalent noise reduces to

$$S(f)_i = 2qIcoth(\nu/2)\ \frac{A^2}{Hz} \rightarrow 2qI\ \frac{A^2}{Hz},$$

which is the characteristic shot noise equation derived by Schottky [65]. For small bias voltages, where $\nu << 1$, the spectral noise approaches the characteristics of thermal noise,

$$S(f)_i = 2qIcoth(\nu/2) \rightarrow \frac{4k_bT}{R_{ch}}\ \frac{A^2}{Hz}.$$

The intuition for these equations is provided by considering the transit characteristics of ions passing through the pore. For small applied voltage biases, the ions translocate with roughly equal probability in both directions across the pore, mimicking the behavior of a classical ohmic resistor and its characteristic thermal noise. For a large applied bias with respect to k_bT/q, the relative probability of ion translocation heavily favors one direction, and the physical model mimics the random jumps across a potential barrier described by the classical Schottky model.

[2]With a bias current of 10pA, a monovalent ion passes through the channel every 16ns, which is roughly the ion's theoretical transit time.

[3]Roughly justified by the limiting constriction in the pore.

For the experiments performed in this thesis, the parameter ν varies from four to eight, yielding a Schottky noise distribution of

$$S(f)_i = 2qI \frac{A^2}{Hz},$$

within a factor 0.07%.

The shot noise of an open nanopore with 10pA of quiescent current results in a spectral noise power of $3.2 \cdot 10^{-30}\ A^2/Hz$, with an rms noise of 0.28pA in a 25 kHz bandwidth and an approximate peak-to-peak noise excursion of 1.7pA. Combining this metric for the noise floor of the channel with the development of channel sensitivity in Appendix A, we expect to resolve physical differences on the order of 3.3 $\AA$ with a signal-to-noise ratio of one, or 7.6 $\AA$ peak-to-peak. This sensitivity is suitable for the detection of single-stranded DNA translocation. The actual channel noise of nanoscale channels, however, is often in excess of this estimate due to other noise processes at low and high frequencies.

3.4.2 Conductance Fluctuations and the Random Telegraph Signal

The fluctuation of the channel conductance can dominate the channel noise at low frequencies [131, 73, 74]. The origins of this noise source are a subset of the general two-state modulation process studied by Machlup [33], which is commonly referred to as the "random telegraph signal" (RTS). The RTS has been proposed to account for many low-frequency noise phenomena, including the excess noise in FETs at low frequencies [133]. As discussed in Appendix B, the protonation state of the amino acids inside a toxin pore modulate the conductance of the channel [73, 74], leading to noise behavior characteristic of the RTS. Recent work with track-etched pores in mica and Teflon suggest the presence of similar gating phenomena in fabricated channels [14], which motivates the consideration of RTS noise is silicon apertures.

Given a current fluctuation of Δi and a mean residency time in each state of τ_1 and τ_2 (Figure 3-6), the RTS noise will have a characteristic spectral density of

$$S_{2state} = 4(\Delta i)^2 \frac{\tau^2}{\tau_1 + \tau_2} \frac{1}{(1 + (2\pi f \tau)^2)}\ A^2/Hz,$$

where τ is the geometric mean of the time constants [33]. This expression is a Lorentzian, which is characterized by a flat spectral density at low frequencies and a 40dB/decade attenuation

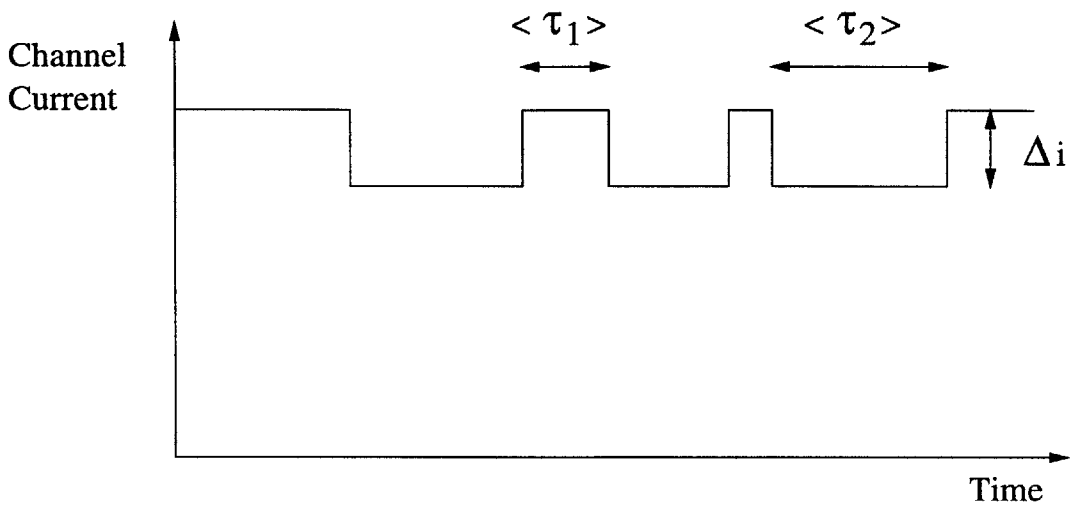

Figure 3-6: The two state conductance fluctuation phenomena. These stochastic noise fluctuations yield excess noise at low frequencies, that can dominate the noise characteristic of the toxin up to 5-10kHz.

rate above a characteristic frequency, $1/\tau$, that is a determined by the fluctuation process. For protonation dynamics along the surface of the alpha toxin channel, this characteristic frequency is on the order of 1-5kHz [73, 74].

By manipulating the bias conditions of a toxin nanopore, the RTS noise can be made negligible in comparison to the shot noise contribution. As developed in Appendix B, the low-frequency RTS noise of a 10pA toxin current is determined by spectral analysis to be roughly $1.1 \cdot 10^{-30} A^2/Hz$ for the bias point used for hybridization detection. The suppression of this noise source is achieved by careful consideration of the pH and salt concentration used with the toxin pore. The origins of the random telegraph signal, however, are highly dependent on the channel characteristics [74]; a nanopore that is fabricated from silicon nitride may exhibit significantly different RTS behavior which will need to be considered when evaluating the channel's noise properties. The conclusion to be drawn here is that the physical biasing of the nanopore's environment can have a significant impact on the RTS noise properties of the sensor, and that this noise may have a significant impact on the low-frequency noise characteristics of the system. For the purposes of interface design, however, the poorly-defined RTS noise will be neglected.

3.4.3 The Effects of Source Capacitance

The voltage noise from the access resistances R_{A1} and R_{A2} reacts with the membrane capacitance C_m to dominate the nanopore's equivalent current noise at high frequencies. For a toxin channel, the noise density associated with R_{Ax} is characterized by its thermal contribution

$$S_{A1}(f) = 4k_bTR_{Ax}\ V^2/Hz,$$

which reacts with the lumped impedance of the sensor network

$$Z = \frac{1 + sR_{Ax}C_{tot}}{sC_{tot}},$$

to yield a spectral noise density of

$$S_C(f) = \frac{4k_bTR_{Ax}(2\pi)^2C_{tot}^2}{1 + (2\pi f R_{Ax}C_{tot})^2} f^2\ A^2/Hz.$$

The lumped circuit approximation for R_{Ax} and C_m works well due to the dominance of the well-defined lipid membrane capacitance [72], as discussed in Appendix B. For the silicon nanopore, however, a noise metric based on the *distributed* access resistance and membrane capacitance must be developed.

The spectral noise distribution resulting from the nanopore's access resistance can be derived by modeling the distributed resistance and capacitance. The incremental capacitance of the membrane, ΔC_m, reacts with an incremental access resistance, ΔR_A, which is defined by a cylindrical shell of ionic solution. Incrementally, this network behaves exactly as the lumped element describing the toxin channel. By integrating the shells of ionic solution over the radius of the insulating membrane, the equivalent rms noise for the nanopore can be estimated. This expression,

$$i_{rms} = 2\pi\sqrt{(4k_bT)\frac{4\pi}{3}\epsilon_r^2\epsilon_o^2\rho L_o ln(\frac{r_o}{r_i})\Delta f^3}\ A,$$

estimates the rms noise for a nanopore constructed from an insulating membrane of relative permittivity ϵ_r, inner radius r_i, outer radius r_o, electrode-pore spacing L_o, and solution resistivity ρ, with a measurement bandwidth of Δf. Using estimated values for a prototype silicon

nanopore[4], the estimated rms noise due to the channel's access resistance is 0.20pA in a 25kHz bandwidth. For the hypothetical nanopore developed here, therefore, the noise in a 25 kHz bandwidth will be dominated by the shot noise contribution of the ionic current.

The frequency weighting of the access resistance noise, however, can severely limit the bandwidth of current measurements. The noise associated with the access resistance intercepts the channel shot noise at a frequency defined by

$$f_{critical} = \sqrt{3\frac{I_{bias}}{k_b T/q}\frac{1}{(32\pi^3\epsilon_r^2\epsilon_o^2\rho L_o ln(\frac{r_o}{r_i}))}}\ Hz,$$

which is approximately 30kHz using the estimated channel parameters and a nanopore current, I_{bias}, of 10pA. Beyond this intercept frequency, the rms noise of the measurement increases as $f^{3/2}$, or a factor 32 per decade of bandwidth. This noise establishes what is effectively a "brick-wall" bandwidth limitation of $f_{critical}$ for low-noise current measurements.

The fact that the sensor capacitance sets such a hard limitation on measurement bandwidth strongly motivates the reduction of the sensor shunt capacitance. A microfabricated channel should lower the magnitude of the sensor capacitance and thereby improve the high-frequency noise performance of the polymer measurements. For example, the reduction of the insulating membrane radius by a factor of ten increases the measurement bandwidth by a factor of roughly 2.5, based on the metric derived above. In addition, the characteristics of high-frequency noise establish the need for low input capacitance and low thermal noise from the *interface circuitry*, which can also contribute high-frequency noise that undermines low-noise current measurements. To yield the full benefits of a microfabricated channel, the interface circuitry will need to be integrated with the nanopore to maintain a low source capacitance.

3.4.4 Noise Summary and Estimated Channel Resolution

This section has established the noise properties of the nanopore channel, and the results are summarized as a spectral noise plot in Figure 3-7. At low frequencies, the open channel noise can be dominated by the conductance fluctuations of the toxin channel. The bias conditions of pH, salt concentration, and voltage bias can hypothetically minimize these effects, however, for

[4] $\rho \approx 100\Omega - cm, r_i \approx 1nm, r_o, L_o$ order of $1cm$, $\epsilon_r \approx 7.5$.

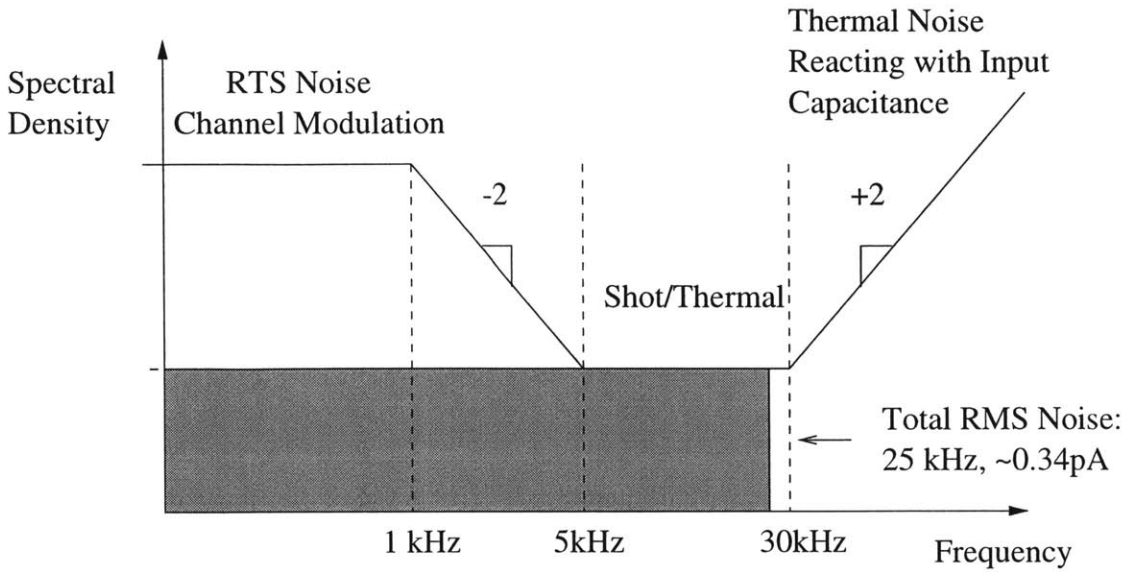

Figure 3-7: The spectral distribution of current noise in an open channel, clearly demarking the three regions of sensor noise. At low frequencies, the noise can be dominated by the random telegraph signal from channel fluctuations, in midband, the noise is dominated by the shot noise of the channel, and at high frequencies, the spectral noise is dominated by the thermal noise of the access resistance shunting through the sensor capacitance.

a channel designed for hybridization detection. Up to approximately 30kHz, therefore, the noise of the channel is dominated by shot noise from the 10pA of quiescent channel current. The spot noise of this source is approximately $3.2 \cdot 10^{-30} A^2/Hz$, and has a uniform frequency distribution. At higher frequencies, defined by $f_{critical}$, the spectrum is dominated by the thermal noise of the access resistance reacting with the membrane capacitance. Collecting the noise contributions and substituting in the characteristic parameters,

$$i_{rms} = \sqrt{2qI_{bias}\Delta f + (4k_bT)\frac{64\pi^3}{3}\epsilon_r^2\epsilon_o^2\rho L_o ln(\frac{r_o}{r_i})\Delta f^3}\ A,$$

the estimated rms noise in the DC to 25kHz band for a nanopore sensor is estimated as 0.34pA, corresponding to a peak-to-peak current noise of roughly 2pA.

The noise associated with the nanopore provides a theoretical estimate for the resolution of a channel to translocating polymers. The equation for the modulation of current due to the

presence of an insulating cylinder is derived in Appendix A. Using this metric,

$$\Delta R = \frac{\rho_o L}{\pi}(\frac{d^2}{D^2(D^2 - d^2)}),$$

and equating the resistive modulation to the equivalent rms noise of 0.34pA in a 25kHz bandwidth, we expect to be able to resolve polymers of size $0.2D$, or 2.8-3.5 $\mathring{A}$, with a signal-to-rms noise ratio of one.

This resolution metric highlights the difficulty of detecting single base modulations with the existing toxin pore. Recalling the discussion of relative base dimensions in chapter one, the toxin channel would need to resolve 0.1-0.5 $\mathring{A}$ physical differences in order to observe the subtle variation in base structure [84]. Although this metric is highly idealized, it does illustrate the difficulty of using this technique for *de novo* DNA sequencing. The detection of single-stranded DNA, which is approximately 1.2nm wide, is a more straightforward measurement. The inherent peak-to-peak noise of the channel corresponds to a physical modulation of roughly 8 $\mathring{A}$, which is significantly smaller than the physical width of the single-stranded DNA. The theoretical ease of detecting single-stranded DNA motivates the novel detection strategies developed in chapter two, which do not rely on sub-$\mathring{A}$ resolution of DNA physical characteristics to recognize genetic sequences. The remaining challenge of applying the nanopore to detect genetic sequences is the design of a suitable interface strategy to resolve the channel current modulations from DNA probes and molecular bar-codes.

3.5 Interface Specifications for Genetic Sequence Detection

The previous section derived an equivalent circuit model for the silicon nanopore proposed for genetic sequence detection. Using this equivalent circuit and models for the noise processes in the channel, a theoretical resolution of 8 $\mathring{A}$ in width was estimated for a nanopore channel and a 25kHz measurement bandwidth. To ultimately achieve this resolution of translocating DNA, a suitable interface circuit must be developed. This section defines the additional interface specifications required for using the nanopore to detect genetic sequences.

3.5.1 Voltage Biasing for DNA Translocation

The interface circuit must provide a bias voltage to drive the translocation of DNA through the limiting aperture. Unlike the $0.5\mu m$ mica channels discussed in chapter 1 [80, 105, 83], a pressure differential is impractical for controlling polymer translocation through a nanometer-scale channel [107]. This observation may be shown explicitly by comparing the characteristic polymer diffusion times through the channel, τ_{diff}, with the time-scale of pressure induced polymer translocation, τ_{pres}. The relative importance of these physical phenomena can be determined by the ratio of their characteristic time constants,

$$\frac{\tau_{diff}}{\tau_{pres}} = \frac{\Delta P R^2}{24\pi D\nu},$$

where ΔP is the pressure differential across the channel, R is the radius of the channel, D is the diffusion coefficient, and ν is fluid viscosity [107]. By setting the ratio τ_{diff}/τ_{pres} equal to one, the scale of the pressure differential required to achieve unidirectional DNA translocation can be estimated[5]. Inserting numbers into this metric that are characteristic for DNA flowing through a toxin channel, a pressure differential of $2 \cdot 10^7$ Pa is required for polymer flow to be on the same order as diffusional flow [107]; this number represents a water column *two kilometers high*, which will not be supported by typical insulating membranes [107, 30, 77]. The unrealistic requirements on a pressure-driven polymer translocation motivate the use of an electric field to drive polymer translocation through a nanopore.

To insure that the DNA polymer can be pulled through the channel and not be overcome by diffusion, a voltage bias significantly greater than k_bT/q must be applied across the pore [102, 103]. The voltage bias creates an electric field across the channel which is believed to pull the negatively-charged DNA through the limiting aperture [103, 31]. Although the underlying dynamics of this process are poorly understood [31], the empirically-determined minimum voltage required for DNA translocation is roughly $4k_bT/q$, or approximately 100mV at room temperature. Since this bias controls the relative rate of DNA translocation versus diffusion, it should be maintained at a level of at least 100mV to reduce the probability of backwards

[5]DNA translocation dominated by a diffusive random walk would clearly complicate the characterization of polymer length, and thereby sequence recognition, with the proposed methods of chapter two.

migration through the channel [31, 103]. This rough voltage specification for insuring unidirectional polymer translocation is supported by experimental data, which demonstrates a linear relationship between translocation time and polymer length. The large variance of the data does suggest, however, some translocation effects arising from polymer diffusion [103, 31].

As a final specification for channel bias, the interface circuit must *limit* the magnitude of the voltage across the insulating membrane to below 300mV. Above this value, lipid membranes are susceptible to dielectric breakdown and are destroyed [30], eliminating the toxin channel in the process. For the semiconductor nanopores modeled in this work, dielectric breakdown can also be a problem. Typical values for breakdown are in the range of $10mV/\mathring{A}$, which specifies a general limit in the range of 300-400mV for the desired silicon nanopore [16]. For all channels with nanometer-scale thicknesses, the sensor bias must be carefully constrained to avoid damaging the limiting aperture.

The primary limitation imposed by a DC voltage bias is to eliminate the use of purely AC conductance measurement techniques. The interface circuit must balance the quiescent current through the nanopore, which requires the design and practical implementation of a low-noise current source.

3.5.2 Frequency Specifications

Bandwidth Requirements for Hybridization Detection

The frequency specification for the interface circuit is determined by the rate of DNA translocation. Preliminary experiments using single-stranded DNA established a translocation rate of roughly 2-5 μsec per base [103, 110, 111]. The minimum bandwidth to detect single-base fluctuations can be estimated from the 10-90% risetime of the circuitry,

$$f \approx 0.35/t_{r(10-90)} = 175kHz,$$

which is well above the critical frequency $f_{critical}$ of 30kHz imposed by the thermal noise of the access resistance reacting with the insulating membrane's capacitance. Clearly, the required bandwidth of the current measurement or the noise of the channel sensor must be lowered for the nanopore technique to be viable.

The use of DNA probes and hybridization detection significantly relaxes the bandwidth requirements for the interface circuitry. The use of probe sequences on the order of twenty bases long reduces the required bandwidth to 7.7kHz for the threshold of detection at room temperature. For the elevated temperatures encountered with the polymerase chain reaction, the rate of DNA translocation is increased by roughly a factor of three [111]. The increased translocation rate raises the minimum bandwidth to 25kHz. With this measurement bandwidth, the detection and characterization of DNA probes and molecular bar-codes is still feasible, allowing for the identification of specific genetic sequences.

Bandwidth Requirements, Looking to the Future

The bandwidth requirements of the picoammeter should allow for scaling with future nanopore experiments. Although constructing a 175kHz picoammeter is overkill for the *present* hybridization experiments, any proposed topology should be able to scale easily to wider bandwidths in consideration of the goals of nanopore sequencing. Recalling the equation for the bandwidth metric derived earlier,

$$f_{critical} = \sqrt{3\frac{I_{bias}}{k_b T/q}\frac{1}{(32\pi^3\epsilon_r^2\epsilon_o^2\rho L_o ln(\frac{r_o}{r_i}))}}\ Hz,$$

if the total input capacitance of the picoammeter could scale down to the order of 0.5pF, the noise barrier for 1pA rms currents would extend to approximately 200kHz. This bandwidth is on the order of that required for single base detection, and with additional gains in base resolution provided by alternative detection strategies[6], may allow for rapid *de novo* sequencing of DNA. The noise benefits associated with an integrated sensor and interface circuit motivate a consideration of topologies amenable to future microfabrication.

Eliminating Instrument Dead-time

In addition to bandwidth considerations, the sensor interface must limit instrument dead-time. Dead-time is defined as any instrument overhead that results in lost or significantly modified

[6]These options include measuring tunneling currents through DNA, or augmenting the detection of base differences with modified nucleic acids.

data. For *de novo* sequencing, a large dead-time would result in the misreading or complete absence of bases in the measured sequence, which is equivalent to creating a false mutation or base-deletion in the sample DNA strand. This concept is illustrated in Figure 3-8. The specification for *de novo* sequencing of DNA would require a dead-time of under 2-5 μsec, based on the existing rate of DNA translocation. Though a true specification for instrument dead-time is still ill-defined at present, the prototype topology should *inherently minimize* the duration of the dead-time to increase it's utility for the intended *de novo* sequencing of DNA.

The other concern of instrument dead-time is the state of the voltage bias during this interval. If the channel's bias voltage is significantly perturbed during the dead-time, an event's duration can be significantly skewed due to the variation in the polymer's translocation rate. This effect would result in the discrete jumps of the DNA during a reset interval, which would undermine the determination of the sequence. This phenomena yields the other specification for the dead-time: during a dead-time interval, the sensor bias must be maintained. Combining a short interval with a stable channel bias minimizes the effects of instrument dead-time.

Eliminating Instrument Dead-time for Hybridization Detection

The minimization of dead-time is also important for the strategies of detecting genetic sequences through hybridization as developed in chapter two. To establish a specific dead-time specification for hybridization detection, the probability of missing or significantly perturbing translocation events should be diminished. Of particular concern is the interference of instrument dead-time with translocating DNA that results in the significant misreading of event durations or identifying features, like a molecular bar-code. Given the wide variation in polymer translocation durations, a simple blanking circuit that throws out events that coincide with a dead-time interval is not an appropriate design strategy. The required duration of the blanking interval, where data would be lost, is strongly biased against longer polymers or double-stranded material that exhibit extended translocation times.

In order to eliminate the effects of a "collision" between a reset interval and a translocation event, a maximum dead-time limit of approximately $15\mu sec$ is specified for the prototype picoammeter. This specification is derived from the 10-90 rise-time of a 25kHz lowpass filter; as long as the dead-time duration falls within this rise-time, it will have a negligible effect

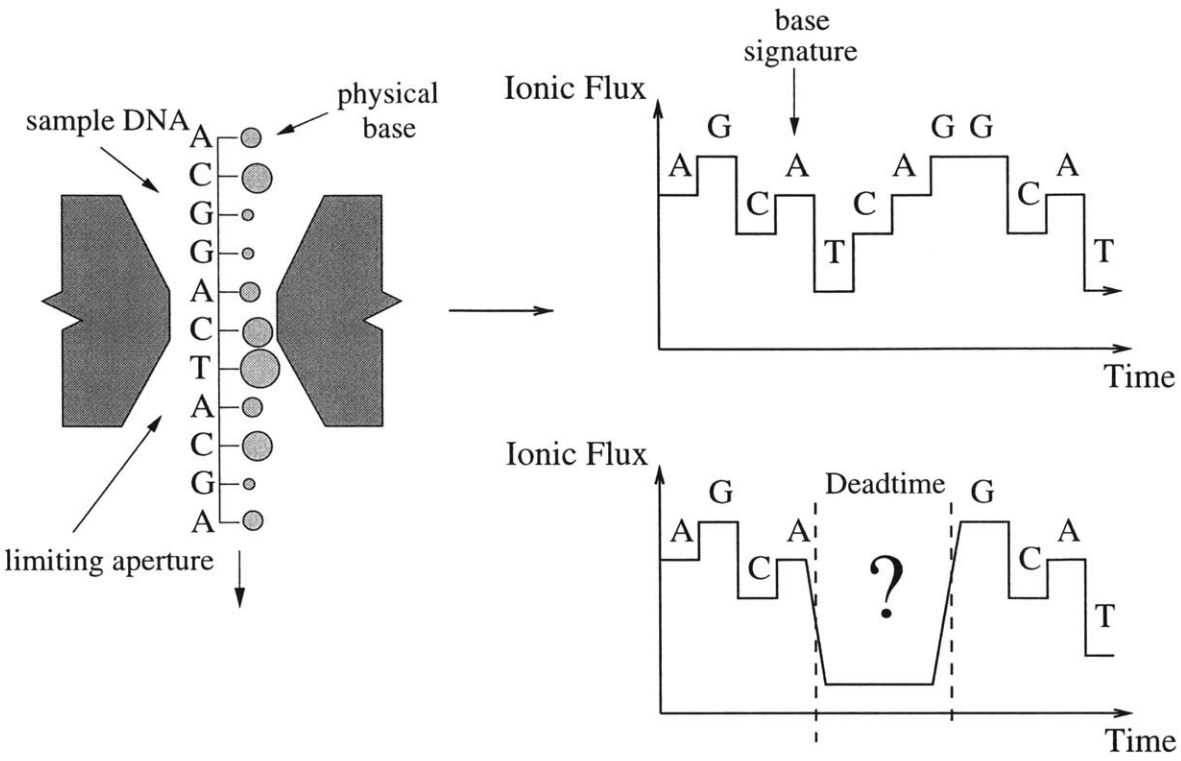

Figure 3-8: The issue with circuit dead-time. During dead-time, the instrument no longer provides the proper sequencing data and base information is lost or distorted.

on the measured polymer distributions. In addition, with a stable sensor bias the polymer translocation rates will not be effected by the collision of a translocation event and a dead-time interval.

3.5.3 Noise Specifications

The noise specifications for the interface circuit are defined by the need to detect rapid fluctuations in the 10pA channel current during DNA translocation. Analysis of the sensor noise behavior demonstrated that the current fluctuations are shot-noise limited within the 25kHz measurement bandwidth. The rms fluctuation of this noise source is .28pA, which allows for the straightforward detection of DNA translocation events that result in $10pA \rightarrow 1.5pA \rightarrow 10pA$ current modulations. The need to recognize molecular bar codes for competitive PCR studies restricts this number slightly. Using the metrics for channel sensitivity derived in Appendix A,

we expect the use of a molecular bar code constructed with 0.5 nm a-basic[7] regions of DNA to result in current fluctuations of roughly $1.5pA \rightarrow 9pA \rightarrow 1.5pA$ superimposed on the quiescent current during DNA translocation [21]. This variation restricts the required noise to approximately 1.25 pA rms to accurately discriminate the presence of molecular bar-codes based on the peak-to-peak noise of the distribution. In reality, this specification may be relaxed somewhat given the signal properties of the molecular bar-codes, where the ability to apply hysteresis in the signal analysis can aid with spurious noise rejection.

The problem of detecting DNA-induced fluctuations of the nanopore current arises from the thermal noise of the picoammeter reacting with the capacitances at the input to the interface circuit. Unlike the white noise sources dominant at low frequencies, this noise source places a severe limitation on measurement bandwidth and the interface circuit should be designed with the goal of adding minimal excess noise at high frequencies. An effective measure of the interface circuit's high frequency noise contribution is

$$\frac{i_n^2(f)}{\Delta f} = e_n(2\pi)^2 C_{tot}^2 f^2 \ A^2/Hz,$$

where e_n is the input-referred voltage noise of the interface circuit and C_{tot} is the *total* capacitance at the input of the interface, including the insulating membrane and parasitic shunt capacitances. In order to obtain reasonable signal-to-noise, the excess noise contribution must be limited to 1.25 pA rms to insure that the peak-to-peak noise does not significantly overlap with the characteristic current levels associated with molecular bar-codes.

3.5.4 Specification Summary

To summarize the specifications, the interface circuit must provide a minimum bias voltage of 100mV to drive DNA translocation. The circuit should also maintain the sensor bias under 300mV to prevent dielectric breakdown of the insulating membrane. The bandwidth of the prototype circuit must be 25kHz to characterize the 20-base DNA probes used for hybridization detection, while the dead-time of the circuit should be inherently minimized to reduce the probability of lost or skewed data. The interface circuit must maintain the total rms noise

[7] Abasic DNA is defined as a region of DNA composed of only a sugar backbone, with no bases attached.

Specification	*Requirement*
Bandwidth	$25kHz$
Dead-Time	Minimize $< 15\mu s$
Voltage Bias	100mV nominal
Voltage Limit	300mV clamp
RMS noise	$1.25pA$

Table 3.1: Summary of specifications for the interface circuitry.

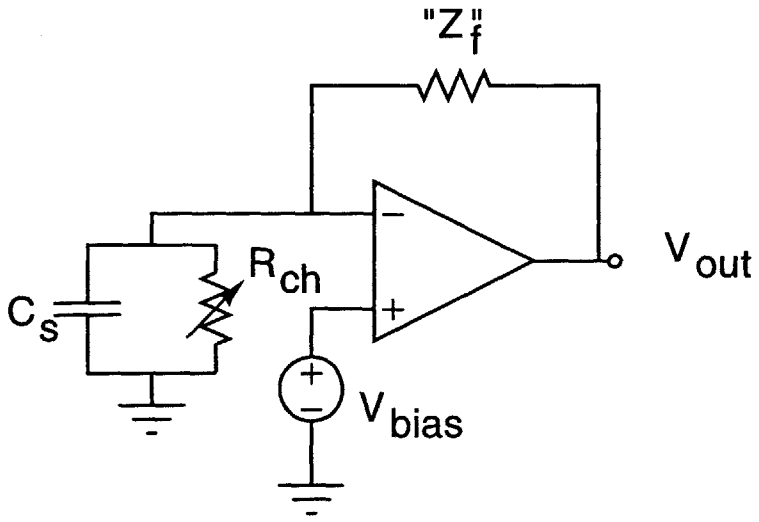

Figure 3-9: The canonical voltage clamp. The operational amplifier maintains the voltage bias across the toxin sensor, eliminating the dynamic issues associated with modulating its voltage.

current to under 1.25pA in a 25kHz bandwidth to allow for the accurate resolution of DNA translocation events and molecular bar-codes. As a final consideration, the circuit topology should be scaleable with the planned microfabrication of future nanopores that may allow for the *de novo* sequencing of DNA.

The design specifications laid out in this section are common to many instrumentation challenges including high-accuracy scanning tunneling microscopy, nuclear particle detectors, and x-ray charge amplifiers [61, 60, 59, 58, 57, 56, 55, 54, 53, 52, 51]. In particular, the problem of reducing instrument dead-time is a recurring problem in low-noise, wide bandwidth charge and current measurements [113]. The next section summarizes state-of-the-art circuit topologies that might address the design specifications outlined here. Commercial instruments do exist that meet *most* of the specifications for the *discrete* picoammeter. These topological approaches to solving the measurement problem, however, rely on complex circuit topologies that do not scale well with integrated sensors.

3.6 The State-of-the-Art in Picoammeters

This section provides a brief overview of topologies suitable for meeting the nanopore Coulter counter's specifications; a summary each topology's performance is provided by Table 3.2. The detailed analysis that lead to this table can be found in Appendix C, which also provides the relevant background and references for the interested reader. This section is designed to provide a brief summary of the benefits and drawbacks of existing circuit topologies, which will motivate the novel picoammeter developed in this thesis.

The challenge of designing a low-noise, wide bandwidth picoammeter derives principally from closing a feedback loop. To achieve wide bandwidth recordings of channel current modulations, the voltage clamp topology shown in Figure 3-9 will be used. The advantage of this topology is that the voltage across the nanopore sensor remains fixed to first-order, which eliminates the dynamic issues associated with charging the sensor capacitance (see Appendix C for details). In addition, with proper design of the operational amplifier, the excess noise from the opamp's input bias currents can be made negligible. Although the voltage clamp allows for wide bandwidth measurements, it does require the closing of a feedback loop with an element

Specification	*Feedback Implementation*		
	Resistive	*Optical*	*Capacitive*
Bandwidth	1-5kHz (or less)	> 25kHz	> 50kHz
Noise Performance	Excess Noise	After-Effect	Excellent
Dead-Time	None	None	$100\mu s$
Sensor Bias Stability	Excellent	Excellent	Reset Issues
Future Integration	Poor	Good	Excellent
Other Drawbacks	Thermal Coefficients	Linearity	Dielectric Absorption
	Voltage Coefficients	After-Effect	Reset Transients

Table 3.2: Summary of state-of-the-art techniques in voltage clamp picoammeters. The capacitive feedback technique would yield the best overall performance, except for the issues associated with resetting the circuit's capacitors.

Z_f. The specifications of Z_f are for large transimpedance, wide bandwidth, and low excess noise. The practical implementation of a Z_f with these features is challenging for the currents and bandwidths specified for the nanoscale Coulter counter.

3.6.1 Resistive Feedback

The most straightforward approach to implementing Z_f would be to use a resistor. The drawback of resistive feedback picoammeters, however, is the required size of resistance needed to achieve acceptable noise performance. The required size is derived by equating the resistor's noise contribution with the noise associated with the nanopore sensor. The 10pA channel shot-noise specifies a feedback resistor on the order of $5G\Omega$ or greater. Resistors of this magnitude suffer from several practical drawbacks, including thermal noise, excess noise, large voltage and thermal coefficients, and limited bandwidth [118, 131]. The issue of bandwidth is especially critical for a nanoscale Coulter counter. In practice, the parasitic capacitance across the feedback resistor is on the order of 0.25pF [18, 118], which creates a dominant pole for the picoammeter at roughly 125Hz–more than two orders of magnitude below the 25kHz specification for DNA probe detection. Relaxing the magnitude of the feedback resistor to $400M\Omega$ to yield roughly 1pA rms in the measurement bandwidth still yields an effective bandwidth of only 1.1 kHz (Appendix B), significantly below the specification required for genetic sequence recognition.

Compensation strategies do exist that help extend the instrument's frequency response. One

approach to improving bandwidth is to segment the feedback resistor to distribute the parasitic capacitance, which can often yield a factor of five extension of the feedback path's bandwidth [42]. Another approach is to use a high-pass compensation filter after the primary amplifier to boost the high-frequency noise performance of the overall measurement. This technique is often limited in practice, however, unless multiple-order compensation filters are used to compensate for the complex dynamics of the large feedback resistors [118, 131].

A final major drawback of the resistive technique is the challenge of implementing a suitable device with standard integrated circuit processes. Typical resistors in modern fabrication processes are limited to the order of $10k\Omega$/square [2]. A 5 GΩ resistor, therefore, would require 500,000 squares to implement the feedback resistance. Assuming a square edge of $1\mu m$, the specifications for the circuit would require a series resistance path a half-meter long, which is not practically feasible. The drawbacks of implementing low-noise resistive picoammeters with suitable bandwidth motivates an investigation of alternative circuit topologies.

3.6.2 Optical Feedback

A large effective resistance may be created through optical feedback [119, 121], as illustrated in Figure 3-10. The effective resistance is created by weakly coupling a voltage-controlled light source at the output of the voltage clamp to a reverse-biased pn junction at the input of the picoammeter. In practice, the pn junction is usually provided by the gate-drain junction of the operational amplifier's JFET [119]. The use of optical feedback for a nanoscale Coulter counter could prove useful in the future, since the coupling of light into the summing node from "off-chip" could be achieved with low excess shunt capacitance.

Several practical problems, however, currently limit optical feedback's utility for picoammeter circuits. First, the non-linearity of the effective resistance complicates the compensation of the picoammeter's dynamics. This problem could be addressed with the use of minor loop feedback, and attempts to implement this correction strategy are bearing results [122]. A more serious issue is the "after-effect", which refers to the repeated flow of charge into a junction after the termination of the light source. The model for this effect results in a parasitic shunt network that contributes a derivative high-pass component to the picoammeters transimpedance. The additional high-pass term can increase the noise gain for the circuit at high frequencies, which

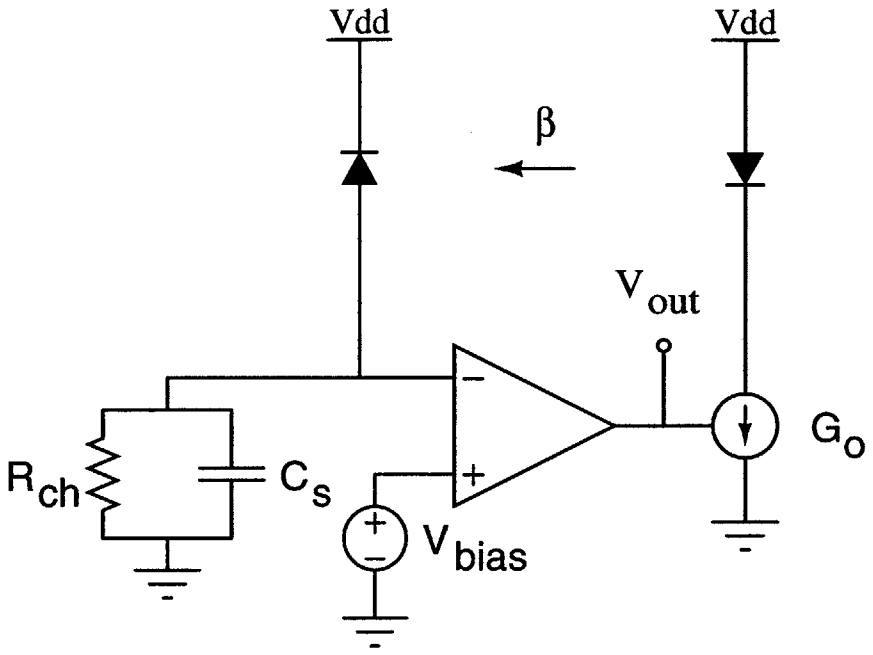

Figure 3-10: The use of optical feedback for charge balancing. By weakly coupling the light source and reverse-biased junction (β), a large effective resistance with wide bandwidth can be created.

undermines noise performance. The parasitic currents associated with the after-effect must be eliminated for the implementation of practical picoammeters [119]. The removal of these effects is a major goal of nuclear instrumentation specialists, and improved JFET design is showing some promise [133]. When these parasitic effects are eliminated, the optical feedback approach may prove to be a useful alternative for wide bandwidth picoammeter design.

3.6.3 Capacitive Feedback

The practical drawbacks of the optical and resistive feedback picoammeters motivate the use of capacitive feedback. Capacitors are essentially ideal feedback elements, with low-noise, excellent linearity and wide bandwidth [65, 118, 119, 127, 128, 42]. In addition, high quality capacitors can be integrated in standard silicon processes, making the scaling properties of this topology particularly appealing [65].

The standard topology for a capacitive picoammeter is shown in Figure 3-11. The ex-

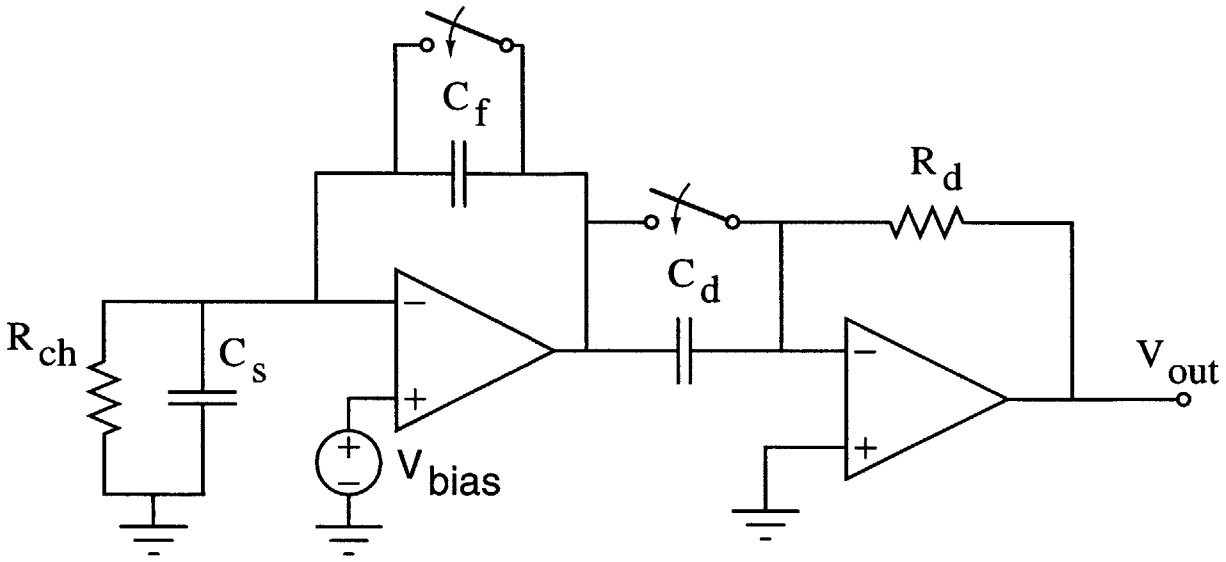

Figure 3-11: The use of capacitive feedback for voltage clamping. The ratio of the capacitors provides a low-noise current gain of C_d/C_f, which is then converted to an output voltage through R_d. Although this topology offers excellent performance, the capacitors C_f and C_d must be periodically reset in the presence of a DC current.

cellent noise properties of the topology arise from the current gain, C_d/C_f, provided by the integrator/differentiator combination. The use of capacitors to achieve the initial low noise and wide-bandwidth current gain relaxes the specifications on the differentiation resistor, R_d. The excellent dynamic properties of the current gain circuitry also help to achieve measurement bandwidths of 50kHz with relative ease compared with alternative feedback topologies. The use of capacitors as the feedback element in the voltage clamp circuit has consistently yielded the highest performance picoammeter topologies with regard to noise, bandwidth and linearity [131, 118].

The major limitation of the integrator/differentiator picoammeter is the need to periodically reset the capacitors in the presence of a DC current [118, 131, 127, 128, 119]. During resets, the output of the picoammeter bears no relation to the input, which can result in a significant dead-time. To hold this dead-time to a minimum, a number of designs have been explored that attempt to make the reset duration as short as possible. These designs all use the same general

strategy of discharging the capacitors as quickly as possible once a limiting voltage has been reached [118, 131, 127, 128, 119]. In practice, however, the overall dead-time has been limited to $100\mu s$ or greater due to limitations of the differentiator resets and overall circuit bandwidth.

The dead-time of the integrating picoammeter is not the only limitation imposed by resets. Additional problems with rapidly discharging the circuit's capacitors include excessive transient voltages across the nanopore interface that can break down the sensor, and poorly characterized transient currents arising from dielectric absorption. The mitigation of these issues can quickly undermine the inherent advantages of the capacitive feedback topology [118, 122].

3.7 Integrating without Resets?

The major limitation of voltage clamp amplifiers constructed with integrators and differentiators is the need to periodically reset the capacitors. Although several topologies exist that rapidly deliver charge to the circuit's capacitors, all existing commercial picoammeters are limited to 100 μsec reset durations in practice. This large dead-time, where information at the input is lost, is not consistent with the specification required for either "glitch-free" hybridization detection or the desired *de novo* sequencing of DNA. For example, a 100 μsec dead-time represents the misdetection of roughly 50 bases during each reset, which is an unacceptably high error rate. In addition, the voltage at the input of the amplifier must be carefully maintained to prevent breakdown of the insulating membranes and effectively control the translocation rate of DNA. The effects of dielectric absorption in the capacitors, which is made especially problematic due to the relatively long integration times and short reset intervals, must also be compensated. Addressing all of these practical issues can quickly undermine the inherent advantages of the integrating topology.

The drawbacks of existing integrating picoammeters motivate a circuit topology that can exploit the low noise and wide bandwidth properties of an integrator/differentiator voltage clamp without the need for discontinuous resets. As a practical matter, capacitors are required to have a zero net steady-state current to maintain the operational amplifier within it's linear region. The maintenance of this requirement, however, can be achieved with alternative methods to a periodic discontinuous reset. This section introduces a different approach

to integrator/differentiator stabilization that allows for the realization of the low noise and wide bandwidth properties of integration without the compromise of discontinuous capacitor discharge.

3.7.1 Chopper Stabilized Integration

The fundamental problem of integrator resets arises from a capacitor's requirement to maintain zero steady-state charge accumulation. Recalling the state equation for a capacitor,

$$V_c = \int \frac{I_c}{C}\, dt,$$

it is clear that if I_c has a DC component, then the voltage across the capacitor C will increase monotonically towards either $\pm$ infinity. The fact the capacitor keeps charging is not a problem; the issue is the fact that the surrounding electronics have a finite range of linearity. As a capacitor's voltage reaches the end of the linear range for the circuit, some sort of action must be taken. In previous topologies, the strategy was to deliver a charge $\frac{I_o\tau}{C}$ as quickly as possible into the summing node, so that the voltage across the capacitor

$$V_c = \sum_n \int [\frac{I_c}{C} - \frac{I_o\tau}{C}\delta(t - \tau n)]\, dt,$$

was maintained within a defined voltage range. This approach of discontinuous resets will always conflict with the natural "inertia" of capacitors as defined by their voltage state.

An alternative method for DC current compensation of an integrator is to use chopper stabilization. Chopper stabilization is a classical technique that has been used to improve the signal-to-noise ratio of low-frequency waveforms passing through amplifiers dominated by 1/F noise [117]. By modulating the DC signal of interest (SOI) to a frequency beyond the noise corner of the amplifier, the SOI can be amplified in a region of reduced noise. After amplification, the SOI is demodulated *in phase* with the original modulation to restore the proper dynamic characteristics of the signal.

A chopper stabilized integrator/differentiator uses the same principle as classical techniques, but for different reasons, as illustrated in Figure 3-12. The signal current is "chopped" by multiplication with +/- 1 prior to entering the integrator. The frequency of chopping is adjusted

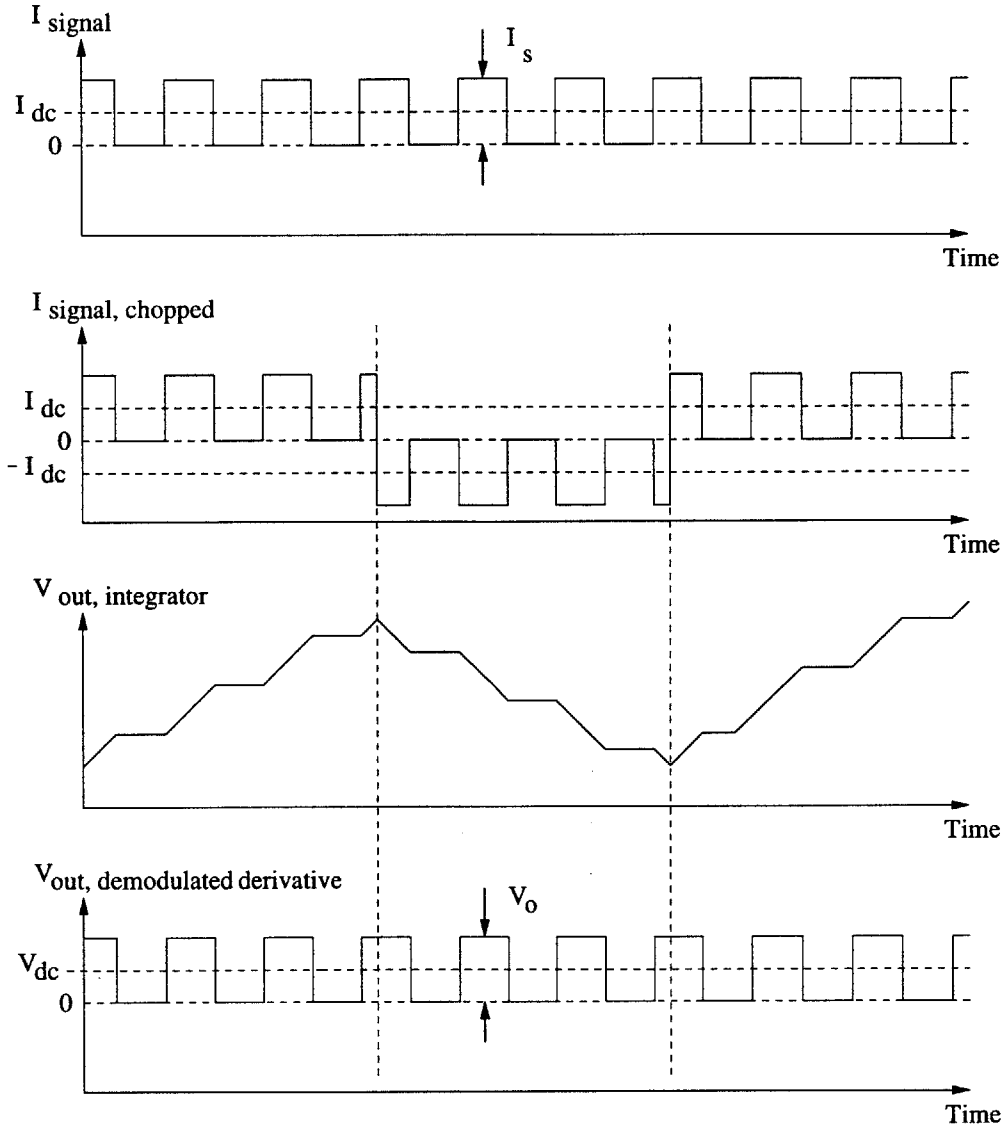

Figure 3-12: Chopper stabilization of an integrator/differentiator picoammeter. The top trace represents a square wave signal current of I_s peak-to-peak, with a DC offset of $I_s/2$. The second trace illustrates the signal current after chopping at an arbitrary frequency. The third trace shows the output of the integrator, demonstrating the smooth transitions across the feedback capacitor. After differentiation and demodulation in phase with the chopping frequency, the proper signal characteristic is obtained. If the chopping frequency is adjusted properly, the system's capacitors will never require external charge compensation.

to maintain the voltage across the picoammeter's capacitors within a predetermined limit. When this threshold is reached, the signal current's multiplication factor is inverted, and the circuit's capacitors begin to charge continuously, but in the *opposite* direction. By modulating the sign of the current through the integrator, the need for discontinuous, external charge balancing is eliminated.

Similar to the classical chopper technique, the output of the integration stage must be demodulated in phase with the chopping waveform. For the picoammeter, however, the signal must be demodulated *and* differentiated by a mechanism that avoids creating new transients. Transient-free modulation/demodulation can be accomplished with state-conserving switching, which requires that all switching in the circuit maintain the continuous voltage state of all capacitors. By maintaining state conservation in the picoammeter, the transients associated with discontinuous resets are ideally eliminated to first-order. The design challenge is to transfer this basic concept into a picoammeter suitable for a nanoscale Coulter counter; this is the subject of the next two chapters.

3.8 Chapter Summary

This chapter explored the development of a suitable interface circuit for the nanoscale Coulter counter. To help specify the requirements on the interface, a useful model for the nanopore was extrapolated from the proposed structure of the device and practical knowledge gained from working with a toxin nanopore. Combining these models with the theoretical work developed in Appendix A, the estimated resolution of the proposed artificial pore should be roughly 8 $\mathring{A}$, which is sufficient for the hybridization detection techniques developed in chapter two.

A rough set of performance specifications suitable for both the genetic sequence recognition strategies and the *de novo* sequencing of DNA where then developed to help guide in the design of a suitable interface. State-of-the-art picoammeter techniques all suffer from significant drawbacks, but of these methods, the integrating picoammeter offers the best overall performance in terms of noise, bandwidth, and linearity. The major problem with this technique is the requirement of periodic discontinuous resets.

The benefits and drawbacks of integrating picoammeters motivate a new interface strategy

which uses the principle of chopper stabilization to achieve low-noise, wide bandwidth current measurements without the need for discontinuous resets. The practical implementation of this novel picoammeter topology is the subject of the next two chapters.

Chapter 4

Picoammeter I: Hourglass Integrator

4.1 Chapter Overview

The chopper-stabilized picoammeter should theoretically provide the low-noise and wide bandwidth of state-of-the-art integration topologies without the overhead of discontinuous resets. The challenge is to transform the broad concept of chopper-stabilization into a concrete circuit topology. This chapter develops the first component of the picoammeter, the hourglass integrator. The first part of the chapter introduces the topological strategy of the integrator and its approach to state-conserving switching. This strategy is then translated into a prototype circuit which details the design challenges and solutions required to construct a functioning picoammeter. The functionality of the prototype is then demonstrated by a series of test waveforms.

4.2 Developing the Hourglass Integrator Topology

This section is a conceptual overview of the hourglass integrator topology. Working within the constraints on the sensor interface, this topology provides the effective multiplication and integration required to implement the first stage of the chopper-stabilized picoammeter.

4.2.1 Continuity Constraints on the Picoammeter

The integrator topology must maintain the continuity of voltage bias across, and quiescent current through, the nanopore sensor. In addition, the signal current must be modulated with respect to the integration capacitors to implement the chopper-stabilization procedure outlined in chapter three. The requirement of a constant voltage bias insures a uniform rate of DNA translocation, and maintaining the *direction* of the electrical field is necessary for the unidirectional translocation of DNA polymers. These requirements eliminate the simple modulation of the bias voltage across the nanopore to achieve the modulation of the signal current. Though the sensor bias can not be modulated to achieve chopping of the signal current, the circuit topology itself can be chopped to achieve the same effect from the perspective of the integration capacitors. Maintaining electrical continuity across the sensor, while simultaneously modulating the polarity of the current signal with respect to the picoammeter, can be achieved with a novel integration topology.

4.2.2 Floating Gyrators and Chopper-stabilized Integrators

The application of a floating gyrator circuit provides the essential building block for implementing the chopper-stabilized integrator. Gyrator circuits are a general class of circuits useful for reflecting the modified characteristics of one node in a circuit topology to another node [2]. Referring to Figure 4-1, a floating gyrator circuit can be constructed by cross-coupling two operational amplifiers, OP_1 and OP_2. The internal feedback of the circuit forces all input nodes to be at V_{bias}, which sets the voltage bias across the current source I_S[1]. Assuming no significant current is drawn into the inverting terminals of OP_1 and OP_2, the outputs V_{o1} and V_{o2} are symmetrically centered around V_{bias}. The current drawn through I_S creates an ohmic drop across the the feedback resistor R_f, such that the output of OP_2 is

$$V_{o2} = V_{bias} + I_S R_f.$$

[1]The current source will be replaced by the sensor to create a voltage clamp.

The ohmic drop across the coupling resistors, R_x, imposes the voltage on OP_1,

$$V_{o1} = V_{bias} - I_S R_f$$

to be anti-symmetric about V_{bias}, with respect to V_{o2}. The effect of the output voltage V_{o1} is to draw a current I_S from the voltage source V_{bias}.

From these I-V relationships, the transfer characteristics of the gyrator are specified. Feedback forces the voltage at the input terminals of the opamps to be the same; the cross-coupling of the amplifiers insures that the current through the feedback elements is equal in magnitude, but opposite in sign. These two-port relationships,

$$V_{IN_1} = V_{IN_2}$$

$$I_{IN_1} = -I_{IN_2},$$

are the desired characteristics for implementing a chopper-stabilized integrator.

By leveraging the input characteristics of the floating gyrator, a chopper-stabilized integrator may be implemented. The conversion of the gyrator into an integrator requires only the addition of feedback capacitors in place of R_f. As drawn in Figure 4-2, this topology will now integrate the input current I_S such that the outputs of the amplifiers obey

$$V_{o2} = V_{bias} + \int \frac{I_S}{C_F} dt$$

$$V_{o1} = V_{bias} - \int \frac{I_S}{C_F} dt.$$

These output relations illustrate the critical feature of this design: the charging of one feedback capacitor at a rate $\frac{I_S}{C_F}$ is accompanied by the simultaneous *discharging* of the other capacitor at the same rate. While maintaining a fixed voltage bias and current through a sensor, the feedback capacitors can be alternately charged and discharged by simply toggling the particular gyrator input to which the voltage and current sources are attached, as illustrated in Figure 4-3. The practical implementation of the source switching can be achieved with a full-bridge circuit as shown in Figure 4-4.

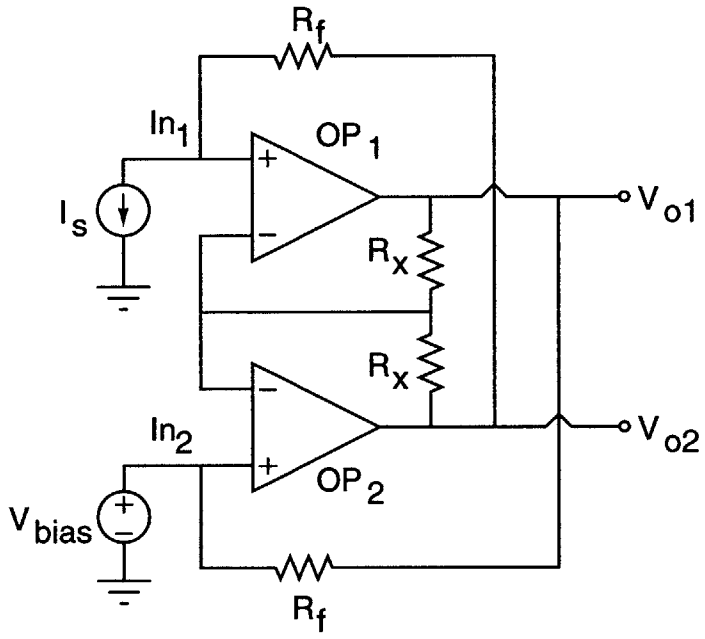

Figure 4-1: The floating gyrator building block. The feedback action of the operational amplifiers forces the voltage input terminals to be the same; the cross-coupling of the amplifiers insures that the current through the feedback elements is equal in magnitude, but opposite in sign.

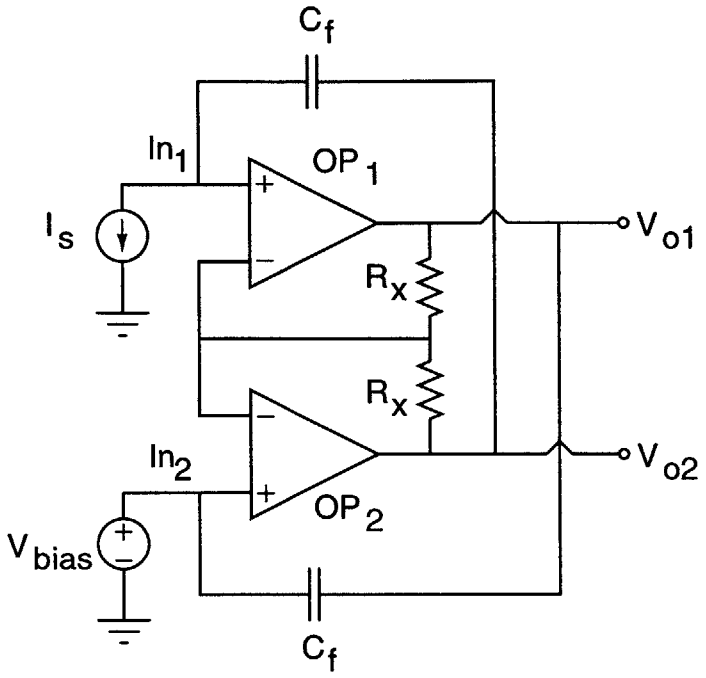

Figure 4-2: Converting the floating gyrator into an integrating circuit.

The control of the phases on the input bridge, Φ_a and Φ_b, can be achieved with a feedback loop that monitors the voltage at the integrator outputs. Once an output exceeds a predetermined threshold, the phase of the bridge is switched and the gyrator begins to charge in the opposite direction. By using feedback, the circuit maintains operation in the linear region without the need for external control of the chopping frequency. With this topology, chopper-stabilized integration is possible without the need for perturbing the sensor's voltage bias or breaking the continuity of the signal current.

4.2.3 The Hourglass Integrator

This section has motivated the concept behind the "hourglass" integrator. The hourglass provides a useful analogy for an integration capacitor; the sand in the hourglass represents the total amount of charge available from the feedback capacitor before circuit saturation. In previous circuit topologies, charge balance is maintained with a discontinuous reset–the equivalent to breaking the bottom vial of the hourglass and transferring sand to the top as

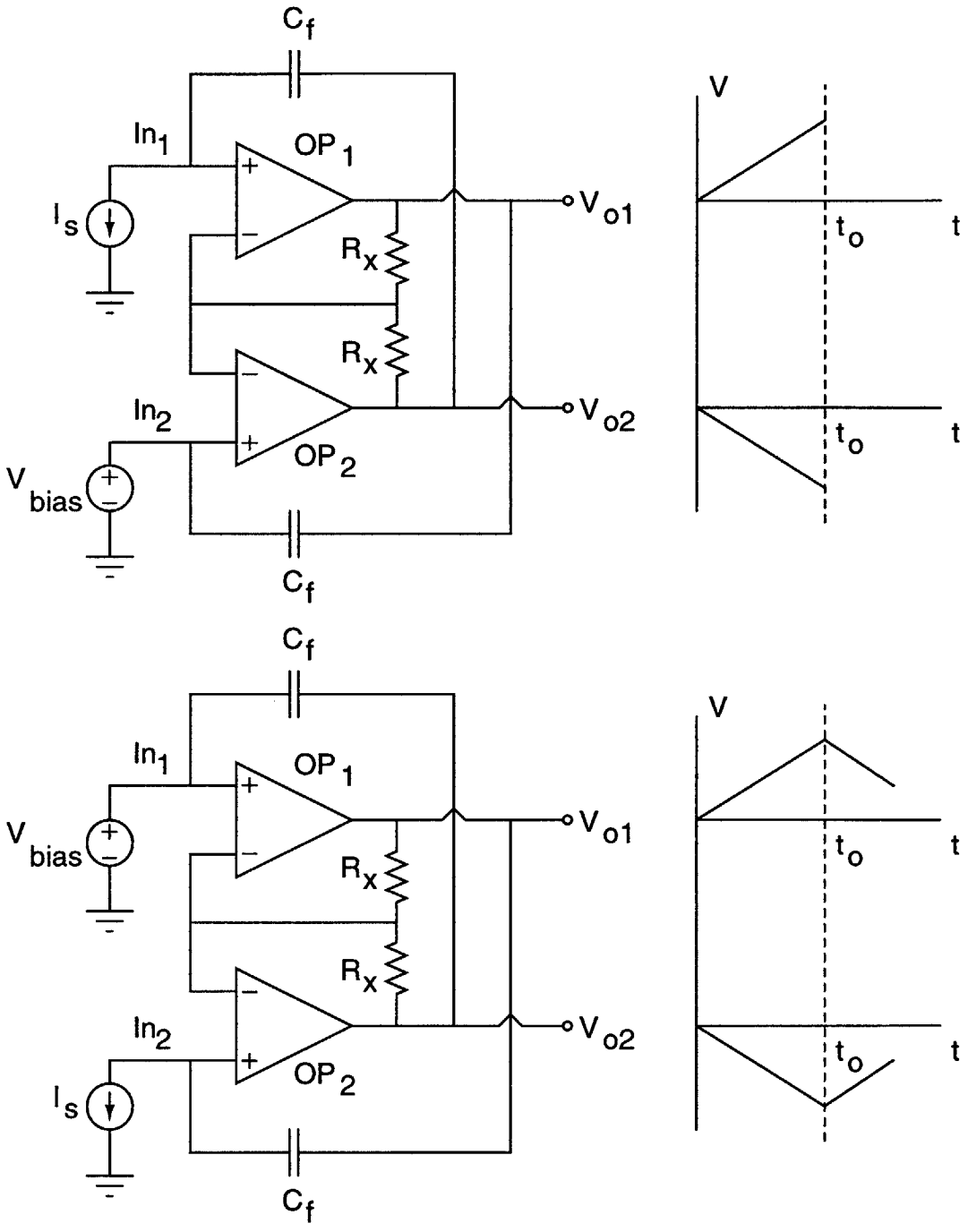

Figure 4-3: By leveraging the symmetry of the circuit, the feedback capacitors may be alternately charged and discharged by alternating the location of the current and voltage biases. For the top circuit, the output V_{o2} ramps upwards as C_f charges, while V_{o1} ramps downwards at an equal rate. Simply swapping the inputs of the current and voltage sources at T=t_o, as shown in the bottom circuit, results in the capacitors charging in the opposite direction.

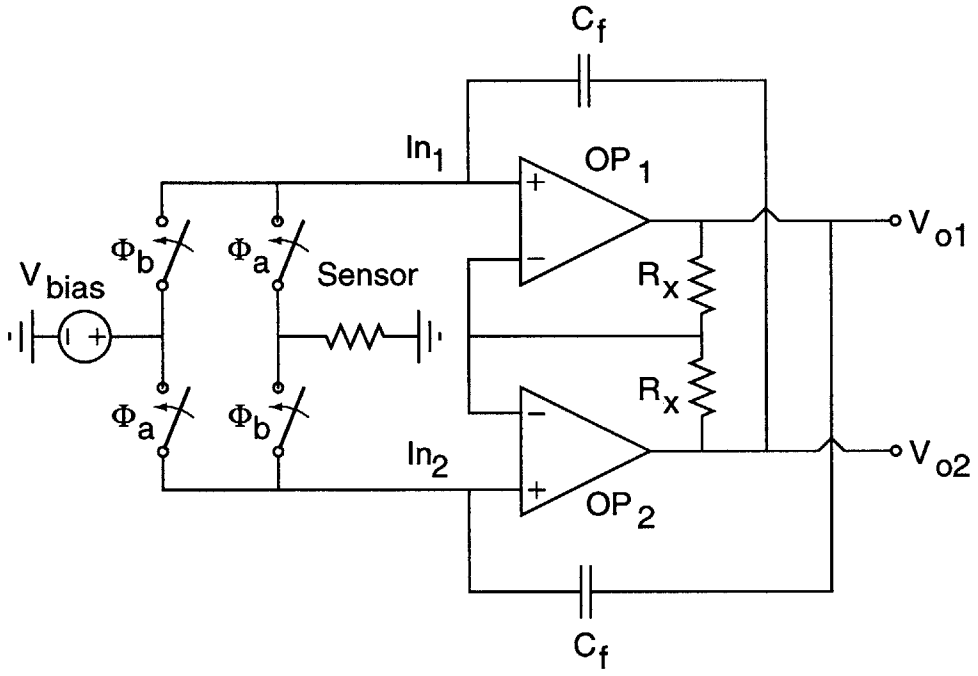

Figure 4-4: The alternating connection of the sources with the gyrator inputs can be implemented with a full-bridge circuit. To implement the voltage clamp picoammeter, the current source is replaced by the sensor.

quickly as possible. Using a gyrator circuit adapted for integration, the circuit can now be effectively "turned-over" when the feedback capacitors have fully charged, in the spirit of the smooth transition of an hourglass. The use of state-conserving, continuous transitions allows for the integrator to operate in a quasi-continuous fashion without the overhead of periodic *discontinuous* resets. The next section explores the development of a particular prototype suitable for genetic sequence recognition using the strategies developed in chapter two.

4.3 Prototype Implementation

4.3.1 Overview

This section provides an overview for the prototype hourglass integrator; the schematic for the circuit is shown in Figure 4-5. The cross-coupled gyrator is shown on the right hand side of the schematic. The gyrator is implemented with two low-noise hybrid opamps, LNA_1 and LNA_2. The feedback capacitors in the gyrator use oxide chip capacitors that have a low dissipation factor for reduced dielectric absorption. The gyrator's cross-coupling resistors, R_x, are .01% $1k\Omega$ thin film resistors. The use of $1k\Omega$ resistors represents a compromise between the noise performance in the integrator and the loading of the LNA's output stage. The modulation of current is accomplished with a MAX4526 mosfet phase-reversal switch, which receives it's supply voltage from low-noise, adjustable power rails.

The central portion of the schematic implements the state-control feedback that maintains the integrator within it's linear region. The LNA outputs V_{o1} and V_{o2} are monitored by LM311 comparators, with $20mV$ of hysteresis to prevent multiple transitions on the output due to noise. Once the voltage of either gyrator output exceeds one volt, a comparator is tripped and a state transition is initiated. The state-change is gated with an external clock that synchronizes the analog-to-digital conversions of the picoammeter output with the state transitions of the integrator. The change in integrator state is fed to both the MAX4526 switch, which "turns the integrator over", and to the OA port of the LNA. An active high on the OA pin initiates an auto-zeroing procedure for the LNA, which lowers the offset voltage across the gyrator inputs to the order of $10\mu V$.

The output of the hourglass integrator is buffered with a low-noise gain-of-ten amplifier.

The gain provided by this circuit allows for the direct digitization of the integrator output, as will be discussed further in the next chapter. The use of a x10 amplifier limits the excursions of the integrator to $\pm 1V$ to maintain operation within the A/D converter's linear range. The post-amplification on the integrator circuit creates an effective 100fF feedback capacitor for the topology based on the output's rate of charging; if the outputs are taken differentially, the effective capacitance is further reduced to 50fF.

The voltage biasing for the nanopore is provided by the circuit shown in Figure 4-6. This circuit provides a stable, low-noise reference voltage between zero and 250mV. The output of this biasing circuit is attached to one fluid bath of the nanopore, while the hourglass integrator is attached to the other fluid bath.

This section has provided a brief overview of the prototype hourglass integrator based on the floating gyrator. The following sections provide a more detailed overview of the design choices crucial for the successful implementation of a chopper-stabilized picoammeter.

4.3.2 Operational Amplifiers

The implementation of the hourglass integrator requires the design and construction of a low-noise, wide-bandwidth operational amplifier (LNA). The general issues associated with amplifier design are well documented in several references [67, 112, 64, 65, 5], and an exhaustive survey of these techniques is not given here. In addition, the origin of noise and its properties are covered in several references [65, 66], and will not be reviewed here. This section is meant to illustrate the *specific* design considerations associated with the chopper-stabilized integrator, and particular noise and performance issues will be discussed as they arise.

Useful Bounds on Specifications

The bounds on the LNA amplifier's specifications are:

- Unity gain bandwidth of 5 MHz to insure approximately 250 kHz closed loop bandwidth when interfaced with a nanopore sensor.
- Input referred thermal noise $< 2.5\ nV/\sqrt{Hz}$ at 100Hz.
- Input quiescent current $<$ 5pA.

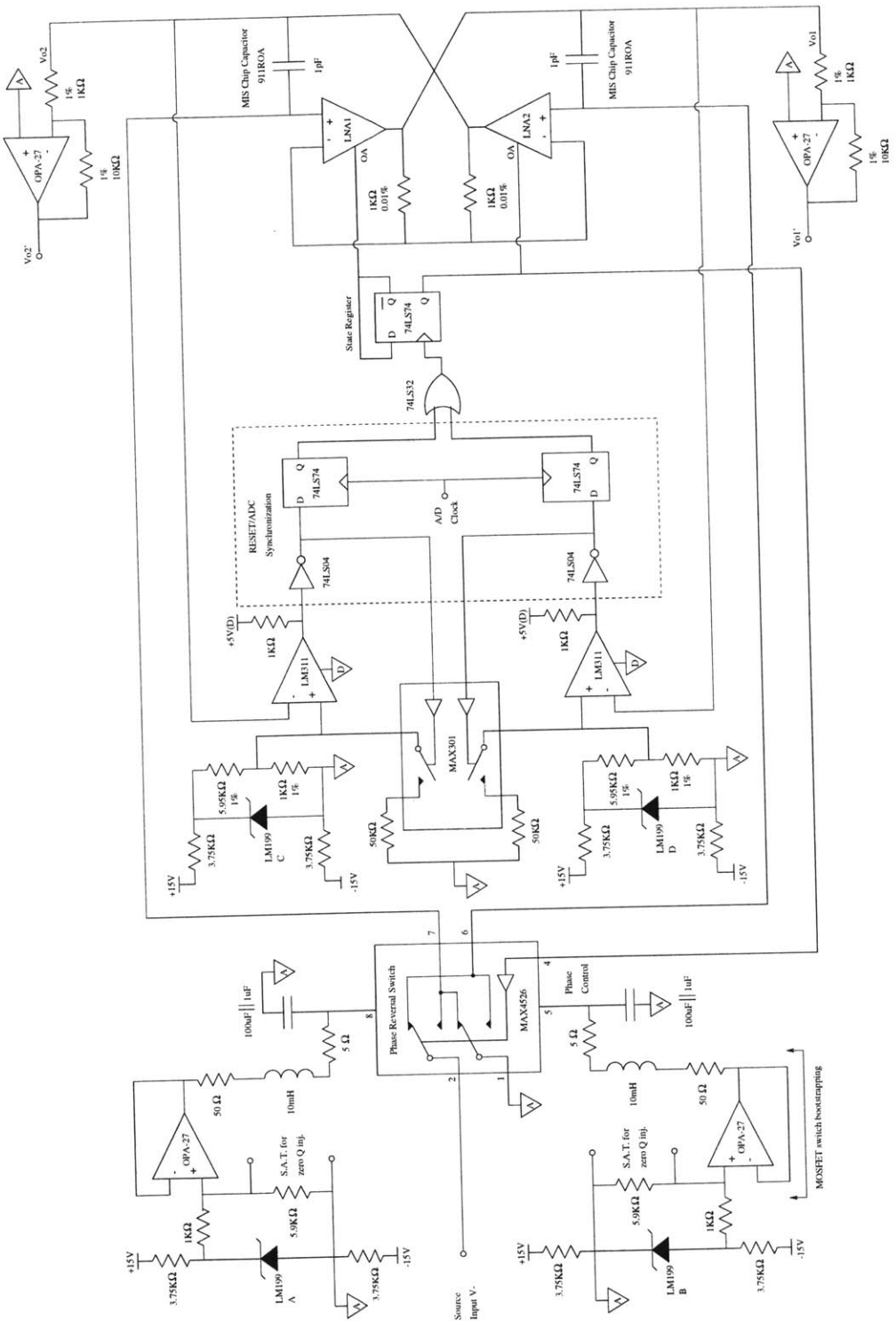

Figure 4-5: The schematic for the hourglass integrator.

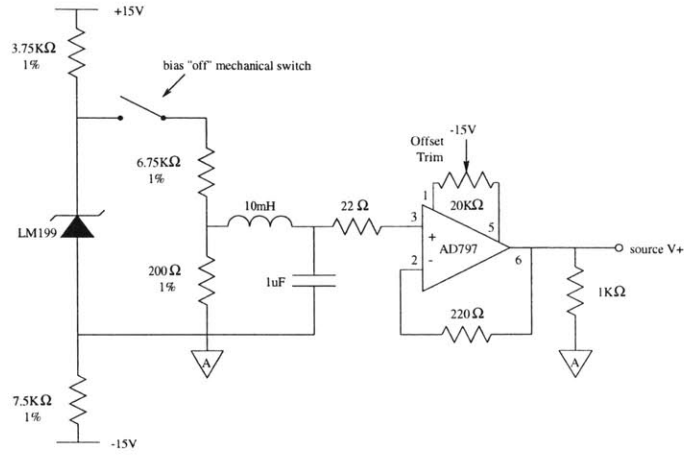

Figure 4-6: The biasing circuit for the hourglass integrator.

- Input Capacitance < 10 pF.
- Offset Voltage $< 10\ \mu V$.

These specifications are based on the noise and bandwidth requirements developed earlier for the picoammeter. A commercial operational amplifier that simultaneously meets these design criteria was not available, so a hybrid amplifier was implemented [118, 62, 69, 131].

Specifying the Input Transistors

The constraints of amplifier thermal noise and input current suggest the use of a junction field-effect transistor (JFET). JFETs have gate bias currents that are orders of magnitude smaller than the base current of a bipolar junction transistor (BJT) at room temperature [4, 133]. In addition, the JFET has much lower input-referred thermal noise compared with a MOSFET due to its higher transconductance [66, 113, 115]. The fact that the conducting channel of the JFET is submerged below the silicon surface also reduces the low frequency noise resulting from the interface defects that generally plague MOSFET transistors [113, 133, 44]. In fact, recent

advances in JFET fabrication have yielded devices with no detectable channel defects, which results in low-frequency performance that rivals BJTs [133].

The choice of a particular JFET reflects the balance between input current, thermal noise, and capacitance. The trade-off between JFET capacitance and thermal noise can be established with a simple relationship [112, 63]. The thermal noise of the JFET is proportional to $1/C_{gs}$ based on the physics of the device [66]. The total input-referred current noise for this transistor, attached to a source capacitance C_s, is then

$$S(f) = (2\pi f)^2 e_n^2 (C_{gs} + C_s)^2 \approx \frac{(2\pi f)^2 (C_{gs} + C_s)^2}{C_{gs}} \; A^2/Hz,$$

where the shot noise from the leakage current at the gate is considered negligible. Taking the derivative of this expression with respect to C_{gs}, it is straightforward to show that the condition for minimal noise is

$$C_{gs} = C_s.$$

This metric makes intuitive sense; the JFET should be scaled larger to lower its thermal noise, but since this decrease in noise is *weakly* dependent on the size of C_{gs}, we should stop scaling the transistor when it's capacitance is on the same order as the source. This result is established in the literature [63], and has been used as the basis for a variety of low-noise amplifier applications [56, 50, 62, 131].

An appropriate choice of transistor and biasing point minimizes the excess noise contribution of the interface circuit. The input capacitance seen by the JFETs is at minimum on the order of 10pF due to the presence of the MAX4526 phase-reversal switch. A reasonable JFET for this source capacitance is the Siliconix U430, which has an equivalent input capacitance of 10pF when biased for an input-referred thermal noise of $2nV/\sqrt{Hz}$ and bias current of 0.5pA [4]. The net effect of the U430's noise contribution,

$$i_{rms} \approx \sqrt{\frac{4\pi^2}{3} \Delta f^3 C_s^2 e_n^2} \; A,$$

is approximately 0.6pA rms in a 25kHz bandwidth. This noise contribution is roughly twice that of the nanopore sensor as derived in chapter two; the noise performance of the picoammeter

will be discussed further in future sections.

The other critical transistor bias considerations are temperature and drain-gate voltage. Both of these design considerations have a significance effect on the gate current of the JFET; gate leakage increases by a factor of 2 for every 10 degree temperature rise, and more than 4 volts across the gate-drain junction will induce avalanche breakdown that also results in a large gate current [4]. With operation at room temperature and reasonable gate-drain voltages, however, it is straightforward to maintain a gate current of under a picoampere with the Siliconix U430.

LNA Topology

The schematic for the *LNA* is shown in Figure 4-7. A matched pair of Siliconix U430 JFETs form a low-noise differential pair. A stable current source biases each JFET at approximately 10mA to provide the 10pF FET capacitance roughly matched to the source for optimal noise performance. The load resistors of 1.0kΩ yield a net differential gain of ten, given the JFET transconductance of approximately 10mS at 10mA bias. The load resistors are isolated with a cascode circuit that both improves the high frequency dynamic performance of the input stage and prevents the noise from the high impedance node being coupled back into the gate at high frequencies [65]. In addition, the voltage levels of the cascode fix the gate-drain voltage of the JFET to 3.5 V, which prevents excessive gate current from avalanche breakdown. With a gain of ten, several commercial IC opamps such as the OPA27, OPA627, LF356 can be used as the following amplification stage; the OPA627 was used in this prototype for its relatively low voltage noise, low bias currents, and excellent slew rate. The excess noise from this operational amplifier and the $1k\Omega$ load resistors is approximately $0.3nV/\sqrt{Hz}$ when referred back to the input. This noise is uncorrelated with the input JFETs and it's effects are negligible.

The compensation of the *LNA* is relatively straightforward. The two capacitors shunting the OPA627 are used as minor loop compensation to insure that the circuit is stable in the presence of the additional x10 loop gain provided by the input stage. In practice, the voltage division provided by the integrating capacitor and the amplifier input capacitance usually provides enough magnitude compensation to account for the additional loop gain, and the shunt capacitors around the OPA627 can be removed to improve dynamic performance. This hybrid design provides a low-noise, wide bandwidth operational amplifier suitable for the prototype

integrator.

Nulling the LNA Offset Voltage

In order for the chopper-stabilized picoammeter to function properly, the offset voltage of the operational amplifier must be reduced significantly. The problem with voltage offsets is two-fold. First, the offset voltage between the terminals of the gyrator is superimposed on the true voltage bias of the sensor. As the integrator changes state, the relative sign of the offset voltage will also change, modulating the effective bias voltage across the nanopore. The modulation changes the bias point and quiescent current of the sensor, which will then modulate the translocation rate and signal characteristics of the sample polymers. For typical biases of 100mV and offsets of 10-20mV, this factor represents a substantial modulation. The second issue with a voltage offset is the need to charge the parasitics at the input of the integrator during every state transition. If the offset voltage is 15mV, and the total capacitance at the gyrator terminal is roughly 20pF, then 300fC of charge must be supplied through the feedback capacitor to charge the capacitance at the input. This charge represents 15% of the total dynamic range of the integrating circuit, and must be eliminated.

The offset voltage of the LNA must be reduced without compromising the $10G\Omega$ input impedance of the gyrator. Most offset compensation circuits require a shunt network across the inputs of the LNA to sample their relative voltage difference and null it through feedback. The problem with this topological approach is that a shunt resistor on the order of $10G\Omega$ is required to prevent significant perturbation of the input due to noise. A resistor of this magnitude passing 1pA of bias current creates an additional 10mV offset, which is on the order of the value we are trying to eliminate.

The topology of the gyrator can be exploited, however, to allow sampling of the offset voltage of the JFET pair without perturbing the signal inputs. Referring to Figure 4-8, in one state of the gyrator, the input of OP_2 is connected to analog ground. The inverting terminal of the LNA will therefore be equal to the offset voltage of OP_2. Since this offset is referred to analog ground, the inverting node of the opamp can be easily sampled and the offset nulled for OP_2, while the integrator is in this state. When the integrator's state changes, the required nulling voltage for OP_2 can be held, and the nulling operation commenced for OP_1. With this

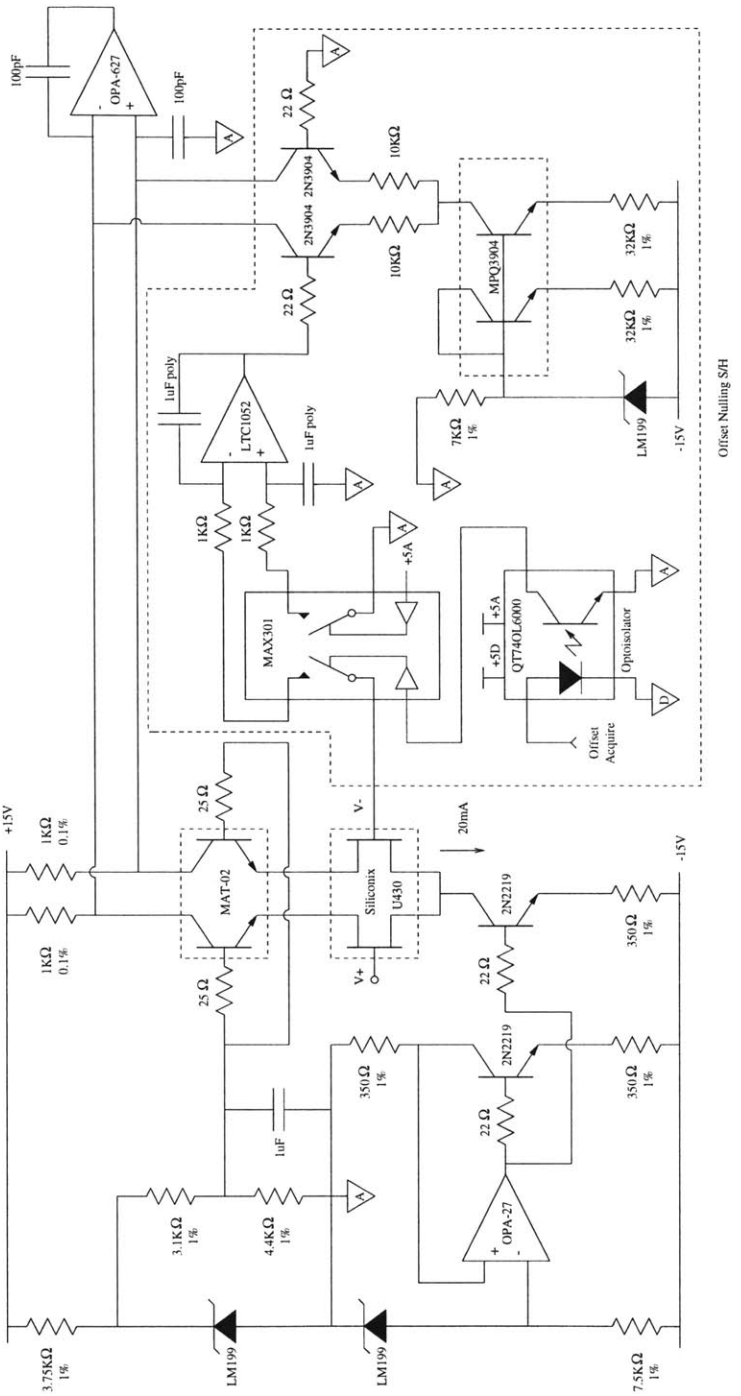

Figure 4-7: The low-noise operational amplifier for the integrator (LNA).

continuous sample and hold of the offset nulling circuit, the offset across the gyrator inputs can be maintained at less than $10\mu V$.

Offset Nulling Circuitry for the *LNA*

The circuit to accomplish this offset nulling is highlighted as the *offset nulling S/H* in Figure 4-7. When the integrator is in the proper state for nulling the opamp, the offset acquire TTL signal is high. This signal is coupled into the opamp through an opto-isolator to separate the digital and analog grounds. A MAX301 mosfet switch then attaches the inverting terminal of the opamp to an integrator referenced to ground. The nulling integrator is formed from a chopper-stabilized LTC1052, which maintains $5\mu V$ of offset voltage while drawing under $10pA$ of input bias current. The low leakage of the LTC1052 and the $1\mu F$ sampling capacitor insure that the drift of the nulling circuit is insignificant over a typical hold interval of 100mS. The symmetric connections to the positive input of the LTC1052 help to eliminate parasitic offset voltages introduced by dissimilar contacts through common-mode rejection. The output of the integrator is fed into a differential pair biased with $200\mu A$ of current. This bias current represents the maximum offset current observed for the U430 JFETs when biased at equal gate-source voltages. The differential pair is connected with the LTC1052 integrator to drive the inverting terminal of the opamp to analog ground while the offset acquire pin is high.

The bandwidth of the nulling circuit is approximately

$$BW \approx \frac{1}{2\pi\tau_{int}} \frac{1}{(g_{m,fet}R_{E,bjt})} \; Hz,$$

where τ_{int} is the sampling integrator's time constant, $g_{m,fet}$ is the input JFET's transconductance and $R_{E,bjt}$ is the degeneration resistor of the differential BJT pair. The loop bandwidth for the nulling circuitry is on the order of ten hertz, which is sufficient for tracking the low-frequency offsets that are the concern of the hourglass integrator.

The excess noise contribution of this nulling circuit is negligible when referred to the picoammeter input. The noise of the sampling circuit is referred to the opamp input through the relative transconductances the input JFET (100 Ω) and the transconductance of the BJT differential pair (10000 Ω). This attenuation factor of one hundred keeps the input-referred

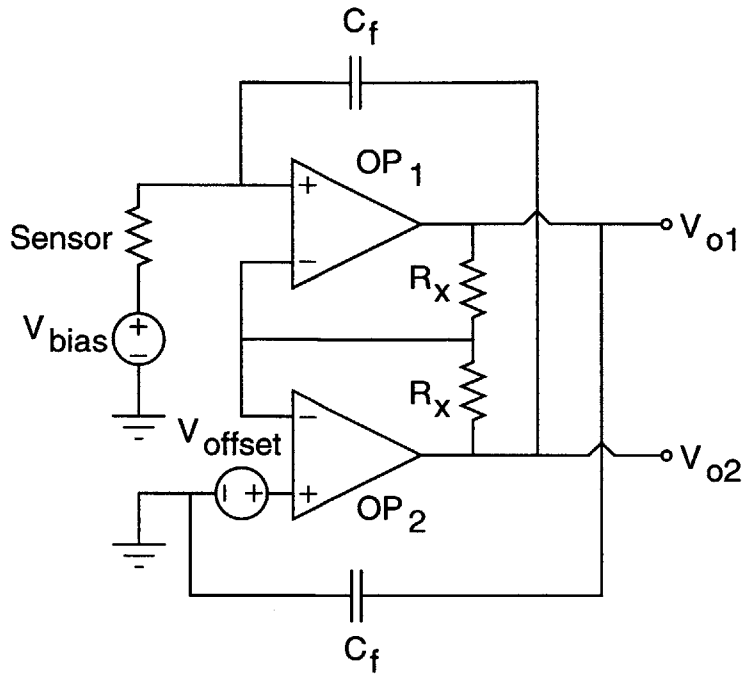

Figure 4-8: The strategy for nulling operational amplifier's offset voltage. During one state, the offset voltage of OP_2 is present at the inverting terminals of the gyrator opamps. This voltage can be sampled, and the offsets nulled. While the integrator is in the other state, the offset voltage for OP_1 is nulled.

excess noise contribution under $1nV/\sqrt{Hz}$, which is uncorrelated with JFET thermal noise.

This section has summarized the design of the LNA used in the hourglass integrator. The U430 JFET offers the best performance trade-off between voltage noise, current noise, and capacitance for the proposed genetic sequencing application. These JFETs were incorporated into a hybrid operational amplifier design that met the general specifications for the prototype hourglass topology. To drive the offset voltage of the amplifier to under $10\mu V$, a novel stabilization procedure was designed that exploits the state-dependent features of the gyrator topology. With the LNA design complete, the core gyrator of the hourglass integrator can be constructed and it's stability analyzed.

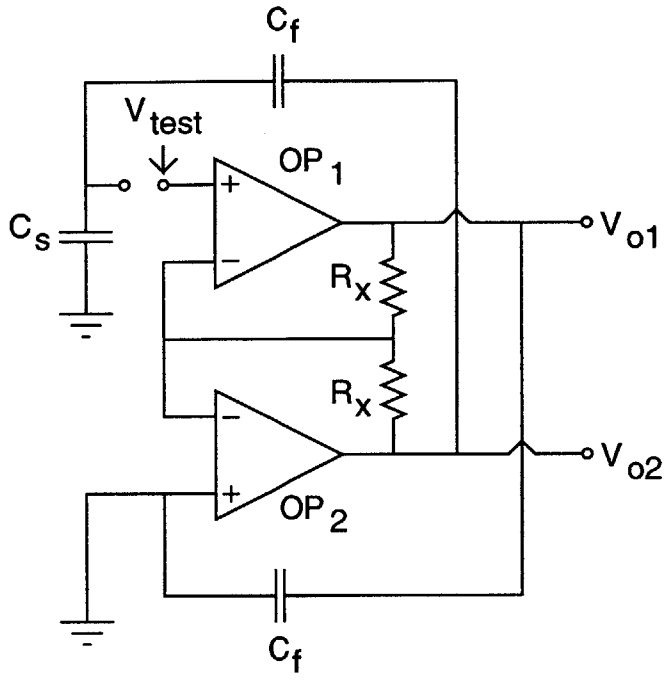

Figure 4-9: The model for analyzing the hourglass integrator's stability. The loop is broken at the input to OP_1 to calculate the net loop gain.

4.3.3 Hourglass Integrator Stability and Compensation

The stability of the hourglass integrator can be derived from basic symmetry arguments. The use of the integrator as a voltage clamp fixes one input of the gyrator at incremental ground, while the other terminal is attached to the sensor. To maintain continuity with previous discussions, we will assume that the input to OP_2 is attached to ground while the input to OP_1 is attached to the sensor. The stability of the gyrator circuit can be analyzed by breaking the loop at the input of OP_1 as shown in Figure 4-9. The feedback path from V_{o2} to the test point will be determined by the capacitive voltage divider,

$$L_f = \frac{C_f}{C_f + C_s},$$

which is a good model for the dynamics in the region of cross-over. The gain associated with the gyrator is determined by observing the net gain from the input V_{test} at OP_1 to the output of OP_2.

The transfer function from V_{test} to V_{o2} can be determined with half-circuit techniques similar to those commonly used in differential pair analysis [15]. The test voltage at OP_1 and the grounded input of OP_2 can be equivalently modeled as the superposition of two inputs: a common-mode voltage of $V_{test}/2$ and a differential-mode voltage of $\pm V_{test}/2$. The equivalent gyrator circuit for each case is shown in Figure 4-10. The transfer function for the common-mode circuit is determined to be

$$A_{cm} = \frac{1}{\tau s/A_o + 1},$$

where

$$\frac{A_o}{\tau s + 1}$$

is the model for the operational amplifier, and the pole of R_x and circuit parasitics is well past cross-over. The transfer function for the differential mode circuit is simply the open loop gain of the operational amplifier,

$$A_{dm} = \frac{A_o}{\tau s + 1},$$

using the same models and assumptions. The output from V_{test} to V_{o2} is then determined from the superposition of $[\ \frac{V_{test}}{2}\ \ \frac{V_{test}}{2}]$ and $[\frac{V_{test}}{2}\ \ -\frac{V_{test}}{2}]$ applied to $[\ OP_1\ \ OP_2]$; this analysis yields a net tranfer function of

$$\frac{V_{o2}}{V_{test}} = \frac{-A_o}{2}\frac{1}{(\tau s + 1)(\tau s/A_o + 1)}$$

for the gyrator circuit. Combining the path dynamics with the gyrator transfer function, the total loop gain for the integrator is then specified by

$$L_{test} = \frac{-A_o}{2}\frac{C_f}{C_f + C_s}\frac{1}{(\tau s + 1)(\tau s/A_o + 1)}.$$

This analysis demonstrates the general stability properties of the hourglass circuit. For the most marginal implementation, where C_f is much larger than C_s, the phase margin of the loop is roughly sixty degrees with half the bandwidth of the LNA's unity-gain frequency, assuming the model for the amplifiers is accurate near crossover. For the prototype and nanopore sensor, however, C_f will generally be smaller than C_s by an order-of-magnitude, which can compromise the loop bandwidth significantly. To compensate for this effect, the unity-gain crossover of the LNA is increased by reducing the minor loop shunt capacitors around the OPA627. The

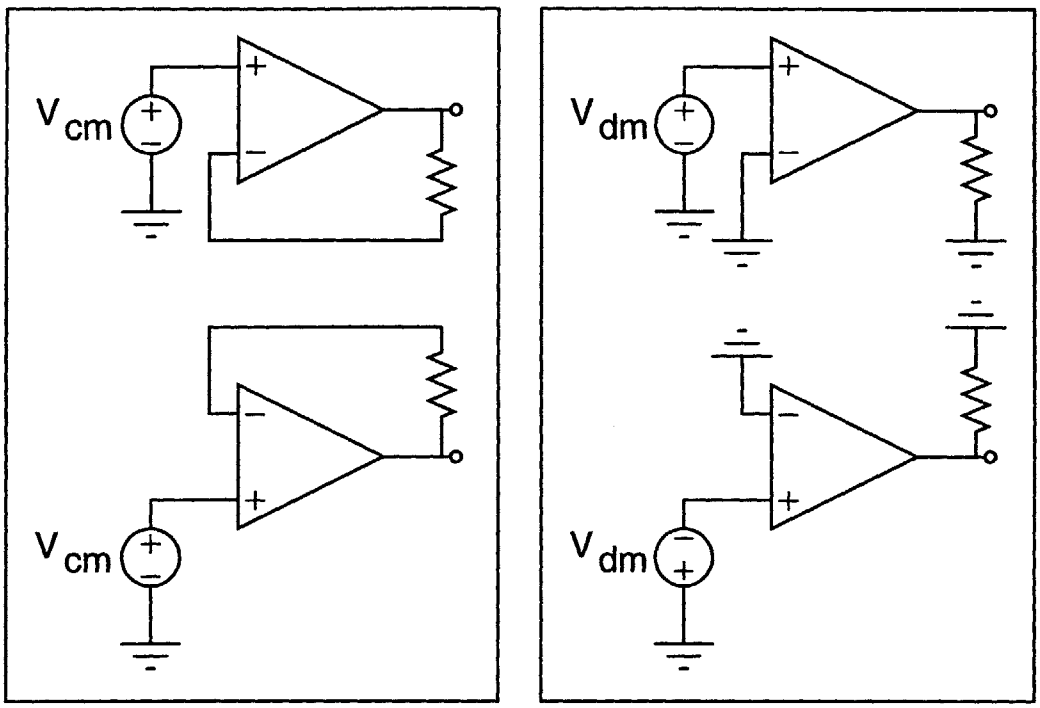

Figure 4-10: The half-circuit approach to analyzing the stability of the hourglass integrator. The left box represents the equivalent common-mode circuit, the right box represents the equivalent differential mode circuit.

integrator can then use the additional gain of the LNA input stage to recover the bulk of the circuit's bandwidth.

The analysis of the loop dynamics for the hourglass integrator demonstrate that it can maintain wide bandwidth with excellent phase margin. With minimal effort, in fact, a stable hourglass integrator with $> 500kHz$ of bandwidth is feasible which is suitable for both present and future applications of nanopore.

4.3.4 Switch Implementation

The addition of switches in the signal path represents the major trade-off of the chopper-stabilized integrator technique. This trade-off is especially problematic in discrete design implementations, where device matching of the switching elements is relatively limited. Several discrete switch designs were explored as part of this thesis, but consistently the best overall performance was achieved with mosfet switches arranged on the same silicon die due to superior matching.

Of the available commercial switches, the MAX4526 phase-reversal switch represents a good compromise for the picoammeter application with $1pA$ of leakage current at room temperature, a series resistance of 200Ω, and a parasitic capacitance of $10.2pF$, measured with a Hewlett-Packard 4192A impedance analyzer. The leakage current and capacitance parasitics are dominated by the protection zener diodes shunting the signal path and power supplies, and their removal would substantially improve the switch's performance. Estimated values of the parasitic capacitance without protection diodes would be on the order of 2-3pF, according to the chip designer. For the purposes of this prototype, however, the standard commercial switches were used to estimate the circuit topology's general performance.

A possible concern of the phase-reversal interval is the state of the sensor during switching. The break-before-make time of the MAX4567 is 100ns, during which time the sensor is effectively floating. Modeling the nanopore and parasitic capacitances as a $10G\Omega$ resistor in parallel with 5pF, the characteristic time constant for this lowpass filter is 50ms. During the floating interval, the sensor voltage bias will decay by a relative amount

$$\frac{\Delta V_{bias}}{V_{bias}} = (1 - exp(-100ns/50ms)) = 2 \cdot 10^{-6},$$

which is only two parts per million. The minor bias decay during switching will be unobservable to the either the picoammeter or the sensor.

A more significant issue with mosfet switching is charge injection. During a state transition in the integrator, the switching of the signal path with the analog mosfets can deliver a significant charge packet to the input of the integrator. The specification for typical charge injection with the MAX4526 is 2pC during a transition; this charge represents the entire dynamic

range of the hourglass integrator's feedback capacitors. To circumvent this problem, the signal dependence of the charge injection can be exploited. The fact that the charge injection of a mosfet analog switch is a function of the signal voltage is well known [38, 39]. In general, this characteristic cannot be fully exploited since the signal voltage varies over a significant range of the supply rail [38]. For the symmetric integrator, however, the input voltage is fixed at analog ground, which allows for some degree of compensation with this "parasitic" charge effect.

The charge injection characteristics of the MAX4526 were explored by integrating the charge injection of the switch as the signal level was varied; the results are shown in Figure 4-11. From this plot, it is clear that both signal paths through the phase-reversal switch, X and Y, exhibit zero net charge injection with a signal voltage biased at -2V. To achieve a signal voltage of -2V, the supplies of the MAX4526 are adjusted asymmetrically as shown in the schematic Figure 4-5. Since the signal path is floating with respect to the power rails, the fact that the true signal path is fixed at analog ground is of no consequence to the charge injection characteristics of the mosfets. The only possible concern with asymmetric power rails is some additional leakage current due to mismatched voltages across the zener diodes; this phenomenon was not detected. With the supply asymmetry of -2V, the charge injection is eliminated without needing to alter the ground referencing of the integrator, which is crucial for the offset stabilization circuitry described earlier.

The use of mosfet switches fabricated on the same substrate as the sensor would dramatically improve the performance of the hourglass integrator. A significant portion of the parasitic capacitance for these discrete switches arises from the need to supply a pad output for connections. These pads add several picofarads to the signal path, without providing any benefits such as lowered switch resistance [2, 3]. Mosfet switches with approximately 50Ω on-resistance, greater than 10 $G\Omega$ off resistance, 100fF of capacitance, and sub-pA leakage are available in common processes [3]. In addition integrated mosfet switches provide charge injection compensation techniques that can better exploit the matching of a monolithic process [38, 39]. The integration of this topology with a fabricated nanopore will help eliminate the most significant trade-off of the chopper-stabilized picoammeter design.

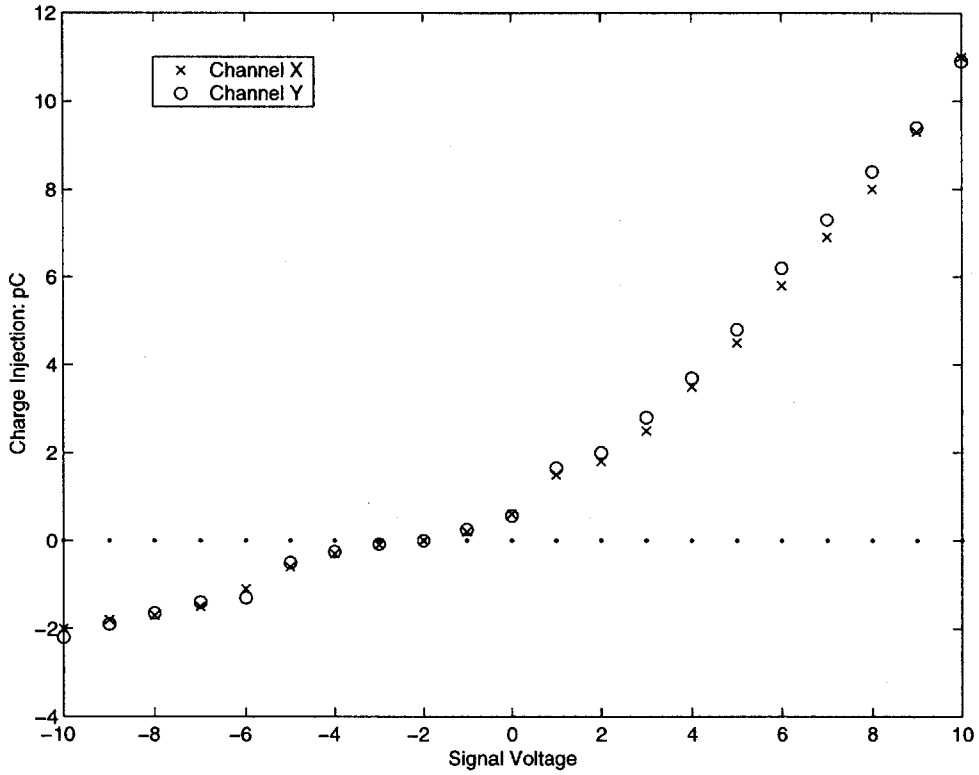

Figure 4-11: The plot of charge injection versus signal voltage for the MAX4526 phase-reversal switch. Note the zero crossing in the vicinity of -2V.

4.3.5 State Logic Control

The hourglass integrator uses global feedback to maintain the voltage across the integration capacitors within the linear region of the amplifiers. The outputs of the integrator are symmetric about analog ground, so monitoring the voltage of each integrator output with respect to a fixed positive reference is adequate for constraining the integrator's voltage excursions. The reference for the state transition threshold is one volt, derived from an LM199 zener reference. The positive feedback of the LM311 to the MAX301 switch provides 20mV of hysteresis during switching. The use of hysteresis prevents the comparator from undergoing multiple transitions due to noise as the integrator output traverses the region of the threshold voltage. Multiple transitions of the comparator can result in an excursion of the integrator outside of the amplifier's linear operating region, which might then lead to integrator saturation.

Once a threshold limit is detected, the comparator changes state and feeds the information forward to a D flip/flip. The flip/flop is clocked with an external reference that is provided by the analog-to-digital conversion circuitry. The state transitions are synchronized with the conversion process to help with the implementation of auto-calibration, a feature will be explored more in the next chapter. The comparator output from each gyrator output is fed into an OR circuit that increments the memory-storage D flip/flop whenever the hourglass integrator needs to change state. When this memory flop is toggled, that information is fed to the offset acquisition bits of the gyrator LNAs, the control bit of the phase-reversal switch, and a state control bit for the differentiator. The change in the state of integrator initiates the auto-nulling procedure of one LNA, while the other LNA enters into a holding state. The signal to the phase-reversal switch effectively turns over the hourglass integrator, and the capacitors begin to charge smoothly in the opposite direction. The state information that is fed-forward to the differentiator is used to synchronize its demodulation with the state changes of the integrator. With this logic scheme and global feedback, the hourglass topology can perpetually integrate a sensor's current.

4.3.6 Voltage Biasing

The voltage biasing for the nanopore sensor is provided by a stable zener reference buffered with a low-noise operational amplifier; the schematic is shown in Figure 4-6. The LM199

zener reference provides a stable 6.95V output with reference to analog ground. This voltage is tapped off with a shunt resistive network that allows for setting the bias from zero to 250mV. To help keep the noise voltage below $1nV/\sqrt{Hz}$ in the critical signal bandwidth, the bias voltage is filtered with a second-order LC network. This filter attenuates the residual $4nV/\sqrt{Hz}$ spot noise from the voltage reference beyond 300Hz. Filtering the reference helps to prevent excess noise caused by charging of the sensor capacitance at high frequencies. With this circuit, a low-noise bias voltage is supplied across the nanopore sensor.

4.4 Noise Analysis

The noise performance of the hourglass integrator is dominated by the thermal noise of the operational amplifiers reacting with the capacitance at the high impedance node of the gyrator. The rms contribution for this noise source is defined by

$$i_{rms} = \sqrt{(2\pi)^2 C_s^2 e_n^2 \int f^2 df} = \sqrt{(2\pi)^2 C_s^2 e_n^2 f^3/3},$$

where C_s represents the total capacitance at the input of the amplifier, e_n is the voltage noise, and Δf is the measurement bandwidth. This noise is especially prominent at high frequencies due to its spectral weighting. At low frequencies, the noise contribution will be dominated by the shot noise of the currents through the picoammeter. The origin of these currents are the input JFETs and the leakage currents of the MAX4526 mosfet switches. The magnitude of these leakage currents, I_l, is below 5pA based on experimental data at room temperature.

The boundary between the shot-limited noise and the reactive noise occurs at a frequency

$$f_{critical} = \sqrt{\frac{2qI_l}{4\pi^2 e_n^2 C_s^2}} Hz,$$

which is estimated to be 5 kHz for the parameters in the prototype integrator. The rms noise in a 25 kHz measurement bandwidth, therefore, the noise will be dominated by the high frequency noise associated with the input shunt capacitance,

$$i_{rms} = \sqrt{(2\pi)^2 C_s^2 e_n^2 f^3/3}.$$

The dominant sources for the noise metric come from the operational amplifiers in the gyrator. Each input JFET contributes approximately $2nV/\sqrt{Hz}$ with the 10mA of bias current used for the $LNAs$. The filtered supplies for the MAX4526 and the sensor bias circuit restrict their noise contribution to under $1nV/\sqrt{Hz}$, which is uncorrelated with the JFETs, and can be neglected in the first-order noise estimate.

The other parameter required for the noise metric is the capacitance seen by each noise source. The fabricated sensor's contribution to capacitance is determined by the integral,

$$C_{sensor} \approx \epsilon_r \epsilon_o \int \frac{2\pi r}{r} dr = \epsilon_r \epsilon_o 2\pi r,$$

which yields an estimated value on the order of 2.5pF for a silicon nitride window; all JFET noise sources will react with this capacitance. In addition, the parasitics from the MAX4526 will add an additional shunt capacitance of roughly 10pF to the picoammeter input. Considering the gyrator circuit, the opamp JFET attached to the high impedance node will react with *its own* capacitance, adding an additional 10pF shunt capacitance for that specific transistor. Collecting these terms, the estimated noise for the picoammeter is

$$i_{rms} = \sqrt{\sum_i (2\pi)^2 C_{s,i}^2 e_{n,i}^2 f^3/3} \approx 1.0pA,$$

for a measurement bandwidth of 25kHz[2]. This noise estimate meets the specification developed in the preceding chapter.

Even with the constraint of significant capacitance from the MAX4526, the noise of the picoammeter is not prohibitive. The theoretical rms noise contributed by the sensor was estimated at 0.34 pA; the excess noise of the picoammeter, which is uncorrelated with the sensor, essentially increases the noise of the ideal sensor by a factor of three. In light of the severe limitations of a discrete switch topology, this represents a good starting point for the hourglass topology–especially considering that a resistive feedback head-stage with an equivalent noise contribution would be limited to roughly 1-5kHz in bandwidth due to the shunt parasitics around the feedback resistance. In addition, the ability to lower the input capacitance through

[2]for $i = 1 \rightarrow 3, C_s = 15pF, while for i = 4, C_s = 25pF; e_n = 2nV/\sqrt{Hz}$ for all sources.

the use of improved switches with lower capacitance will greatly improve the performance of the picoammeter. For example, scaling the switch parasitics down to 4 pF by removing the protection zeners would improve the noise metric to under 0.5pA rms.

4.5 Waveform Examples and Performance Summary

4.5.1 Test Bench

Representative waveforms demonstrate the general performance of the hourglass integrator; the test setup is illustrated in Figure 4-12. To model the nanopore sensor, a $5G\Omega$ source resistor was placed between the sensor bias voltage and the hourglass integrator. This value of resistor creates a Johnson noise source equivalent to the shot noise from a 10 pA channel current. To model the capacitance of the sensor, a 5 pF shunt capacitance was placed in parallel with the resistor. To effectively test the bandwidth of the electrometer, a capacitive-T network was shunted into the input of the picoammeter. With this circuit, triangle waveforms can be applied to the capacitive-T shunt and a square-wave current on the order of 10pA delivered to the integrator with wide bandwidth. As a final consideration, the measurements were performed in a Faraday cage to minimize the coupling of external 60Hz fields into the high impedance nodes. The output of the hourglass integrator was digitized with a 16-bit 100kHz MX card from National Instruments; the software code for this interface is included in Appendix E.

4.5.2 Waveforms

The first waveform, Figure 4-13, demonstrates the issues of offset voltage across the JFET pairs of the gyrator; the figure is a plot of one output from the hourglass integrator. A bias voltage of 50mV is applied across the sensor model for an expected quiescent current of 10pA. Prior to offset compensation, however, the 25mV offset across the integrator inputs results in the superposition of a 5pA current whose sign changes with the state of the integrator. The modulation in signal current creates the state-dependence of the integrator's slope characteristics. In addition, the charging of parasitics due to the offset voltage result in discontinuous jumps during each transition. The state change of the integrator requires the charging of the picoammeter parasitic capacitance by $2V_{OS}$, or roughly 50mV. The total charge injection is estimated

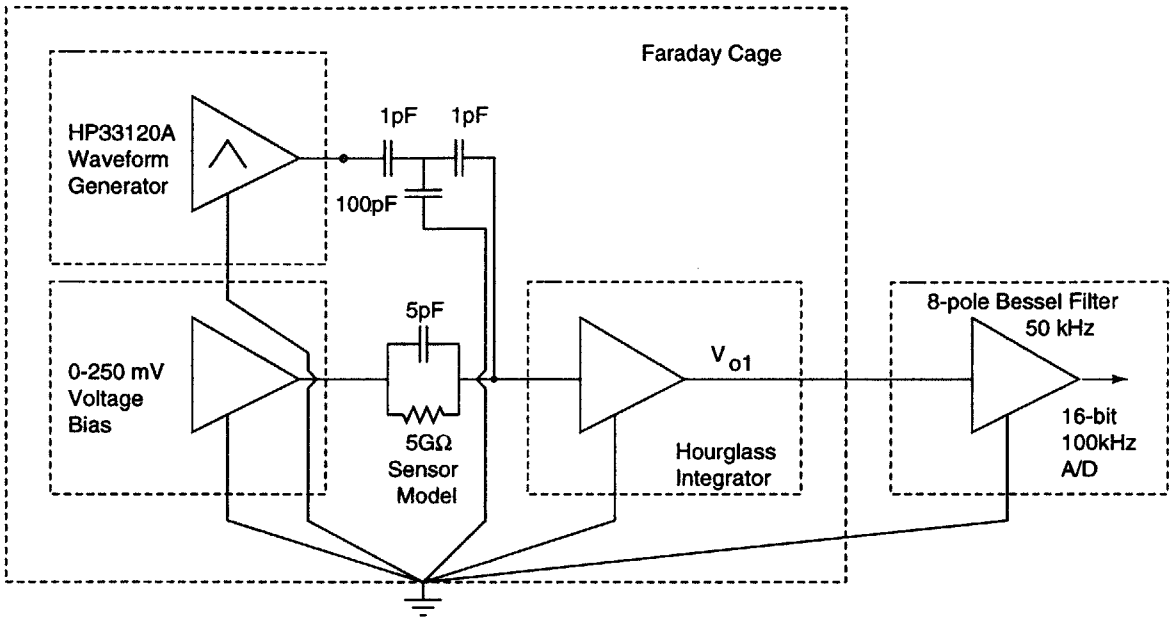

Figure 4-12: The test circuit for studying the picoammeter's performance.

at 520fC, based on the 5.2V discontinuity across the effective 100fF integration capacitor, as seen at the output of the integrator. This value is consistent with the expected charge of 750fC based on the estimates of the picoammeter's input capacitance of 15pF; the small discrepancy is most likely due to residual charge injection supplied by the MAX4526 phase-reversal switch. Note that the saturation at the negative transition occurs within the output of the x10 buffer amplifier; the hourglass integrator is maintained within it's linear region.

Figure 4-14, demonstrates the efficacy of the charge injection compensation for the MAX4526 and the offset nulling of the LNAs within the gyrator. The MAX4526 has been biased for zero net charge injection (reference Figure 4-11), and the LNA's auto nulling circuitry has been activated by the state control logic. The offset in voltage of the gyrator is now reduced to under $10\mu V$, and the net charge injection to under 5fC. The slope of the waveform now corresponds to 10pA during each state of the integrator. The acquisition of signal currents is now feasible at the picoampere scale. Figure 4-15 more clearly illustrates the superposition of currents and the continuous state transition; a 40pA (peak-to-peak, $\pm$ 20 pA), 125 Hz square wave is superimposed on the 10pA quiescent current. As the gyrator state changes, the integrator begins to

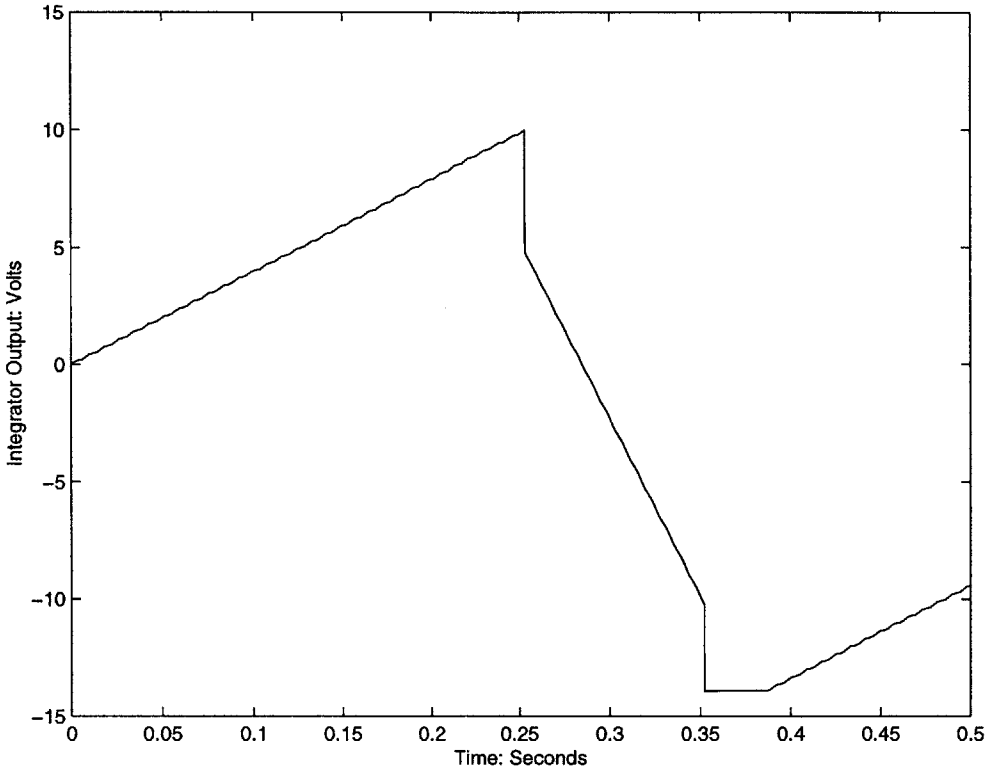

Figure 4-13: Demonstration of the switching characteristics of the hourglass integrator before offset and charge compensation. The discontinuous transition characteristics and variable slope illustrates the problems of charge injection and electrometer voltage offset. The quiescent current into the picoammeter is roughly 10pA, with a modulation of $\pm$ 5pA depending on the state of the integrator.

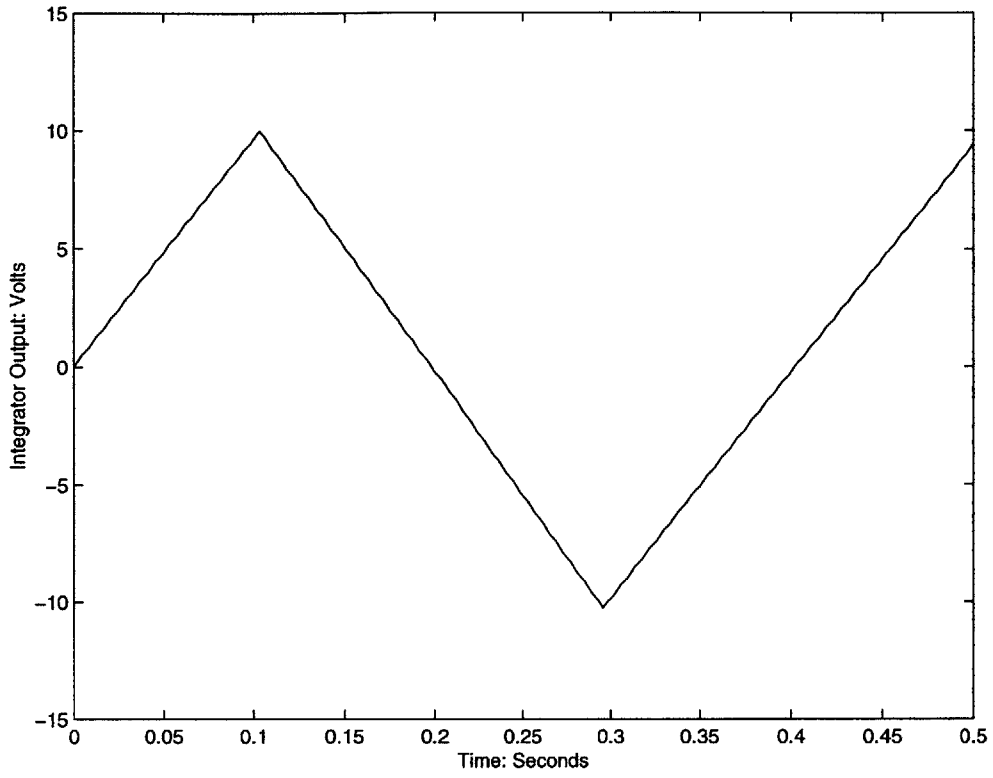

Figure 4-14: Demonstration of the switching characteristics of the hourglass integrator after offset and charge compensation. The triangle waveform demonstrates the integrator output after the MAX4526 is properly biased for zero net charge injection and the LNA offset null circuitry is activated. The quiescent current into the picoammeter is 10pA, superimposed with a 125Hz, 1pA test current.

charge in the opposite direction, but at an equal magnitude.

The next illustration, Figure 4-16, demonstrates the feedback of the state control logic to maintain the hourglass integrator within the linear region of the amplifier. A step waveform in current from 10pA to 50pA is supplied to the picoammeter input. The slope of the integrator changes in synchrony with the signal current modulation and the reset rate is adjusted accordingly. The use of global resets gives the hourglass electrometer significant dynamic range. The lower sensitivity of the picoammeter is set by the leakage current of the input, roughly 1 pA, and the upper limit is defined by the integrator's slew rate (charging rate $< 10V/\mu s$), or roughly $1\mu A$.

A final demonstration of the integrator's novel properties is illustrated in Figure 4-17. A

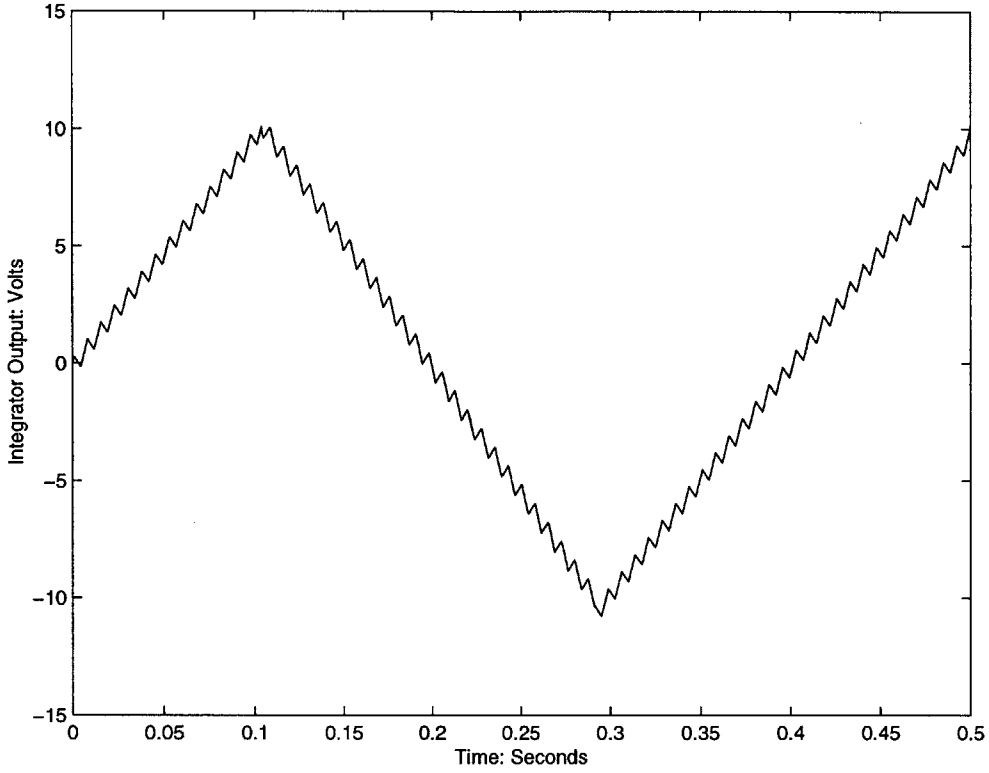

Figure 4-15: A clearer illustration of the integrator functionality. A 125 Hz, 40pA (peak-to-peak, ± 20pA) square wave is superimposed on the 10pA quiescent current. Note the smooth transition in charging rate as the integrator state is changed.

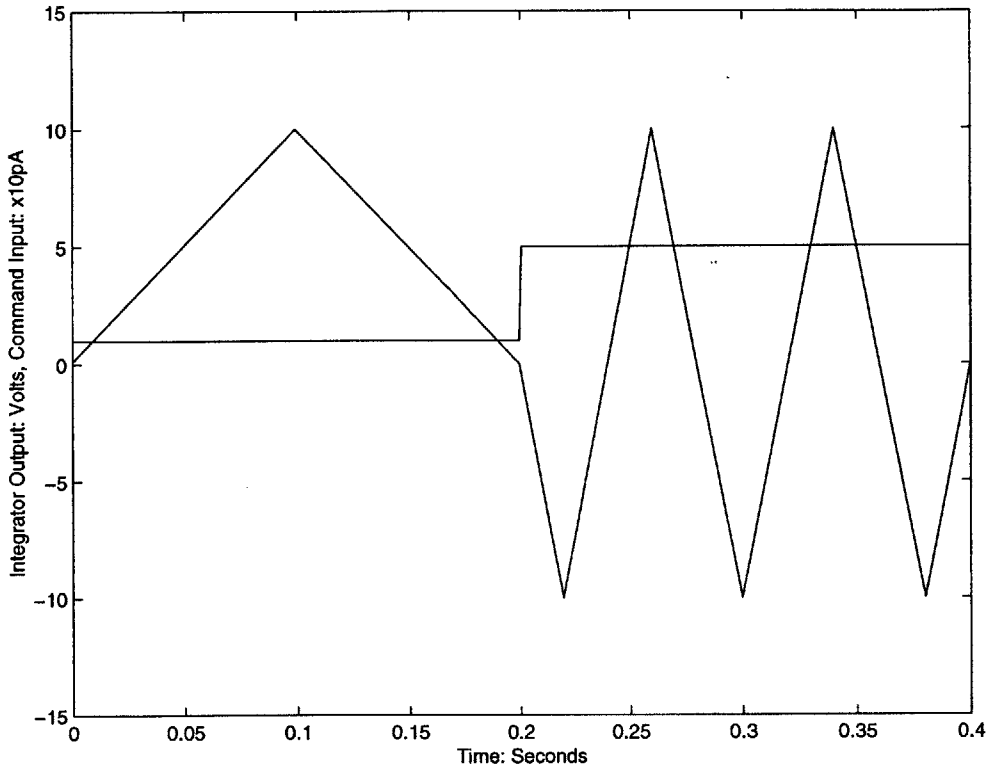

Figure 4-16: Demonstration of the feedback logic for adjusting integrator state changes. The input current is stepped from 10 to 50pA and the chopping frequency is adjusted accordingly. The use of global feedback maintains the integrator in its dynamic range over large variations in signal current, and counters slow drift due to mismatches in the signal current between the two integration states.

100Hz sinusoidal current of 12nA (peak-to-peak) is supplied at the input of the picoammeter. The expected waveform out of the integrator is

$$i_o = \int \frac{I_o cos(\omega t)}{C_f} dt,$$

which is roughly 190V (peak-to-peak) for the test current specified.

To maintain the output of the integrator within its confined voltage level of $\pm 1V$, the signal is chopped repeatedly as shown in Figure 4-17. This waveform can be unwrapped by simply multiplying each state region of the integrator output by the proper sign, and then reconstructing the signal, as illustrated in Figure 4-18. As demonstrated by the reconstructed waveform, a standard integrator topology would require a linear range of roughly ± 100 Volts to integrate this signal continuously (the DC offset arises since the signal was not triggered the input current's zero crossing). This demonstration provides an alternative intuitive view of the hourglass topology; the hourglass integrator achieves a "linear region" of operation that extends effectively to infinity by folding the output voltage of the gyrator into a region constrained by $\pm 1V$. To complete the functional picoammeter, a method of unfolding the waveform and taking the derivative must be found.

The noise and bandwidth characteristics of the integrator will be discussed at the end of the next chapter, which develops the second half of the picoammeter circuit: the demodulating differentiator. By combining these two circuits, the excellent noise and bandwidth properties of the chopper-stabilized picoammeter will be made more evident.

4.6 Chapter Summary

This chapter has developed the first component of the chopper-stabilized picoammeter, the hourglass integrator. By modifying a floating gyrator, a topology that allows for quasi-continuous integration of a waveform without the need for external charge compensation was created. To implement this topology successfully, a low-noise operational amplifier (LNA) was constructed to meet the demanding specifications of the picoammeter circuit. In particular, a novel approach to offset-nulling was developed that avoided compromising the $10G\Omega$ input impedance of the picoammeter by exploiting the state properties of the gyrator. The current steering

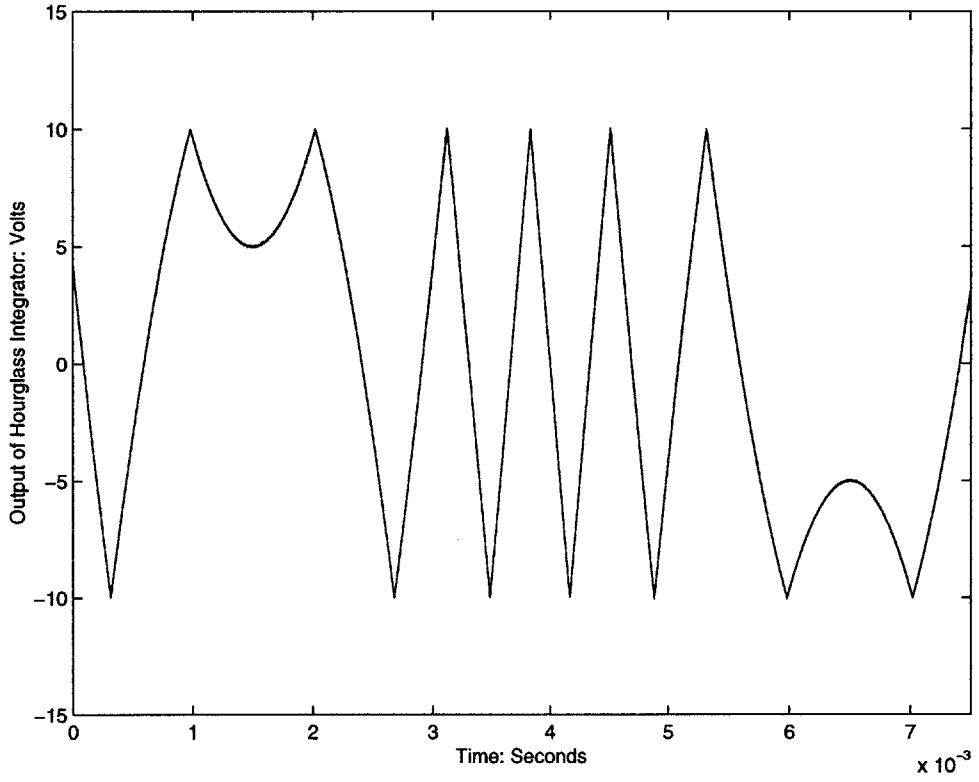

Figure 4-17: Demonstration of the wrapping property of the hourglass integrator. A 100Hz sinusoidal input current of 12nA (peak-to-peak) is supplied at the picoammeter input. To maintain the output of the integrator within $\pm 1V$. the signal must be chopped repeatedly.

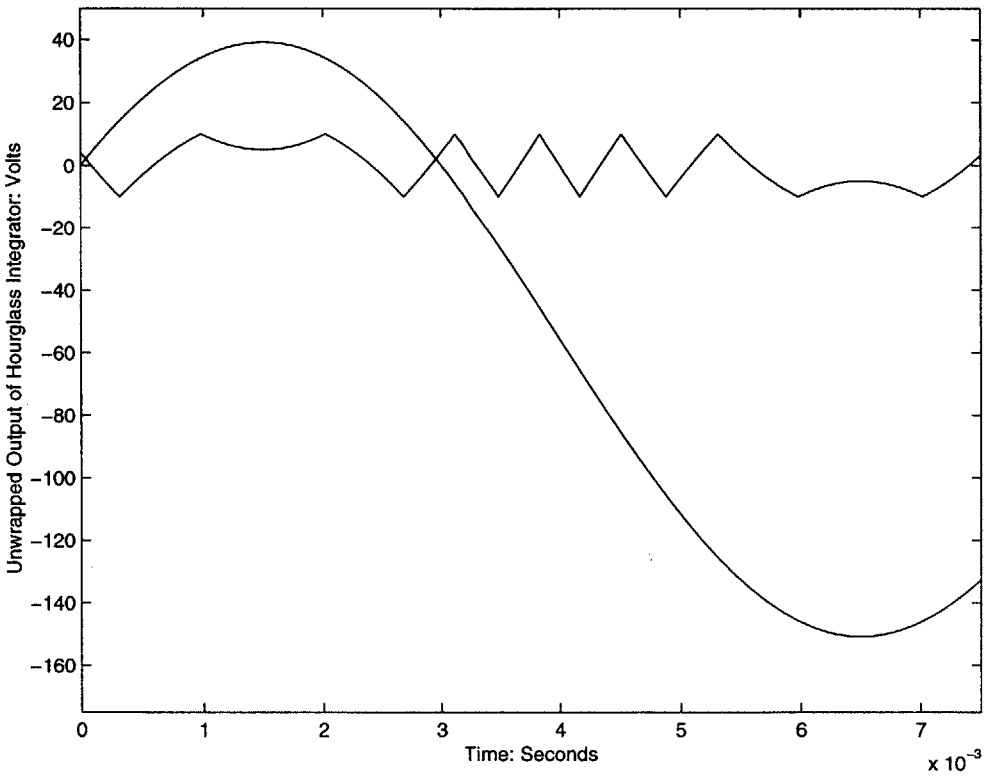

Figure 4-18: Demonstration of the wrapping property of the hourglass integrator. By reconstructing the signal from the hourglass output, the "infinite" effective dynamic range of the circuit is clear.

for the integrator was achieved with a phase-reversal mosfet switch that was biased to reduce the charge injection from switching to under 5fC–three orders of magnitude below the device's general specification. A global feedback circuit maintains the integrator within its linear operating regime over six decades of current, without the need for external clock adjustment. The properties of the hourglass integrator were then demonstrated by a series of test waveforms that illustrate the state-conserving principles outlined previously.

To complete the chopper-stabilized picoammeter topology, some mechanism must now effectively "unwrap" the integrator's output waveform with demodulating differentiation. The implementation of this signal processing is the subject of the next chapter.

Chapter 5

Picoammeter II: Demodulating Differentiator

5.1 Chapter Overview: Requirements on Taking the Derivative

The chopper-stabilized picoammeter requires the simultaneous demodulation and differentiation of the integrator output. The signal current from the nanopore sensor is integrated by the hourglass topology and periodically multiplied by an effective sign of ± 1 to maintain the feedback capacitor's voltage within the linear region of the amplifiers. The differentiator circuit following the integrator must therefore take the derivative of the integrator's output *and* demodulate the signal in synchrony with the integrator.

The derivative operation can be problematic due to its weighting of high frequency noise, and care must be taken to avoid adding excess noise that might compromise the picoammeter's noise specifications. In addition, the demodulation of the signal must not compromise the quasi-continuous operation of the chopper-stabilization process. A demodulating differentiator may be implemented in either the analog, digital, or mixed-signal domains. For brevity, the discussion in this chapter is restricted to the most promising analog and digital implementations. The analog solution is useful for wide bandwidth current measurement applications, while the digital approach is appealing for the relatively low-bandwidth requirements of genetic sequence recognition with hybridization detection.

5.2 Analog Approaches to Differentiation

5.2.1 Basic High-Pass Filter

The simplest derivative available is the high-pass network illustrated in Figure 5-1. the derivative operation is supplied by the high-pass zero formed by R_d and C_d. The problem with this topology is the limited bandwidth of the differentiation illustrated by the circuit's transfer function

$$\frac{V_{out}}{V_{in}} = \frac{sR_dC_d}{1+sR_dC_d} = \frac{s\tau_d}{1+s\tau_d},$$

which has a pole at $(2\pi R_dC_d)^{-1}$. Above this pole, the circuit no longer provides the desired derivative of the input signal. The value of $(2\pi R_dC_d)^{-1}$ is constrained by the input-referred noise of the resistive element R_d,

$$S(f) = \frac{4k_bT}{R_d}(\frac{C_f}{C_d})^2 = \frac{4k_bT}{\tau_d}(\frac{C_f}{C_d})\ A^2/Hz,$$

which can be used as a metric to establish the acceptable range of the filter's time constant, τ_d.

The noise metric estimates a possible τ_d of roughly one μs or less by using large filter capacitors and small filter resistors. The value of R_d, however, is constrained practically to the order of $1k\Omega$, where it's $4nV/\sqrt{Hz}$ thermal noise contribution will not be significantly undermined by the 2-3 $nV/\sqrt{Hz}$ contributed by the following amplifier stage. With a resistor of this scale, a capacitor C_d on the order of 10nF is required to minimize the input-referred noise of R_d. The bandwidth of the high-pass filter is then limited to order of 16 kHz, which is below the specification for the final measurement bandwidth. In practice, it is good design philosophy to have a significantly higher bandwidth for the integrator/differentiator combination to help improve the transient performance arising from the chopper switching [118]. A reasonable specification is roughly four-to-five times the final measurement bandwidth to allow for the subtraction or suppression of the switching transients; the limited performance of the simple high-pass filter makes meeting this dynamic specification difficult. More sophisticated analog techniques, however, can extend the bandwidth of the differentiator circuit significantly while also obtaining effective signal demodulation.

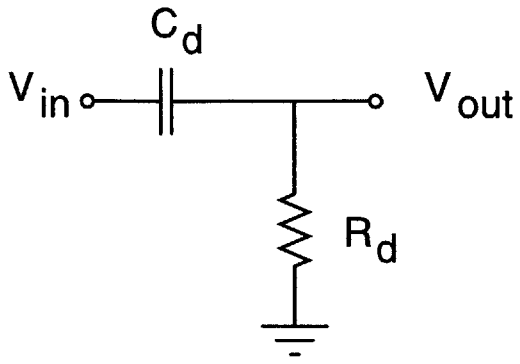

Figure 5-1: The basic high-pass filter topology for taking an analog derivative.

5.2.2 Feedback Approaches to Differentiation

The use of feedback allows for wide bandwidth differentiation with low excess noise. A common topology for implementing differentiation with feedback is shown in Figure 5-2; the Miller effect of the amplifier around the feedback impedance extends the bandwidth of the high-pass filter, allowing for the use of larger filter elements that improve noise performance. The loop transfer function for this circuit is

$$\frac{V_o}{V_i} = \frac{sR_dC_d}{1 + sR_dC_c},$$

which provides the desired differentiator characteristic for frequencies below $(2\pi R_dC_c)^{-1}$. The zero in the feedback path provided by C_c serves two purposes; first, to insure stability of the circuit at crossover, and second, to limit the gain of the circuit at high frequencies where noise may be of concern.

The standard feedback differentiator can be converted into a topology suitable for the chopper-stabilized picoammeter; the schematic is shown in Figure 5-3. The anti-symmetric outputs of the hourglass integrator are attached to the inputs V_{INa} and V_{INb} of the differentiator.

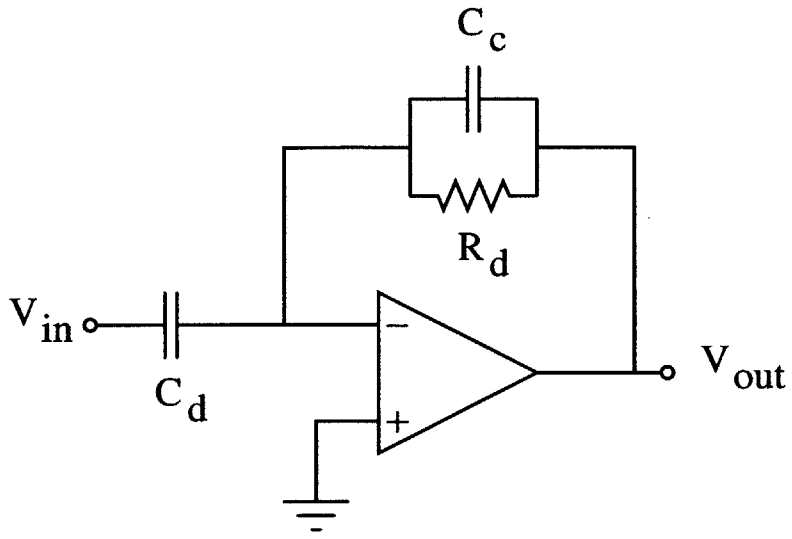

Figure 5-2: The basic feedback topology for taking an analog derivative.

Ignoring the switches for now, the transfer function for the differentiator,

$$V_{out} = \frac{sR_dC_d}{1 + sR_dC_c}(V_{INa} - V_{INb}),$$

yields a net picoammeter transresistance of

$$\frac{V_{out}}{I_s} = \frac{2R_dC_d}{C_f(1 + sR_dC_c)}\ \Omega,$$

that mimics an effective feedback resistor of $(2R_dC_d/C_f)$ within the measurement bandwidth. This effective resistance is essentially identical to that of classical integrator/differentiator topologies.

The addition of signal switching at the differentiator's input allows for state-conserving demodulation. When the integrator charges to it's threshold limit and changes state, the slope of the integrator's outputs changes polarity. If the integrator state change is also fed-forward to the differentiator, then the signal paths of the differentiating capacitors, C_d, can be exchanged with respect to the differential amplifier. The state of the capacitors in the circuit

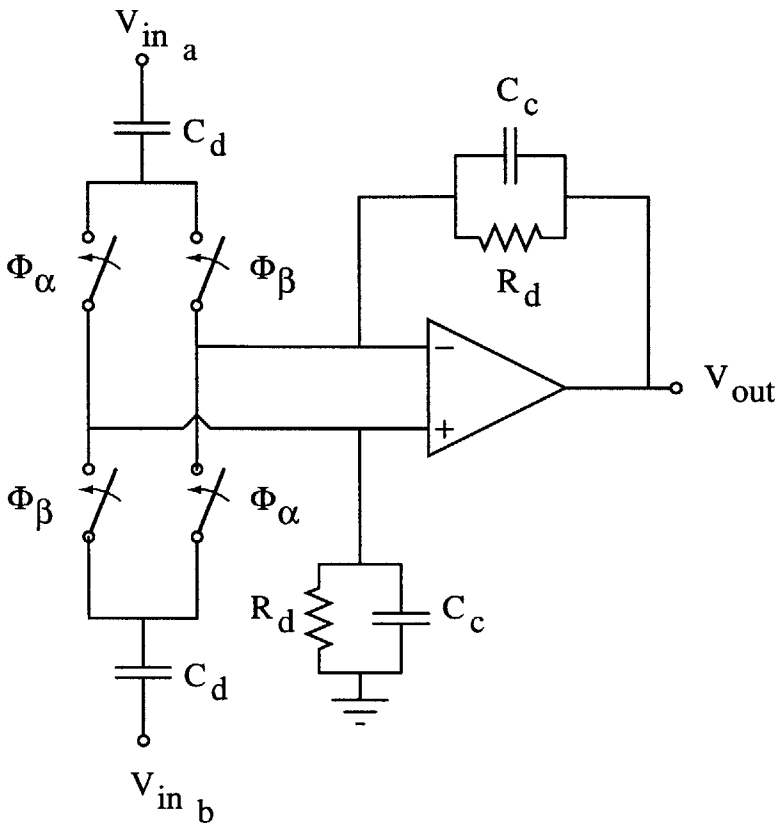

Figure 5-3: A modified feedback differentiator suitable for the chopper-stabilized picoammeter. The switches at the input demodulate the signal in synchrony with the integrator. To first order, all capacitive states in the topology are conserved during switching.

are maintained to first-order, which allows for quasi-continuous demodulation of the integrator outputs. In practice, some signal perturbation is created by the amplifier voltage offsets and switch charge injection. These parasitic effects can be removed, however, or at least greatly attenuated, by implementing circuit techniques similar to those discussed with the hourglass integrator prototype.

A metric may be derived that explicitly defines the relationship between noise performance and bandwidth for this topology. The noise for the feedback resistor, when referred back to the

input of the picoammeter, is characterized by

$$S(f) = \frac{4k_bT}{R_d}(\frac{C_f}{C_d})^2 \ A^2/Hz.$$

Equating this with the shot noise of the channel current, I_s,

$$S(f) = 2qI_s \ A^2/Hz,$$

establishes a requirement on the differentiator's resistor size. The differentiator resistor will react with the input capacitor C_d, from which a characteristic time constant for the circuit can be derived. This time constant,

$$\tau_d = \frac{2k_bT}{qI_s}\frac{C_f^2}{C_d},$$

serves as a metric for the allowable differentiator bandwidth when constrained by the input-referred noise.

Our metric predicts that for a circuit with C_f on the order of 1pF, C_d on the order of $100nF$ and an I_s of 10pA, τ_d should be approximately $5 \cdot 10^{-8}$s. In practice, however, this theoretical time constant is unachievable due to the thermal noise of the operational amplifier, which would otherwise dominate the topology's noise properties for feedback resistors smaller than 1-5 kΩ. This additional constraint on the resistor specification leads to a time constant for the lag pole that is on the same order as that with a high-pass filter, $\tau_d \approx 1 \cdot 10^{-5}$s. The large time constant does not restrict the bandwidth of this circuit to 16kHz, however, due to the additional loop gain provided by the operational amplifier. What the finite pole does undermine is the ability to construct stable, wide bandwidth differentiators suitable for quasi-continuous picoammeter operation. The fact that the theoretical noise/bandwidth performance of the feedback topology can not be achieved in practice motivates the use of an alternative differentiator topology.

5.2.3 Current Conveyors and Analog Multiplication

The use of a current conveyor allows for stable, wide-bandwidth differentiation by isolating the differentiator capacitor and resistor; the basic topology for a current conveyor is shown in Figure 5-4. A voltage buffer drives the differentiation capacitor C_d, and the current through

the buffer's supply rails is mirrored onto the differentiation resistor R_d. Assuming negligible bias current from the buffer input, Kirchoff's current law dictates that the current through R_d is equivalent to that through C_d. The resulting transfer characteristic,

$$\frac{V_o}{V_i} = sR_dC_d,$$

is of the desired form for analog differentiation.

The bandwidth gains of this circuit arise from the effective decoupling of R_d and C_d. The capacitor C_d will be driven by the output resistance of the voltage buffer, r_o, while the resistor R_d will be shunted by the parasitic capacitance, C_p, of the current mirrors. The dominant time constants, r_oC_d and R_dC_p, are generally several orders of magnitude smaller than the R_dC_d time constant associated with the alternative differentiator topologies. The small circuit time constants allow for enhanced differentiation bandwidth without relying on feedback. The inherent stability of this open loop design and its wide bandwidth have resulted in several recent publications exploiting this technique [34, 35, 36, 37].

The current conveyor topology can be modified to meet the demodulating specifications of the chopper-stabilized picoammeter. As shown in Figure 5-5, the currents mirrored into the load resistor R_d can be steered from either voltage buffer. If the current steering of the mirrors is performed in synchrony with the integrator modulation, then the output voltage across the load resistors represents the signal current multiplied by a transresistance of $2R_dC_d/C_f$.

5.2.4 Prototype Current Conveyor Differentiator

A prototype current conveyor demonstrates the general properties of this topology; the schematic for the circuit is illustrated in Figure 5-6. The inputs to this circuit are differentially connected across an MAT-02 matched BJT pair (Q_1 and Q_2). The bias currents for the matched pair are provided by extremely stiff current sources, with equivalent output resistances of approximately $100G\Omega$. This large incremental resistance implies that the differential current through the matched pair will be determined by the shunt capacitor across the emitter terminals. The signal current through the differential pair is then,

$$I_d = s2C_d(V_+ - V_-),$$

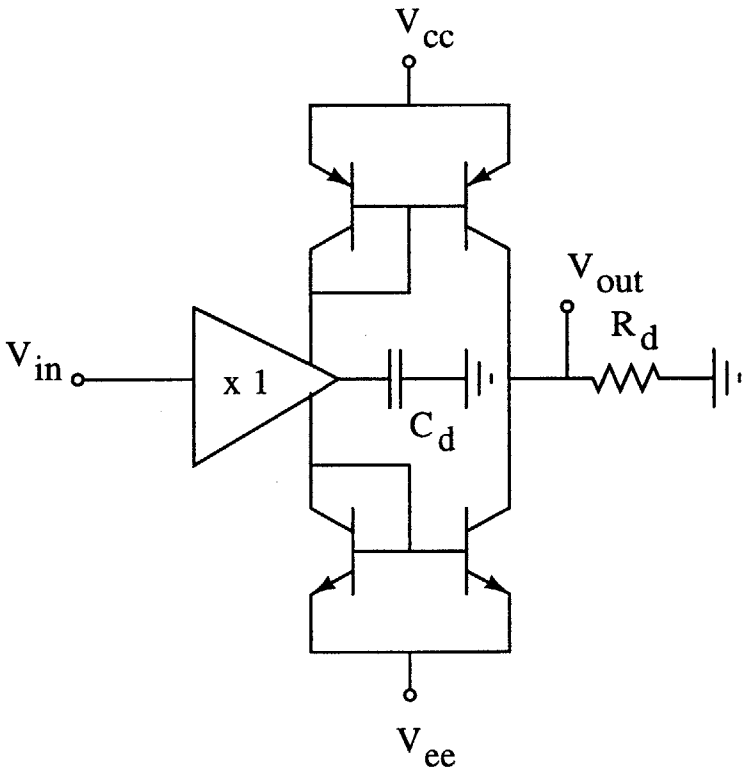

Figure 5-4: The basic topology of the current conveyor for differentiation. The current through the capacitor C_d is mirrored and forced through R_d. The capacitor C_d is driven with the output resistance of the buffer, while R_d is shunted by the parasitics of the current source. In general, these time constants are much smaller than R_dC_d.

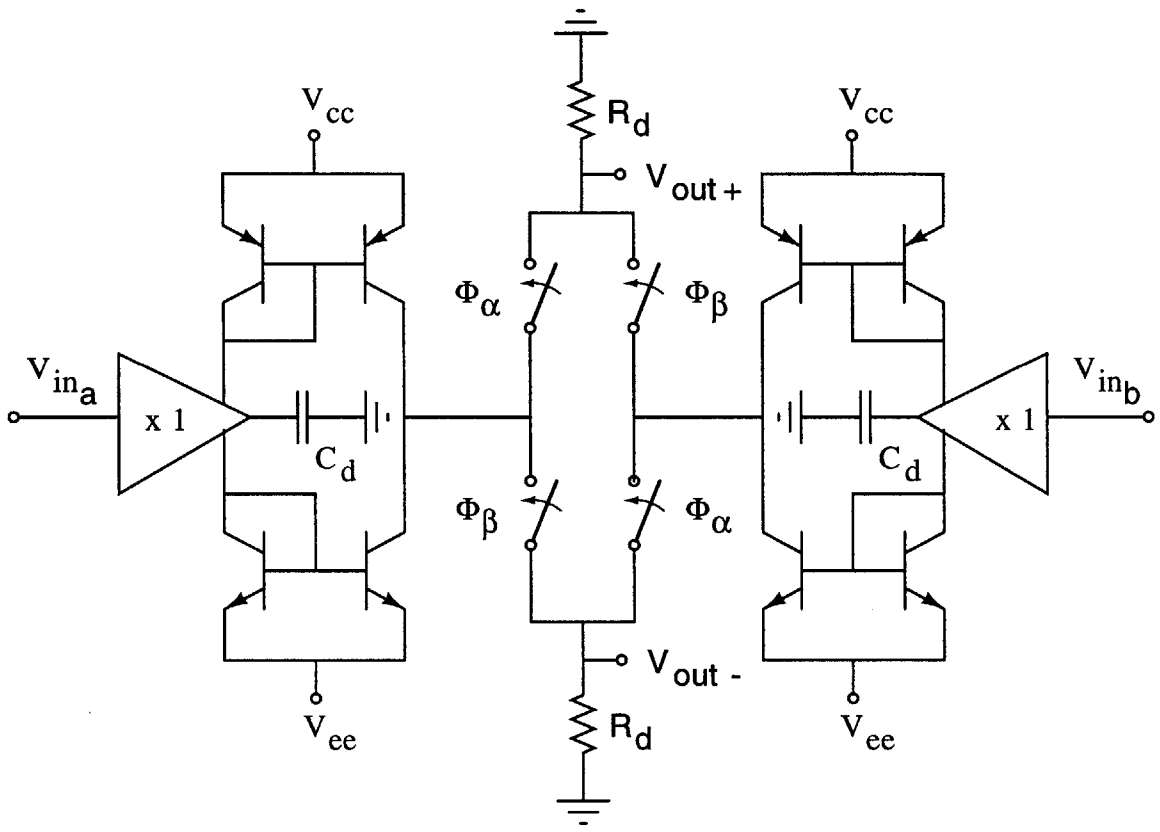

Figure 5-5: Demodulation with the current conveyor. By steering currents into the load resistors R_d, the demodulation and differentiation of the signal may be accomplished.

where C_d is $200nF$ in the prototype. A second differential pair (Q_3 and Q_4), shunts the capacitor C_d to provide α compensation of the primary differential BJT pair and it's cascode circuitry. The use of α compensation helps to improve transistor matching to third-order in α [6]. Note that the dynamic range of the inputs is limited to roughly $\pm 1V$ using the totem-pole topology in this prototype; this range could be extended in the future with a folded cascode design.

The differential signal currents are buffered through a cross-coupled cascode circuit that performs the current steering necessary to demodulate the signal waveform. For example, transistors Q_5 and Q_6 control whether the signal current I_1 is steered into resistor R_{L1} or R_{L2}; transistor pair Q_7 and Q_8 perform the same function for I_2. The effect of alternatively steering the currents between the two load resistors provides the effective ± 1 multiplication needed for signal demodulation. Control signals for the current steering are derived on the upper left hand corner of the schematic, and consist of a differential pair that converts a TTL logic signal into an alternating 4.1/3.5 V bias that controls the effective signal path.

The buffered small signal currents are applied differentially to the resistor loads, yielding a differential transfer function for the circuit of

$$\frac{V_{out}}{\Delta V_{in}} = s2C_dR_d.$$

The load resistance, R_d is limited to roughly $1k\Omega$ by the dynamic range of the voltage rails. The differential voltage across the matched resistors is extracted by the INA114 differential amplifier, configured for a gain of two. The function of the zener diodes is to clamp the resistive load due to any excess perturbations at the picoammeter input.

The combination of the hourglass integrator and current-conveying differentiator results in a low-noise, high gain picoammeter. The transresistance of picoammeter topology using this current conveyor is $8R_dC_d/C_f$; for the values of C_d, C_f, and R_d used in the prototype, the chopper-stabilized picoammeter has a net transresistance of $1.6G\Omega$. This transresistance is on the order of that required from a purely resistive feedback implementation, given the noise constraints on the resistor. Resistive feedback is limited, however, to a bandwidth on the order of 1-5kHz without the use of additional boost circuitry. The chopper-stabilized integrating

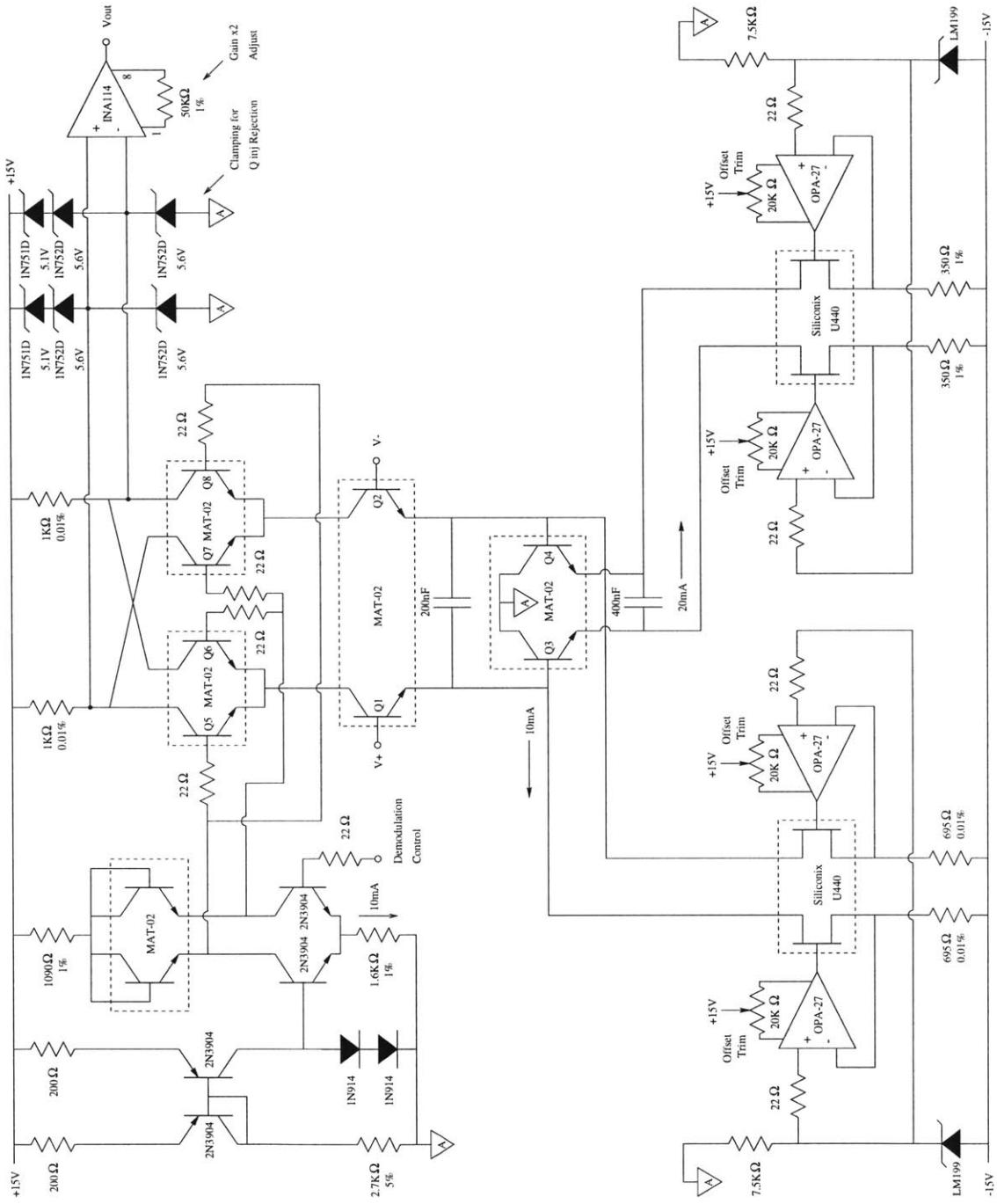

Figure 5-6: The prototype current conveyor for wide bandwidth, low noise differentiation and demodulation.

picoammeter, therefore, allows for extended bandwidth and improved noise performance by exploiting the inherent performance of quality capacitors.

Similar to the previously explored topologies, the noise constraints of the current conveyor ultimately limit the bandwidth of this topology. A suitable metric can be derived that yields the estimated bandwidth of the circuit based on the input-referred noise specifications. The dynamics of the circuit are limited by the output resistance of the MAT-02 transistors, r_o and the differentiating capacitor, C_d. The noise at the input of the current conveyor will be dominated by the shot-noise of the bias current, I_{bias}, through Q_1 and Q_2. To determine the effect of these bias currents at the input of the picoammeter, they will be reflected through the current gain, $2C_d/C_f$. Equating the shot noise of the input-referred bias currents with the shot noise of the source, the maximum bias current,

$$I_{bias,max} = 2(\frac{C_d}{C_f})^2 I_s,$$

for the current-conveyor's input transistors can be specified. With $I_{bias,max}$ defined, the bandwidth for the circuit can be estimated by substitution of circuit parameters.

The time constant for the input stage is defined by

$$\tau_d = 2r_o C_d = \frac{2k_b T}{qI_s}\frac{C_f^2}{C_d}.$$

Although this expression is the same as that derived for a feedback topology, the current-conveyor is not constrained by the size of the differentiation resistor. The bandwidth-limiting resistance arises from another source, the output resistance of the input transistors. This topological difference allows for the noise/bandwidth performance of this topology to be more fully exploited. With the 10pA quiescent currents of the nanopore sensor, the performance metric estimates a feasible bandwidth of

$$f_{-6dB} = 1/\tau_d = 5.2MHz;$$

the $-6dB$ point is specified due to the equivalent time constants contributed by the input transistor pair *and* the α compensation circuitry. In reality, this specification can not be met

with the $200nF$ C_d capacitor used, because the required bias current would be $4 \cdot 10pA \cdot 10^5$, or 800 mA. This leaves the option of lowering the differentiator capacitance, C_d, to achieve the attainable bandwidth or lowering the bias current, I_{bias}, to improve the noise performance.

The noise/bandwidth metric was optimized for noise performance in the prototype differentiator. For this prototype, the bandwidth specification is only 125kHz, so a large value of C_d was maintained while the *bias current* was lowered to 10mA. Maintaining the large C_d at the expense of the bias current helps to improve the input-referred noise characteristics of this topology even further. The input-referred shot noise of this circuit is now equivalent to $10mA \cdot (5 \cdot 10^{-6})^2$, or 250 fA of input-referred current, which is an order of magnitude below the estimated signal currents through a nanopore. For these low-noise bias conditions, the differentiator bandwidth is still maintained at roughly 125 kHz, the desired specification for quasicontinuous picoammeter operation.

5.2.5 Demonstration Waveforms

The general functionality and limitations of the current-conveyor differentiator are demonstrated by the following series of waveforms. The first figure establishes the modulation waveform that was used for this demonstration series; a sinusoidal current waveform of 1Hz, 40pA (peak-to-peak) was applied to the input of the hourglass integrator. The output of the integrator should be 6.37V peak-to-peak, but the folding of the waveform to maintain linearity constrains the waveform within $\pm 1V$[1]. This waveform provides a good illustration of topology's major limitations within a current range suitable for a nanoscale Coulter counter.

The next set of figures demonstrates the functionality of the derivative and demodulation properties of this topology. Figure 5-8 shows the output of the differentiator without the current steering enabled. The envelope of the waveform shows the proper magnitude for the signal current, but the signal transitions in sign whenever the hourglass integrator changes state. The removal of the sign transitions is accomplished by feeding forward the state transition information to the TTL control pin on the prototype as shown in Figure 5-9. Signal currents are now steered through $Q_5 - Q_8$ in synchrony with the integrator state transitions to demodulate

[1]The output of the x10 buffer circuit was used for the data acquisition, the x1 output of the integrator was fed into the current-conveying differentiator

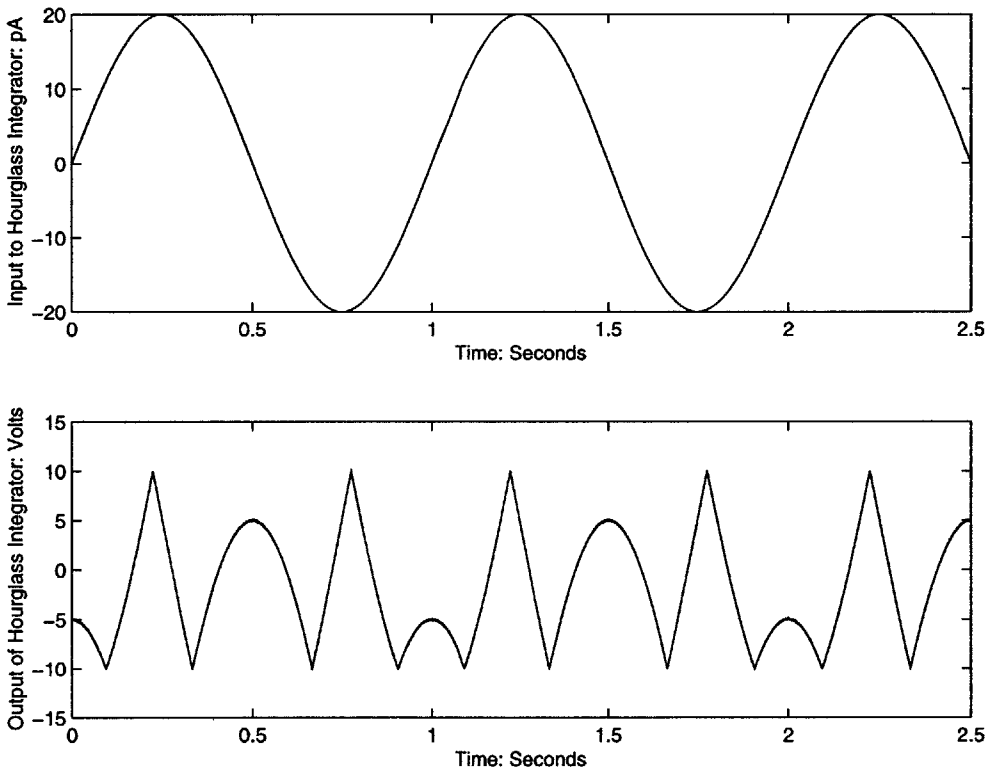

Figure 5-7: The creation of a test waveform for the current conveyor differentiator. Top Trace: A 1Hz, 40 pA (peak-to-peak) current waveform is supplied to the input of the hourglass integrator. Bottom Trace: The folded output of the hourglass integrator after a gain of ten.

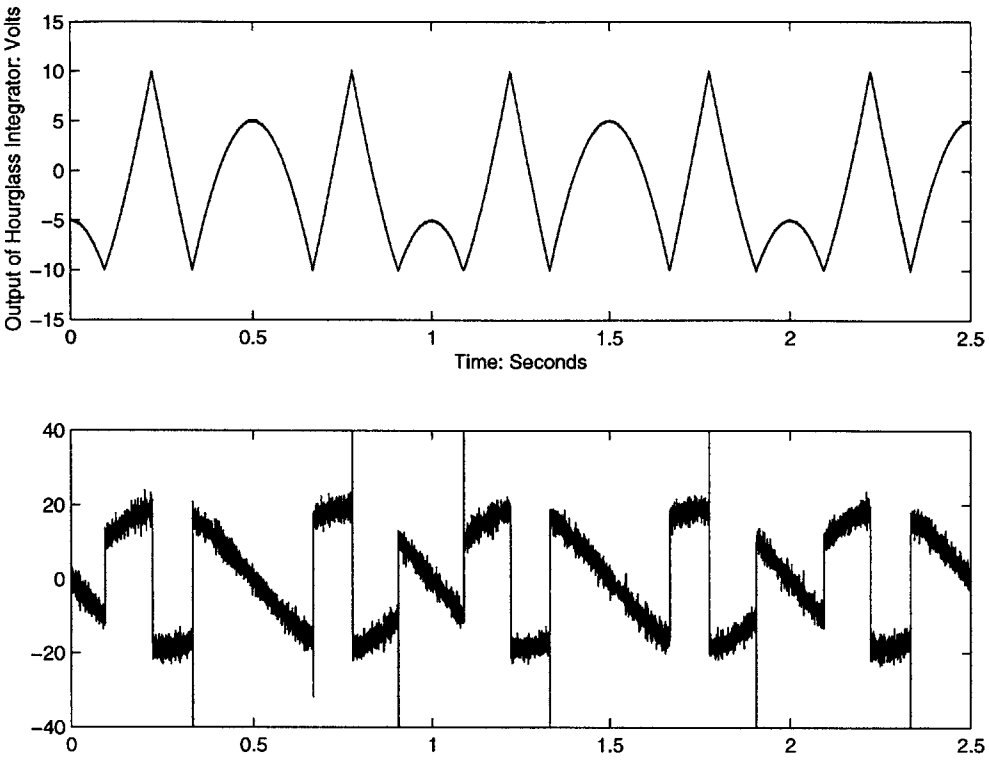

Figure 5-8: The output of the current conveyor without demodulation. The envelope of the output is defined by the magnitude of the signal current, while the transition between polarities represents the chopping of the signal by the hourglass integrator.

the signal as well as differentiate it.

The primary drawback of this topology arise from the relative matching required by the discrete components, as clearly demonstrated by Figure 5-9. For example, with the nanopore signal current of 10pA, the differentiator capacitor C_d will create a differential current of only $8\mu A$. This small current is superimposed on the $10mA$ bias currents within each branch of the current conveyor. Although shot noise is not an issue with the bias current, the relative *mismatches* of the bias currents can easily undermine the demodulation performance of the topology. This is illustrated by the $\pm 5pA$ disturbance that occurs during switching, which corresponds to a bias current mismatch of roughly $4\mu A$. The mismatches in bias current are superimposed onto the signal waveform during demodulation and must be removed to allow for proper data reduction. In practice, these offset currents can be reduced with additional trimming of the biasing components; the improved waveform is illustrated in Figure 5-10.

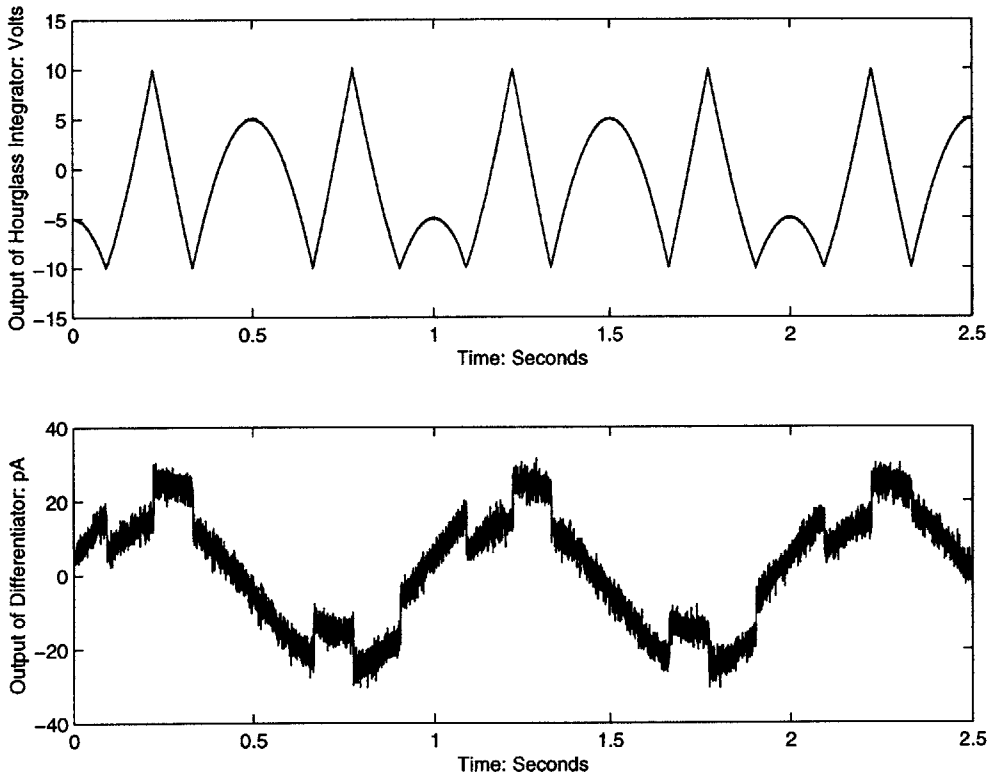

Figure 5-9: The output of the current conveyor with demodulation. The envelope of the output is still defined by the magnitude of the signal current, while the additional current steering demodulates the signal as well. Note the $\pm 5pA$ disturbance that occurs during switching due to mismatches in the bias currents.

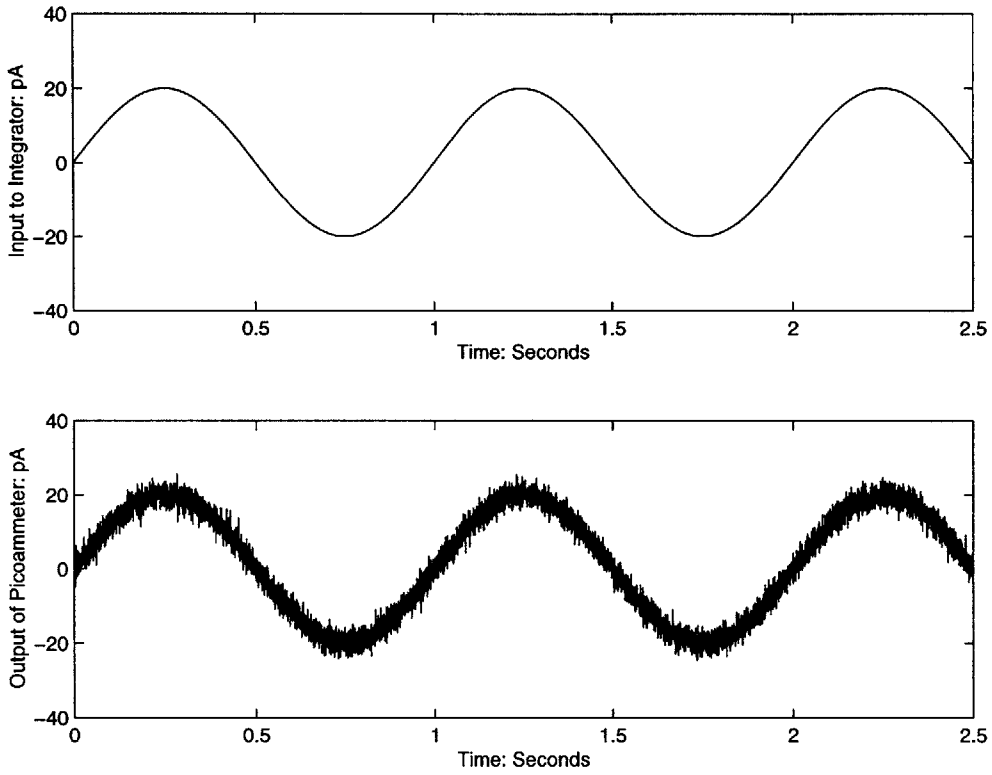

Figure 5-10: The output of the current conveyor with demodulation and offset correction.

The current conveyor topology has the capability of providing low-noise, wide bandwidth differentiation and demodulation. This topology is especially attractive for the wide bandwidth differentiation required by the chopper-stabilized picoammeter for *de novo* sequencing of DNA with a nanopore. The relatively mild bandwidth requirements of the prototype picoammeter for genetic sequence *recognition* with a nanopore, however, motivate the use of digital signal processing for differentiation and demodulation, where auto-calibration techniques may be easily applied to correct for circuit mismatches, offset currents and deterministic transients.

5.3 Digital Approach to Demodulated Differentiation

The limited bandwidth and matching requirements of the chopper-stabilized picoammeter motivate the use of digital signal processing to implement the differentiator. The use of digital processing requires the creation of differentiating filter that can also realize state-conserving demodulation. In addition, the use of digital processing allows for the application of auto-calibration techniques that subtract the deterministic transients arising from the chopping process.

5.3.1 Constraints on Quantization Noise

The challenge of implementing a digital differentiator has historically arisen from the constraints on quantization noise. The discretization process assigns discrete values to continuous signal levels that add uncertainty to the measurement. This uncertainty can be modeled as a white noise process with spectral density,

$$S(f) = \frac{(\delta V)^2}{\sqrt{12 f_s}} \, V/Hz,$$

where δV is the quantizer bin width and f_s is the sampling rate. The derivation of this expression is straightforward, but comes with several caveats. Excellent reviews exist on this material [10, 11, 12], and these issues will not be reviewed in detail here.

The important conclusion from oversampling theory is that for the spectral noise approximation be applicable, the signal being quantized must look "busy" with respect to the quantization bin size. The intuition for this caveat comes from considering the major assumption underlying

the derivation of the spectral noise: the error between the true signal and the quantized estimate was assumed to be random and uncorrelated from sample point to sample point. As long as the signal traverses several bin widths between samples, then this approximation is roughly justifiable and the noise obeys the general properties predicted by the model [11, 12].

The problem with direct analog-to-digital conversion of the integrator's output is that the quantization noise can easily become the dominant noise source. The noise from the quantization process can be compared to that contributed by the hourglass integrator, and a metric for the required converter resolution derived. This metric,

$$n = \frac{log(\frac{\Delta V}{e_{n,s}\sqrt{12 f_s}})}{log(2)},$$

specifies the required number of bits for a converter with a full-scale range of ΔV, a sampling rate of f_s, and a source noise from the integrator of $e_{n,s}$. The hourglass integrator will have an estimated noise contribution of roughly $50nV/\sqrt{Hz}$ from the thermal noise of the input FETs reacting with the input capacitance of the picoammeter. The sampling rate for the metric will be specified as $100kHz$, to insure sufficient oversampling to implement a 25kHz derivative. For the full scale range of the A/D converter, we will specify 20V, which is a standard value for commercial converters. Using our metric, a 19-bit converter is specified to insure that the quantization noise is not the dominant noise contribution for the picoammeter. Converters of this accuracy and bandwidth are difficult to achieve, and this excessive requirement on converter resolution is the primary motivation for the use of *analog* differentiators in commercial systems.

The hourglass topology's immunity to resets can be exploited, however, to allow for direct quantization of the integrator output. The fact that resets and dead-time are not an issue with the hourglass integrator means that the rate of resets can be increased ten-fold without significant trade-offs in the picoammeter performance. By increasing the rate of resets, the effective feedback capacitor of the integrator can be decreased ten-fold to achieve more gain between the input of the picoammeter and the analog-to-digital converter. The effect of this gain is to increase to the source noise to roughly $500nV/\sqrt{Hz}$, which lowers the required resolution of the conversion process to 15 bits, according to our metric. Analog-to-digital conversion boards with 16 bit resolution at 100kHz are commercially available from several vendors, allowing for

the practical implementation of a digital differentiator.

The outstanding reset properties of the hourglass integrator may be exploited to *increase* the gain of the integrator and thereby allow for direct digitization of the integrator output without adding excessive noise from quantization. To fully exploit this approach, a digital filter must be developed that allows for differentiation and demodulation of the signal waveform.

5.3.2 Standard Bandlimited Digital Filters

The implementation of a discrete derivative filter is straightforward. The instrumentation literature has proposed several designs for band-limited digital differentiators [7, 8], largely for rate-estimation of disk encoder wheels. All of these techniques hinge on extracting filter coefficients using the duality of the Fourier transform. The desired frequency response, F_{ideal}, is shown in Figure 5-11 for a 25kHz bandwidth differentiator with a 100kHz sampling rate (in the discrete domain, this is bounded by $\pm\pi/2$ within the interval $\pm\pi$). The filter values can be derived by recognizing the anti-symmetry of the frequency response and imposing that anti-symmetry on the filter coefficients [7]. The superposition of anti-symmetric filter coefficients yields a series of sine functions in the frequency domain. The digital filter values are then derived from,

$$F_{filt}[n] = \int_{-\pi/2}^{\pi/2} F_{ideal}(f) sin(n \cdot f) df,$$

which is the projection of the filter sinusoids onto the desired frequency response. From this projection, the relative filter coefficients can be derived and an approximate filter constructed as shown in Figure 5-12. The filter illustrated uses two hundred coefficients to approximate the band limited derivative, and the Gibb's phenomena is quite clear[2]. The problem with this filter is the required length, which extends over two hundred samples of the integrator output. The extended length of sampled data represents a significant state history for the filter, which must be eliminated in order to get the desired demodulation propertied from the digital filter.

[2]Gibb's phenomena can be suppressed with an appropriate windowing function, but this will not be developed here.

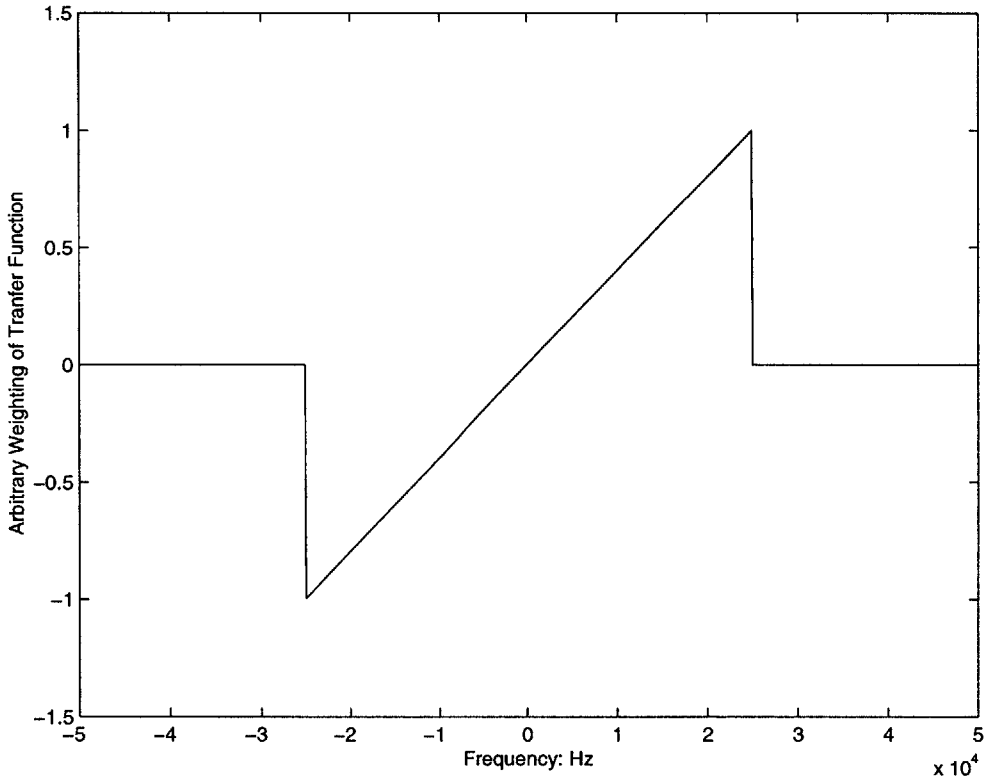

Figure 5-11: The desired filter response for a band-limited differentiator.

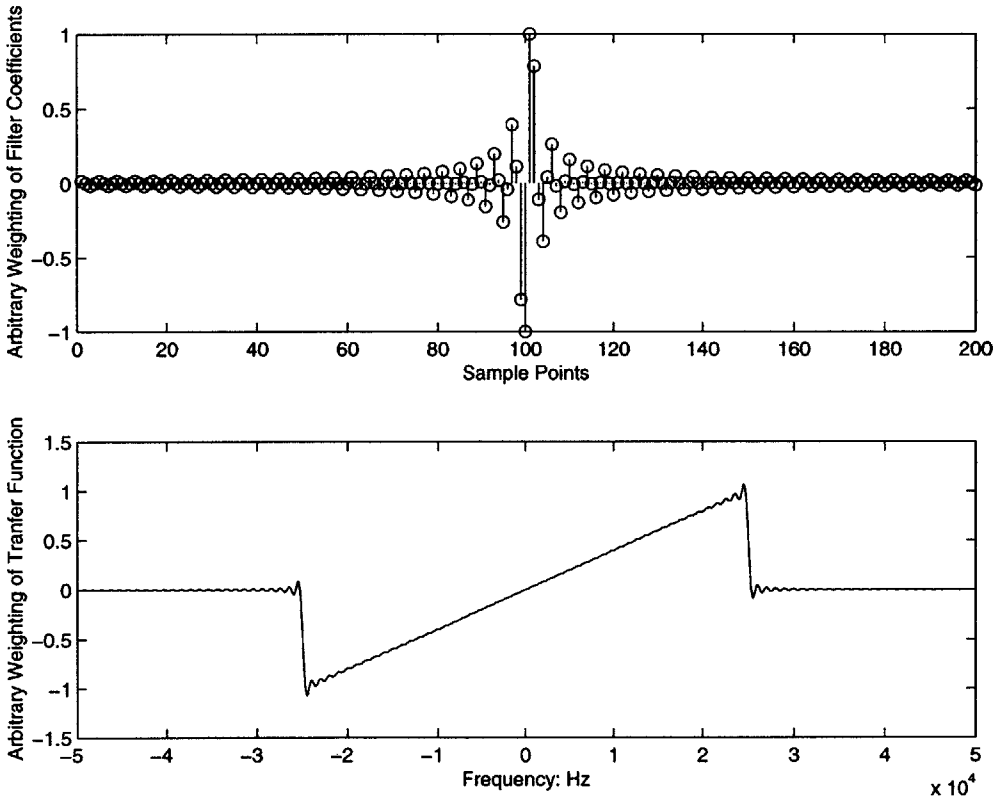

Figure 5-12: The first pass for a digital filter implemented from the first 100 Fourier components of the desired filter response. Top trace: The filter coefficients, derived by the fourier decomposition of F_{ideal}. Bottom trace: The filter's frequency domain behavior, the Gibb's phenomenon is clear at the discontinuous transitions.

5.3.3 Digital Filter for a Demodulating Derivative

The desired differentiation of the signal may be accomplished by deconvolving the derivative component of the filter from the band-limiting elements. To a good approximation, a simple first-difference filter composed of

$$y[n] = x[n] - x[n-1]$$

will provide the required differentiation over the measurement bandwidth, as demonstrated in Figure 5-13; a shorthand for describing this filter is defined as

$$(1 - 1).$$

The low-pass characteristic can then be implemented with a digital lowpass filter *following* the first-difference equation, yielding the net filter characteristic shown in Figure 5-14. The advantage of this algorithm is that the demodulation of the signal waveform is achieved by simply alternating the coefficients in the first-difference filter, e.g. (1 $-$ 1) $\rightarrow$ (1 $-$ 1) $\rightarrow$ (1 $-$ 1), when the integrator changes state. By using only two values of the sampled data, the demodulation process will introduce minimum perturbation to the underlying signal waveform. This method is the closest approach to state-conserving demodulation that we can obtain with a digital system. In addition, if the integrator reset and the data conversion are synchronized with each other, the deterministic transients of the chopper-stabilization may be subtracted from the data, improving the overall performance of the picoammeter. These design considerations are demonstrated in the next section.

5.3.4 Test Waveforms

To demonstrate the functionality of the digital differentiator and hourglass electrometer, a test circuit was constructed to model the nanopore and current fluctuations. This circuit is shown in Figure 5-15; A 5GΩ resistor shunted by 5pF models the nanopore and parasitics for the sensor. A nominal 125mV bias was applied across the "nanopore" to yield 25pA of quiescent current. A capacitive-T network was used to supply a wide bandwidth, 850Hz, 10pA peak-to-peak square

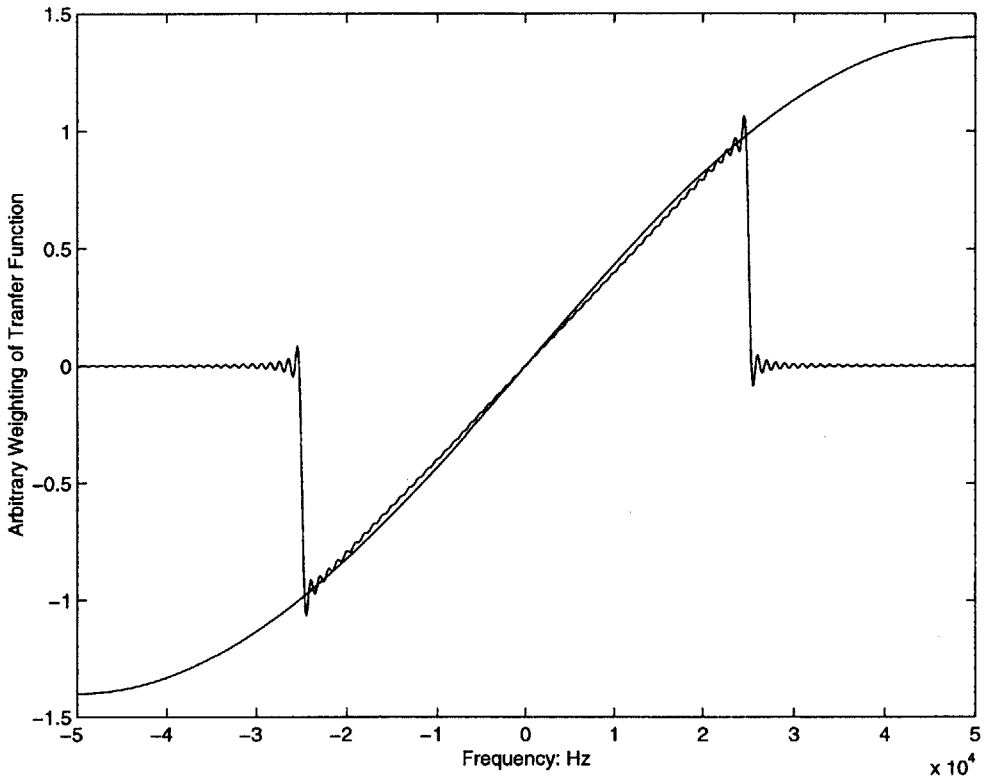

Figure 5-13: In practice, the derivative operation is approximated well by the first difference equation over the measurement bandwidth of interest.

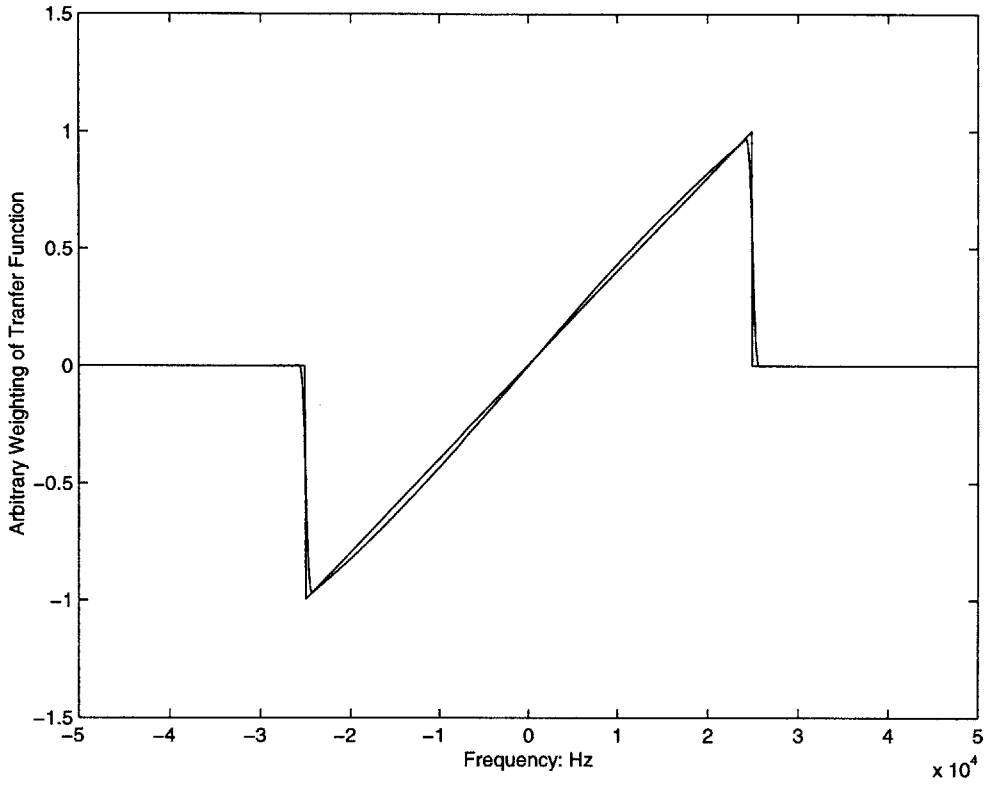

Figure 5-14: Deconvolving the first difference equation and a low-pass filter yields the desired band-limited derivative, with characteristics suitable for low-glitch demodulation.

wave into the picoammeter; the triangle wave was created by an HP33120A function generator. The use of an effective 10fF capacitor was necessitated by the need to supply roughly

$$\Delta V = \frac{I_s}{2C_i f_s} \approx 0.58V,$$

peak-to-peak of signal voltage, which is a reasonable dynamic range for the function generator. The parasitic coupling between the input node and the picoammeter input was measured to be under 1fF, which eliminated concerns of spurious coupling of the signal source and picoammeter input. The output of the hourglass integrator was fed differentially into a x10 buffer amplifier, which yields an effective feedback capacitance of 50fF. The threshold limit of the integrator was readjusted to 0.75V to maintain a peak-to-peak excursion of fifteen volts into the analog-to-digital converter[3]. The output of the differential amplifier was low-pass filtered at 45kHz with a Rockland 8-pole Bessel filter to provide anti-aliasing before digitization.

The trace in Figure 5-16 demonstrates the output of the hourglass input after adjustment of the phase-reversal switch voltage and the chopper stabilization of the picoammeter offset voltage. The transition time is roughly 15mS, as expected for a 25pA current through an effective feedback capacitance of 50fF. The second waveform, Figure 5-17, focuses on the state transition of the hourglass integrator, which will be used to demonstrate the demodulating differentiation obtainable with digital signal processing.

With the integrator output digitized, digital signal processing can restore the proper time/frequency characteristics of the input current signal. The band-limited derivative of the sample in Figure 5-17 is shown in Figure 5-18. The 10pA square wave is fairly distinct, as is the transition of the hourglass integrator. The integrator state transition results in the current signal being effectively inverted from the perspective of the picoammeter, as demonstrated by the waveform in Figure 5-18. The delay on the differentiator output is the result of the lowpass FIR digital filter, which was created using a Hanning window of 256 sample points with a cut-off at 25kHz. The use of a 256-point filter creates a delay of 128 sample points, or 1.28ms at the 100kHz sampling rate shown here.

The demodulation and auto-calibration procedures complete the chopper-stabilization of

[3]This is conservative in practice, but maintained the signal well within the linear region of the National Instruments A/D board and the Rockland filter

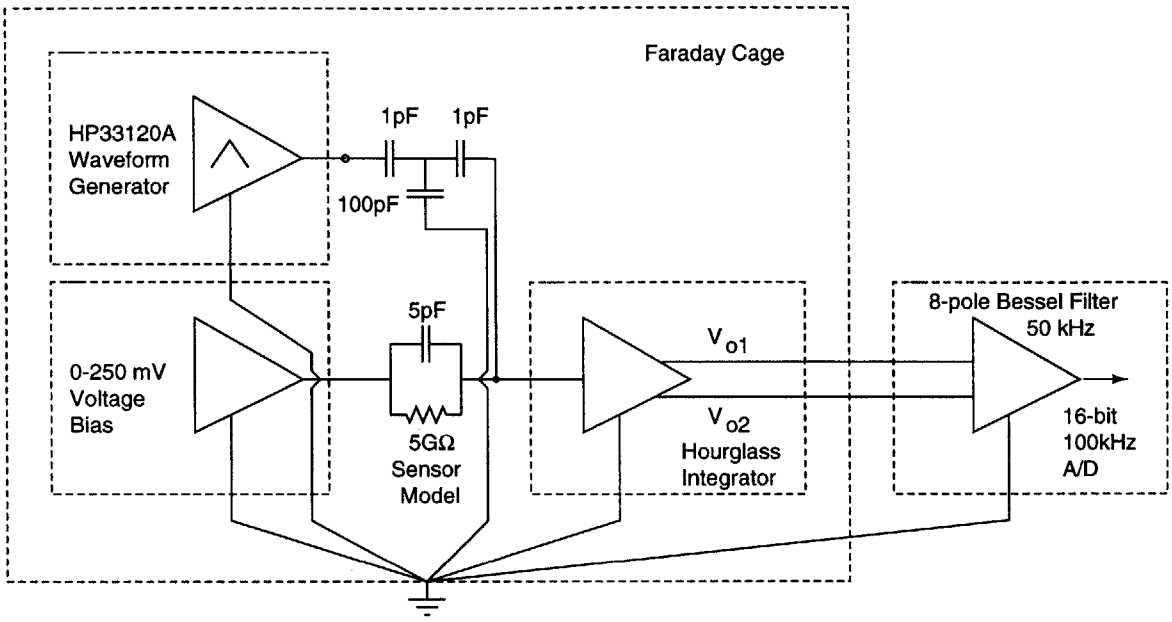

Figure 5-15: The test circuit for studying the picoammeter's performance.

the picoammeter; the MATLAB code for achieving this function is part of Appendix E. The demodulation was achieved by identifying the transitions of the hourglass integrator and multiplying by the proper sign during the first difference calculation. The data can then be processed with the auto-calibration procedure. First, the picoammeter is allowed to float and the relative leakage and bias currents are measured in each state. This establishes a charging rate for each integrator state,

$$\frac{\Delta V_1}{\Delta t} = \alpha_1 I_{l1},$$

$$\frac{\Delta V_2}{\Delta t} = \alpha_2 I_{l2},$$

where α is the integrator gain and I_{lx} is the leakage current. For the data here, the numbers are -3pA in the first integrator state and -1pA in the second integrator state. A known current value, I_{ref}, is then supplied at the input of the picoammeter. Combining this measurement of each state's charging rate,

$$\frac{\Delta V_1}{\Delta t} = \alpha_1 (I_{ref} + I_{l1}),$$

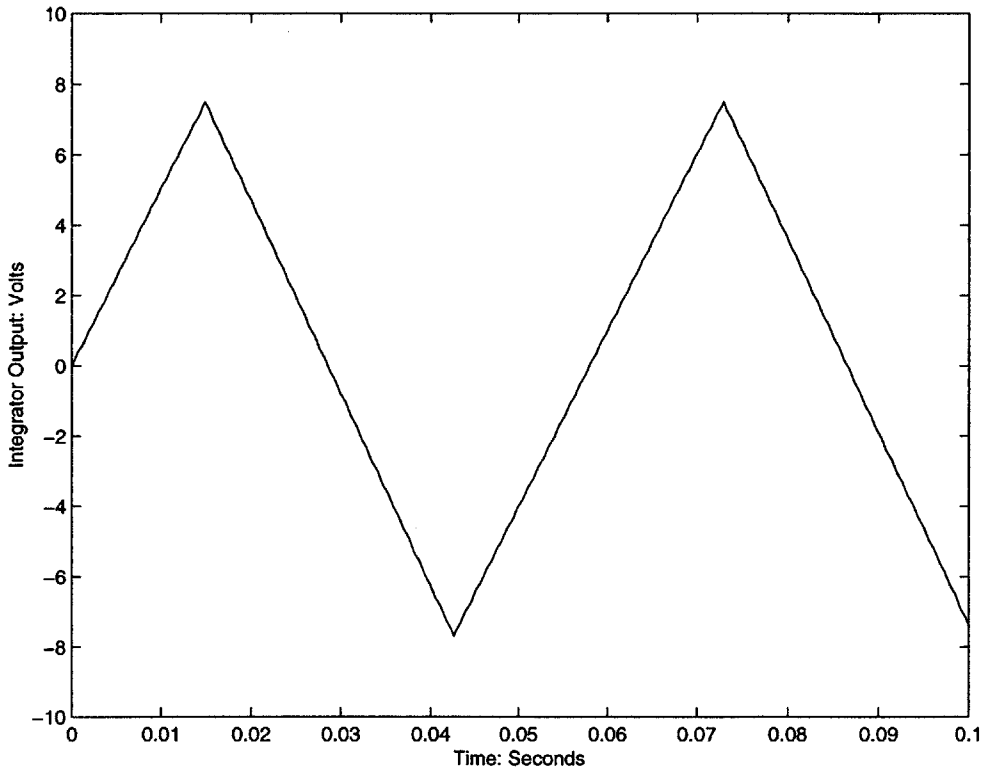

Figure 5-16: The output of the integrator for a 25pA quiescent current, superimposed with a 10pA (peak-to-peak) 850Hz square wave.

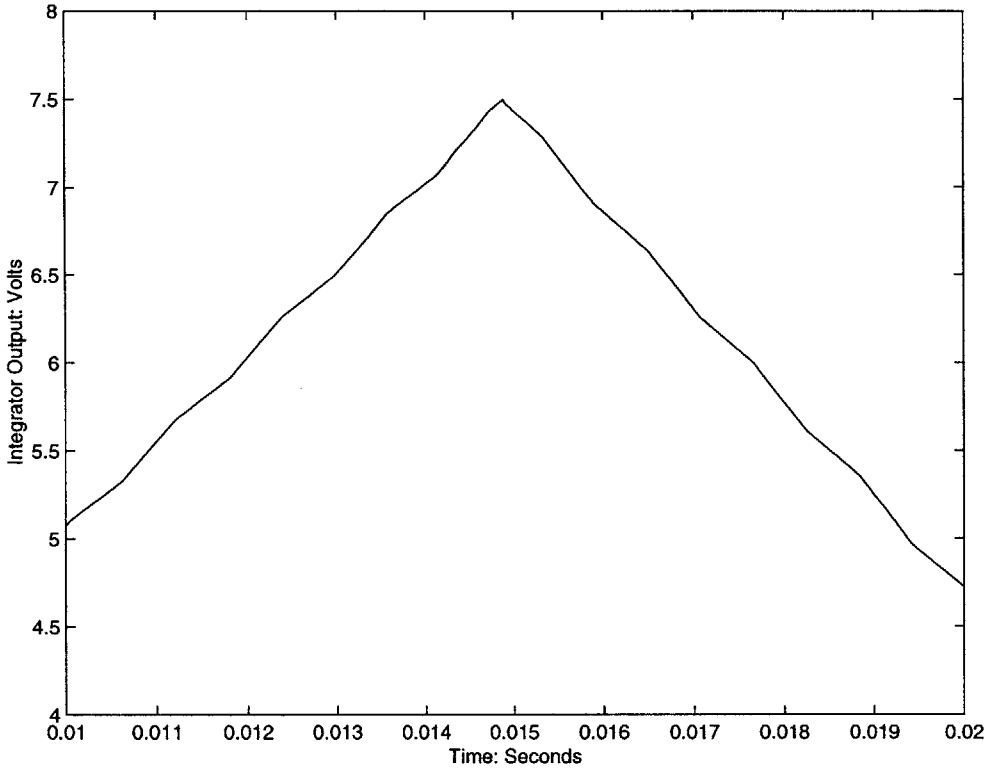

Figure 5-17: Focus on the transition in the integrator.

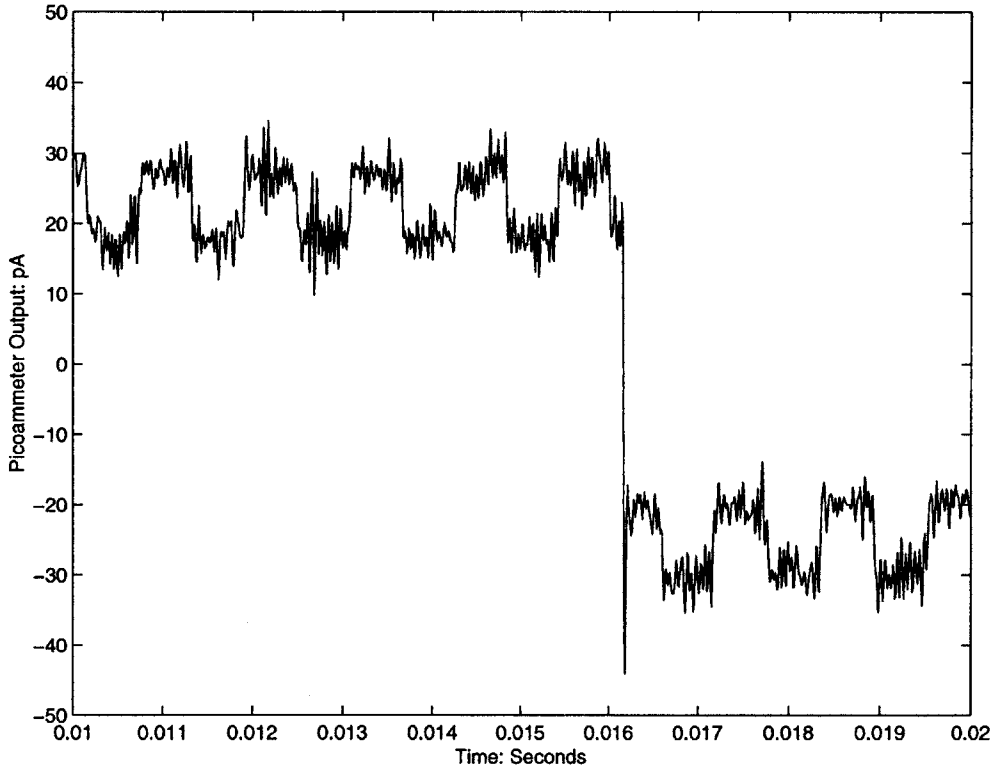

Figure 5-18: The output of the band-limited (25kHz) differentiator, without demodulation of the waveform.

$$\frac{\Delta V_2}{\Delta t} = \alpha_2(I_{ref} + I_{l2}),$$

with the previous measurements, the scale factors and leakage currents for the hourglass integrator may be calculated and the digital filter scaled to compensate accordingly. To address the problem of transition edges, which are still dominated by charge injection, the integrator resets and the data conversion clock are *synchronized.* The deterministic transients of the picoammeter are then averaged, and the resulting waveform subtracted from the data. By performing auto-calibration before filtering, the deterministic transients can be removed to first-order, and the transient perturbation suppressed. The final step in the signal processing is to convolve the wideband derivative signal with the 256-point FIR lowpass filter. As illustrated in Figure 5-19, the auto-calibration procedure almost lowers the transition glitches into the 6pA peak-to-peak noise.

The residual switching transient is caused by the finite bandwidth of the analog-to-digital conversion process. Although this transient is deterministic, it can vary from transition-to-transition based on the instantaneous signal level, so that the averaging technique does not work well. Given the high bandwidth of the integrator, the simplest method to removing this error is to use a faster sampling rate with a higher performance data acquisition system. Otherwise, more sophisticated signal processing can be used to estimate and eliminate this final transient.

5.4 Noise Analysis

The observed noise from the waveform in Figure 5-19 is calculated to be approximately 1.3pA rms for the sample waveform. This noise correlates well with the expected noise distribution, based on estimates from the model nanopore's thermal noise and the high-frequency contributions due to capacitance at the picoammeter input. The expected noise with the model nanopore in Figure 5-15 is ,

$$i_{rms} = \sqrt{2qI_{bias}\Delta f + \frac{4\pi^2}{3}\sum_i e_{n,i}^2 C_{s,i}^2 \Delta f^3},$$

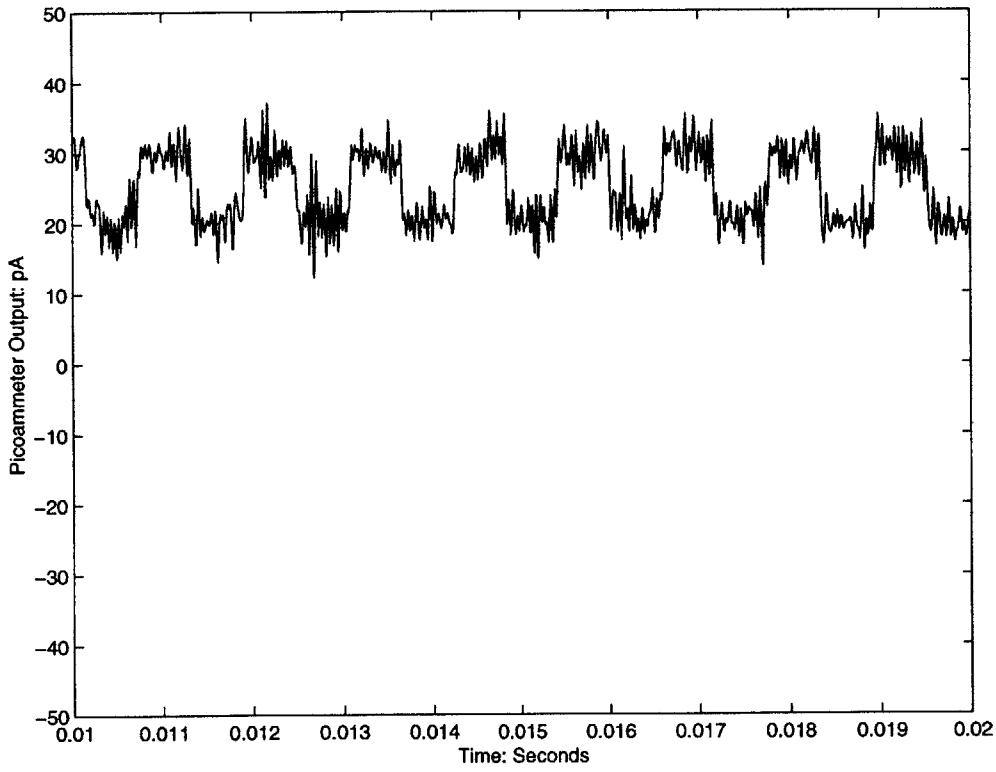

Figure 5-19: The output of the band-limited (25kHz) differentiator, with demodulation and auto-calibration.

where the high-frequency noise includes the contributions from the hourglass integrator and input-referred quantization noise modeling the analog-to-digital conversion. Substitution of measured values for the circuit[4] yields an *expected* rms noise current of 1.15pA. This is in good agreement with the experimental observations, and the minor discrepancy most likely arises from errors in measuring parasitic capacitance at the input of the picoammeter.

The correlation between the measured noise performance and expectation is also demonstrated by the spectral power of the waveform illustrated in Figure 5-20. The 850Hz test square wave is clearly detected by its fundamental and harmonics. The high frequency noise shows the general property of rising as f^2 with frequency, and intercepts the white noise at a critical frequency of roughly $5kHz$, as estimated by

$$f_{critical} \approx \sqrt{\frac{k_b T}{\pi^2 e_n^2 C_i^2 R_m}},$$

where R_m is the 5 $G\Omega$ model resistor. The low frequency noise suggests the presence of a Lorentzian noise source as discussed in chapter three. This excess noise most likely arises from a defect in one of the input JFETs. The magnitude of this excess noise, however, is low enough to have little net effect on the total rms noise of the wideband current measurement. The asymptotic low-frequency white noise of approximately $3 - 4 \cdot 10^{-30} A^2/Hz$ is close to the predicted thermal noise contribution of the $5G\Omega$ sensor model, $3.2 \cdot 10^{-30} A^2/Hz$. The general matching of the spectral characteristics of the picoammeter output with theoretical calculations provides supporting evidence on the functionality of the picoammeter.

The general performance of the chopper-stabilized picoammeter allows for the detection of current fluctuations with sufficient bandwidth and low noise to be useful for the nanoscale Coulter counter. The noise performance of this prototype is primarily limited by the switch capacitance of the MAX4526 used to chopper-stabilize the integrator. By fabricating the switches on the same substrate as the nanopore and interface electronics, the performance of this topology could be dramatically improved. Even with this current design trade-off, the noise performance of the prototype picoammeter is quite good. The state-of-the-art picoammeter by Axon Instruments, the Axopatch 200B, has a *specified* rms noise of 100 fA in a 5 kHz band-

[4] $e_n \approx 2nV/\sqrt{Hz}, C_s approx 20 - 25pF$, input-referred quantization noise $\approx 1.9nV/\sqrt{Hz}$, and $\Delta f = 25kHz$.

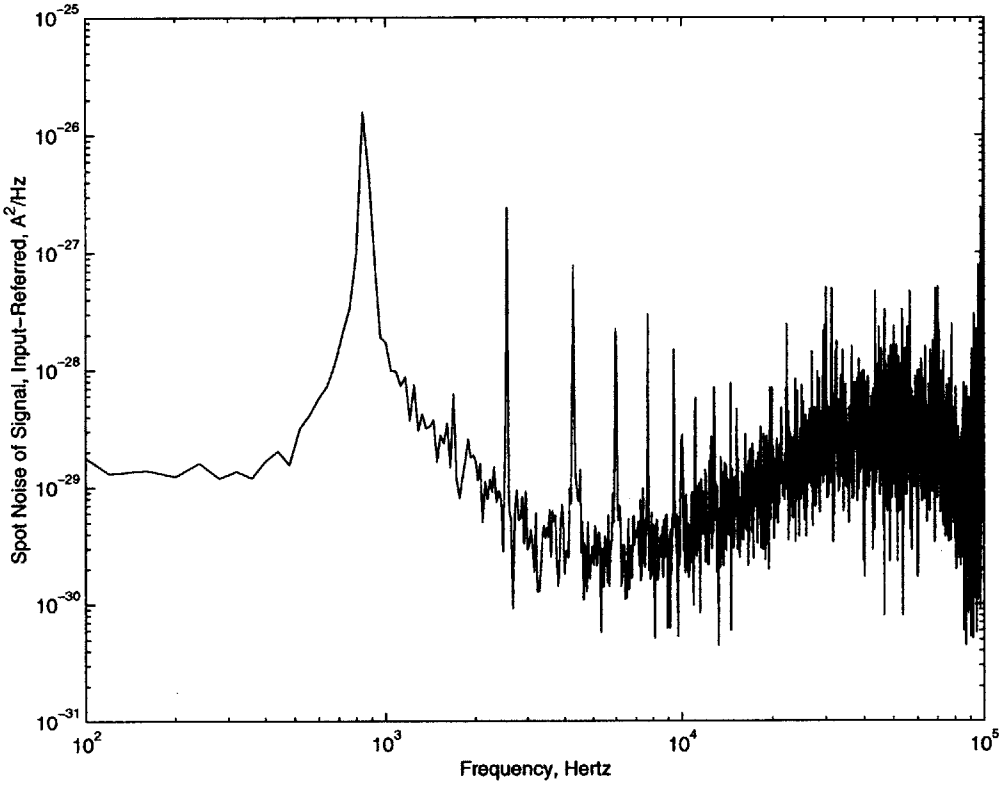

Figure 5-20: The output power spectrum of the picoammeter. The peaks represent the harmonics of the square wave excitation, the fundamental is at 850Hz. The low frequency noise seems to have minor excess noise with a Lorentzian profile, while the high frequency noise shows f^2 frequency weighting characteristic of the thermal noise and input capacitance. The intercept with the white noise is in the region of 5kHz, as predicted by the modeling.

width at room temperature. The prototype chopper-stabilized integrator has a similar noise specification of 125 fA in the same bandwidth at room temperature. In a 25 kHz measurement bandwidth, the noise performance of these two topologies is essentially identical. The lack of capacitance from the input switches of the chopper-stabilized integrator is offset by the compensation circuitry required for addressing discontinuous reset transients. By using a novel application of chopper-stabilization to implement a quasi-continuous integrating picoammeter, a circuit that yields state-of-the-art noise and bandwidth performance can be constructed in a relatively straightforward manner.

5.5 Chapter Summary

This chapter developed the second major component of the chopper-stabilized picoammeter: the demodulating differentiator. Two approaches were described in detail. An analog differentiator was designed that obtains excellent noise and bandwidth characteristics by exploiting a current conveyor topology. This design is highly suited for wide bandwidth measurements, and may prove especially useful in future nanopore applications when the channel and interface electronics are integrated for *de novo* sequencing.

A digital approach to differentiation was also implemented. This method exploits the quasi-continuous operation of the hourglass topology to substantially increase the gain of the integrator. Increased gain allows for the direct digitization of the integrator output, without compromising noise performance due to quantization. In addition, by synchronizing the integrator modulation with the A/D acquisition clock, an auto-calibration procedure could be implemented that removed the residual deterministic transients resulting from the chopper-stabilization procedure. The total noise for a model nanopore sensor was determined to be roughly 1.3pA rms in a 25kHz bandwidth; this noise performance is suitable for the sequence recognition strategies developed in chapter two, and is the comparable to the performance of state-of-the-art commercial picoammeters. The excellent correlation between noise theory and measurement also suggests that future scaling of the picoammeter should yield the predicted benefits of improved noise.

Chapter 6

Thesis Summary and Future Directions

6.1 Summary of Thesis Contributions

The goal of this thesis is the development of a nanoscale Coulter counter for the direct electrical detection of specific genetic sequences. The general approach used to accomplish sequence recognition is a refinement of the resistive pulse technique. To help develop the techniques and instrumentation explored in this thesis, the biological toxin, alpha hemolysin, was implemented as "prototype" limiting aperture. With the practical knowledge gained from using a toxin channel, a general model for the nanopore as a low-noise sensor was developed. With this model, two broad goals were achieved. The first achievement was the development of novel genetic recognition strategies that exploit the properties of the nanopore within the limitations imposed by DNA structure and existing channel geometries. The second achievement was the design and prototyping of novel interface picoammeter for the measurement of the current fluctuations associated with DNA translocation through a nanopore.

6.1.1 Novel Genetic Detection Strategies with an Nanopore

Observations of polymer translocation through a toxin channel have revealed several technical difficulties related to the originally proposed sequencing of DNA. These limitations arise from

several issues, including the limited resolution of the channel to single base physical differences, the convolution properties of the nanopore, the sensitivity to DNA secondary structure, and the rapid rate of DNA translocation. Each of these drawbacks undermines the utility of the Coulter technique for *de novo* sequencing with existing state-of-the-art nanopore technology. The translocation of DNA through a nanopore does exhibit a highly useful trait, however; the length of a DNA molecule can be characterized based on the duration of the translocation event. The resolution to polymer length can be exploited to detect specific genetic sequences within DNA.

Two novel methods were explored in this thesis that demonstrate the ability to recognize genetic sequences with a nanopore. The first approach used the limiting aperture of the toxin to sense the presence of double-stranded versus single-stranded DNA as a target probe hybridizes with its matching template. A series of experiments was performed that clearly demonstrated the ability to recognize genetic sequences by monitoring the interactions between probes and target strands. With proper biasing of the environmental conditions of the fluid bath, this method was able to provide the single base sensitivity necessary for detection of many genetic mutations. Although this method represents the first direct electrical detection of genetic sequence information, it does suffer from the major drawback of requiring large sample amounts.

A refinement of the basic hybridization technique was proposed and *conceptually* demonstrated that uses the sizing capability of the pore to detect the *transformation* of short DNA primer strands to longer DNA polymers with the polymerase chain reaction. Although this method requires an artificial nanopore in practice, it maintains single-base sequence resolution with the additional benefits of single molecule sensitivity and positive controls to prevent false sequence detection. Both of these methods allow for direct electrical detection of genetic sequence information without the need for external radioactive or fluorescent markers.

6.1.2 A Novel Picoammeter Topology

The exploration of novel approaches to picoammeter design is motivated by several potential applications of the nanoscale Coulter counter. The detection of hybridization events with single-base sensitivity requires the detection of picoampere fluctuations through the channel with a bandwidth of roughly 25 kHz. The development of new picoammeter topologies is also

Specification	*Requirement*	*Prototype*
Bandwidth	25 kHz	25 kHz
Dead-Time	Minimize $< 15\mu s$	$\approx 10\mu s$
Voltage Bias	100mV nominal	0-250mV
Voltage Limit	300mV clamp	$< 10\ \mu V$
RMS noise	1.25 pA	$\approx$ 1.25 pA

Table 6.1: Summary of prototype picoammeter specifications.

critical to the future of *de novo* sequencing with a nanopore. The high-frequency detection of base sequences is largely limited by the capacitance of the source and interface circuit. The reduction of this capacitance, coupled with the need to overcome the practical limitations of the toxin channel, motivates the fabrication of a silicon nanopore. To yield the full benefits of an integrated pore, the interface electronics must also scale to maintain a low shunt capacitance at the input to the current amplifier.

The exploration of current measurement techniques motivated the chopper-stabilized picoammeter. This picoammeter topology applies a novel stabilization strategy to obtain low-noise, wide bandwidth current measurements suitable for nanopore measurements. To successfully design this instrument, a stabilized integrator and differentiator were designed and prototyped.

Hourglass Integrator

By modifying a floating gyrator topology, a circuit that allows for quasi-continuous integration of a waveform without the need for external charge compensation was created. To implement this topology successfully, a hybrid low-noise operational amplifier (LNA) was constructed to meet the demanding specifications of the picoammeter circuit. In particular, a novel approach to offset-nulling was developed that avoided compromising the $10G\Omega$ input impedance of the picoammeter by exploiting the state properties of the gyrator. The current steering for the integrator was achieved with a phase-reversal switch that was biased to reduce the charge injection from switching to under 5fC–three orders of magnitude below the device's general specification. A global feedback circuit maintains the integrator within its linear operating regime over six decades of current, without the need for external clock adjustment. The properties

of the hourglass integrator were demonstrated by a series of test waveforms that illustrate the state-conserving principles upon which this design is based.

Demodulating Differentiator

To complete the chopper-stabilized picoammeter topology, some mechanism must effectively "unwrap" the integrator's output waveform with demodulating differentiation. Two approaches were developed in detail. An analog differentiator was shown to obtain excellent noise and bandwidth characteristics by exploiting a modified current conveyor topology. This design is suited for wide bandwidth measurements such as *de novo* sequencing with future synthetic nanopores.

A digital approach to differentiation was also implemented that is suitable for the sequence recognition strategies explored in this thesis. This technique leverages the quasi-continuous operation of the hourglass topology to substantially increase the gain of the integrator. Increased gain allows for the direct digitization of the integrator output, without compromising noise performance due to quantization. A digital filter suitable for state-conserving, demodulating differentiation was developed to unwrap the signal waveform.

By synchronizing the integrator modulation with the A/D acquisition clock, an auto-calibration procedure was also implemented to remove the deterministic transients resulting from the chopper-stabilization. The total noise for the resulting picoammeter was determined to be roughly 1.3pA rms in a 25kHz bandwidth; this noise performance is suitable for the sequence recognition strategies developed in chapter two, and is the comparable to the performance of state-of-the-art commercial picoammeters. The excellent correlation between noise theory and measurement also suggests that future scaling of the picoammeter should yield the predicted benefits of improved noise.

6.2 Future Directions

de novo Sequencing

Future sequencing goals for the project require increased bandwidth to help detect the presence of individual translocating bases. The hourglass topology is suitable for this enhanced specifi-

cation, but will require integration with the nanopore sensor to reduce the sensor capacitance.

Integration of the interface circuitry would significantly improve the noise performance of the nanopore Coulter counter. Working with the nanopore model developed in chapter three, the expected rms noise of a nanopore sensor will be

$$i_{rms} = 2\pi\sqrt{4k_bT\epsilon_r^2\epsilon_o^2 4\pi/3\rho L_o ln(\frac{R_o}{R_i})\Delta f^3} \approx 0.5\ pA,$$

for the typical parameters expected for a silicon pore[1] and a 150kHz measurement bandwidth. The shot noise for the channel current,

$$i_{rms} = \sqrt{2qI\Delta f},$$

with 10pA of quiescent will be 0.49 pA rms, yielding a total sensor rms noise of roughly 0.71 pA. The noise from the interface circuitry,

$$i_{rms} = \sqrt{(2\pi)^2 C_s^2 e_n^2 f^3/3},$$

will contribute an additional noise of approximately 0.45 pA rms as the the interface electronics are scaled to the order of 0.1 pF–roughly an order of magnitude smaller than existing nanopore capacitances. The total expected rms noise for the measurement is then 0.87 pA rms; using our metric from Appendix A, this channel noise yields an approximate physical resolution of 0.5 $\mathring{A}$, which is approximately the size difference between the nucleic acids.

Current measurements with this bandwidth and noise performance further motivate the chopper-stabilized picoammeter technique. Standard integration topologies would require a discontinuous reset every 1-10ms, which can result in excessive instrument deadtime and reset transients. Resistive feedback techniques are practically impossible; a measurement with this noise specification requires an effective 10 $G\Omega$ resistor. In addition to the bandwidth and excess noise issues associated with this device, the use of a *discrete* resistor would compromise the 0.1 pF capacitance at the sensor interface, significantly reducing the noise performance of the Coulter counter. This parasitic problem can not be addressed by simply fabricating an

[1] $L_o \approx .1cm, R_o \approx .01cm, R_i \approx 1nm, \rho \approx 10\Omega - cm, \epsilon_r \approx 7.5$

integrated resistor given the relatively large scale of the device with respect to typical processing parameters.

Although the benefits of this topology for wide bandwidth current measurements can not be fully demonstrated until a silicon nanopore can be fabricated, the general scaling properties of the chopper-stabilized picoammeter topology scale correctly for enhanced noise and bandwidth performance with integrated sensors.

6.2.1 Current Clamping with the Hourglass Integrator

A significant goal for biophysical instrumentation development is a "universal" interface circuit that yields both excellent voltage and current clamp measurements with the same underlying topology. Essentially all existing topologies have required the optimization of the interface circuit for either voltage or current clamp measurements, sacrificing the performance characteristics of the "dual" measurement. Recalling the circuit in Figure 6-1, the floating gyrator can also be used to force a *current* through the sensor load, and the resulting voltage measured at the opposing input node. The topological changes needed to achieve this measurement are shown in Figure 6-2, where the voltage across the load is tapped from the central node of the gyrator, and the current flow through the load can be inferred from the differential voltage drop across the opamp outputs. Although this current clamp scheme was not pursued as part of this thesis due to the limitations described in Appendix C, it would make a useful addition to a general instrumentation system developed for bio-electrical measurements.

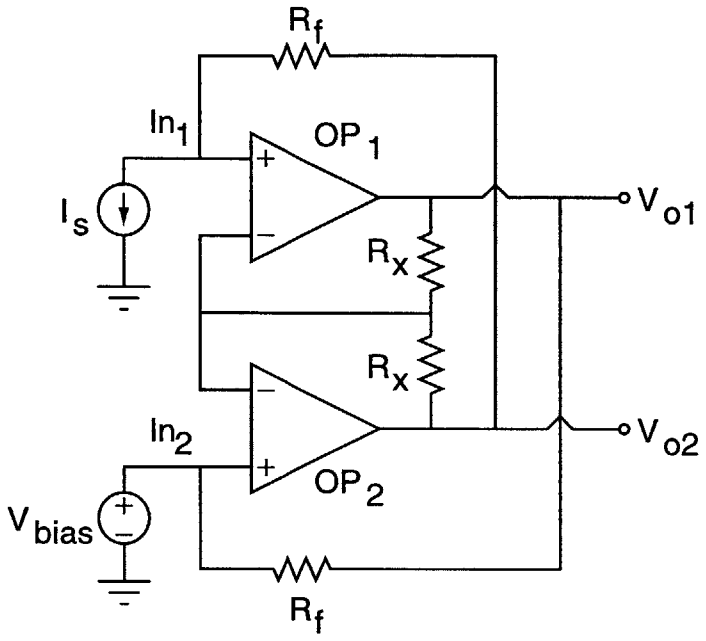

Figure 6-1: Recalling the floating gyrator circuit.

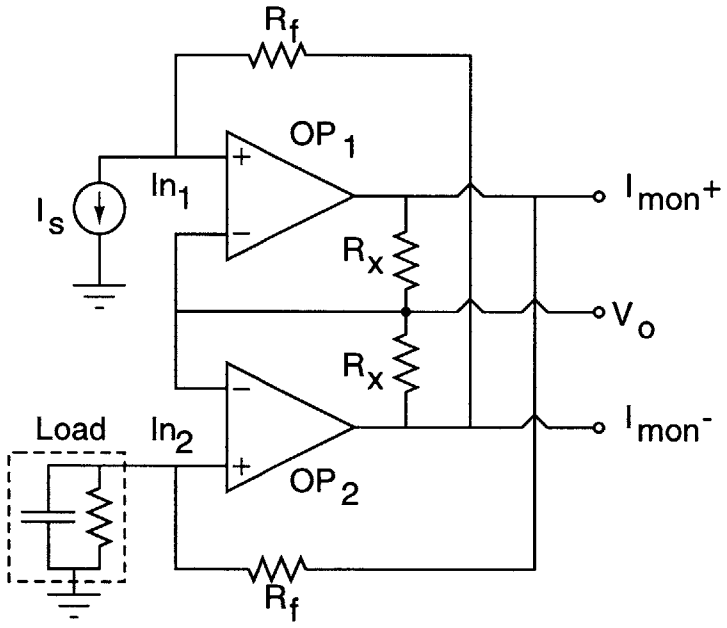

Figure 6-2: Converting the floating gyrator into a *Current Clamp.*

Bibliography

[1] Andersen, O., "Sequencing and the Single Channel," Biophysical Journal, Vol. 77, 2899-2901, 1999.

[2] Lee, T., *The Design of CMOS Radio-frequency Integrated Circuits,* Cambridge University Press, Cambridge, 1998.

[3] Johns, D. and Martin, K., *Analog Integrated Circuit Design,* Wiley, 1997.

[4] rev. by Ed Oxner, *Designing with Field-effect Transistors,* McGraw-Hill, New York, 1990.

[5] Roberge, J., *Operational Amplifiers : Theory and Practice,* Wiley, New York, 1975.

[6] Grebene, A., *Bipolar and MOS Analog Integrated Circuit Design,* Wiley, New York, 1984.

[7] Usui, S. and Amidror, I., "Digital Low-pass Differentiation for Biological Signal Processing," IEEE Transactions on Biomedical Engineering, Vol. BME-29, No. 10, 686-693, 1982.

[8] Vainio, O., Renfors, M., and Saramaki, T., "Recursive Implementation of FIR Differentiators with Optimum Noise Attenuation," IEEE Transactions on Instrumentation and Measurement, Vol. 46, No. 5, 1202-1207, 1997.

[9] Kavanagh, R. and Murphy J., "The Effects of Quantization Noise and Sensor Nonideality on Digital Differentiator-based Rate Measurement," IEEE Transactions on Instrumentation and Measurement, Vol. 47, No. 6, 1457-1463, 1998.

[10] Hauser, M., "Principles of Oversampling A/D Conversion," Journal Audio Eng. Soc., Vol. 39, No. 1/2, 1991.

[11] Potzick, J., "Noise Averaging and Measurement Resolution," Review of Scientific Instruments, Vol. 70, No. 4, 2038-2040, 1999.

[12] Gray, R., "Quantization Noise Spectra," Transactions on Information Theory, Vol. IT-36, 1220-1244, 1990.

[13] U.S. Patent Application , "A Method for Controlling Nanofabrication," submitted 1999.

[14] Lev A., *et. al.*, "Switching of Ion Current in Narrow Pores," Proceedings of the Royal Society, Vol. 252, 187-192, 1993.

[15] Fonstad, C., *Microelectronic Devices and Circuits,* McGraw-Hill, New York, 1994.

[16] Zambuto, M., *Semiconductor Devices,* McGraw-Hill, New York, 1989.

[17] Innis, M., Gelfand, D., Sninky J., and White, T., "PCR Protocols: A Guide to Methods and Applications," Academic Press, London, 1990.

[18] Pease, R., *Troubleshooting Analog Circuits,* Butterworth-Heinemann, 1991.

[19] Proceedings of the National Academy of Sciences, Vol. 83, 3746-3750, 1986.

[20] Udou, T. and Ichikawa, Y., "Effect of Sodium Chloride on the Activity and Production of Staphylococcal Exonuclease," Journal of General Microbiology, Vol. 116, 69-74, 1980.

[21] Deamer, D. and Akeson, M., "Nanopores and Nucleic Acids: Prospects for Ultrarapid Sequencing," Trends in Biotechnology, 2000.

[22] Rappolee, D. *et. a;.*, "Wound Macrophages Express TGF-alpha and Other Growth Factors in-Vivo", Science, Vol. 241, 708-712, 1988.

[23] Unpublished Data and Personal Correspondence, Dr. Amit Meller, Rowland Institute for Science.

[24] Bunt, G., "Reducing Stray Capacitance on a Signal Line," Electronic Engineering, Vol. 51, No. 618, 31, 1979.

[25] Cantor, C., *Biophysical Chemistry, Part 1,* W. H. Freeman, San Franscisco, 1980.

[26] Cantor, C., *Biophysical Chemistry, Part 2*, W. H. Freeman, San Franscisco, 1980.

[27] Lauger, "Shot Noise in Ion Channels," Biochim. Biophy. Acta, Vol. 413, 1-10, 1975.

[28] Jeans, J. H., *The Mathematical Theory of Electricity and Magnetism*, The University Press, Cambridge, 1925.

[29] Mak, D. and Webb, W., "Conductivity Noise in Transmembrane Ion Channels Due to Ion Concentration Fluctuations Via Diffusion," Biophysical Journal, Vol. 72, 1153-1164, 1997.

[30] Akinlaja, J. and Sachs, F., "The Breakdown of Cell Membranes by Electrical and Mechanical Stress," Biophysical Journal, Vol. 75, 247-254, 1998.

[31] Lubensky, D. and Nelson, D., "Driven Polymer Translocation through a Narrow Pore," Biophysical Journal, Vol. 77, No. 4, 1824-1838, 1999.

[32] Klemic, K. *et. al.*, "Quartz Microchip Partitions for Improved Planar Lipid Bilayer Recording of Single Channel Currents," Biophysical Journal, Vol. 78, No. 1, 1575, 2000.

[33] Machlup, S., "Noise in Semiconductors: spectrum of a two-parameter random signal," Journal of Applied Physics, Vol. 25, 341-343, 1954.

[34] Patranabis, D. and Ghosh, D., "Integrators and Differentiators with Current Conveyors," IEEE Transactions on Circuits and Systems, Vol. CAS-31, No.6, 567-569, 1984.

[35] Lee, J-L and Liu, S-I, "Dual-input RC Integrator and Differentiator with Tuneable Time-constants Using Current Feedback Amplifiers," Electronics Letters, Vol. 35, No. 22, 1910-1911, 1999.

[36] Lee, J-L and Tsao, H-W, "True RC Integrators Based on Current Conveyors with Tuneable Time-constants Using Active Control and Modified Loop Technique," IEEE Transactions on Instrumentation and Measurement, Vol. 41, No. 5, 709-714, 1992.

[37] Sarker, U., Sanyal, S., and Nandi, R., "A High-Quality Dual-Input Differentiator," IEEE Transactions on Instrumentation and Measurement, Vol. 39, No. 5, 726-729, 1990.

[38] Wegmann, G., Vittoz, E., and Rahali, F., "Charge Injection in Analog MOS Switches," IEEE Journal of Solid-State Circuits, Vol. SC-22, No. 6, 1987.

[39] Castello, R. and Gray, P.R., "Performance Limitations in Switched-Capacitor Filters," IEEE Transactions on Circuits and Systems, Vol. CAS-32, No. 9, 1985.

[40] Dow, P.C., "An Analysis of Certain Errors in Electronic Differential Analyzers, II. Capacitor Dielectric Absorption," IRE Transactions on Electronic Computers, March 1958.

[41] Wright, J.N., *A Method of Compensating for Dielectric Absorption in Capacitors,* M.S. Thesis, MIT, 1978.

[42] Pease, B., "Understand Capacitor Soakage to Optimize Analog Systems," www.national.com/rap/Application.

[43] Roberge, J.K., class notes, 6.331 Advanced Circuit Techniques.

[44] Goulding F.S., "Some Aspects of Detectors and Electronics for X-ray Fluorescence Analysis," Nuclear Instruments and Methods, Vol. 142, 213-223, 1977.

[45] Lakatos, T., Hegyesi, G., and Kalinka, G., " A Simple Pulsed Drain Feedback Preamplifier for High Resolution High Rate Nuclear Spectroscopy," Nuclear Instruments and Methods in Physics Research A, Vol. 378, 583-588, 1996.

[46] Fazzi, A., Jalas, P., Rehak, P., and Holl, P., "Charge-sensitive Amplifier Front-end with an nJFET and a Forward-biased Reset Diode," IEEE Transactions in Nuclear Science, Vol. 43, 3218-3222, 1996.

[47] Bertuccio, G., Rehak, P., and Xi, D., "A Novel Charge Sensitive Preamplifier without the Feedback Resistor," Nuclear Instruments and Methods in Physics Research A, Vol. 326, 71-76, 1993.

[48] Nashashibi, T., and Sangsingkeow, P., "Integrated FET and Charge Reset Device for Gamma Spectrometers," IEEE Transactions on Nuclear Science, Vol. 38, No. 2, 77-82, 1991.

[49] Landis, D.A., et. al., "Transistor Reset Preamplifier for High Rate High Resolution Spectroscopy," IEEE Transactions on Nuclear Science, Vol. NS-29, No. 1, 619-624, 1982.

[50] De Geronimo, G., Bertuccio, G., and Longoni, A., "A Low-Noise Wide-Band Transimpedance Amplifier for Current Noise Spectra Measurements," Review of Scientific Instruments, Vol. 67, No. 7, 2643-2647, 1996.

[51] Bertuccio, G., Fasoli, L., Fiorini, C., and Sampietro, M., "Spectroscopy Charge Amplifier for Detectors with Integrated Front-End FET," IEEE Transactions on Nuclear Science, Vol. 42, No. 4, 1399-1405, 1995.

[52] Acharya, Y.B., and Vyavahare, P.D., "Response Time of a Light Emitting Diode-Logarithmic Electrometer," Review of Scientific Instruments, Vol. 69, No. 2, 595-598, 1998.

[53] Ericson, M.N., Falter, K.G., and Rochelle, J.M., "A Wide-Range Logarithmic Electrometer with Improved Accuracy and Temperature Stability," IEEE Transactions on Instrumentation and Measurement, Vol. 41, No. 6, 968-973, 1992.

[54] Shaw, S-Y., and Chang, R-S., "A Novel Wide Range Electrometer with Quasilinear Output," Review of Scientific Instruments, Vol. 68, No. 10, 3917-3919, 1997.

[55] Rajput, S.S., and Garg, S.C., "A High Resolution Autogain Ranging Linear Electrometer Amplifier," Review of Scientific Instruments, Vol. 67, No. 2, 609-611, 1996.

[56] Bordoni, F., and Pallottino, G.V., "Low Noise Preamplifier for Gravitational Research," Review of Scientific Instruments, Vol. 48, No. 7, 757-761, 1977.

[57] Jersch, J. et. al., "Wide-band Low-noise Tunnel Current Measurements in Laser Assisted Experiments," Review of Scientific Instruments, Vol. 70, No. 7, 3173-3176, 1999.

[58] Heer, R., Eder, C., Smoliner, J., and Gornik, E., "Floating Electrometer for Scanning Tunneling Microscope Applications in the Femptoampere Range," Review of Scientific Instruments, Vol. 68, No. 12, 4488-4491, 1997.

[59] Ashton, G.R., Epstein, K.A., "High-speed Electrometer for Use in Voltage-mode Xerographic Time-of-Flight Measurements," Review of Scientific Instruments, Vol. 57, No. 7, 1396-1398, 1986.

[60] Band, A., Unguris, J., "Optically Isolated Current-to-Voltage Convertor for Electron Optics System," Review of Scientific Instruments, Vol. 68, No. 1, 250-251, 1997.

[61] Demming, F., Dickmann, K., and Jersch, J., "Wide Bandwidth Transimpedance Preamplifier for a Scanning Tunneling Microscope," Review of Scientific Instruments, Vol. 69, No. 6, 2406-2408, 1998.

[62] Jefferts, S.R., Walls, F.L., " A Very Low-noise FET Input Amplifier," Review of Scientific Instruments, Vol. 60, No. 6, 1194-1196, 1988.

[63] Netzer, Y., "The Design of Low-Noise Amplifiers," Proceedings of the IEEE, Vol. 69, No. 6, 728-741, 1981.

[64] Leach, W.M., "Fundamentals of Low-noise Analog Circuit Design," Proceedings of the IEEE, Vol. 82, No. 10, 1515-1538, 1994.

[65] Mothchenbacher, *Fundamentals of Low-Noise Circuit Design,* 1995.

[66] Van Der Ziel, A., "Noise in Solid-State Devices and Lasers," Proceedings of the IEEE, Vol. 58, No. 8, 1178-1206, 1970.

[67] Erdi, G., "Amplifier Techniques for Combining Low Noise, Precision, and High-Speed Performance," IEEE Journal of Solid-state Circuits, Vol. SC-16, No. 6, 653-661, 1981.

[68] Roberge, J.K., *Operational Amplifiers: Theory and Practice,* Wiley and Sons, 1975.

[69] Hamill, O.P., Marty, A., Neher, E., Sakmann, B., and Sigworth, F., "Improved Patch-Clamp Techniques for High-Resolution Current Recording from Cells and Cell-free Membrane Patches," Pflugers Arch., Vol. 391, 85-100, 1981.

[70] Wittwer, C. T., Herrmann, M. G., Moss, A. A. and Rasmussen, R.P., "Continuous Fluorescence Monitoring of Rapid Cycle DNA Amplification," BioTechniques, Vol. 22, 130-138, 1997.

[71] Tyagi, S. and Kramer, F.R., "Molecular Beacons: Probes that Fluoresce upon Hybridization," Nature Biotechnology, Volume 14, 303-308, 1996.

[72] Wonderlin, W.F., Finkel, A. and Fench, R.J., "Optimizing Planar Lipid Bilayer Single-Channel Recordings for High Resolution with Rapid Voltage Steps," Biophysical Journal, Vol. 58, 289-297, 1990.

[73] Bezrukov, S.M. and Kasianowicz, J.J., "Current Noise Reveals Protonation Kinetics and Number of Ionizable Sites in an Open Protein Ion Channel," Physical Review Letters, Vol. 70, N0. 15, 2352-2355.

[74] Kazionowicz, J.J., and Bezrukov, S.M., "Protonation Dynamics of the α-Toxin Ion Channel from Spectral Analysis of pH-Dependent Current Fluctuations," Biophysical Journal, Vol. 69, 95-105, 1995.

[75] Menestrina, G., "Ionic Channels Formed by *Staphylococcus aureus* Alpha-Toxin: Voltage-Dependent Inhibition by Divalent and Tri-Valent Cations," Journal of Membrane Biology, Vol. 90, 177-190, 1986.

[76] Niles, W.D., Levis, R.A., and Cohen, F.S., "Planar Bilayer Membranes Mader From Phospholipid Monolayers Form by a Thinning Process," Biophysical Journal, Vol. 53, 327-335.

[77] Montal M. and Meuller, P., "Formation of Bimolecular Membranes from Lipid Monolayers and a Study of Their Electrical Properties," Proceedings of the National Academy of Sciences, Vol. 69, No.12, 3561-3566.

[78] Korchev, Y.E., et. al., "Low Conductance States of a Single Ion Channel are not Closed," Journal of Membrane Biology, Vol. 147, 233-239, 1995.

[79] Hille, B., *Ionic Channels of Excitable Membranes,* Sinauer, 1998.

[80] Allen, T., *Particle Size Measurement,* Chapman and Hall, 1997.

[81] Maxwell, J.C., *A Treatise on Electricity and Magnetism,* Vol 1, 440.

[82] Berge, L.I., Feder, J., and Jossang, T., "A Novel Method to Study Single-Particle Dynamics by the Resistive Pulse Technique," Review of Scientific Instruments, Vol. 60, No. 8, 2756-2763.

[83] Kubitschek, H.E., "Counting and Sizing Micro-organisms with the Coulter Counter," from *Methods in Microbiology,* Academic, London, 1969.

[84] Bray et. al., *Molecular Biology of the Cell,* Garland Publications, 1994.

[85] Welsh, M.J., and Smith, A.E., "Cystic Fibrosis," Scientific American, Vol. 273, No. 6, 52-59, 1995.

[86] Riordan, J.R., "The Cystic Fibrosis Transmembrane Conductance Regulator," Annual Review of Physiology, Vol. 55, 609-630, 1993.

[87] "From the Bioweapons Trenches, New Tools for Battling Microbes," Science, Vol. 284, 54-55, 1999.

[88] Kim, U-G. et. al., "Dynamics and Structures of DNA: Long-Range Effects of a 16 Base-Pair (CG)8 Sequence on Secondary Structure," Biopolymers, Vol. 33, 1725-1745, 1993.

[89] Lipshutz, R.J. and Fodor, S.P.A., "Advanced DNA Sequencing Technologies," Current Opinions in Strucutral Biology, Vol. 4, 376-380, 1994.

[90] Jaklevic, J., Garner, H. and Miller, G., "Instrumentation for the Genome Project," Annual Review of Biomedical Engineering, Vol. 1, 649-678, 1999.

[91] Drmanac, R. et. al., "Sequencing of Megabase-plus DNA by Hybridization: Theory of the Method," Genomics, Vol. 4, 114-128, 1989.

[92] Sanger, F., Nicklev, S. and Coulson, A., "DNA Sequencing with Chain-Terminating Inhibitors," Proceedings of the National Academy of Sciences, Vol. 74, No. 12, 5463-5467, 1977.

[93] Smith, L.M., et. al., "Flourescence Detection in Automated DNA Sequence Analysis," Nature, Vol. 321, 674-679, 1986.

[94] Luckey, J., and Smith, L., "Optimization of Electric Field Strength for DNA Sequencing in Capaillary Gel Electrophoresis," Ana. Chem., Vol. 65, 2841-2850, 1993.

[95] Huang, X.C., Quesadam M.A., and Mathies, R.A., "DNA Sequencing Using Capillary Array Electrophoresis," Anal. Chem., Vol. 64, 2149-2154, 1992.

[96] Southern, E.M., "Detection of Specific Sequences Among DNA Fragments Seperated by Gel Electrophoresis," Journal of Molecular Biology, Vol. 98, 503-577, 1975.

[97] Southern, E.M., Maskos, U., and Elder, J.K., "Analyzing and Caomparing Nucleic Acid Sequences by Hybridization to Arrays of Oligonucleotides: Evaulation Using Experimental Models," Genomics, Vol. 13, 1008-1017, 1992.

[98] Fodor, S.A. et. al., "Light-directed Spatially Addressable Parallel Chemical Synthesis," Science, Vol. 251, 767-773, 1991.

[99] Cheung, V. et. al., "Making and Reading Microarrays," Nature Genetics Supplement, Vol. 21., 15-18, 1999.

[100] Fodor, S.P.A., et. al., "Multiplexed Biochemical Arrays with Biological Chips," Nature, Vol. 364, 555-556, 1993.

[101] Breslauer, K., et. al., "Prdeicting DNA Duplex Stability from the Base Sequence," Proceedings of the National Academy of Sciences, Vol. 83, 3746-3750, 1986.

[102] Church, G., *et. al.*, "Characterization of individual polymer molecules based on monomer-interface interactions," US Patent No 5,795,782, Aug. 18, 1998..

[103] Kazionowicz, J. et al., "Characterization of Individual Polynucleotide Molecules Using a Membrane Channel," Proceedings of the National Academy of Sciences, Vol. 93, 13770-13773, 1996.

[104] Bunville, L.C., *Modern Methods of Particle Size Analysis*, Wiley, 1984.

[105] DeBlois R.W. and Bean, C.P., "Counting and Sizing of sub-Micron Particles by the Resistive Pulse Technique," Review of Scientific Instruments, Vol. 41, No. 7, 909-916, 1970.

[106] Coulter, W.H., U.S. Patent No. 2,656,508, 1953.

[107] Bezrukov, S.M., Vodyanoy, I., and Parsegian, V.A., "Counting Polymers Moving Through a Single Ion Channel," Nature, Vol. 370, 279-281, 1994.

[108] Merzlyak P *et. al.*, "Polymeric Nonelectrolytes to Probe Pore Geometry: Application to the alpha -toxin Transmembrane Channel," Biophysical Journal, vol.77, No.6, 3023-33, 1999.

[109] Song, L., et. al., "Structure of Staphylococcal alpha-Hemolysin, a Heptameric Transmembrane Pore," Science, Vol. 274, 1859-1865, 1996.

[110] Akeson, M., et. al., Biophysical Journal, Vol. 77, 3227-3233, 1999.

[111] Meller, A. et. al., "Rapid Nanopore Discrimination between Single Polynucleotide Molecules," Proceeding of the National Academy of Sciences, Vol. 97, No. 3, 1079-1084, 2000.

[112] Netzer, Y., "Low-noise Optimization of JFET Input Stage for Capacitive Current Sources," Proceedings of the IEEE, vol.65, no.7, 1068-70, 1976.

[113] Kandiah, K., "The Evolution of Nuclear Detection Instrumentation," Nuclear Instruments and Methods, Vol. 162, 699-718, 1979.

[114] Hammill, O.P., "Improved Patch-Clamp Techniques for High Resolution Current-Recording from Cells and Cell-free Membrane Patches," Pflugers Arch., Vol. 391, 85-100, 1981.

[115] Kandiah, K. and Whiting, F.B., "Limits of Resolution in Charge Sensitive Detector Systems," Nuclear Instruments and Methods in Physics Research, Vol. A326, 49-62, 1993.

[116] Anso, M. Kh., et. al., "Electrometer Current Meters (Review)," Pribory i Tekhnika Eksperimenta, No. 6, 25-38, 1989.

[117] Enz, C.C. and Temes, G.C., "Circuit Techniques for Reducing the Effects of Op-Amp Imperfections: Auto-zeroing, Correlated Double Sampling, and Chopper Stabilization," Proceedings of the IEEE, Vol. 84, No. 11, 1996.

[118] Levis, R.A. and Rae, J.L., "Constructing a Patch-Clamp Setup," Methods in Enzymology, Vol. 207, 14-63, 1992.

[119] Goulding, F.S., Walton, J.T., and Pehl, R.H., "Recent Results of the Optoelectronic Feedback Preamplifier," IEEE Transactions on Nuclear Science, NS-17, No. 1, 218, 1970.

[120] Goulding F.S., Walton, J., Malone, D.F., "An Opto-Electronic Feedback Preamplifier for High-Resolution Nuclear Spectroscopy," Nuclear Instruments and Methods, Vol. 71, 273-279, 1969.

[121] Llacer, J., "Accurate Measurement of Noise Parameters in Ultra-Low Noise Opto-Feedback Spectrometer Systems," IEEE Transactions on Nuclear Science, Vol. NS-22, No. 5, 1975.

[122] Personal Communication, Dr. Martin Thomas, Cairn Research, UK.

[123] Personal Communication, Paul Matsudiara, MIT.

[124] Gibson, U., Heid, E.M., and Williams, P.M., Genome Reearch, Vol. 6, 995-1001, 1996.

[125] Melissison, *Experiments in Modern Physics*, Academic Press.

[126] Gray and Meyer, *Analysis and Design of Analog Integrated Circuits*, 1990.

[127] Landis, D.A. et. al., "Pulsed Feedback Techniques for Semiconductor Detector Radiation Spectrometers," IEEE Transactions on Nuclear Science, NS-18, No. 1, 115, 1971.

[128] Landis, D.A., Goulding, F.S., and Jaklevic, J.M., "Performance of a Pulsed-Light Feedback Preamplifier for Semiconductor Detector X-Ray Spectrometers," Nuclear Instrumentation and Methods, Vol. 87, 211-213, 1970.

[129] EDN Nov 1999; Microfluidics MEMS structures.

[130] Wetmur, J.G., "DNA Probes: Applications of the Principles of Nucleic Acid Hybridization," Critical Reviews in Biochemical and Molecular Biology, Vol. 26, 227-257, 1991.

[131] Sigworth, F., "Electronic Design of the Patch Clamp," in *Single-Channel Recording,* Plenum Press.

[132] Kornber, A. and Baker, T., *DNA Replication*, Freeman, 1992.

[133] Lund, M.W., et. al., "Low Noise JFETS for Room Temperature X-ray Detectors," Nuclear Instruments and Methods in Physics Research, Section A, Vol. 380, 318-322, 1996.

[134] Personal Communication, Mike Hogan, Affymetrix Corporation.

Appendix A

The Resistive Pulse Technique and Its Limitations

Nuclear track-etched pores in mica have previously resolved microscopic objects with roughly 20nm of resolution, but the extension of this sensitivity to smaller dimensions has until recently proven illusive due to the large size of the limiting apertures [107]. The application of nanopores to detect and characterize single polymers begs the question, "How small of a hole do you need to sense DNA?" This appendix develops a general performance metric for ionic channels that motivates the use of nanopores on the order of the alpha-hemolysin biotoxin, and justifies the lengths that must be taken to develop picoamp-sensitive interface circuitry to sense the current modulations through the channel.

A.0.2 Overview of the Resistive Pulse Technique

Coulter counters are based on the resistive pulse technique illustrated in Figure A-1. This technique, first patented by Coulter [106] in 1953, uses the modulation of channel conductance to detect the presence of particulates. As the suspended objects are forced through a limiting aperture by hydrostatic pressure, the channel's conductance varies in proportion to the particle's relative dimensions [80, 83].

The relationship between a particle's size and the channel's conductance modulation can be modeled in a straightforward manner [105, 83]. Historically, the characteristics of insulating

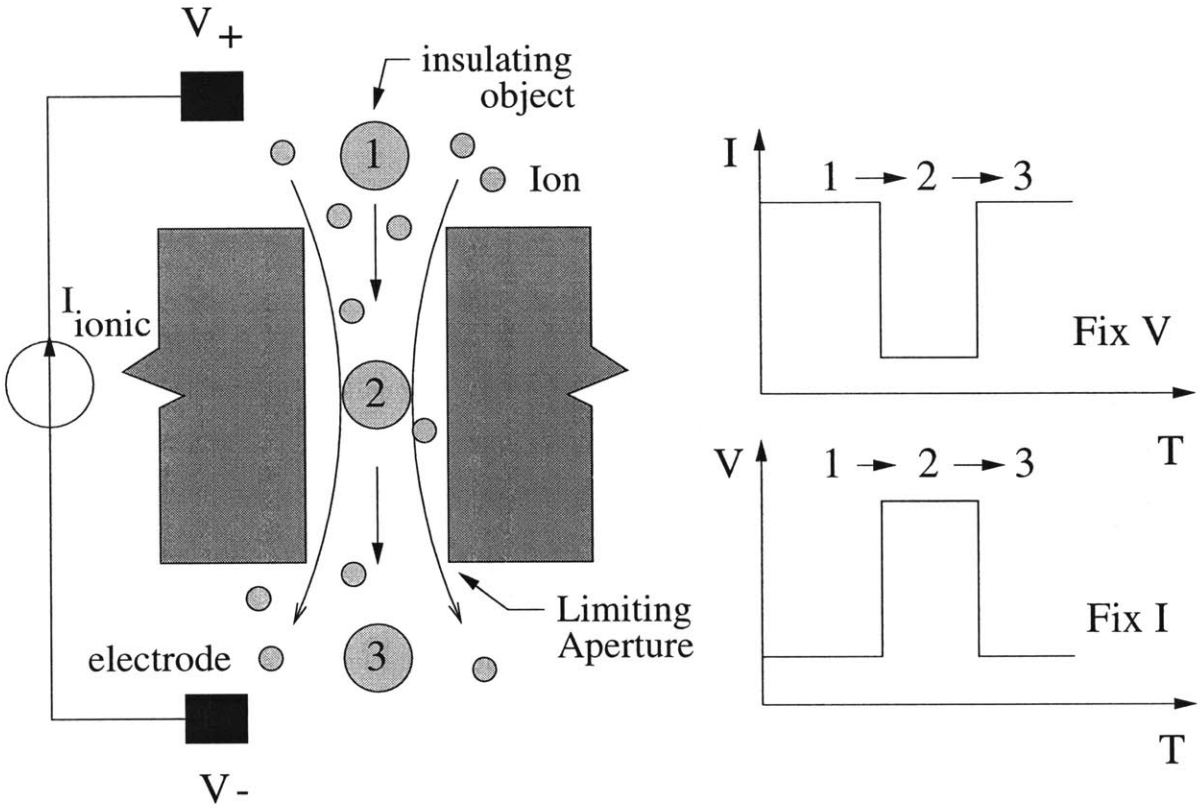

Figure A-1: The general principle of the resistive pulse technique. The presence of an insulating particle modulates the conductance of the limiting aperture. The conductance modulation can be used to characterize the objects based on size.

spheres were modeled because they effectively describe the bacteria and cell structures that were the primary test samples. The analysis of spheres here provides a starting point to modeling polymer translocation, and also serves as a validation for the channel performance metrics that are derived.

A dilute suspension of insulating spheres immersed in a solution with bulk resistivity, ρ_o, can be modeled as a solution with an effective resistivity ρ_{eff} [81]. Maxwell's approximation for ρ_{eff}, in terms of the volume fraction of insulating spheres, f, is given by [81]

$$\rho_{eff} = \rho(1 + \frac{3f}{2} + \cdots).$$

Referring to Figure A-2, the volume fraction for a sphere of diameter d, within a channel of length L and diameter D, is

$$f = \frac{4d^3}{3D^2L},$$

where the end effects of the channel have been ignored and the sphere diameter is assumed to be much smaller than D. Substituting this volume fraction into Maxwell's resistivity estimate, the resistance for the channel with an insulating sphere present is

$$R_{sphere} = \frac{4\rho_o L}{\pi D^2}(1 + \frac{d^3}{D^2 L} + \cdots).$$

To first order, therefore, an incremental resistance change of

$$\Delta R = \frac{4\rho d^3}{\pi D^4}$$

should result from a sphere passing through the channel. The fact that the incremental resistance scales as the third power of the particle's radius makes it particularly useful to size particulate volume [105, 80, 83].

The simple model described here has been shown to accurately quantify resistive pulse responses for particles up to approximately half the channel diameter [80, 105, 83]. More detailed expressions using Laplace's equation have accurately predicted pulse scaling for particles up to a diameter of $0.9D$ [105, 80]. The correlation between experimental data and simple resistive modeling motivates a similar analysis of polymer translocation through a channel.

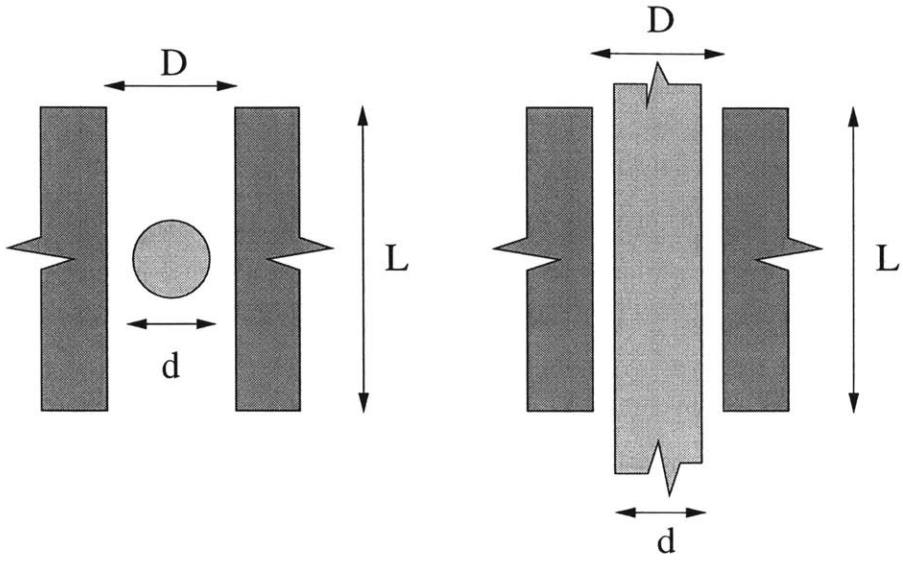

Figure A-2: Calculating the modulation in conductance. Left: An insulating sphere of diameter d passing through pore, Right: An insulating cylinder for modeling the translocation of a long polymer.

For modeling *polymer* translocation through a pore, the modulation of channel conductance due to an insulating *cylinder* should be considered. Referring again to Figure A-2, the insertion of an insulating cylinder into the channel results in an incremental channel resistance of

$$R_{cyl} = \frac{\rho_o L}{\pi(D^2 - d^2)},$$

where again the issue of end effects is ignored. A modulation of the channel resistance,

$$\Delta R = \frac{\rho_o L}{\pi}[\frac{d^2}{D^2(D^2 - d^2)}],$$

should be observed during a "long" polymer translocation. The relative change in channel resistance,

$$\frac{\Delta R}{R} = \frac{d^2}{(D^2 - d^2)},$$

scales as d^2 for polymers much smaller than the channel diameter, and diverges as the polymer approaches the size of the aperture. This observation is consistent with physical intuition: for small d, the incremental change scales as the area of the polymer, but as d approaches the same

dimension as the channel, the resistance diverges as the polymer effectively blocks the channel.

The expression for $\frac{\Delta R}{R}$ appears to suggest that for high sensitivity to incremental changes in polymer diameter, the channel aperture should be roughly the same order of magnitude as the polymer of interest. The problem with this simple conclusion is that the effects of increased Johnson noise in a higher resistance channel must also be considered. To get a more useful metric for a given channel geometry, the expression for resistance modulation should be combined with a reasonable noise model for the channel. This metric then provides a back-of-the-envelope estimate for the resolution of a particular channel sensor.

A.0.3 Resolution of Channels to Polymer Translocation

The limit of detection for the resistive pulse technique can be related to the size of the limiting aperture. Referring to Figure A-3, if the channel is maintained with a fixed voltage bias and the current modulation is measured, then the fractional change in current, $(\Delta I_o)/I_o$ is related to the particle and pore dimensions through

$$\frac{\delta I_o}{I_o} = \frac{d^2}{D^2};$$

where d is the particle diameter and D is the channel diameter[1]. Alternatively, if the channel is maintained with a fixed current and the voltage across the channel is measured, then the fractional change in voltage due to particle translocation is

$$\frac{\Delta V_c}{V_c} = \frac{d^2}{D^2}.$$

These expressions illustrate that either approach to conductance measurement obeys a squared dependence on polymer and channel dimension.

The ultimate resolution of the conductance measurement will be limited by the thermal (Johnson) noise associated with the channel resistance, R_c [105]. The magnitude of this noise is given by

$$e_n = \sqrt{4k_bTR_c\Delta f} \;\; V/\sqrt{Hz},$$

[1]Since the lower bound on sensitivity is being estimated, d << D in this analysis.

where k_b is Boltzmann's constant, T is the temperature in Kelvin and Δf is the measurement bandwidth. By manipulating the thermal noise expression and the incremental sensitivity of the channel, the maximum pore dimension allowed to resolve a polymer of a given size can be specified. For a sample polymer with diameter d, the required pore diameter to detect translocation is determined to be

$$D \approx \frac{\sqrt{\pi} d^2 V_{bias}}{2\sqrt{4 k_b T \Delta f \rho L}},$$

where L is the estimated length of the channel and V_{bias} is the quiescent voltage applied across the pore(Figure A-3). This expression illustrates that to resolve small polymers of size d, the pore must scale as d^2 to account for both the *size* of the polymer as well as *increased noise* associated with smaller apertures.

The general validity of this rough metric can be demonstrated by comparing theoretical estimates of resolution with data from the literature. Using a similar development as that for a cylinder, the smallest sphere diameter theoretically resolvable with a channel,

$$d \approx \frac{1}{2}\left(\frac{4 k_b T \rho D L^5 \delta f}{\pi V_{bias}^2}\right)^{1/6},$$

can be compared with existing data on sphere translocation extracted from the literature. Using parameters from [105] for a $.5\mu m$ track-etched channel of length $2.9\mu m$, biased with $353mV$ and immersed in an $75\Omega - cm$ KCL salt bath, the rms noise for a 10 kHz bandwidth measurement should be roughly $12.5nm$ according to the our estimate. The correlation of this model with actual data is illustrated in Figure A-4 [105, 107], which demonstrates the detection of 357 nm and 91 nm beads passing through the specified aperture. The peak-to-peak noise is roughly 60 nm, corresponding to an rms noise of approximately 10 nm, assuming a Gaussian noise source. Our simple metric, therefore, seems to reliably parameterize the resolution of channels with sub-micron dimensions. The goal now is to specify the required channel dimensions necessary to resolve structures on the physical scale of DNA.

To scale the signal-to-noise ratio for the channel so that DNA translocation is observable, our metric suggests that increasing V_{bias} or shrinking the channel diameter yields the largest return. Attempts to improve resolution with an increased bias voltage, however, have led to

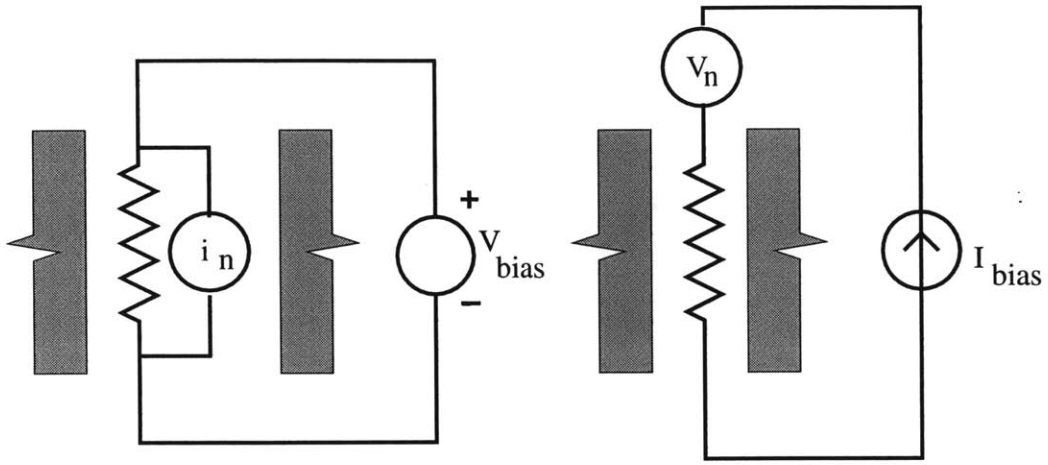

Figure A-3: Establishing the minimum detectable polymer for a specified pore. The channel may be biased with either a voltage or a current source, and the resulting channel current or voltage monitored, respectively. The effect of Johnson noise can then be considered relative to the deterministic conductance modulations from translocating objects.

problems with power dissipation in the channel apertures. Significant dissipation seems to cause local boiling of the ionic solution that fills the channel with water vapor, rendering it useless for particle detection [83, 80]. The shrinking of the channel aperture, it seems, is the most likely path to resolving single polymers of DNA.

The constraints on channel size for recognition of DNA, however, are beyond the limitations of standard silicon fabrication technology. Using the channel scaling expression,

$$D \approx \frac{\sqrt{\pi} d^2 V_{bias}}{2\sqrt{4 k_b T \Delta f \rho L}},$$

the estimated channel diameter required to sense a $1nm$ radius DNA polymer immersed in a $10\Omega - cm$ salt bath is roughly $2.2nm$ for a $1\mu m$ long aperture–an order of magnitude smaller than state-of-the-art track-etched pores [80][2]. Attempts to scale down existing track-etched pores are limited by the relative thickness of the mica membrane, which makes fabrication of the actual limiting aperture difficult to control [80]. In addition to increased noise, the long

[2]Bandwidth $\approx$ 10kHz

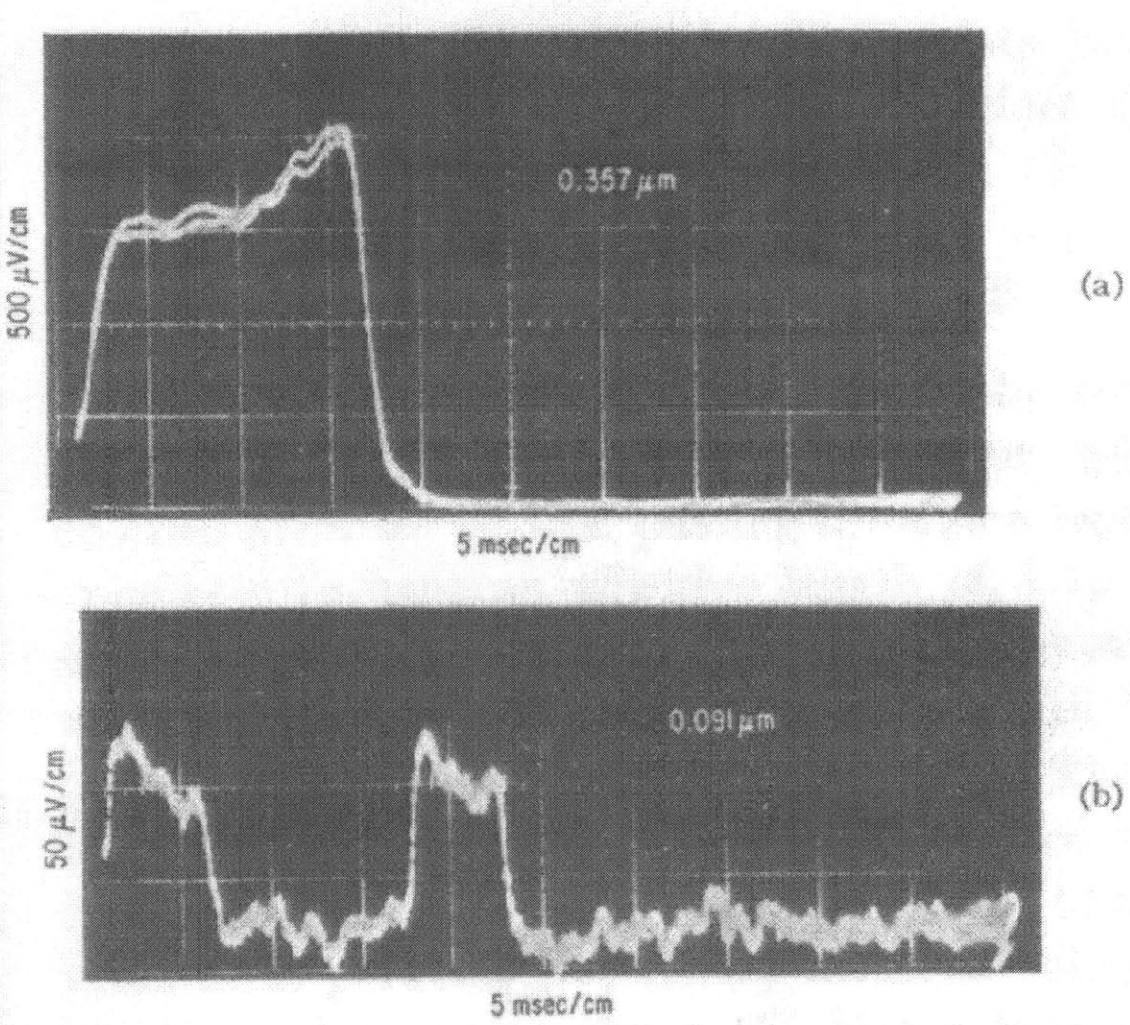

Figure A-4: The detection of 357nm and 91nm beads passing through a 0.5um nucleopore aperture. The signal-to-noise ratio is approximately four in the bottom trace, demonstrating the calculated limit to resolution of 12.5 nm rms for these apertures. Reproduced from DeBlois.

mica channels also create an effective boxcar average of the polymer's physical characteristics. This averaging filters out the single base properties of the polymer chain that are required for sequencing.

A final motivation for a channel diameter of roughly 2nm is the need to insure the DNA passes through the aperture in single file. In solution, the natural tendency of DNA is to collapse into a complex three dimensional structure [84]. The characterization of base components is then limited, since the information is hidden within the folded DNA. An aperture on the same order as the DNA width insures that the DNA translocates through the channel in an extended, linear fashion, allowing some possibility of detecting the base constituents. The need for a limiting aperture on the order of $2-5nm$ in diameter and $10nm$ in length to resolve single molecule DNA translocation motivates a radically new approach to channel "fabrication."

For the work performed in this thesis, a biotoxin channel formed from *Staphylococcus aureus* will be used. The limiting aperture of the toxin channel is illustrated in Figure A-5. The 1.5 nm limiting aperture and 4 nm barrel length allow for the detection of 1.2 nm single-stranded DNA with minimal effort. Given the noise properties of the measurement developed in chapter three, the minimum resolvable structure with the toxin channel is roughly 8 Å, well below the characteristic size of ssDNA. Channels of this dimension result in equivalent gigaohm source resistances with picoampere current fluctuations, motivating the need for low-noise, wide bandwidth picoammeter development.

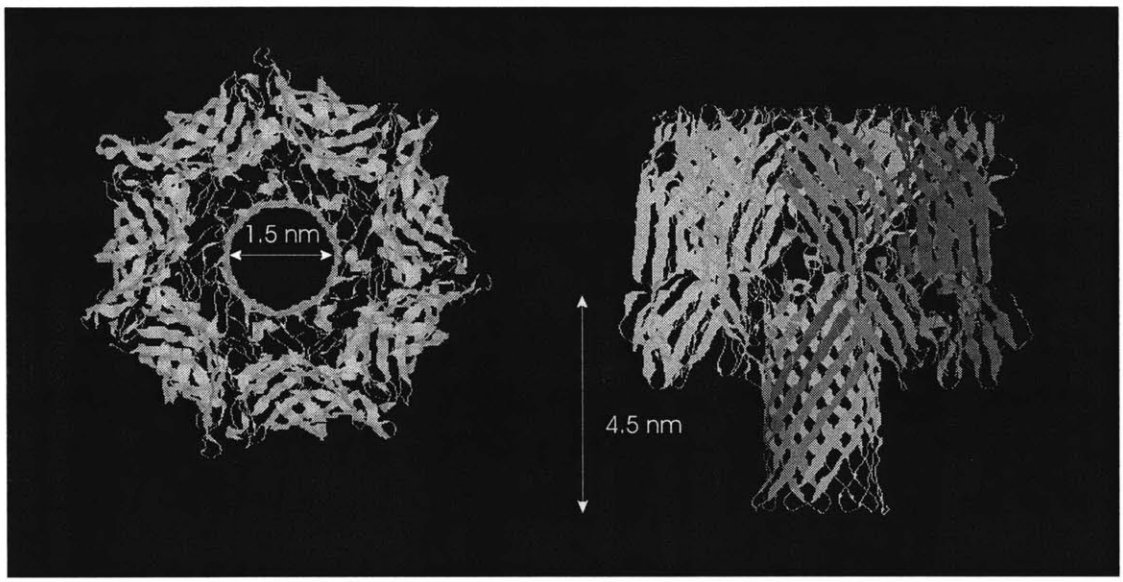

Figure A-5: The channel dimensions of the alpha-hemolysin pore. Note that the limiting aperture is approximately 1.5nm, slightly larger than 1.2nm single-stranded DNA.

Appendix B

Fabrication of a Toxin Nanopore

B.1 A New Channel Scheme: Alpha-Hemolysin

The theoretical detection resolution of the resistive pulse technique is limited to approximately $20nm$ with state-of-the-art track-etched channels. Extending this resolution to the order of $1nm$ requires a significant reduction in channel width and length. In order to obtain a channel with dimensions suitable for the detection of single nanometer-scale molecules, a biological pore can be employed [107, 103, 102, 110, 111].

Biological pores are ubiquitous in microbiology, and range in size from relatively small ion-selective channels used in the nervous system to large channels that serve as conduits for proteins and metabolites [79, 107]. The large channels, in addition to passing proteins, freely conduct ions in the bath solution [79]. This fact allows for them to be applied as the limiting aperture of a Coulter counter, as first proposed by Bezrukov [108]. Considering the resolution metrics derived previously, the translocation of molecules should be detectable with the nanometer-scale apertures of biological pores. The challenge is to find a biological pore with the proper channel dimensions for detecting DNA.

The physical properties of the *Staphylococcus aureus* toxin are consistent with those required to detect single-stranded DNA. The aperture characteristics of the toxin channel were determined by x-ray crystallographic analysis [109], and the channel geometry is illustrated in Figure A-5. From these measurements, a barrel approximately $2nm$ in diameter and $4nm$ length was found for the toxin channel, with a $1.5nm$ limiting constriction at its entrance [109]. These

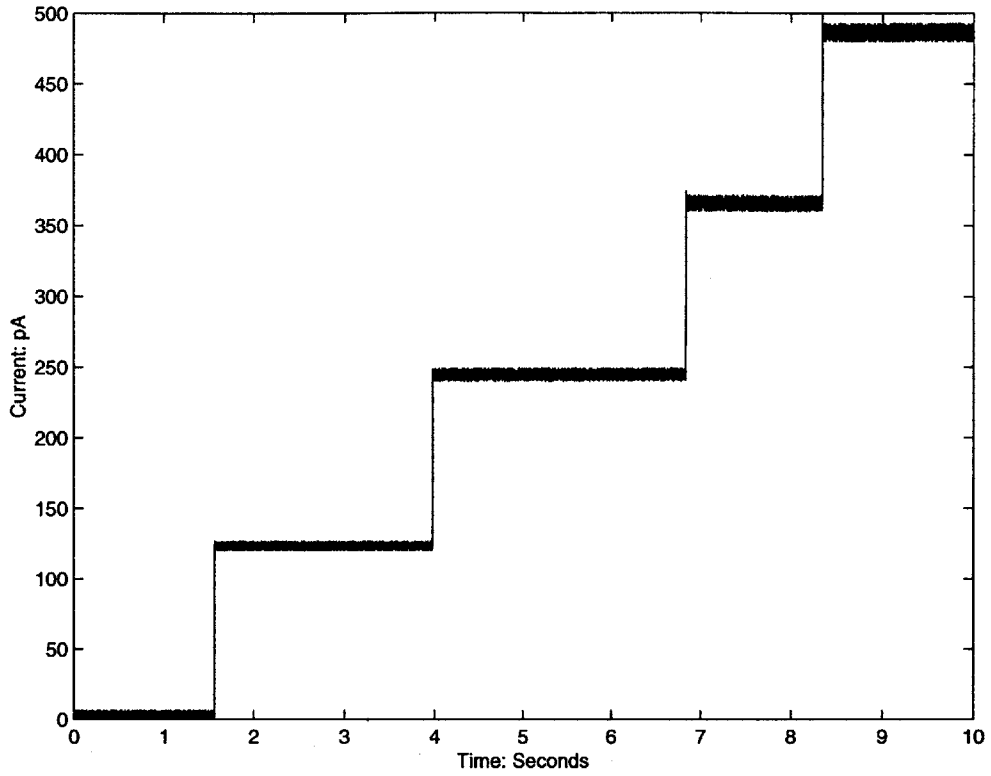

Figure B-1: The insertion of discrete alpha-hemolysin channels into a lipid membrane (representation). The bias voltage is 120mV, resulting in discrete current jumps of 120pA when bathed in a 1M KCL ionic bath. Note also the increase in current noise for multiple channel insertions.

relative dimensions allow for the detection of single molecules of DNA if the channel is biased correctly [103, 102]. In addition, the alpha-toxin readily inserts into artificial lipid bilayers [75], as demonstrated by the discrete conductance jumps in Figure B-1. The ability of the alpha toxin to self-insert into the lipid membrane greatly simplifies the fabrication of a stable channel [79]; the toxin monomer is simply added to the solution and creates a stable channel without external interference [75]. These physical characteristics make the *Staphylococcus aureus* toxin an ideal model system for developing nanoscale Coulter techniques [107, 103, 102, 110, 111].

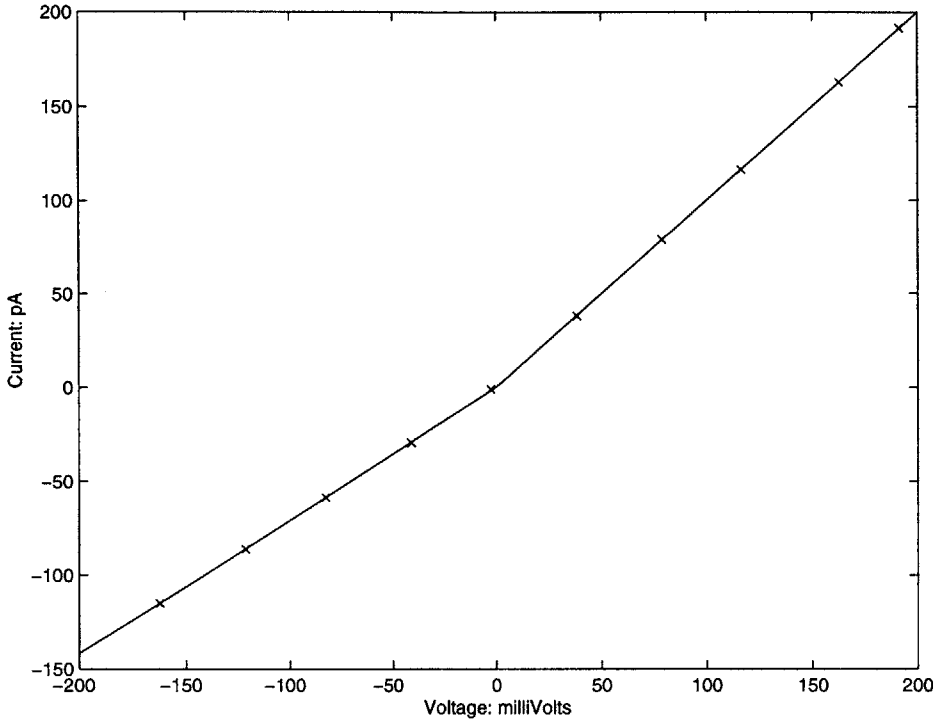

Figure B-2: The I-V characteristics of the alpha toxin immersed in a 1M KCL bath, with pH of 8.0 and biased at 20^o C. For either polarity, the channel mimics to first-order a pure resistance. The asymmetry in the graph demonstrates the mild rectifying properties of the channel, which does not impact the Coulter measurements.

B.2 Obtaining a Stable, Low-Noise Toxin Channel

The alpha-toxin pore allows for the resolution of single-stranded DNA translocation using the resistive pulse technique, as several previous studies have shown [103, 110, 111]. To achieve this recognition of DNA, however, the pore must be surrounded by the proper physical environment. Like most sensors, the noise characteristics of the channel must be adjusted by manipulating the bias conditions. In order to optimize the alpha toxin as a sensor for detecting DNA translocation, an experimental protocol was established that creates a stable, low-noise channel. The details of this procedure are outlined in several references, and represent an extension of previous work with the toxin channel [103, 110]. A summary schematic for this procedure is illustrated in Figure B-3.

B.2.1 Mechanical Apparatus for Supporting The Lipid Membrane

The alpha toxin must be incorporated into an insulating lipid bilayer that both supports the toxin channel and serves as an insulating partition between the two fluid volumes [103, 110]. The lipid bilayer is formed from a $2nm$ film of Diphantnyionl PC that will extend across a physical aperture in a manner similar to a soap bubble clinging to a metal ring. In general, a Teflon aperture of roughly $20 - 40\mu m$ forms an excellent low-noise, highly insulating structure upon which to attach the lipid [72].

The fabrication of the Teflon support, denoted the "patch tube," is shown schematically in Figure B-4 [103, 110, 72], and is based on previous work by Wonderlin and Branton. A stainless steel mandrill is surrounded by PTFE heat-shrinkable tubing. A second Teflon tube, protruding from beneath the mandrill form, will provide the physical junction to the other fluid bath. Heating of the PTFE causes it to shrink tightly around the form of the mandrill, creating a conic cavity with a sharp tip once the mandrill is removed. To form the aperture in the Teflon window, a microtome cutting blade is used to shave off successive layers of PTFE until a hole of the desired diameter is opened. Using this technique, Teflon apertures on the order of $10 - 50\mu m$ can be reliably fabricated [110, 72].

The support of the patch tube is provided by the "patch stand," which serves as a solid platform during experimental procedures. Two implementations of the patch stand were used in

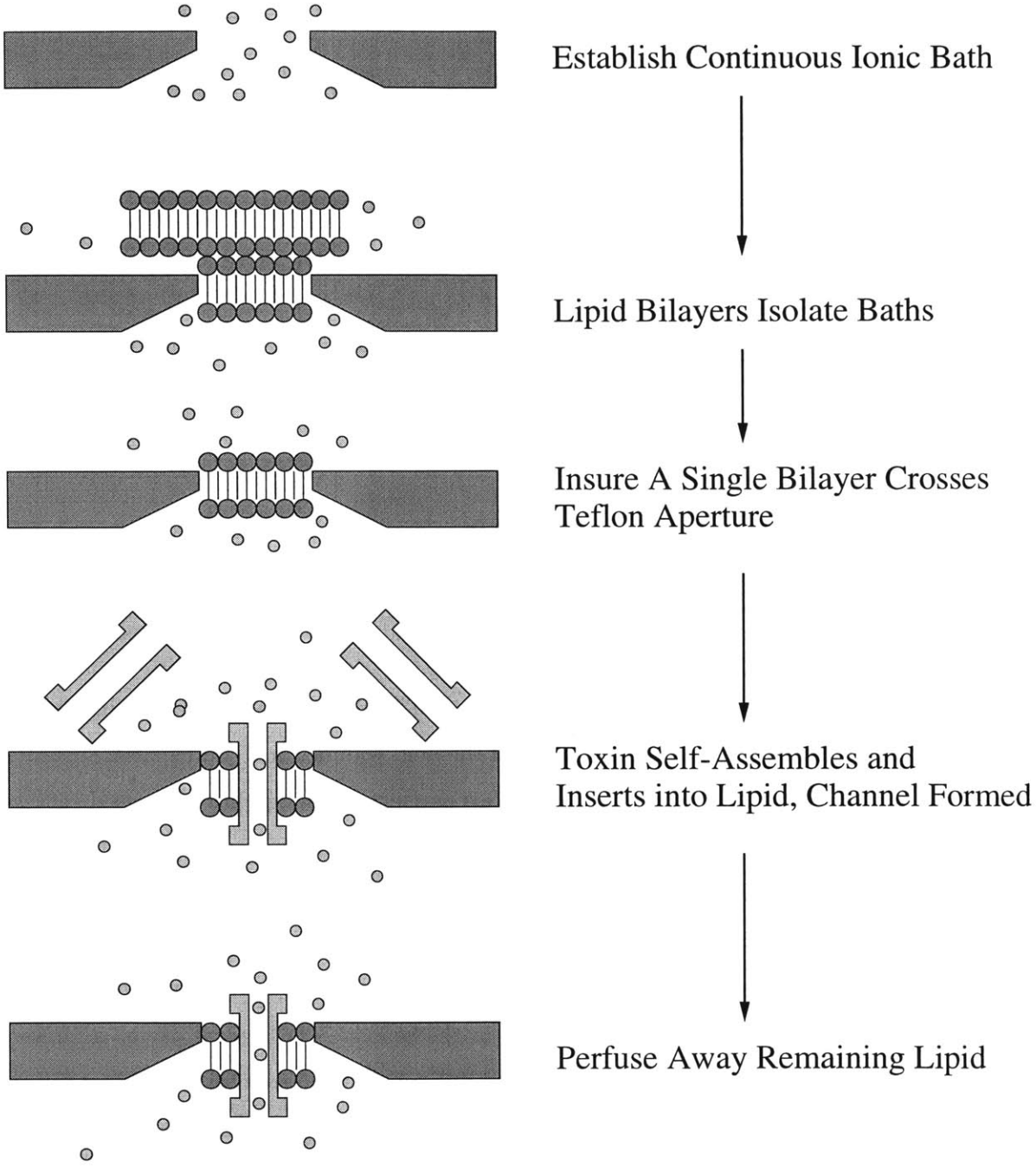

Figure B-3: The general protocol for obtaining a conducting toxin channel across as insulating lipid membrane.

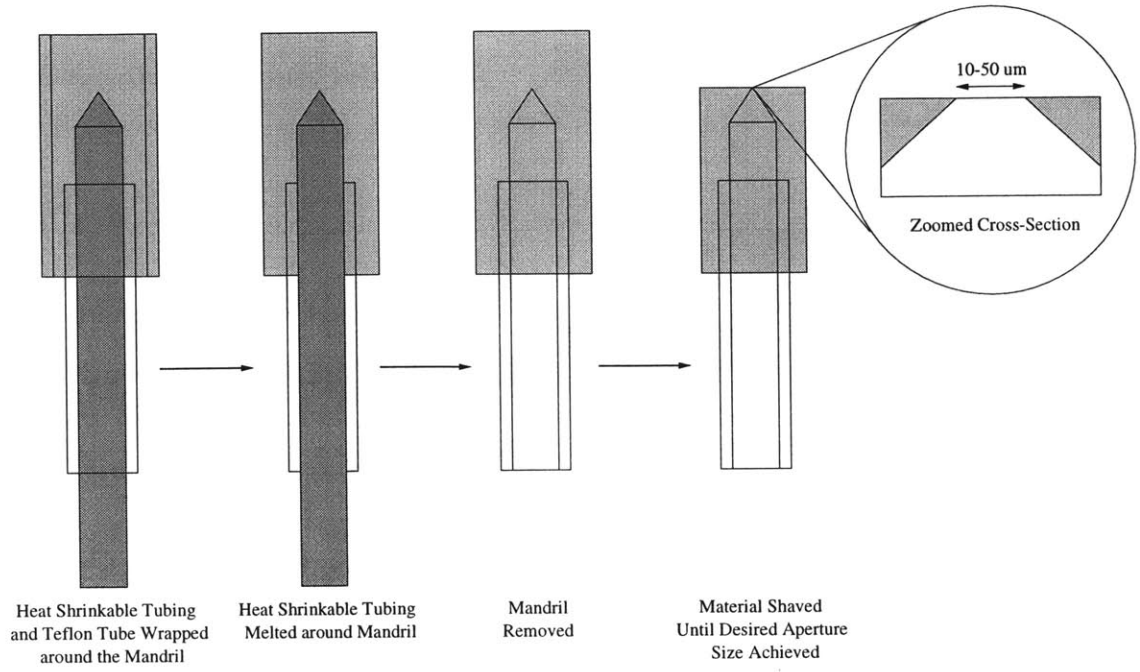

Figure B-4: Fabrication of the Teflon support aperture for the lipid membrane.

this thesis. The first patch stand folds the patch tube back in a U, as illustrated in Figure B-5. This structure allows for easy manipulation of the fluid volumes and good spatial separation of the fluid baths to reduce stray capacitance. This patch stand design has been used successfully in a number of previous studies [103, 110, 111], and was used for the bulk of experiments performed in this thesis.

A second patch stand was developed with the specific goal of rapid temperature control, and is shown in Figure B-6. Two small, $50\mu L$, fluid chambers are connected via a short horizontal patch tube, with a hollow cavity in the center. The central cavity addresses the problem of capillary action between the patch tube and the surrounding patch stand, which can create a shunt leakage path between the fluid baths. The air/Teflon interface was found experimentally to provide an excellent barrier to further fluid propagation, so an air "trench" was employed. Alternative fixes to the leakage problem, including Vaseline and vacuum grease, proved problematic due to contamination of the fluid baths.

Thermal adjustments with the patch stand are made with a Peltier junction through a 10/1000" Teflon floor. This thickness was found to be a good compromise between thermal re-

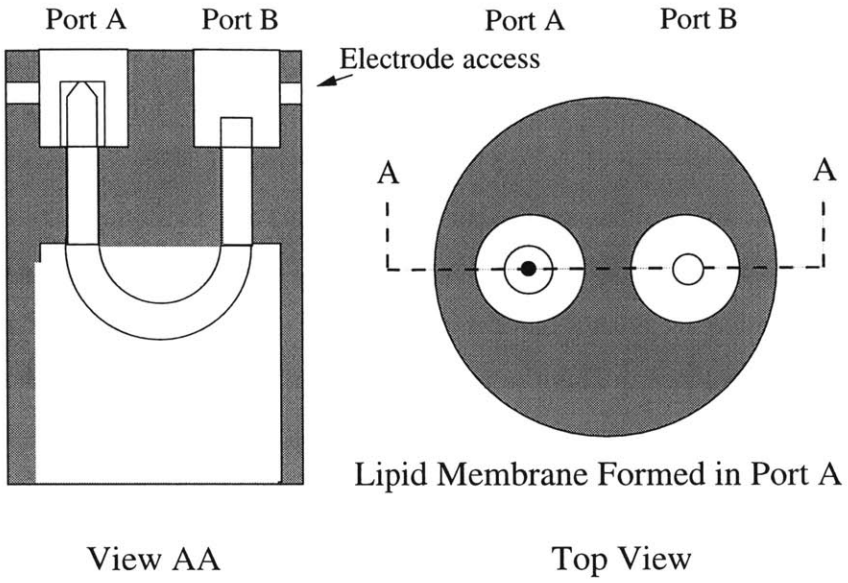

Figure B-5: Patch stands to support the toxin channel; the U-tube arrangement.

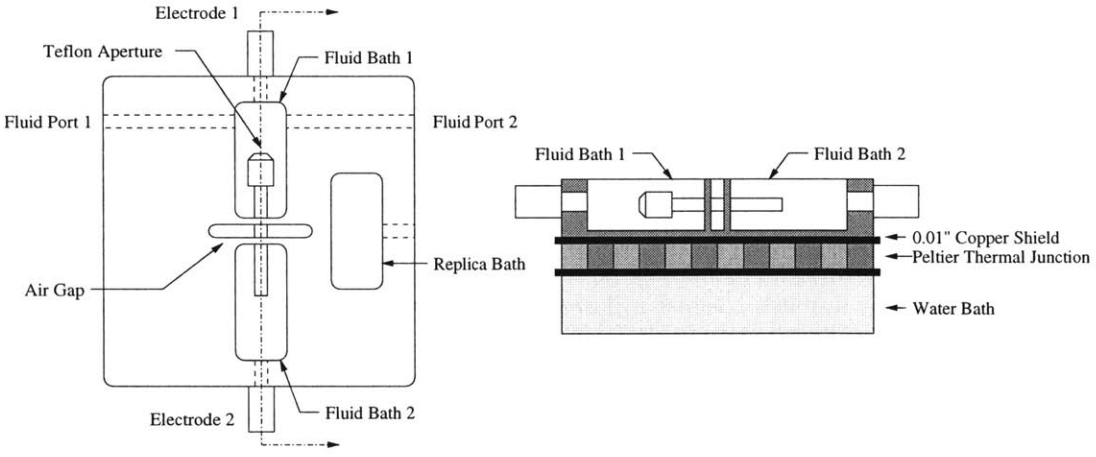

Figure B-6: Patch stands to support the toxin channel; the patch stand design for improved thermal control.

sistance and physical support. Alternative floor structures using a sapphire window did improve thermal conduction slightly, but at the expense of an increased fluid leakage compromising the insulating membrane between the bathes. The thermal dynamics for this patch stand can be modeled effectively as a low-pass filter with a 1 sec time constant, derived from the heat capacitance of the bath solution and the series thermal resistance of the Teflon barrier. A model 3040 thermal regulator from Newport Instruments was used to regulate the bath temperature to 0.5^o C of the command reference with a bandwidth of 0.2 Hz. This performance is adequate for the detection strategies explored in this thesis, since the time constants of the chemical reactions studied were on the order of ten seconds.

The sensing of the bath temperature was achieved with a "replica" reservoir fabricated with identical dimensions to the actual fluid bathes being controlled. The use of a replica physically isolates the temperature and electrical measurements, eliminating the noise coupling that plagues other thermally-regulated patch stand designs [111]. Calibration measurements demonstrated that the fluid volumes track to within 0.1^oC, which is satisfactory for the hybridization experiments explored with the nanoscale Coulter counter.

B.2.2 Protocol for Obtaining a Toxin Channel

The general method for incorporating lipid bilayers across mechanical apertures was first developed by Montal [77] and Niles [76]. To summarize, the Teflon aperture is primed with a mixture of (diphanenoil-PC) DPC lipid and hexane that is allowed to dry around the aperture edge. This process creates a suitable bonding surface for the lipid membrane that will eventually cover the aperture. The patch tube is then filled on both sides with an ionic solution ($10\Omega - cm$ KCL) that establishes a $0.5mS \pm 0.25mS$ conductance across the aperture. The window is covered with a lipid bilayer by dipping a pipette tip into a mixture of DPC lipids and hexadecane and blowing a bubble across the aperture; the successful creation of an lipid barrier is indicated when the resistance across the Teflon window jumps from $2 - 10k\Omega$ to greater than $100G\Omega$. For successful pore insertion, however, it is necessary that the lipid barrier be formed from a *single* bilayer.

The detection of a single bilayer may be achieved by monitoring the capacitance of the membrane. This measurement can be taken with the picoammeter used for DNA translocation

by applying a suitable triangular waveform with slope β V/sec across the membrane, as shown in Figure B-7. This voltage reacts with the lipid capacitance to create a current square wave of magnitude,

$$I_{mem} = \beta C_{mem}.$$

Using a 250Hz, 2 Volt peak-to-peak triangle wave yields a current measurement of 1nA/pF that is readily detected by the Axopatch 200B voltage clamp.

Given a method of measuring the lipid membrane capacitance, the establishment of a single insulating bilayer is straightforward. The lipid bilayer can be modeled to first order as a parallel plate capacitor [77, 79]; the effect of multiple bilayers, therefore, is to decrease the effective capacitance of the lipid partition. As the partitions capacitance is measured, a *clean* pipette is used to blow air bubbles over the aperture and peal off successive bilayers. As layers are removed, discrete steps in capacitance are observed, as illustrated in Figure B-7. The lipid capacitance converges approximately as

$$\frac{C_{mem}}{3} \rightarrow \frac{C_{mem}}{2} \rightarrow C_{mem},$$

until a final capacitance is achieved that represents the parallel combination of a single bilayer ($\approx 10pF$) and the shunt parasitics ($\approx 5pF$). Further attempts to lower the capacitance destroy the membrane partition; the previous capacitance measurement is noted and the process is repeated, this time terminating when the capacitance attributable to a single bilayer is obtained.

With a single bilayer now crossing the Teflon aperture, a resistance of greater than $100G\Omega$ separates the ionic solutions. Neither proteins nor ions can cross the lipid/Teflon barrier [79]; the only channel available for translocation between the bathes will be the alpha toxin. Monomeric alpha-toxin is added to one side of the lipid membrane while the conductance of the partition is monitored. When seven sub-units of alpha-toxin self-assemble and insert into the lipid, a quantal jump in conductance of $1nS$ is observed[1], as illustrated in Figure B-8. After this conductance step is detected, the fluid chamber containing the toxin is rapidly perfused to prevent incorporation of additional channels. When the experiment proceeds as described, a 1.5-2nm limiting aperture is created that will pass single-stranded DNA.

[1]Using the $10\Omega - cm$ salt bath

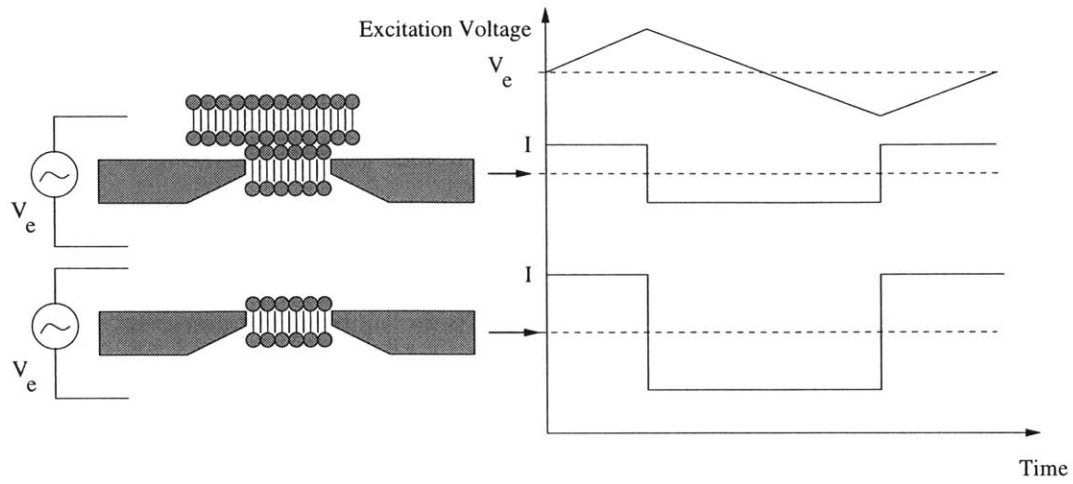

Figure B-7: The detection of lipid bilayer thickness with capacitance. A triangular voltage is applied across the lipid capacitance, resulting in a square wave of current proportional to to the capacitance. As successive bilayers are removed, the capacitance increases until a maximum is achieved with a single bilayer.

B.3 Biasing the Toxin to Obtain a Stable, Low-Noise Channel

The incorporation of a single alpha toxin into a lipid membrane ideally creates a limiting aperture suitable for applying the resistive pulse technique to the detection of ssDNA. The physical conditions surrounding the pore, however, must be properly biased to insure that the toxin mimics a stable, low-noise channel. The proper environmental conditions to obtain the highest performance channel in terms of noise and signal performance can be deduced from previous scientific studies of the alpha toxin and applied here. This section is a summary of the most important bias considerations.

B.3.1 Ionic Species

Alpha toxin shows the propensity to stochastically change its conductance value between several states. These "gating" events are difficult to distinguish from DNA translocation events and must be eliminated. Menestrina established that the elimination of di- and tri-valent cations, such as calcium or magnesium, would suppress channel gating [75]. In the presence of mono-

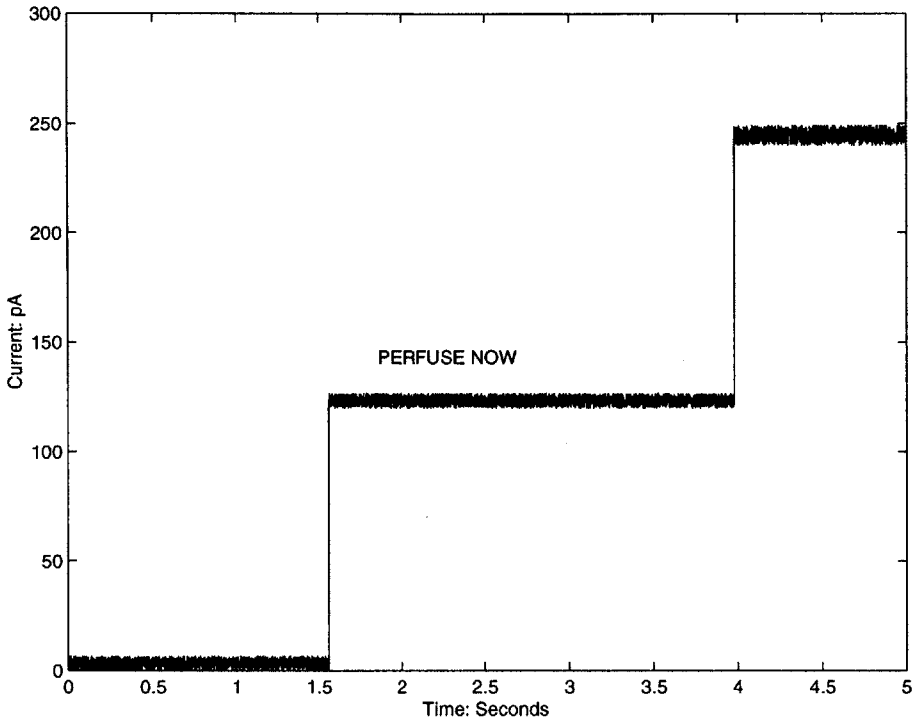

Figure B-8: The quantal jump in membrane conductance upon the insertion of a single toxin pore; the solution is perfused to prevent subsequent toxin insertions. At the right, a second pore is observed inserting into the membrane.

valent potassium, however, the toxin channel was found to remain in its high conducting state, which is useful for maintaining a high signal-to-noise ratio [75]. For the experiments performed throughout this thesis, a one molar solution of potassium chloride was used.

B.3.2 pH Biasing

The choice of pH also has a critical effect on gating behavior and channel noise. Korchev [78] found that at low-pH (≈ 4), the toxin channel would undergo reversible, voltage-induced, fluctuations in conductance similar to those found in the presence of di- and tri-valent cations. In addition, Kasionowicz observed a pH-dependent noise peak in channel current related to the protonation dynamics of the pore sub-units [73, 74]. The protonation state was postulated to modulate the conductance of the channel. At the pK point of 6.0, the probability of being in either one of the two protonation states is equal, resulting in a maximal protonation variance that translates into maximal current noise [33, 73, 74]. The plot of current noise versus pH with a 1M sodium chloride bath is shown in Figure B-9, which clearly demonstrates this noise-peaking phenomena. The pH-dependent noise-peaking for an alpha toxin bathed in the 1M *potassium* chloride bath used in this thesis is overlaid on Kazianowicz's data. The noise behavior was extracted from data traces using spectral analysis methods described in [73, 74], and yields characteristics similar to those found in the sodium bath solutions. The combination of reduced gating behavior and decreased current fluctuations led to a pH bias of 8.5 for the toxin channel.

B.3.3 Salt Concentration

The salt concentration of the ionic solution is chosen to be one molar potassium chloride to increase signal current and thereby sensitivity to polymer translocation. In addition, an increased salt concentration has been shown to decrease the noise of the channel by shrinking the DeBye length to dimensions under the diameter of the channel aperture [73, 74]. The effective screening of the surface charges along the channel is postulated to suppress the interactions responsible for conductance modulations and gating [73, 74]. As illustrated in Figure B-10, the current noise of the alpha toxin has an clear inflection point at the 0.5M salt concentration that corresponds to a DeBye length of 0.4nm that is on the order of the 1.5nm channel diameter

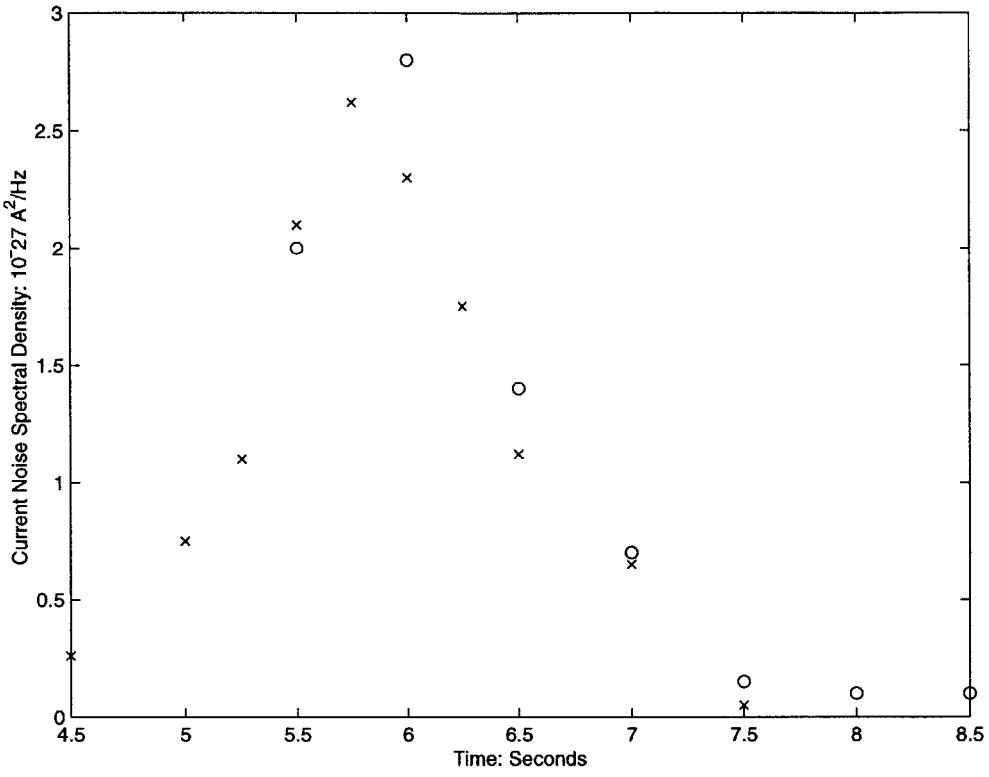

Figure B-9: The choice of bath pH has an effect on the open-channel noise. (X): The noise from conductance fluctuations passes through a maximum at the pK point for the channel protein, from Kazionowicz. (O): Verification of the pH dependent noise behavior in the 1 M KCL ionic bath used throughout this thesis.

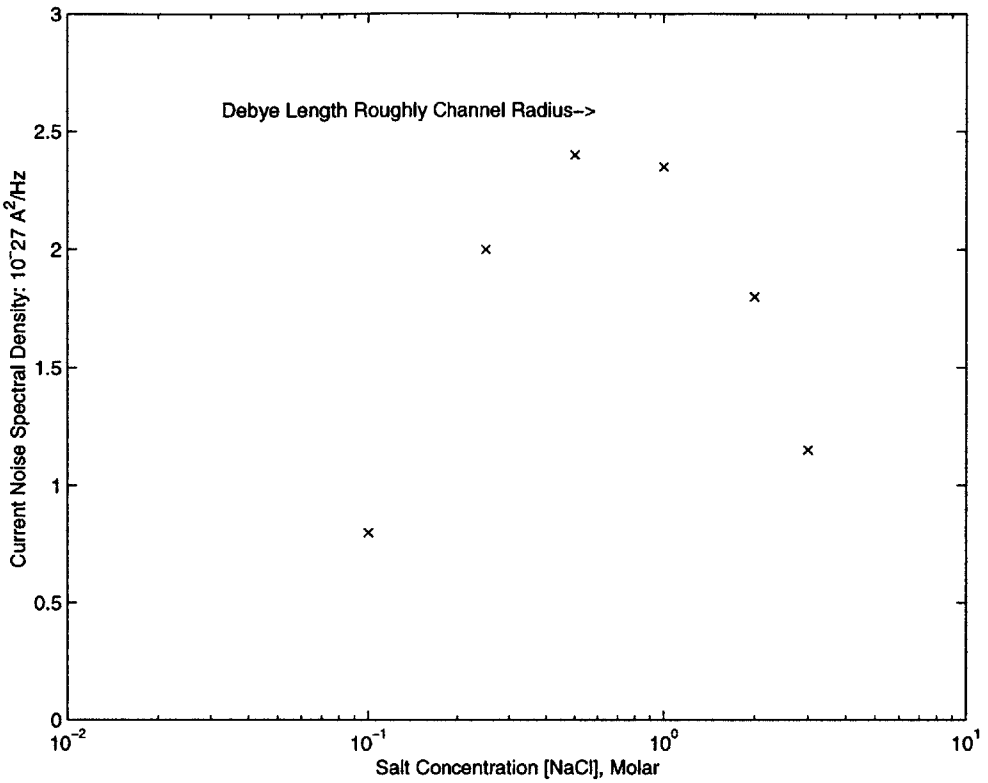

Figure B-10: The current noise is found to decrease as the DeBye length of the ionic solution becomes shorter than the alpha toxin's diameter. The surface charges of the channel wall are effectively screened, limiting their influence on channel conduction. Data reproduced from Kazionowicz.

[74]. This fact motivates salt concentrations in excess of 0.5M.

As discussed in chapter two, the use of high salt is a compromise with the conditions necessary for high fidelity sequence recognition [25]. In addition, the use of the polymerase chain reaction will require a salt concentration well below 150 mM to insure enzyme activity. The use of one molar potassium chloride in these experiments is motivated by the severe signal-to-noise limitations of the existing toxin system and the need to avoid channel gating at low salt. The hope is that future microfabricated nanopores will allow for operation at lower salt concentrations by both reducing the capacitance of the sensor so that access resistance is no longer an issue, and eliminating the origin of channel gating with alternative surface treatments [14].

B.3.4 Temperature Biasing

The temperature of the bath solution is also a degree of freedom. For the work in this thesis, the temperature is modulated to enhance DNA chemical interactions, but not to accentuate any particular physical features of the toxin channel. The properties of the toxin as a function of temperature have recently been established [111]. The channel properties, when biased with 1M KCL and pH 8.5, are found to mimic an ohmic device from 5°C to 40°C, with variations in channel conductance correlating to the conductance variations of the ionic bath [111].

B.4 Summary

This appendix has motivated the experimental procedures and bias conditions used for the toxin channels explored in this thesis. Applying the results from previous studies of pore behavior and confirming their validity with the current nanopore system, a low-noise 1.5nm aperture is available for detecting DNA translocation and developing novel approaches for genetic detection.

Appendix C

General Topologies for Measuring Conductance Fluctuations

Two general methods exist for measuring conductance fluctuations through a channel. The first, denoted current clamping, fixes the current through the pore and measures voltage fluctuations. This approach is appealing because the signal out of the detector increases as the DNA is translocating, improving the signal-to-noise. The second approach, voltage clamping, fixes the voltage across the toxin and measures the current fluctuations through the channel. This technique is useful for maintaining a steady voltage bias to avoid lipid breakdown and channel gating. Although these methods are the dual of each other, the physical characteristics of the nanopore sensor strongly motivate the use of voltage clamping topologies for the detection of DNA hybridization events.

C.1 Current Clamping

The dynamic characteristics of the current clamp make it impracticle for a nanoscale Coulter counter using a nanopore channel. The general topology of a current clamp is illustrated in Figure C-1. A current source forces I_{bias} through the toxin pore, and the channel resistance is obtained by measuring the voltage across the aperture with a high impedance buffer. The channel resistance of 10 GΩ requires a stiff current source for I_{bias}, which can be implemented with any number of feedback techniques. A more serious issue with the channel resistance

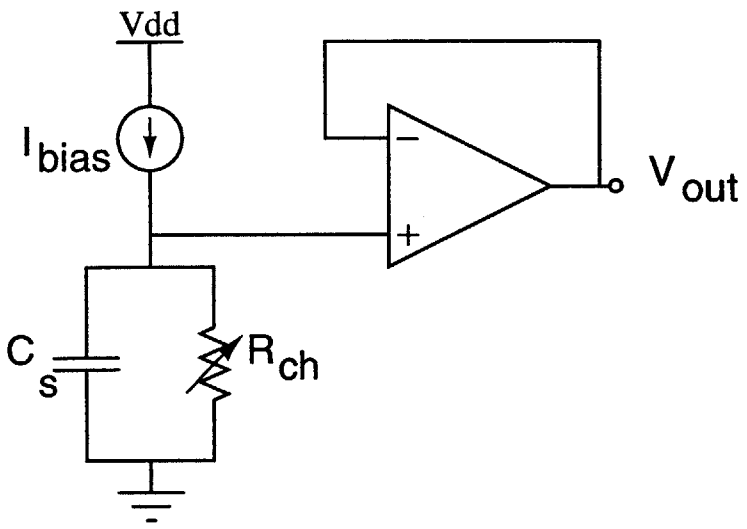

Figure C-1: The general topology for current clamp. A current source forces I_{bias} through the sensor, and the voltage across the channel is measured.

is that it creates a dominant pole on the order of 10 Hz with the parallel shunt capacitance. The charging currents for the entire nanopore impedance are limited to I_{bias}, so that dynamic regulation of the current *through the limiting aperture* is minimal beyond the 10 Hz pole. The bandwidth problem can be addressed by reducing the magnitude of either the channel resistance or the shunt capacitance. The resistor value is essentially fixed by the required dimensions of the nanopore (see Appendix B) and the ionic solution required for proper biasing, however, so improvements to the measurement bandwidth must come from reduction of the shunt capacitance.

The bandwidth of the current clamp can theoretically be improved by reducing the magnitude of the parallel source capacitance. It is assumed that simple physical scaling of the lipid membrane and reduction of parasitics has already been attempted, so the next option is to create a *negative* capacitance in parallel with the sensor. Negative capacitors are generally rare in nature, but an effective negative capacitor can be achieved with an impedance converter, as shown in Figure C-2 [24]. This implementation uses positive feedback and the Miller effect to achieve a capacitance,

$$C_{eq} = (1 - A_o)C_c,$$

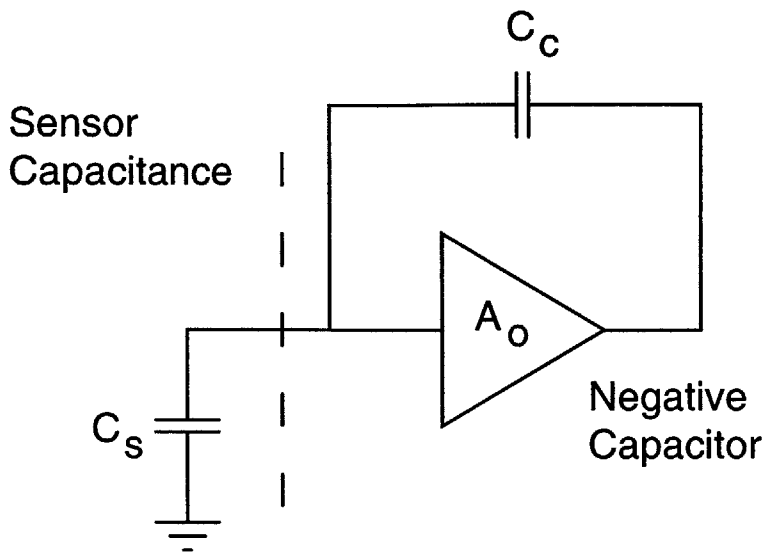

Figure C-2: Using positive feedback can "theoretically" compensate for the dynamics associated with source capacitance. The Miller effect around C_c creates a negative capacitor to cancel the source capacitance, C_s.

which acts to cancel the reactance of the sensor capacitance C_s. To maintain stability around the positive feedback loop of the impedance converter, however, the loop gain,

$$\frac{C_c}{C_c + C_s} A_o,$$

must be less than 1. Unfortunately, the loop gain approaches unity just as the negative capacitor achieves perfect cancellation of the source capacitance.

The practical limitation of this circuit arises from the need to cancel 99.9% of the sensor capacitance to obtain the specified bandwidth suitable for DNA probe detection. To meet the specified bandwidth of 25 kHz with a channel resistance of 10 GΩ, the net parallel capacitance seen by the channel must be reduced to 1 fF. This value requires an approximate loop gain of 0.999 for the negative impedance converter, placing it on the edge of stability. Unfortunately, the 1 fF shift in sensor capacitance required to set the circuit into oscillation can easily be provided by the coupling between external perturbations like a human hand and the patch

electronics, essentially guaranteeing that this compensation technique will not work in practice.

The other major drawback of the current clamp technique for use with the proposed nanopore is the relative conductance modulation observed during DNA translocation. As developed in chapter three, the quiescent voltage across the channel must be on the order of 100mV to insure DNA translocation. When a polymer passes through the pore, the conductance drops by roughly an order-of-magnitude, which results in the clamp voltage rising to approximately one volt. Beyond the issues of pore gating at higher voltages [75, 78] and the modulation of translocation rate, this transient is above the dielectric breakdown voltage of the insulating membrane [30]. The first DNA translocation event would destroy the channel sensor, rendering the technique useless.

The combination of severe bandwidth limitations and lethal voltage transients eliminates the current clamp as a viable technique for interfacing to the toxin channel. When silicon nanopores are created in the future, the use of a current clamp interface circuit may be revisited since the dioxide or nitride membrane are moderately less susceptible to dielectric breakdown [15]. The severe requirements on sensor capacitance for reasonable measurement bandwidth, however, will most likely continue to limit this topology's utility for the nanopore Coulter technique.

C.1.1 Voltage Clamping

The problem of charging the source capacitance severely limits the utility of the current clamp technique as an interface to the alpha toxin, and attempts to reduce the effect of this capacitance with a negative impedance converter lead to problems of stability. Another approach to reducing the effect of the source capacitance is to *fix* the sensor voltage and measure current fluctuations through the channel. This is the function of a voltage clamp illustrated in Figure C-3; the operational amplifier maintains the voltage bias across the pore, eliminating to first order the dynamic issues associated with modulating the source capacitor's voltage.

The superior bandwidth characteristics of the voltage clamp are more clearly demonstrated by considering the block diagram derived from Figure C-3. The reduced block diagram illustrates that the total transfer function of input current to output voltage is specified solely by

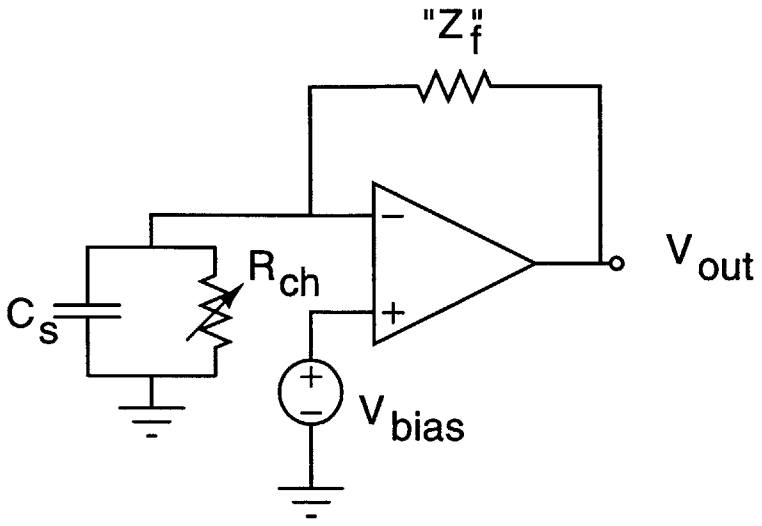

Figure C-3: The canonical voltage clamp. The operational amplifier maintains the voltage bias across the toxin sensor, eliminating the dynamic issues associated with modulating its voltage.

the feedback element Z_f, as long as the loop gain,

$$L(s) = \frac{R_{ch}}{Z_f + R_{ch}} \frac{A_o}{(1 + sR_{ch}||Z_f C_s)(1 + \tau_{op} s)},$$

is greater than one[1]. The effect of the source capacitance, C_s, is to add a lag pole into the loop gain for the system. The location of this pole is still on the order of 10Hz, but with a reasonable operational amplifier and judicious compensation, the bandwidth of the conductance measurement can be extended to over a megahertz.

The voltage clamping topology allows for wide bandwidth detection of conductance fluctuations through a capacitive sensor. In addition to eliminating the need to charge the sensor capacitance, this technique insures that the sensor bias voltage does not induce channel gating phenomena or drive the lipid into dielectric breakdown. The design challenge is to translate the canonical voltage clamp into an operational instrument. This requires the development of a low-noise, wide bandwidth operational amplifier and implementation of a suitable feedback element, Z_f.

[1]This circuit might require some stability compensation, depending on the nature of Z_f.

C.2 State-of-the-Art Implementations of a Voltage Clamp

The implementation of a voltage clamp suitable for interfacing to the toxin channel requires two components: a low-noise, wide bandwidth operational amplifier, and a low-noise, wide-bandwidth feedback element Z_f. The construction of an operational amplifier that meets the performance requirements outlined previously is a relatively straightforward design procedure, which will be demonstrated in the next chapter. A more challenging design problem is the implementation of the feedback element. This device must simultaneously provide large trans-resistance, relatively wide bandwidth, and little excess noise. Given these constraints, the successful implementation of Z_f has proven to be a difficult design problem for the order of 10 pA current fluctuations with the order of 25 kHz of measurement bandwidth [118, 131].

Resistor Feedback

A rational first approach to implementing the feedback element is to use a resistor, which will map the current fluctuations through the toxin channel into output voltages according to Ohm's law. To achieve a low-noise measurement, however, the thermal noise contributions of the resistor must be considered relative to the channel shot noise. The thermal noise of the resistor can be referred back to the input of the voltage clamp as an equivalent current source with spectral density,

$$i_n^2/\Delta f = \frac{4k_bT}{R_f}\ A^2/Hz.$$

The magnitude of this spectral density is constrained to be less than or equal to the shot noise from the quiescent current of the toxin channel,

$$i_{shot}^2/\Delta f = 2qI\ A^2/Hz.$$

To balance the contribution of these noise sources, a minimum feedback resistor of 5 GΩ is required for 10 pA of quiescent channel current.

Resistors of this magnitude suffer from several practical limitations. First, it is difficult to lower the parasitic capacitance across these resistors to less than 0.25 pF [118, 42]. This shunt capacitance, in parallel with the 5 $G\Omega$ resistor, creates an effective bandwidth of only 320 Hz

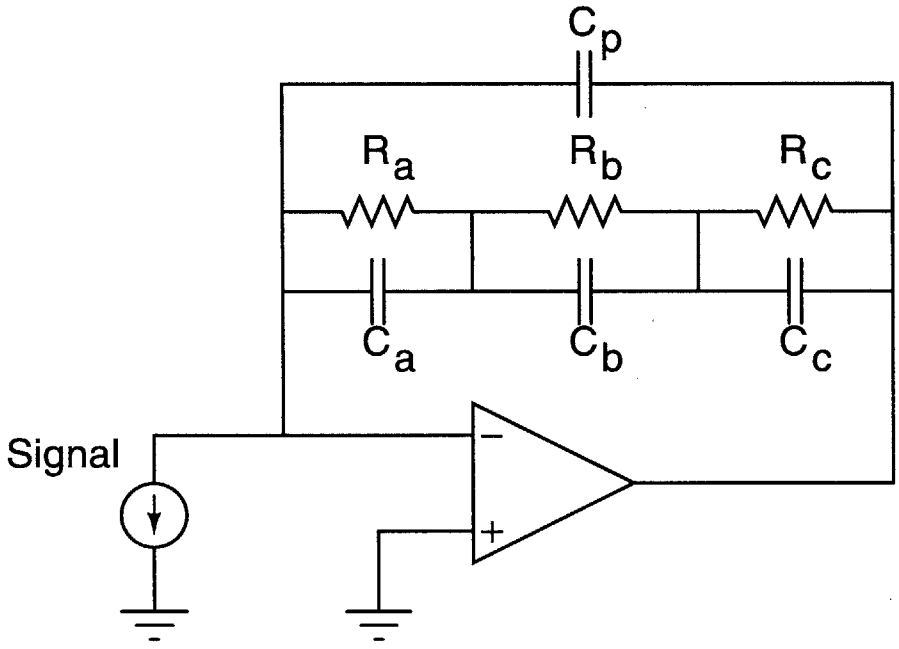

Figure C-4: The problems associated with the resistive feedback technique. The large feedback resistor, represented by R_a, R_b, R_c, forms in a lowpass network with the parasitic shunt capacitor, C_p. In addition, mismatches in the distributed shunt capacitors, C_a, C_b, C_c, can create excess noise at high frequencies as the real part of the feedback impedance decreases.

for the measurement circuit. This bandwidth is almost two orders-of-magnitude less than that specified for hybridization detection. If the effects of parasitic capacitance could be lumped into a simple shunt element, then the dominant pole could be compensated for with a single-zero "boost" circuit (high-pass filter) following the first stage of amplification. The large physical dimensions of these resistors, however, create multiple internal shunt capacitances that require complex pole-zero compensation circuits [131, 118] (Figure C-4). Even with the four pole, three zero, compensation networks found in many commercial amplifiers, a signal distortion of 5-10 % during a step response is relatively common, with bandwidth limited to 10kHz [131, 118].

The distributed RC network can also undermine the feedback resistor's ideal noise performance. If the parasitic capacitance is evenly distributed along the resistor, then the *real* part of the network, and hence the thermal noise contribution, is constant [65]. In practice, the parasitic capacitance is unevenly distributed along the resistor, leading to excess noise at higher frequencies as the real part of the resistance decreases [118].

The noise and dynamic problems associated with shunt capacitance can be addressed somewhat in a discrete design by distributing the $5G\Omega$ feedback resistor among several smaller resistors, as demonstrated with the test picoammeter in Figure C-5 [42]. This prototype picoammeter consists of a low-noise operational amplifier[2] with two options for the feedback path: a single $5G\Omega$ resistor and a distributed $5G\Omega$ resistor implemented with 5 1 $G\Omega$ series-connected resistors.

In addition to bandwidth, the distribution of the shunt capacitance across the smaller elements helps to reduce the excess noise of the resistor. This is accomplished by pushing out the mismatched dynamics that alter the real part of the impedance to higher frequencies. In practice, a 10kHz picoammeter with a $2.5G\Omega$ feedback resistor can be implemented with additional dynamic compensation, but extending this bandwidth can be challenging [118, 131].

Another drawback of the resistive feedback technique for implementing a nanoscale Coulter counter is the inability to fabricate a suitable resistive device on a silicon substrate. Typical specifications for modern integrated poly resistors run from 1-to-10 kΩ per square [3, 2]; a $5G\Omega$ resistor would require 500,000 series-connected squares to fabricate. Assuming a square side of $1\mu m$, this requires a resistor half a meter long! The distributed capacitance associated with

[2]The design features of this amplifier are similar to those discussed in chapter four with the LNA.

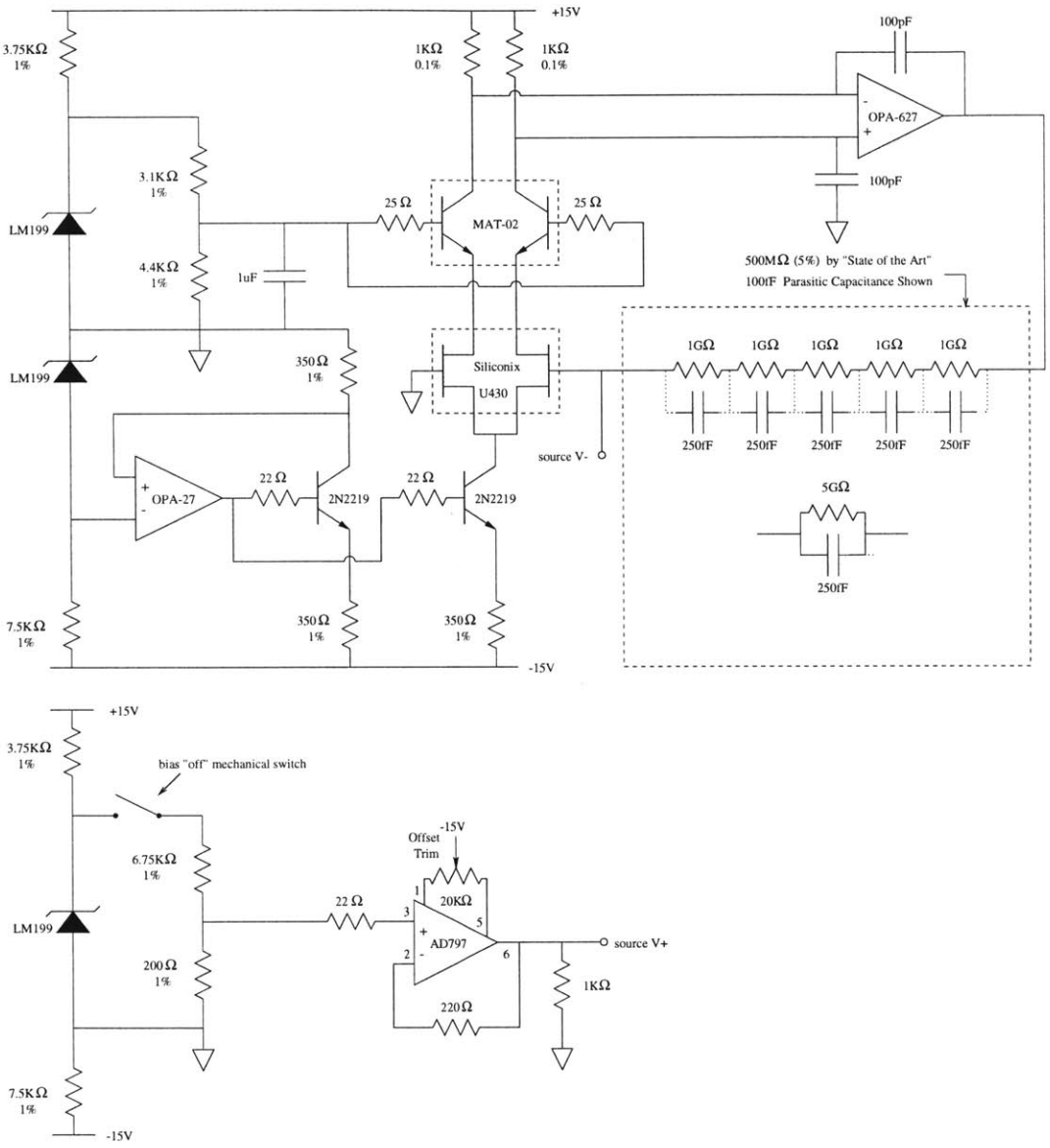

Figure C-5: A prototype electrometer using a $5G\Omega$ feedback resistor. To improve the noise and dynamic characteristics of the feedback resistor, it can be distributed among five $1G\Omega$ series resistors.

this device and the folding required to fit it into a reasonable area would severely undermine the noise and dynamic performance of this device. Alternative approaches using transistors or diffused channels are also problematic, once again due to the relatively high resistance required for adequate noise performance, shunted by substantial parasitic capacitance [2]. The severe bandwidth and noise limitations imposed by $G\Omega$ resistors in discrete designs, coupled with the inability to fabricate suitable resistors on a silicon wafer, motivates the consideration of alternative feedback schemes.

OptoElectronic Feedback

The practical limitations of the resistive feedback technique have fostered an interest in alternative methods of supplying feedback current; one of the more promising methods is the use of photon-induced currents flowing through a reverse-biased pn junction [119, 120, 121]. The concept for this approach is illustrated in Figure C-6. A voltage controlled current source, G_o, at the output of the amplifier drives an LED. Light emitted from the LED is weakly coupled into a reverse-biased pn junction, providing the necessary charge balance at the inverting node of the amplifier. In practice, the reverse-biased junction is usually the gate-drain region of the input JFET, which prevents additional capacitance and leakage current from another shunt element at the picoammeter input [119]. A potential advantage of the optoelectronic feedback loop is the ability to scale with integrated instrumentation, since the light can be coupled into the circuit from off-wafer without adding significant capacitance.

The high gain for this circuit is obtained by weakly coupling the LED and pn detector. Modeling the effective coupling parameter as a dimensionless β, the effective trans-resistance for this circuit is

$$R_f \approx \frac{1}{\beta G_o}.$$

In general, G_o^{-1} is on the order of 100 Ω, and the light is coupled with β on the order of 10^{-6} to 10^{-10}, resulting in effective resistances of 10^8 to $10^{12}\Omega$. The dynamics of the components in this circuit are fast, which results in an effective multi-$G\Omega$ resistor with an inherent bandwidth of several megahertz [119, 122]. The loop bandwidth for the voltage clamp is still compromised by the lag filter imposed by the effective R_f reacting with the source capacitance, but this could in principle be compensated with a small shunt capacitor in parallel with the optical feedback

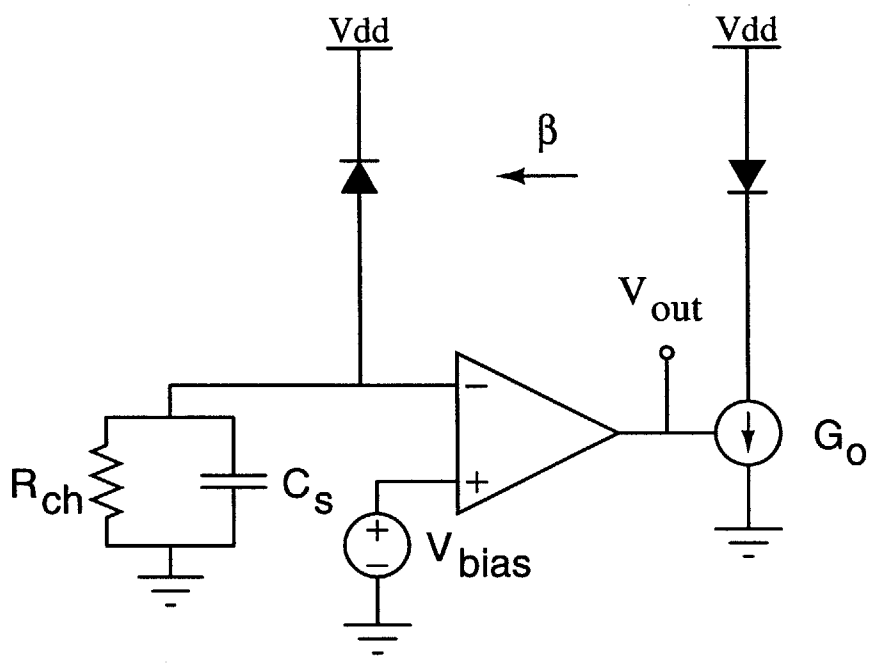

Figure C-6: The use of optical feedback for charge balancing. By weakly coupling the light source and reverse-biased junction (β), an large effective resistance with wide bandwidth can be created.

stage and a boost circuit following the input preamplifier.

Although the optoelectronic feedback technique creates wide bandwidth elements with a high effective transresistance, several practical limitations have limited the techniques utility in voltage clamp circuits sensitive to pA currents. The first issue that many authors find troublesome is the "increased" white noise of this technique [119, 121]. The opto-feedback element will be shot noise limited, which contributes "excess" noise for large sensor currents when compared to the theoretical thermal noise contribution from an equivalent ohmic resistance. This view is a bit extreme, however since the optical feedback's shot noise contributes roughly the same noise power as the sensor noise which is also shot-noise limited. In general, this is a reasonable design specification. Two more serious drawbacks can truly undermine the application of optoelectronic feedback. First, the LED/pn junction combination does not obey a linear function of β/G_o with varying feedback currents [119]. The effect of this non-linearity is to create a

signal dependent shift in the effective resistance of the feedback path. The resulting distortion is aggravated by the shift the location of the feedback lag pole, making the frequency compensation (boost) circuit and the lag pole mismatch [119]. It should be possible, however, to compensate for non-linearity of the LED/pn detector with minor loop feedback. In fact, recent attempts at this correction are bearing some results in commercial instrumentation [122]. In addition, for the signal perturbations associated with hybridization detection with a channel, a small amount of nonlinearity is acceptable.

A more significant problem with optical feedback is the "after-effect", which is the continued flow of currents into the gate node after the light source is extinguished [119, 133]. The origin of this current is poorly understood, but is thought to come from both the slow diffusion of charges from non-depleted areas of the junction and the slow decay of activated surface states [133]. The dynamics of the after-effect can be modeled as a series inductor/resistor network in parallel with the effective resistance, β/G_o, of the optical feedback path[3]. With this model, illustrated in Figure C-7, the after-effect is seen to create transient responses akin to those of dielectric absorption in capacitors. The after-effect shunt path can supply several picoamps of transient current over several hundred milliseconds, creating a significant error signal when referred to the input of the voltage clamp [119, 121]. The effective dynamics of the after-effect are similar to a high-pass circuit, which add an effective derivative term to the feedback characteristics that can lead to excess noise.

Circuit compensation techniques to suppress these transients are problematic since the dynamics are poorly characterized, and in practice have not been able to reduce transients by more than an order of magnitude [122]. Attempts to address the after-effect with improved device fabrication and modeling are beginning to yield some results [133, 119], and in the future may yield devices suitable for a picoammeter topology. To date, however, the best feedback performance can be obtained with a capacitive device.

Capacitive Feedback

The practical limitations of measuring 10pA currents motivate the use of capacitive feedback. Capacitors are essentially ideal feedback elements, with low-noise, excellent linearity and wide

[3]This view is in the spirit of Dow's model for dielectric absorption, presented in the next section [40].

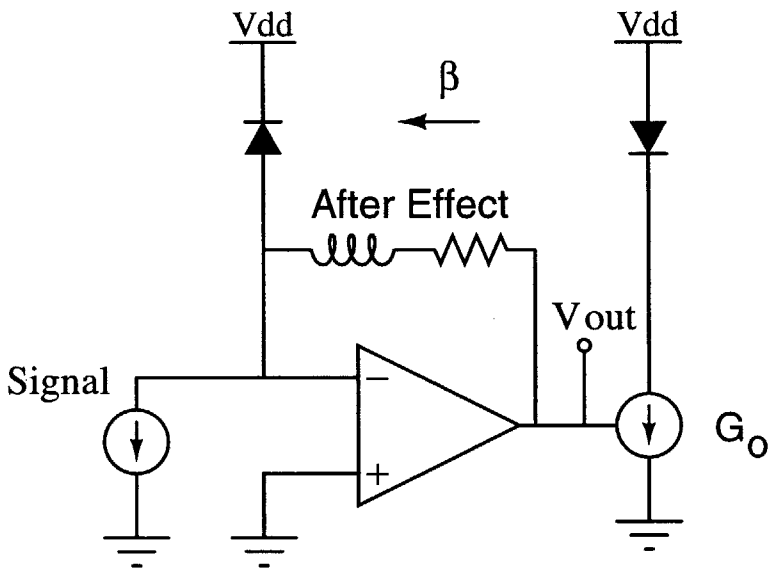

Figure C-7: Modeling the after-effect in the optical feedback path. The parallel L-R path models the continued flow of charge into the input after the light source is extinguished.

bandwidth [65, 118, 119, 127, 128, 42]. In addition, high quality capacitors can be integrated in standard silicon processes, making the scaling properties of this topology particularly appealing [65].

A canonical voltage clamp that uses capacitive feedback is illustrated in Figure C-8. A feedback capacitor C_f integrates the signal current I_s. The bandwidth of the integrator is compromised by only the voltage division from the feedback capacitor and the source capacitance, which lowers the operational amplifier's cross-over frequency by a factor of

$$\frac{C_f}{C_f + C_s}.$$

This loop attenuation can be overcome by readjusting the compensation of the operational amplifier, yielding integrators with crossover frequencies in the megahertz range without excessive design effort.

The output of the integrator is fed into a high-pass differentiator circuit that restores the proper time/frequency behavior. The coupling of the integrator and differentiator yields an effective trans-resistance of

$$R_{eff} = \frac{R_d C_d}{C_f}.$$

The parameter values used for the picoammeter are generally determined by the noise specifications for the interface circuit. The value of C_f is generally chosen to be roughly 1/10 of the source capacitance as a trade-off between minimizing the excess noise contribution at high frequencies and the required frequency of capacitor resets [118]. The values of C_d and R_d can be derived from consideration of the noise contribution of the differentiator resistor. The input-referred current noise of R_d is calculated to be

$$i_n^2/\Delta f = \frac{4k_bT}{R_d}(\frac{C_f}{C_d})^2 \ A^2/Hz.$$

Assuming a 1nF differentiator capacitor and 1pF integration capacitor are used, the required R_d to yield an input-referred noise source equivalent to 10pA of shot noise is only 5 $k\Omega$. The ability to lower R_d substantially results from the low-noise current gain of the integration circuit, C_d/C_f, prior to amplification with the "noisy" resistor in the feedback loop.

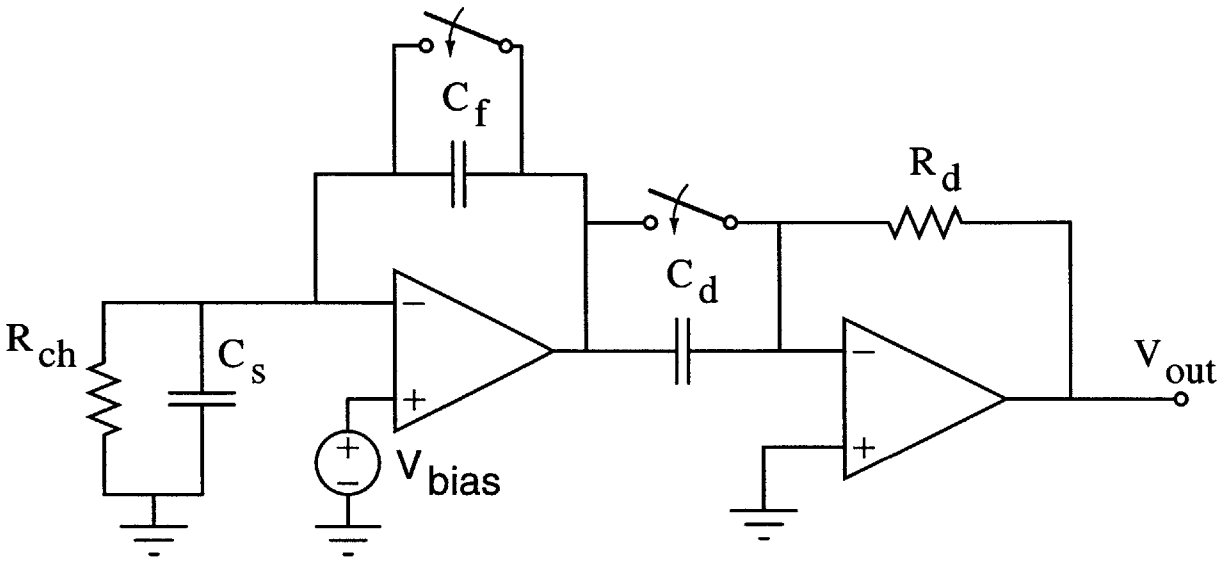

Figure C-8: The use of capacitive feedback for voltage clamping. The ratio of the capacitors provides a low-noise current gain of C_d/C_f, which is then converted to an output voltage through R_d. Although this topology offers excellent performance, the capacitors C_f and C_d must be periodically reset in the presence of a DC current.

As a final consideration, the time constant τ_d in the differentiator feedback loop is still relatively small at $R_dC_d \approx 5\mu s$. A lag time constant on this order insures that a bandwidth of 50-100 kHz is still possible with the picoammeter. By leveraging the near-ideal characteristics of capacitors, the coupled integrator/differentiator topology has consistently yielded the best simultaneous noise, bandwidth and linearity performance in charge and current measuring instruments [118, 127, 128].

C.2.1 The Chink in the Armor: Resets

The major limitation of the integrator/differentiator amplifier is the need to periodically reset the capacitors in the presence of a DC current [118, 131, 127, 128, 119]. During resets, the output of the picoammeter bears no relation to the input, which can result in a significant dead-time. To hold this dead-time to a minimum, a number of designs have been explored that

attempt to make the reset duration as short as possible. Of these techniques, the use of diode and transistor current switching into the high impedance node has shown the greatest promise, with integrator reset times on the order of $1-10\mu s$ being achieved with research instrumentation [49, 48, 128]. Optoelectronic pulse feedback has also demonstrated fast capacitor discharges, but the after-effect can extend reset transients for several tens of milliseconds [133, 128, 49]. More extreme approaches, including pulsed-avalanche breakdown of the input JFETs [45] and momentary forward-biasing of the JFET pn junctions [47, 46], have attempted to improve transient performance. The large input voltage transients of these approaches are generally incompatible with the breakdown specifications of the insulating membranes, however, and the techniques do not appear to yield substantial dynamic improvements in discharging capacitor discharging [47, 46, 45].

C.2.2 Additional Problems with Resets

Reasonable techniques exist that can reset the integrator capacitor on the order of 1-10 μs, and perhaps these transients can be additionally lowered with improved operational amplifiers, switching circuits, and integrated instrumentation. However, the instrument dead-time is not the only concern associated with discontinuous resets.

Resetting the Differentiator

The output waveform of the integrator must be filtered with a high-pass differentiator in order to restore the proper signal characteristic. The differentiator's capacitor must be scaled by several orders of magnitude with respect to the integrator capacitor to obtain sufficient current gain in the first stage of amplification. The value of a typical differentiator capacitor is 10nF, which requires a 100mA charging current to discharge 10V in 1 μsec. Currents of this magnitude are obtainable, but reset circuits are generally limited to approximately 10mA, 10 μsec resets in practice [118]. The reason for this extended reset duration is the finite bandwidth of the differentiators, which is limited by the $5\mu s$ time constant of the lag pole, τ_d. τ_d limits the settling time of the reset transients to the order of 50-100 μsec, resulting in little gain for a faster initial capacitor discharge. Differentiator resets, in fact, are the dominant contribution to instrument dead-time [118].

Maintaining Sensor Bias

The voltage at the inverting node of the amplifier should not deviate significantly from the bias voltage during a reset. The bias voltage controls the rate at which DNA translocates through the pore, and this rate should be maintained or, at minimum, effectively controlled. In addition, the lipid membrane undergoes dielectric breakdown at 300mV, and will not survive transients in excess of this voltage [30]. To demonstrate the concerns of voltage transients across the sensor, the previous electrometer shown in Figure C-5 was driven with a 100pA square wave. During the slewing of the opamp, the inverting node voltage rises to greater than 1 Volt as the loop effectively loses control of the node. Transients of this magnitude pose a significant threat to the break-down of the insulating membrane, as well as undermining control of the sample polymer's translocation rate. The relatively low transconductance of the JFET input pair can result in a significant voltage deviation during a reset transient, and care must be taken when resetting the capacitor to restrict the magnitude of this voltage spike by reducing the rate of the capacitor discharge.

Dielectric Absorption

The dielectric absorption properties of capacitors are accentuated by the requirement of rapid resets in combination with relatively slow integration intervals. Although the actual mechanisms of dielectric absorption are poorly understood, the effects can be modeled as an equivalent shunt RC network as illustrated in Figure C-10. This model, proposed by Dow, gives a handle on designing circuitry to minimize or compensate for dielectric absorption [40]

The equivalent dynamic response for this capacitor is

$$C_{dow} = \frac{1}{C_f} + \sum_{k=1}^{m} \frac{C_k}{1 + R_k C_k s},$$

where the range of m can be selected to accurately estimate a capacitor's dynamic behavior [41]. In a typical voltage clamp circuit attached to a toxin channel, the integrator and differentiator charge relatively slowly at a rate of 10-100 V/sec. This slow voltage ramp allows for the shunt branches of the Dow model with time constants faster than 10-100msec to effectively charge their capacitances. The reset interval lasts for a duration of only 10-50 μsec, however, and

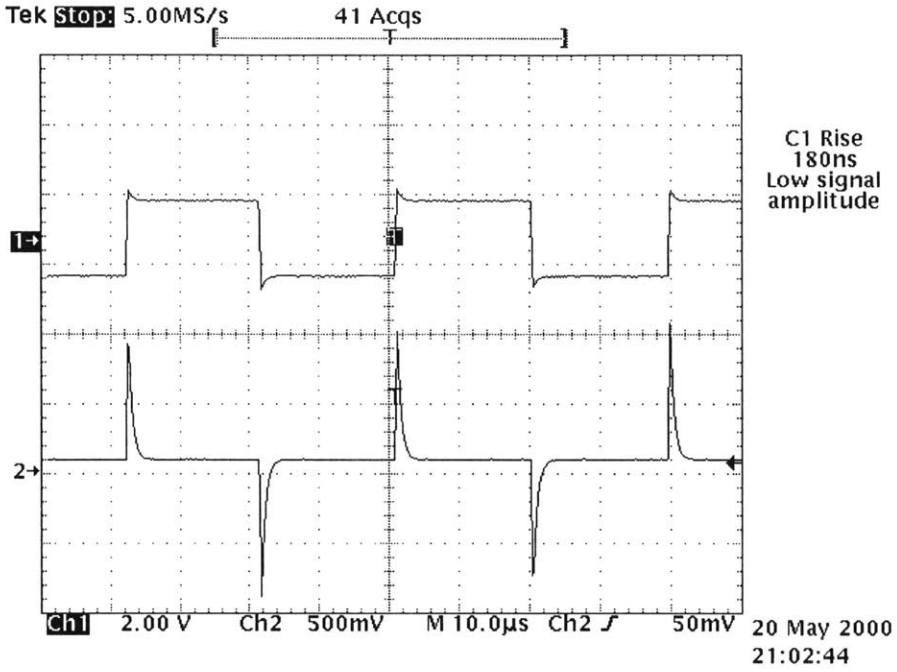

Figure C-9: The voltage transient on a low-noise picoammeter during a fast transient. Top trace: The 100pA command signal; Bottom trace: The resulting picoammeter output. If the operational amplifier begins to slew, the bias voltage across the sensor can rise dramatically, potentially leading to dielectric breakdown of the lipid membrane.

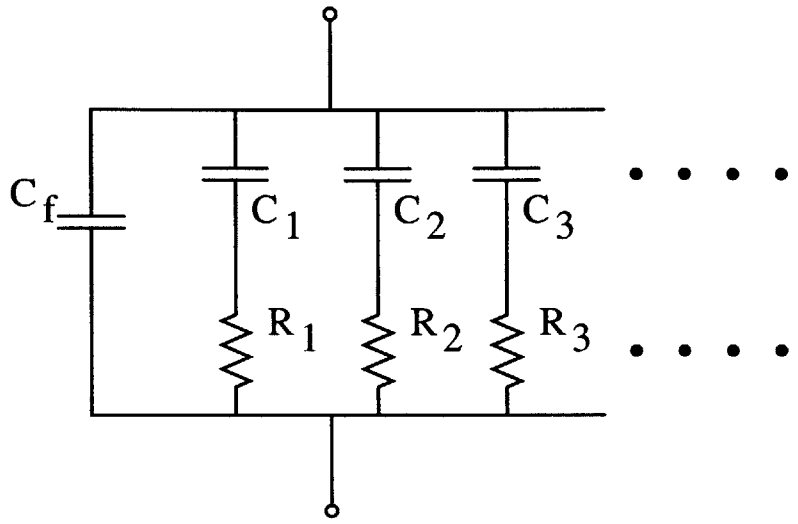

Figure C-10: Dow's model for dielectric absorption in a capacitor. The charge relaxation characteristics of the capacitor are modeled by an infinite series of shunt R-C branches.

only the shunt elements with time constants *smaller* than this value can requilibrate during the reset interval. The shunt elements with *intermediate* time constants will decay as a sum of exponentials, with time constants up to 100msec superimposed on top of the actual signal waveform. Although the transient effects of dielectric absorption can be compensated for with additional circuitry, these methods require a reasonable model for the shunt elements, and improving performance by better than a factor of ten is difficult [41, 42].

Appendix D

Circuit Schematics

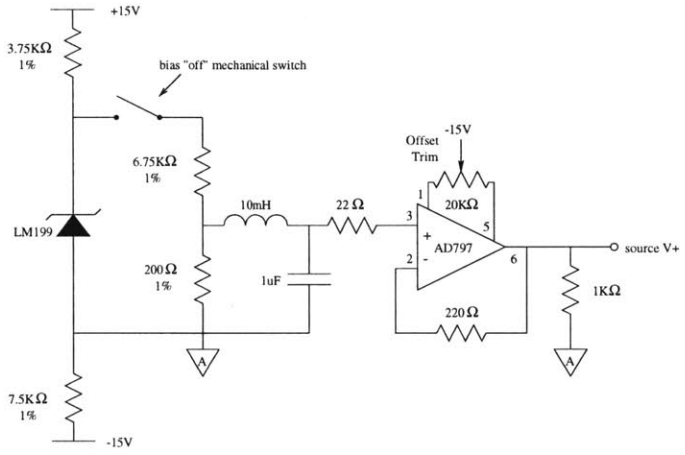

Figure D-1: The biasing circuit for the hourglass integrator.

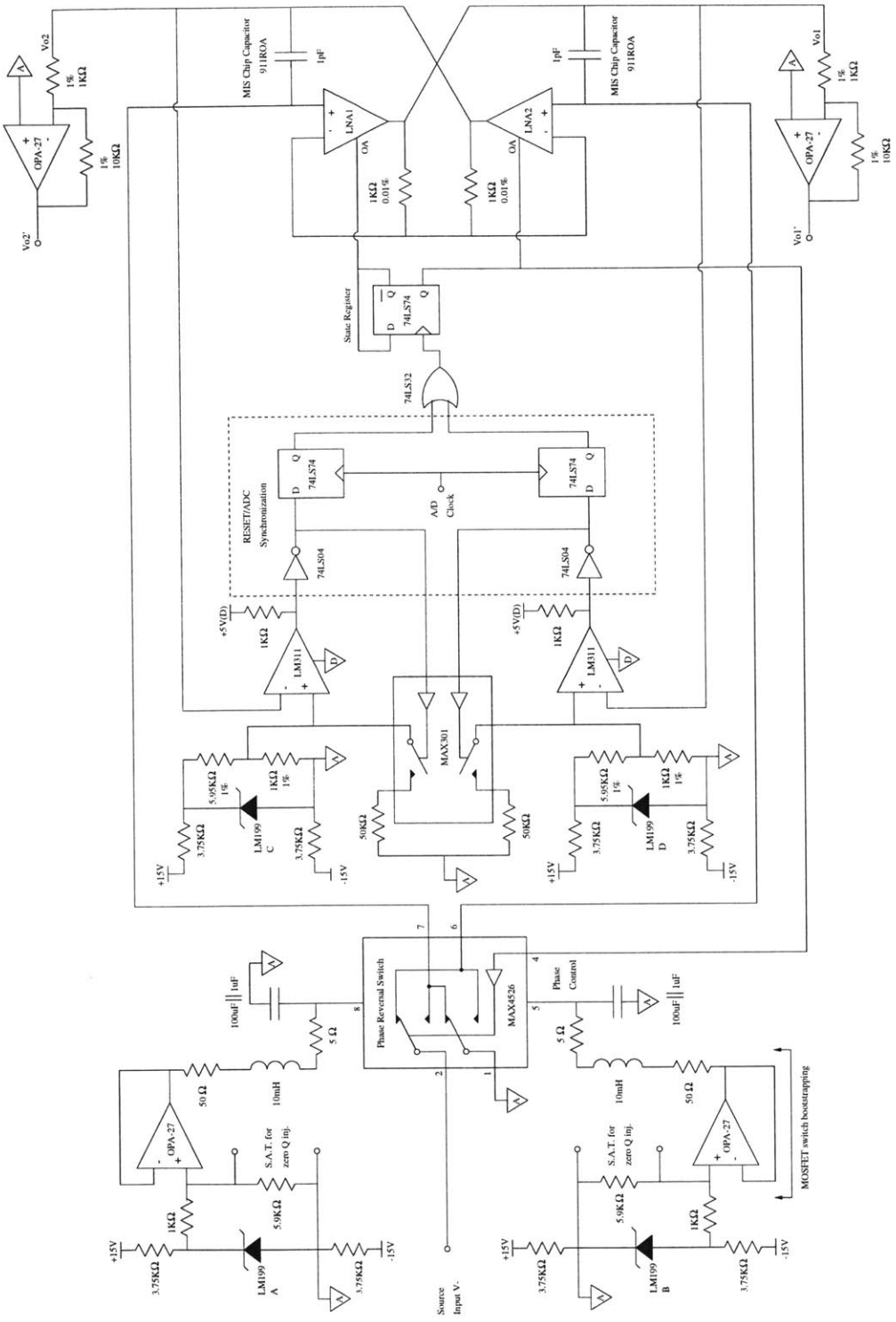

Figure D-2: The schematic for the hourglass integrator.

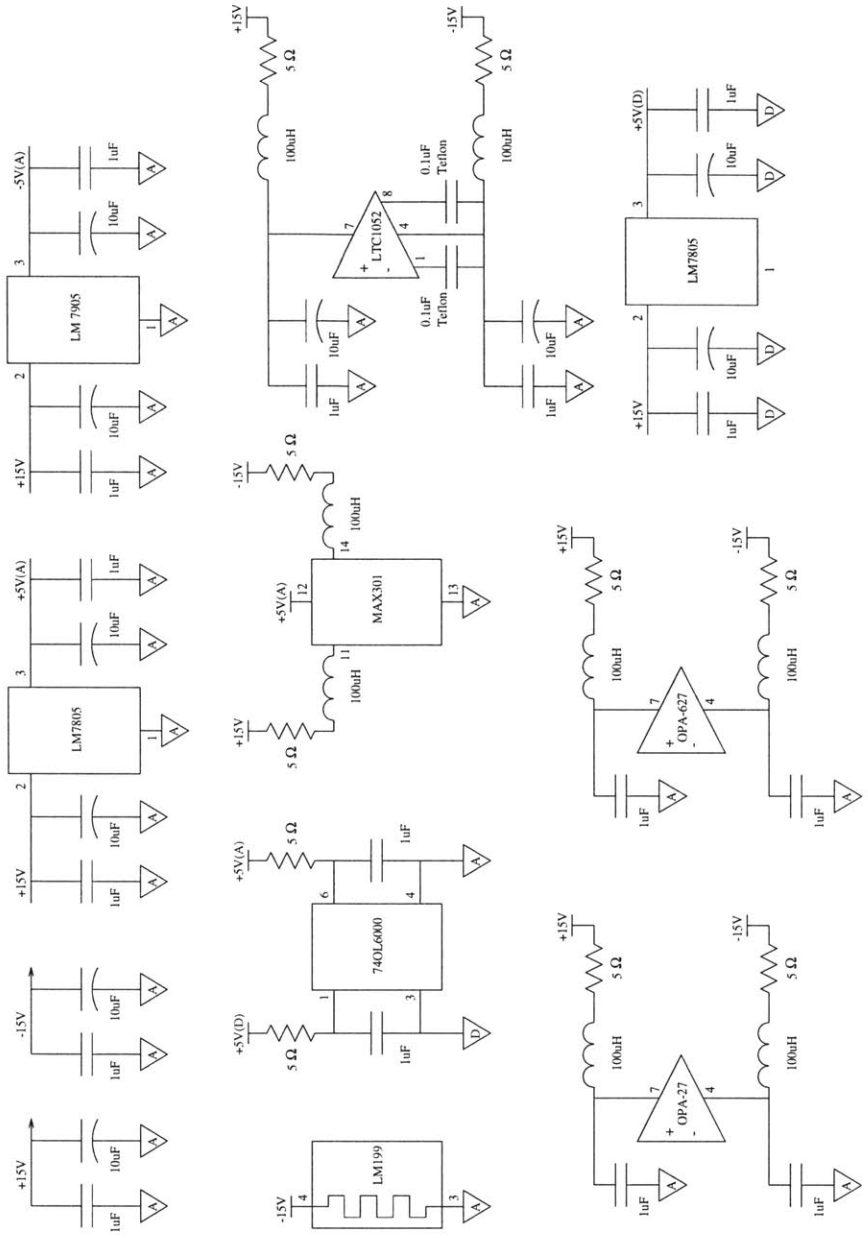

Figure D-3: Power supply connections for the hourglass integrator.

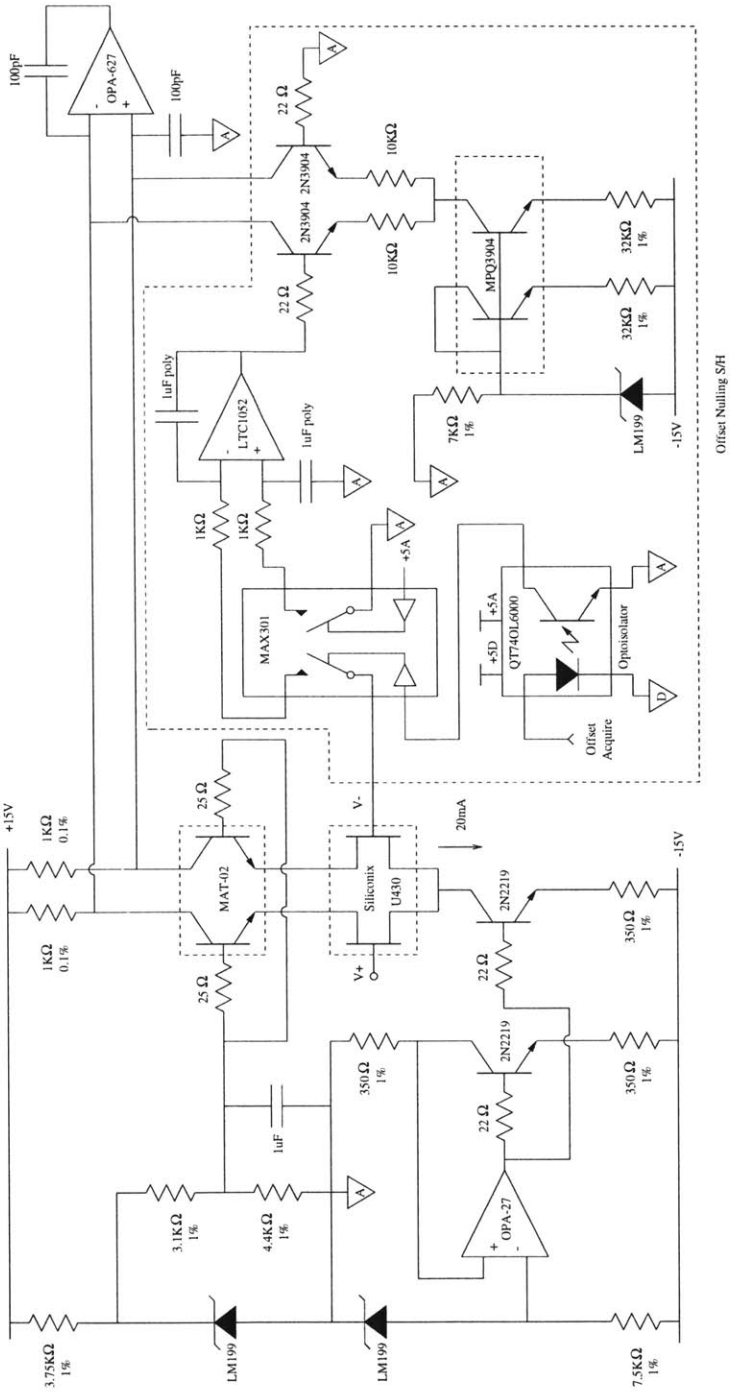

Figure D-4: The low-noise operational amplifier for the integrator (LNA).

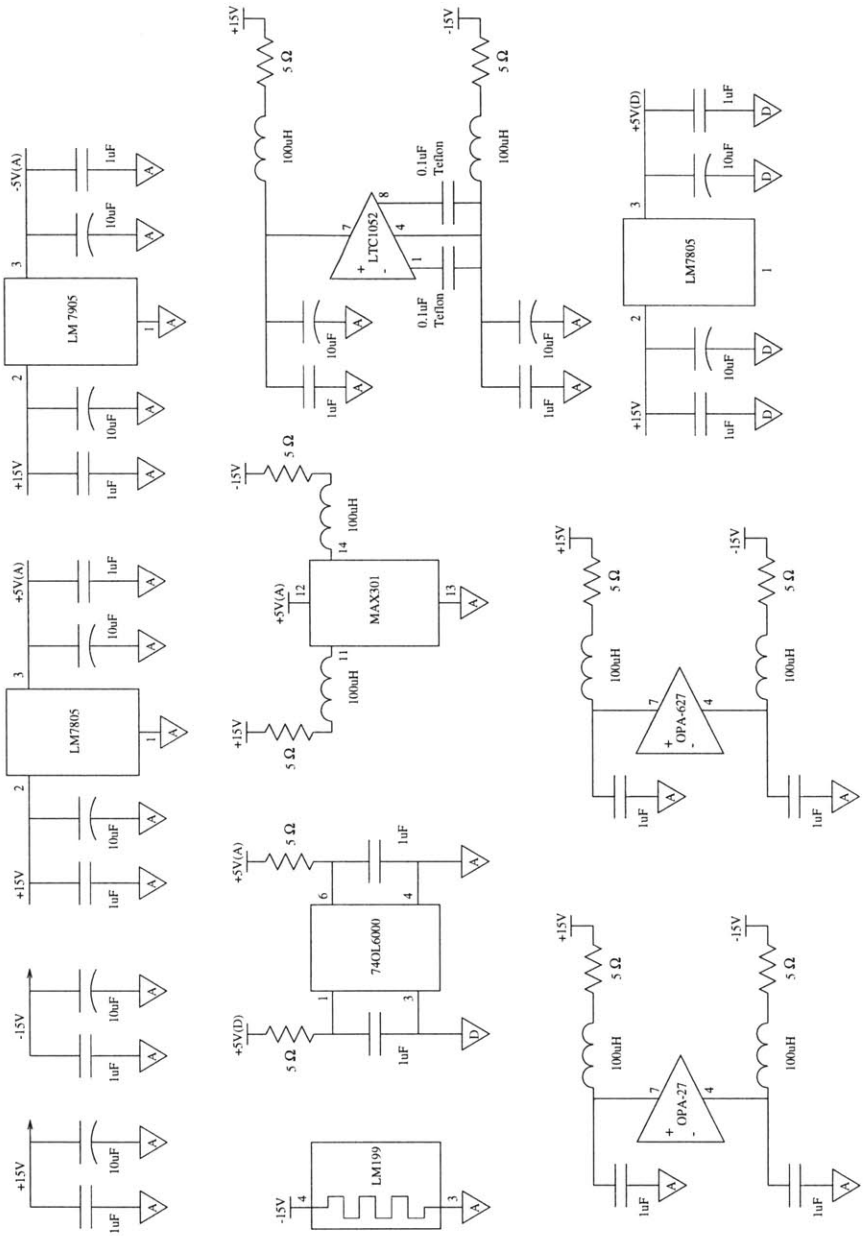

Figure D-5: Power supply connections for the LNA.

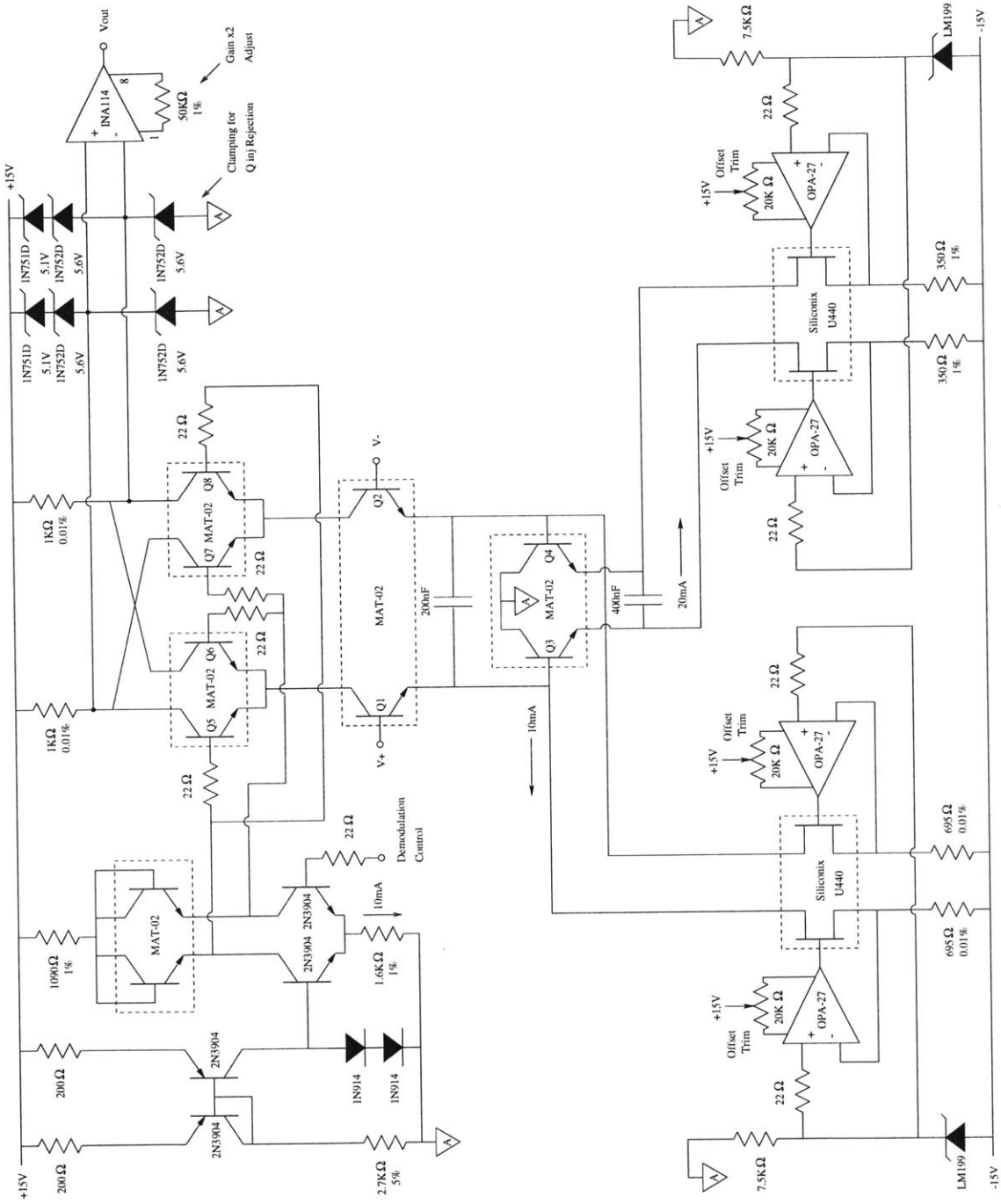

Figure D-6: The prototype current conveyor for wide bandwidth, low noise differentiation and demodulation.

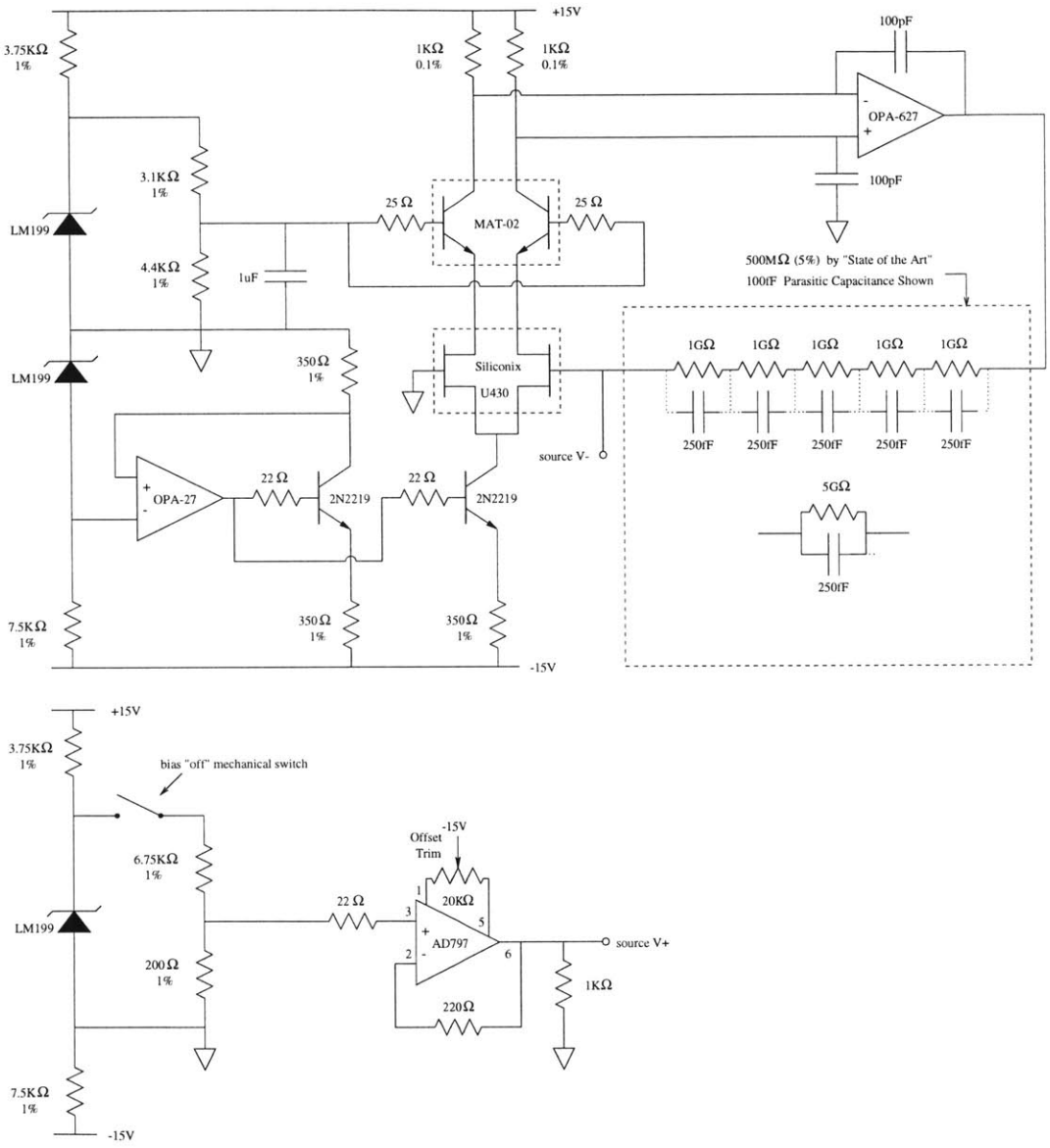

Figure D-7: A prototype electrometer using a $5G\Omega$ feedback resistor. To improve the noise and dynamic characteristics of the feedback resistor, it can be distributed among five $1G\Omega$ series resistors.

Appendix E

Software Code

E.1 MATLAB Code

E.1.1 axoread.m

This code transforms the Axon Binary Code for translocation events into an ASCII code readable by MATLAB; it is provided on the web by MATHWORKS.

```
function        r=axoread(fname,size,numchan)

%AXOREAD  Reading of Axotape/PClamp data files
%
%Syntax R = axoread(FNAME[, SIZE[, NUMCHAN]]);
%
%Input  FNAME   File name including file path
%       SIZE    Number of data points to read per channel [ALL]
%       NUMCHAN Number of AD-Channels to read   [ALL]
%
%Comment        Program is only tested for Axotape, continuous recording
%
%       (c) A.K. 5.8.1996
```

```
fid=fopen(fname);

disp('*******************************************************');
h=fread(fid, 4, 'char');
disp(['File Type: ' setstr(h') ' Version ' num2str(fread(fid, 1, 'float'))]);

fseek(fid, 10, 'bof');
nsamples=fread(fid, 1, 'long');
disp(['Number of Samples: ' num2str(nsamples)]);

nignore=fread(fid, 1, 'int16');

% Data format
fseek(fid, 100, 'bof');
df=fread(fid, 1, 'int16');

fseek(fid, 120, 'bof');
nchan=fread(fid, 1, 'int16');
disp(['Number of Channels: ' num2str(nchan)]);
if nargin<3, numchan=nchan; end
if nargin<2, size=nsamples/nchan; end

fseek(fid, 122, 'bof');
sample=fread(fid, 1, 'float');
disp(['Sample Interval (us) ' num2str(sample)]);

fseek(fid, 244, 'bof');
ADCRange=fread(fid, 1, 'float');
fseek(fid, 252, 'bof');
ADCResolution=fread(fid, 1, 'long');
```

```
counts2volt=ADCRange/ADCResolution;
% Factor 1/4 determined empirically for Axotape files
counts2volt=counts2volt/2;

fseek(fid, 294, 'bof');
h=fread(fid, 16, 'char');
disp(['Created with ' setstr(h')]);
h=fread(fid, 56, 'char');
disp(['User comment: ' setstr(h')]);

fseek(fid, 602, 'bof');
h=fread(fid, 16, 'char');
disp(['User units: ' setstr(h')]);

fseek(fid, 922, 'bof');
scalef=fread(fid, 1, 'float');
disp(['ScaleFactor 0: ' num2str(scalef*1000) 'mv/' setstr(h(1:8)')]);
for i=2:nchan
    scalef=[scalef fread(fid, 1, 'float')];
end %for i
disp('*******************************************************');
disp('Important: Allways check correct scale by comparing with original file.')

fseek(fid, 2048+2*nignore, 'bof');
if df==0,
   h=fread(fid,size*nchan,'int16').*counts2volt;
elseif df==1,
   h=fread(fid,size*nchan,'float').*counts2volt;
end %if
fclose(fid);
```

```
% Each channel in seperate column
r=zeros(length(h)/nchan, numchan);
for i=1:numchan
    r(:,i)=h(i:nchan:length(h))./scalef(i);
end %for i
r=r';
```

E.1.2 getcounts.m

This is a function to extract the events within a defined region of an EVENT PLOT that correspond to a specific DNA polymer type. Used for analyzing the hybridization experiments of chapter two.

```
function [SUBSET]= getcounts(DATA, IHI, ILO, TMIN, TMAX)
%This is a function to extract the events within a defined region of
%an EVENT PLOT that correspond to a specific DNA polymer type.

%DATA must is stored in a 2-dimensional linear array, provided by
%chop.m, where each index point stores the mean current and the
%translocation time for each event.

%Denison 1999

%Get the total number of events

totEvents=size(DATA);
j=1;

%Now sort the DATA according to the limit box defined by
%ILO, IHI, TMIN, TMAX; if event falls into the box,
```

```
%store in a new array subSET.

for i = 1:totEvents,

if ((DATA(i,1)<IHI)&(DATA(i,1)>ILO)&(DATA(i,2)<TMAX)&(DATA(i,2)>TMIN))
subSET(j,1:2)=DATA(i,1:2);
j=j+1;
end
end

SUBSET=subSET;

%Statistics can now be performed on the event counts.
```

E.1.3 gettransient.m

This is a function to extract the deterministic transients from within a defined region (SAMPLES) of the DATAstream.

```
function [TRANS]= gettransient(DATA, RESINDEX, SAMPLES)
%This is a function to extract the deterministic transients
%from within a defined region (SAMPLES) of
%the DATAstream.

%DATA must is stored in a 1-dimensional vector,
%with the integrator state changes designated in another vector
%designated by RESINDEX.

%The deterministic transient is stored in a two-dimensional
%array, where one column is the state transition from 1->2,
```

```
%and the second column is the state transition from 2->1.

%Denison 1999

%Get the total number of resets

totResets=size(RESINDEX);
if (mod(totResets(2), 2)==0),
totResets=size(RESINDEX);
else
totResets=size(RESINDEX)-1;
end

Resets=totResets(2)/2;

%Initialize transient vectors

state12trans=zeros(1,SAMPLES+1);
state21trans=zeros(1,SAMPLES+1);

j=1;

%Now average the DATA according to the time indices in RESINDEX

%Do 1->2 transitions

for i=1:Resets,
state12trans(1:SAMPLES+1)=state12trans(1:SAMPLES+1)+
DATA((RESINDEX(2*i)-SAMPLES/2):(RESINDEX(2*i)+SAMPLES/2));
end
```

```
%Do 2->1 transitions

for i=1:Resets,
state21trans(1:SAMPLES+1)=state21trans(1:SAMPLES+1)+
DATA((RESINDEX(2*i-1)-SAMPLES/2):(RESINDEX(2*i-1)+SAMPLES/2));
end

%Map the final averages into output array:

TRANS(1,1:SAMPLES+1)=state12trans(1:SAMPLES+1)./Resets;
TRANS(2,1:SAMPLES+1)=state21trans(1:SAMPLES+1)./Resets;

%These transients can now be subtracted from the data.
```

E.1.4 uwrap.m

This is a function to unwrap the chopped signal waveform from the hourglass integrator. The digitized DATA is demodulated with the transition points specified in RESINDEX. The deterministic transients are stored in the 2-dimensional array TRANS as well as the scale and offset corrections, CALSCALE and CALLOFF, which are all used to correct for deterministic errors.

The functionality of this algorithm is demonstrated with the test waveforms illustrated below.

```
function [UWRAPDATA, Resets]= unwrap(DATA, RESINDEX, TRANS, CALSCALE, CALLOFF)
%function [UWRAPDATA]= unwrap(DATA, RESINDEX, TRANS, CALSCALE, CALLOFF)
%This is a function to unwrap the chopped signal waveform from the hourglass integrato
%The digitized DATA is demodulated with the transition points specified in RESINDEX.
%The deterministic transients are stored in the 2-dimensional array TRANS
%as well as the scale and offset corrections, CALSCALE and CALLOFF, which
```

```
%are all used to correct for deterministic errors.

%Denison 2000

%Get the total number of resets
totResets=size(RESINDEX);
if (mod(totResets(2), 2)==0),
totResets=size(RESINDEX);
else
totResets=size(RESINDEX)-1;
end

Resets=totResets(2)/2;

%Initialize the unwrapped data vector

UWRAPDATA=DATA;

%Do 1->2 transitions
%Need to autocalibrate, as well as invert the signal

for i=1:Resets,
UWRAPDATA(RESINDEX(2*i-1):RESINDEX(2*i))=-CALSCALE(1)
*(DATA(RESINDEX(2*i-1):RESINDEX(2*i)) - CALLOFF(1));
end

%Do 2->1 transitions
%Only need to autocalibrate

for i=1:Resets-1,
```

```
UWRAPDATA(RESINDEX(2*i):RESINDEX(2*i+1))=CALSCALE(2)
*(DATA(RESINDEX(2*i):RESINDEX(2*i+1)) - CALLOFF(2));
end

%Now subtract off the transients
%Get length of transient to subtract off

Length=size(TRANS);
tranLength=Length(2);

%Do 1->2 transitions

for i=1:Resets,
UWRAPDATA2(RESINDEX(2*i-1):RESINDEX(2*i-1)+tranLength)=
UWRAPDATA(RESINDEX(2*i-1):RESINDEX(2*i-1)+tranLength) - TRANS(1);
end

%Do 2->1 transitions

for i=1:Resets-1,
UWRAPDATA2(RESINDEX(2*i):RESINDEX(2*i)+tranLength)=
UWRAPDATA(RESINDEX(2*i):RESINDEX(2*i)+tranLength) - TRANS(2);
end

%Data is now demodulated, with the deterministic waveforms subtracted.
```

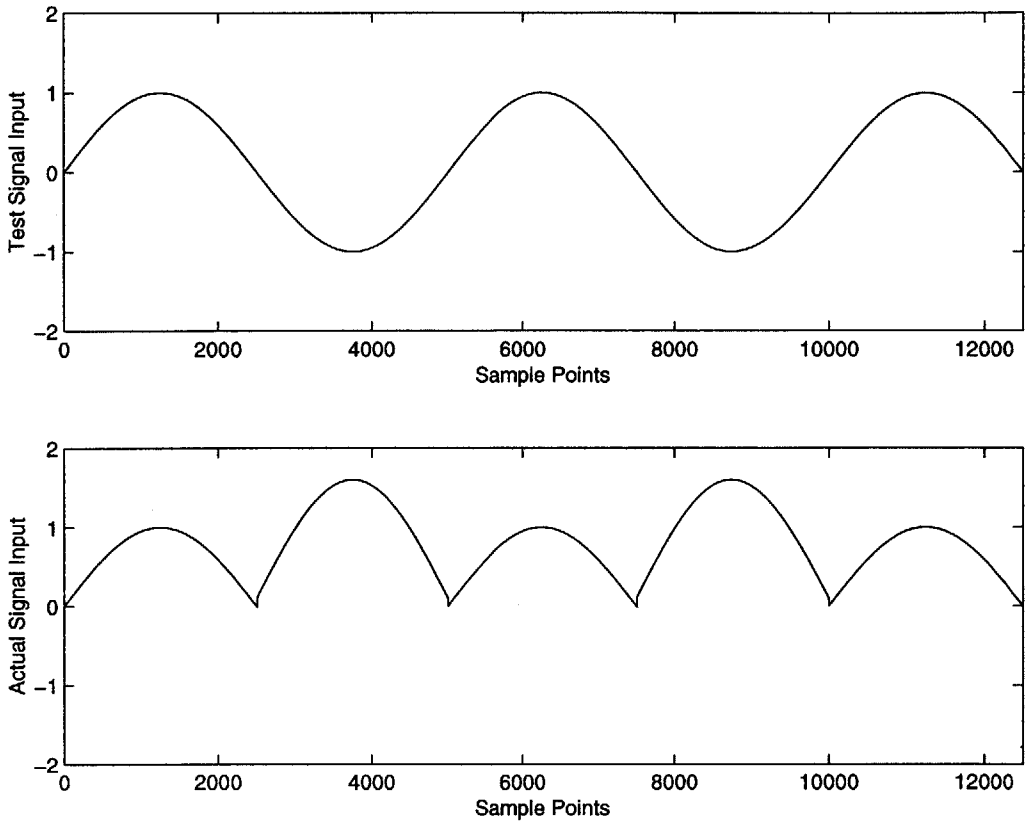

Figure E-1: Demonstration of the unwrapping algorithm. Top trace: desired waveform; Bottom trace: actual waveform after chopping, scaling and addition of offsets.

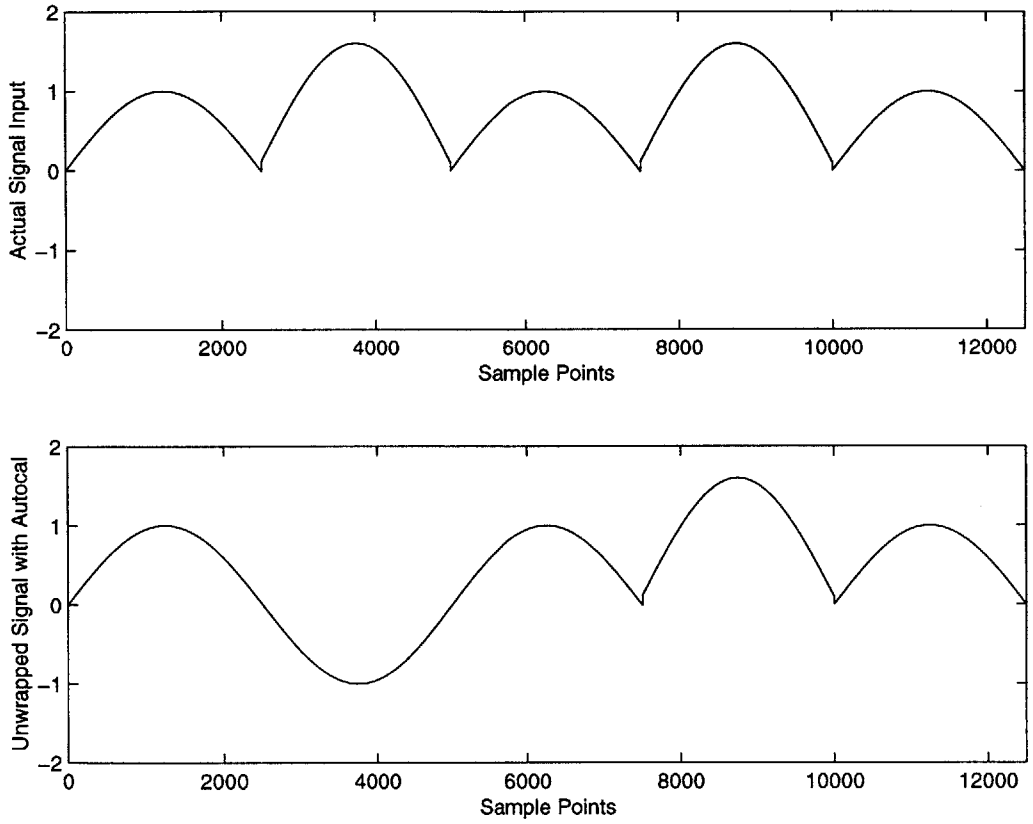

Figure E-2: Demonstration of the unwrapping algorithm. Top trace: Input waveform to algorithm with chopping, scaling and addition of offsets; Bottom trace: demonstration of unwrap algorithm on first half of waveform.

E.2 Labview Interface

The 16-bit, 100 kHz signal acquisition was obtained with a Labview PCI-MIO-16XE-10 card from National Instruments. The graphical code for this acquisition board is illustrated in Figure reffig-ADCODE. The block diagram for this program is relatively straightforward, and the details of the board's operation can be found in the DAQ PCI E-series manual from National Instruments. The user interface for monitoring the board's operation is shown in Figure reffig-ADCODE2. The output data file was formatted in ASCII, to allow for direct integration with the MATLAB programs discussed previously.

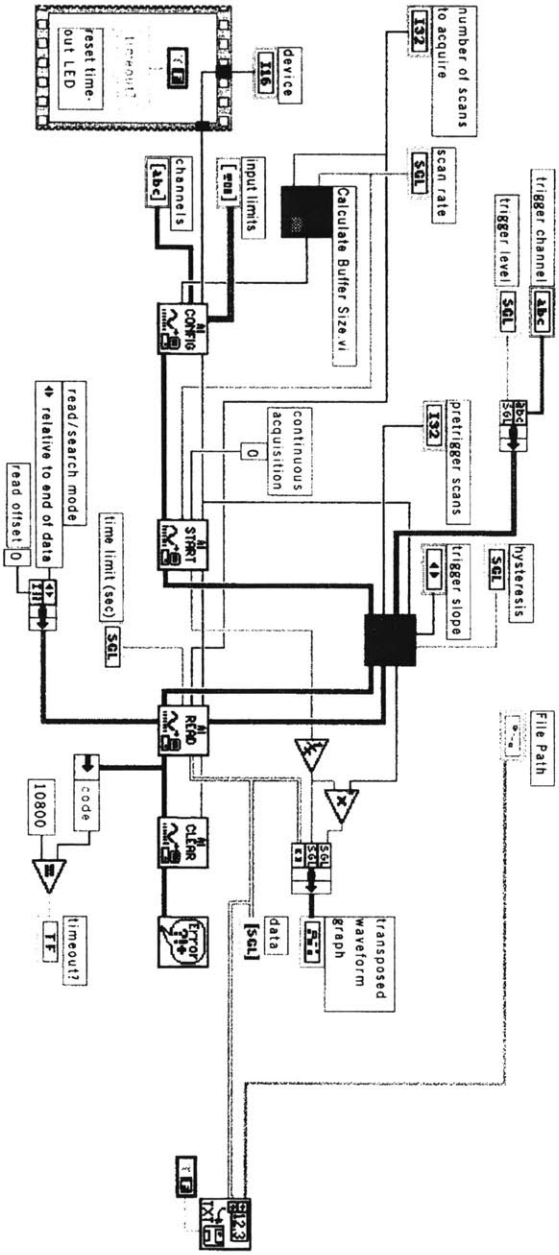

Figure E-3: Graphical program for the 100 kHz, 16-bit data acquisition board.

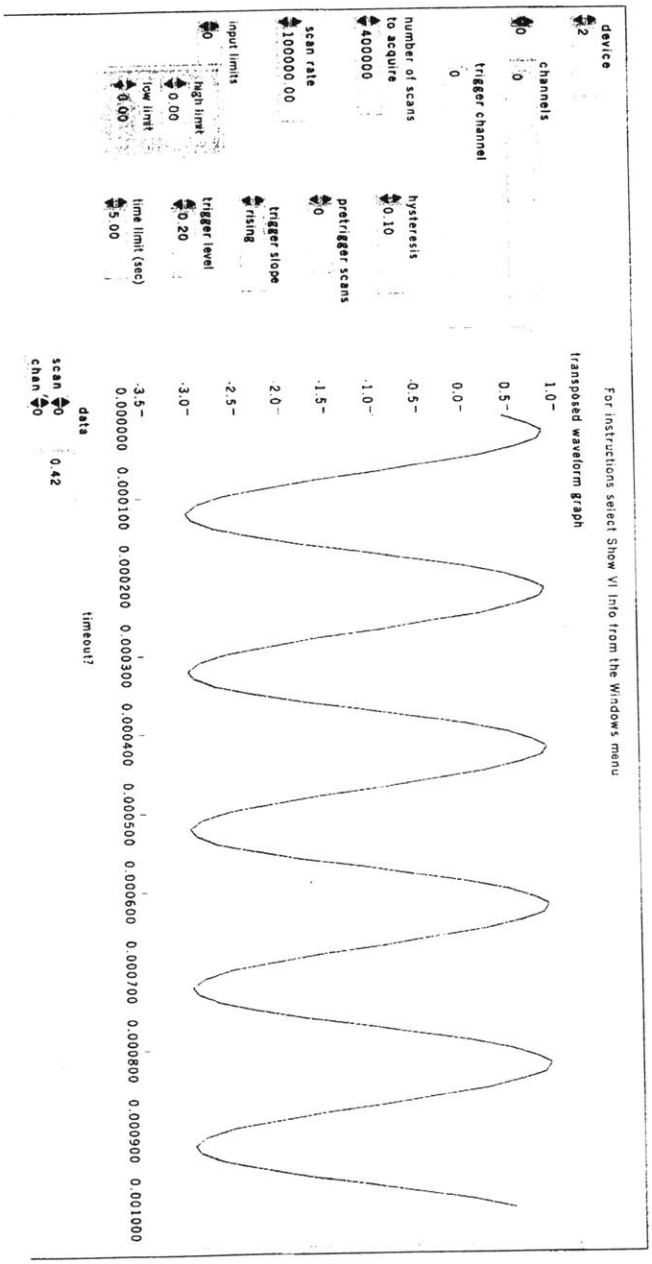

Figure E-4: Window monitor for the acquisition hardware.

7617-27